Technische Universität München
Physik-Department
Lehrstuhl für Plasmarand- und Divertorphysik

Max-Planck-Institut für Plasmaphysik

Hydrogen Isotope Exchange in Tungsten at Low Temperatures

Johannes Bauer

Vollständiger Abdruck der von der Fakultät für Physik der Technischen Universität München zur Erlangung des akademischen Grades eines

Doktor der Naturwissenschaften (Dr. rer. nat.)

genehmigten Dissertation.

Vorsitzende:	Prof. Dr. Nora Brambilla
Prüfende der Dissertation:	1. Prof. Dr. Ulrich Stroth
	2. Prof. Dr. Winfried Petry

Die Dissertation wurde am 12.10.2017 bei der Technischen Universität München eingereicht und durch die Fakultät für Physik am 05.01.2018 angenommen.

To Krissi and my family

Kurzfassung

Gegenstand dieser Arbeit ist der Wasserstoffisotopenaustausch von Deuterium (D) mit Protium (H) in Wolfram (W) bei tiefen Temperaturen um das "fill-level" Modell als zugrundeliegenden Austauschmechanismus zu untersuchen und es gegenüber dem "classical" Modell abzugrenzen.

Zunächst wird die Implantation von Deuterium mit einer Energie von 3.0 keV/D in Wolfram bei einer Temperatur von 150 K mittels in situ Kernreaktionsanalyse (NRA) und ex situ mittels Rasterelektronenmikroskopie (SEM) und Elektronenrückstreubeugung (EBSD) untersucht. Bei diesen tiefen Temperaturen zeigt sich ein linearer Anstieg der Deuteriumrückhaltung bis zu einer eingestrahlten Deuteriumfluenz von $1.6 \times 10^{21}\,\mathrm{D\,m^{-2}}$. Dieser lineare Anstieg entspricht der Rückhaltung von 100 % der implantierten Deuteriumfluenz woraus sich ein Partikelreflektionskoeffizent für Deuterium auf Wolfram von 0.27 ergibt. Für größere eingestrahlte Fluenzen ist die Zunahme der Deuteriumrückhaltung weniger stark und sättigt schließlich bei $2.07 \pm 0.25 \times 10^{21}\,\mathrm{D\,m^{-2}}$. Mittels Tiefenprofilierung ergibt sich eine Deuteriumkonzentration von 42 at.% wenn die Sättigung bei 150 K erreicht ist. Des weiteren zeigt sich, dass das Deuterium überwiegend im Bereich der Implantationszone zurückgehalten wird. Die polykristallinen Proben besitzen eine Texturierung mit Körnern deren Orientierung nahe der $\{100\}$ Ebene liegt. Die Deuteriumimplantation bei 150 K führt zur massiven Bildung von Blistern innerhalb der Körner, wobei die Form, Größe, Flächendichte und Bedeckung stark von der Kornorientierung abhängt. Auf Körner mit einer Orientierung nahe der $\{100\}$ Ebene bilden sich überwiegend kreisförmige Blister. Blister auf diesen Körnern erscheinen bereits bei einer eingestrahlten Deuteriumfluenz von $8.5 \times 10^{19}\,\mathrm{D\,m^{-2}}$ und wachsen im Durchmesser bis zu einer Fluenz von ungefähr $1.6 \times 10^{21}\,\mathrm{D\,m^{-2}}$. Für größere Fluenzen scheint die Blistergröße konstant zu bleiben. Eine mögliche Erklärung dieser Beobachtung ist das Aufbrechen der Blister während der Deuteriumimplantation. In Kombination mit der Sättigung von ionenstrahlinduzierten Defekten kann dies den linearen Anstieg und die darauffolgende Sättigung der Deuteriumrückhaltung erklären.

An solchen Deuterium gesättigten Wolframproben wird der Wasserstoffisotopenaustausch mit Protium in verschiedenen Experimenten mittels in situ Kernreaktionsanalyse und Massenspektroskopie untersucht. Im ersten Experiment wird der Austausch als Funktion der Deuteriumrückhaltung vor der Protiumimplantation bei 150 K erforscht. Die unterschiedlichen Deuteriumrückhaltungen werden durch kontrolliertes Heizen der Proben auf 200, 250 und 290 K erreicht, wodurch ein Teil des ursprünglichen zurückgehaltenen Deuterium freigesetzt wird. Ohne vorheriges Heizen tritt die Reduktion der enthaltenen Deuteriummenge bereits nach der Implantation der kleinsten Protiumfluenz ein. Im Gegensatz dazu muss eine gewisse kritische Protiumfluenz implantiert werden, um die Reduktion der zurückgehaltenen Deuteriummenge zu beobachten, wenn die Proben vorher aufgeheizt wurden. Dabei nimmt die kritische Protiumfluenz zu, je kleiner die Deuteriumrückhaltung zu Beginn der Protiumimplantation bei 150 K ist. Der Wirkungsquerschnitt des Austausches von Deuterium mit Protium bei 150 K ist unabhängig von der anfänglichen Deuteriummenge. In einem zweiten Experiment wird der Austausch einer definierten Deuteriummenge durch Protiumimplantation bei 150, 200, 250 und 290 K untersucht. Es zeigt sich, dass die kritische Protiumfluenz mit zunehmender Temperatur abnimmt während der Wirkungsquerschnitt des Austausches zunimmt. Mittels eines einfachen kombinatorischen Modells kann die Abhängigkeit des Wirkungsquerschnitts von der Temperatur als auch von der anfänglichen Deuteriummenge qualitativ erklärt werden. Abschätzungen, basierend auf SDTrimSP, zeigen, dass die kinetische Freisetzung von in der Implantationszone zurückgehaltenen Deuteriumatomen durch Kollisionen mit energetischen Protiumatomen nicht vernachlässigt werden kann und als alternativer Austauschmechanismus in Betracht gezogen werden muss.

Alle durchgeführten Experimente werden mit TESSIM-X im Rahmen des "fill-level" und des "classical" Modells, jeweils mit und ohne Berücksichtigung der kinetischen Freisetzung simuliert. Das "fill-level" Modell beschreibt die experimentellen Daten qualitativ und in manchen Fällen quantitativ, unabhängig davon ob die kinetische Freisetzung berücksichtigt wird oder nicht. Das reine "classical" Modell kann den beobachten Wasserstoffisotopenaustausch nicht erklären. Jedoch kann unter Hinzunahme der kinetischen Freisetzung das "classical" Modell die experimentellen Ergebnisse qualitativ reproduzieren. Es zeigt sich, dass ein Ensemble von "classical traps" sich unter Berücksichtigung der kinetischen Freisetzung wie eine "fill-level trap" verhält. In beiden Fällen kann die beobachtete Abhängigkeit der kritischen Protiumfluenz von der Temperatur und von der anfänglichen Deuteriummenge mit der Protiummenge erklärt werden, welche benötigt wird um die "traps" zu sättigen. Diese Sättigung verhindert den Wiedereinfang des freigesetzten Deuteriums, wodurch es zur Probenoberfläche gelangen und desorbieren kann. Im Bezug auf den Wirkungsquerschnitt des Austausches, kommt ein kombinatorische Modell für "classical traps" zu den gleichen qualitativen Ergebnissen wie das für "fill-level traps".

Abstract

In this thesis the hydrogen isotope exchange of deuterium (D) by protium (H) in tungsten (W) is investigated at low temperatures to explore the fill-level model as underlying exchange mechanism and discriminate it against the classical model.

Before the actual hydrogen isotope exchange experiments are performed the implantation of deuterium with an energy of 3.0 keV/D into tungsten at 150 K is investigated by in situ nuclear reaction analysis (NRA), ex situ scanning electron microscopy (SEM) and electron backscattering diffraction (EBSD). At these low temperatures the deuterium retention is found to increase linearly up to an irradiated deuterium fluence of $1.6 \times 10^{21}\,\mathrm{D\,m^{-2}}$. This linear increase corresponds to 100 % retention of the implanted deuterium fluence from which a particle reflection coefficient of deuterium on tungsten of 0.27 can be deduced. For higher irradiated fluences the deuterium retention levels off and saturates at $2.07 \pm 0.25 \times 10^{21}\,\mathrm{D\,m^{-2}}$. Deuterium depth profiling reveals a deuterium concentration of 42 at.% once saturation at 150 K is reached and shows that most of the deuterium is retained within the implantation zone. The polycrystalline samples possess a texture of grains with an orientation close to {100} plane. The deuterium implantation at 150 K results in massive intra-grain blister formation with the blister shape, size, number density and covered area depending strongly on the grain orientation. On grains with an orientation close to the {100} plane predominantly circular-shaped blister are observed. The blisters on those grains emerge already after irradiation of $8.5 \times 10^{19}\,\mathrm{D\,m^{-2}}$ and appear to increase in diameter for increasing irradiated deuterium fluences up to approximately $1.6 \times 10^{21}\,\mathrm{D\,m^{-2}}$. For larger fluences their size seems to remain constant. A possible explanation of this observation is the rupture of the blisters during the deuterium implantation. This, in combination with the saturation of ion-beam-induced defects, can explain the observed linear increase and the subsequent saturation of the deuterium retention during the implantation.

On such deuterium saturated tungsten samples the hydrogen isotope exchange with protium is studied in different experiments using in situ nuclear reaction analysis and mass spectroscopy. In the first experiment, the exchange is studied as a function of deuterium retention prior to protium implantation at 150 K. The different deuterium retentions are obtained by releasing a fraction of the initially implanted deuterium in Ramp & Hold cycles to 200, 250 and 290 K.

When the sample is not heated the reduction of the deuterium retention is observed directly after implantation of the first incremental protium fluence. In contrast to that, a certain critical protium fluence needs to be implanted in order to observe a reduction of the deuterium retention if the samples were heated before the exchange. This required critical protium fluence increases for decreasing deuterium retention prior to protium implantation at 150 K. Furthermore, the exchange cross section of deuterium by protium is independent of the deuterium retention prior to the exchange at 150 K. In the second experiment, the exchange of a defined deuterium amount by protium implantation at 150, 200, 250 and 290 K is studied. It is found that the required critical protium fluence decreases, while the exchange cross section increases for increasing temperatures. A simple combinatorial model based on fill-level traps is successfully applied to interpret the observed dependences of the exchange cross section on temperature and deuterium retention prior to the exchange. Furthermore, estimations based on SDTrimSP show that the kinetic de-trapping of deuterium in the implantation zone, due to collisions with energetic protium atoms, must not be neglected and needs to be considered as an alternative exchange mechanism.

All experiments are modeled with TESSIM-X in the framework of the fill-level and classical model, each with and without taking the kinetic de-trapping mechanism into account. The fill-level model with and without the kinetic de-trapping mechanism reproduces the experimental data qualitatively and in some cases quantitatively. The pure classical model is not able to explain the observed hydrogen isotope exchange. However, the classical model in combination with the kinetic de-trapping mechanism can reproduce the experimental data qualitatively. It can be shown that an ensemble of classical traps with kinetic de-trapping behaves similar to a fill-level trap. In both cases the observed dependences of the critical protium fluence on the temperature and the deuterium retention prior to exchange can be associated with the amount of protium required to saturate the traps. This prevents re-trapping of de-trapped deuterium and allows the deuterium solute front to reach the surface at which the deuterium can finally effuse from the sample. Regarding the exchange cross section, a combinatorial model for classical traps with kinetic de-trapping shows qualitatively the same results as the one for the fill-level traps.

Contents

Kurzfassung **i**

Abstract **iii**

1 Introduction **1**

1.1 A Pragmatic View on Energy Supply 1
1.2 Nuclear Fusion by Magnetic Confinement 2
1.3 Tungsten as Plasma-facing Material 4
1.4 Hydrogen Isotope Exchange in Tungsten 6
1.5 Purpose, Strategy and Outline of the Thesis 7

2 Experiments and Methods **11**

2.1 Dual Beam Experiment 11
  2.1.1 UHV Chamber 13
  2.1.2 DBE Flange 13
  2.1.3 Detectors and Data Acquisition 17
  2.1.4 Ion Sources 19
2.2 Nuclear Reaction Analysis 20
  2.2.1 Depth Profiling of D in W 21
  2.2.2 Data Evaluation with SIMNRA and NRADC 23
2.3 Electron Microscopy and Diffraction 25
  2.3.1 HELIOS NanoLab 600 26
  2.3.2 Electron Backscattering Diffraction 27
2.4 Sample Preparation 28

3 Hydrogen Isotopes in Tungsten: Principles and Modeling **31**

3.1 Transport of Hydrogen Isotopes 31
3.2 Trapping and De-trapping of Hydrogen Isotopes 34
  3.2.1 Classical Model 34
  3.2.2 Fill-level Model 35
3.3 Hydrogen Isotope Exchange 37
  3.3.1 Classical Model 37
  3.3.2 Fill-level Model 38
3.4 TESSIM-X 39
  3.4.1 Diffusion-Trapping Equation 40

3.4.2 Classical Model 41
3.4.3 Fill-level Model 42
3.4.4 Surface Processes 45
3.4.5 Implementation 46
3.5 SDTrimSP 47

4 Implantation of D into W at 150 K 49
4.1 Experimental Procedures 50
4.1.1 D Retention and Depth Profile 50
4.1.2 Surface Morphology 51
4.2 Results 52
4.2.1 Evolution of D Retention 52
4.2.2 Evolution of D Depth Profile 53
4.2.3 Evolution of Blister Formation 55
4.2.4 Grain Orientation Dependence of Blistering 62
4.3 Discussion 65
4.3.1 Initiation and Growth of Blisters 66
4.3.2 Kikuchi Pattern 69
4.3.3 Grain Orientation Dependence of Blistering 70
4.3.4 100 % D Retention 71
4.3.5 Saturation of D Retention 73
4.3.6 D Depth Profile 75
4.4 Conclusion 76

5 Exchange of D by H in W at Low Temperatures 79
5.1 Initial D Implantation 79
5.2 Exchange after Ramp & Hold to Different Temperatures 80
5.2.1 Experimental Procedure 80
5.2.2 Results 83
5.3 Exchange at Different Temperatures 89
5.3.1 Experimental Procedure 89
5.3.2 Results 92
5.4 H Implantation between Two Ramp & Holds 93
5.4.1 Experimental Procedure 93
5.4.2 Results 95
5.5 Discussion 98
5.5.1 Critical Protium Fluence 98
5.5.2 Exchange Cross Section 100
5.5.3 Influence of Different Trap Types 102
5.5.4 Alternative Exchange Mechanisms 105
5.5.5 Comparison with Literature Results 108
5.6 Conclusion 110

6 Comparison of Exchange Mechanisms with TESSIM-X 111
6.1 Modeling Inputs and Procedure 111
6.1.1 Target and Boundary Conditions 111
6.1.2 Diffusion 112
6.1.3 Implantation 113
6.1.4 Trapping and Thermally Activated De-trapping 113
6.1.5 Kinetic De-trapping 115
6.1.6 Modeling Procedure 116
6.2 Modeling Results 118
6.2.1 De-trapping Energies of Trap Types and Fill Levels . . . 118
6.2.2 Exchange after Ramp & Hold to Different Temperatures 120
6.2.3 Exchange at Different Temperatures 123
6.2.4 H Implantation between Two Ramp & Holds 125
6.3 Discussion 128
6.3.1 Evolution of D Retention 128
6.3.2 Evolution of D Depth Profile 131
6.3.3 Critical Protium Fluence 140
6.3.4 Exchange Cross Section 141
6.4 Conclusion 144

7 Summary 147

Appendix 151
A.1 3 MeV Tandem Accelerator 151
A.2 H and D Implantation into W 153
A.3 H and D Recoil Creation by H Implantation into W 154

Bibliography 155

List of Publication 177

Acknowledgment 179

Chapter 1

Introduction

1.1 A Pragmatic View on Energy Supply

From a current perspective the global energy demand is expected to increase in the future. The worldwide economic growth as well as the increasing population are the main reasons for this trend. Especially developing nations with an expanding population, such as China and India, will face an increasing energy demand. The current (2014) global primary energy mix consists of approximately 81 % fossil fuels, 14 % renewable energy and nearly 5 % nuclear fission power [1].

An undoubted advantage of power from fossil fuels, such as coal, oil or gas, is its independence from external influences. This means that the power is generated steadily and can be adjusted quickly if the energy demand changes, thus only limited energy storage is required. Furthermore, the location of the power plant is in principle not relevant for the power generation process. However, considering the natural limitation of coal, oil and gas and the political efforts to counteract climate change by the restriction of CO_2 emissions, the portion of fossil fuels in the energy mix will shrink.

In contrast to that, the portion of renewable energy, yielding no limitations regarding resources, will increase and partly substitute the fossil fuels. The use of renewable energy, such as solar, wind or hydro power, is highly depending on external conditions, e.g. incident solar radiation, windiness or local geology and geographical topology. In addition, solar and wind power are liable to daily and seasonal fluctuations and require therefore an efficient energy storing concept in order to provide the energy when it is required.

Similar to fossil fuels, nuclear fission power is mainly unaffected by external factors but faces the shortcoming of limited uranium reserves. A long-term substitution of fossil fuels by nuclear fission power is therefore not possible.

Without considering ecological and economical aspects, the energy problem can be summarized on a very abstract level as follows: Power from fossil fuels and nuclear fission power possess the advantage to be independent of external influence but have the problem of restricted resources. In contrast to that, renewable energy is not limited regarding resources but is highly affected by external factors. Hence, in a long-term an ideal energy source which substitutes fossil fuels as well as nuclear fission power to cover the increasing energy demand would fulfill both criteria: Independence of external influences and unlimited resources. An energy source which comes close to these requirements is nuclear fusion.

1.2 Nuclear Fusion by Magnetic Confinement

Nuclear fusion describes the process in which at least two atomic nuclei are brought close enough to each other that the attractive strong nuclear force exceeds the repulsive Coulomb force which results in the formation of a new atomic nucleus, other elementary particles and the release of energy. Depending on the energy balance, the fusion reactions are distinguished into endothermic and exothermic reactions. In the first one the energy to initiate the reaction is larger than the released energy, while in the latter one the opposite is the case. Numerous nuclear fusion reactions exist, but only a few are reasonable candidates for a nuclear fusion reactor [2]. Among these, the exothermic reaction of the hydrogen isotopes deuterium (D) and tritium (T) to helium (He) and a neutron given by

$$ {}^{2}_{1}\mathrm{D} + {}^{3}_{1}\mathrm{T} \rightarrow {}^{4}_{2}\mathrm{He}\,(3.5\,\mathrm{MeV}) + {}^{1}_{0}\mathrm{n}\,(14.1\,\mathrm{MeV})\,, \tag{1.1} $$

is the most promising and thus most extensively investigated one. Compared with other relevant nuclear fusion reactions the D-T reaction possesses the highest cross section and the lowest energy threshold, which is a prerequisite to ensure a high fusion rate for efficient power generation. In addition, the released energy of 17.6 MeV per reaction is also higher than for most of the other reactions [2]. Furthermore, the fuel required for the D-T reaction is not the limiting factor compared with nuclear fusion reactions based on ^{3}He. Deuterium is a stable hydrogen isotope with a natural abundance of 156 ppm [3] and could be obtained by electrolysis of heavy water. In contrast to that, tritium is an unstable hydrogen isotope which decays via a β-decay,

$$ {}^{3}_{1}\mathrm{T} \rightarrow {}^{3}_{2}\mathrm{He} + \mathrm{e}^{-} + \bar{\nu}_{e}, \tag{1.2} $$

with a half-life of 12.3 a [2]. Its natural abundance on earth is therefore very limited. However, tritium can be artificially generated in the fusion reactor itself by irradiation of lithium with neutrons via the following reactions [2]:

$$ {}^{6}_{3}\mathrm{Li} + {}^{1}_{0}\mathrm{n(thermal)} \rightarrow {}^{4}_{2}\mathrm{He} + {}^{3}_{1}\mathrm{T} + 4.78\,\mathrm{MeV}, \tag{1.3} $$

$$ {}^{7}_{3}\mathrm{Li} + {}^{1}_{0}\mathrm{n(fast)} \rightarrow {}^{4}_{2}\mathrm{He} + {}^{3}_{1}\mathrm{T} + {}^{1}_{0}\mathrm{n} - 2.47\,\mathrm{MeV}. \tag{1.4} $$

The amount of lithium on earth is estimated to approximately 226×10^{9} t, which could provide tritium for nuclear fusion reactors for several million years [3].

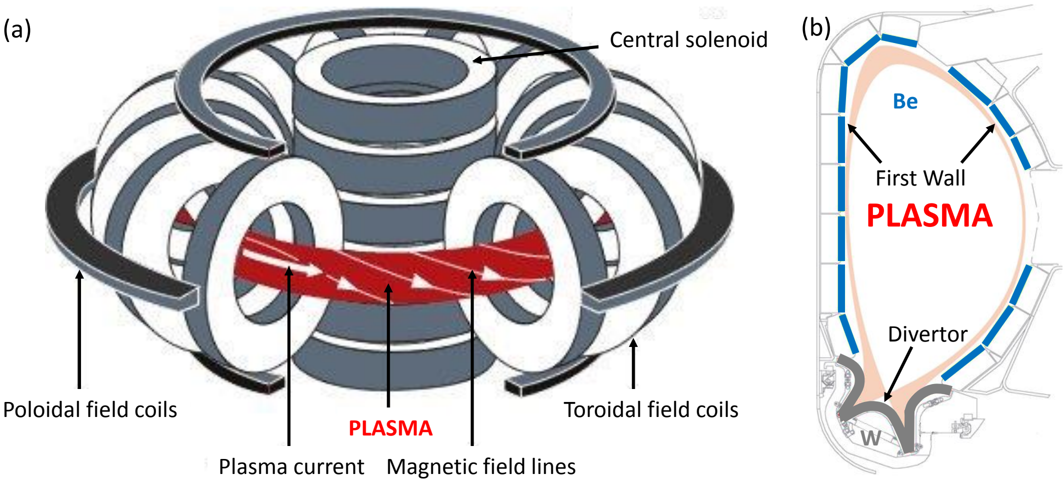

Figure 1.1: (a) Schematic illustration of the tokamak concept to obtain nuclear fusion by magnetic confinement [7]. (b) Schematic cross section of the ITER torus [8].

Nowadays, the most advanced concept to realize nuclear fusion is by magnetic confinement in a tokamak [2, 4], schematically shown in figure 1.1 (a). In such a device a plasma of deuterium and tritium is confined by a superposition of a toroidal and poloidal magnetic field in a vacuum vessel. The toroidal field component is created by the toroidal coils and the poloidal one is generated by the current induced in the plasma by the central solenoid. Additional poloidal field coils are used to control the shape and position of the plasma [2]. In order to initiate the fusion reaction in the D-T plasma, the kinetic energy of the reactants must be high enough to overcome the Coulomb barrier to some extent and get close enough to each other that the tunneling effect becomes relevant [5, 6]. This is achieved by heating the plasma with different means, such as ohmic heating, neutral beam injection, electron and ion cyclotron resonance heating, up to a temperature of $10\,\mathrm{keV}$ which corresponds to approximately $1.2 \times 10^8\,\mathrm{K}$ [2].

Figure 1.1 (b) shows a schematic illustration of the cross section of the ITER tokamak [8, 9], which is currently built in Cadarache, France. The D-shaped cross section can be divided into the main chamber and the divertor region. The main chamber is the region where most of the D-T plasma is contained and, in its center, the actual nuclear fusion reaction takes place. At the bottom of the main chamber the divertor region is located. In order to reduce the heat and particle flux onto the first wall of the main chamber, the plasma is guided in close proximity to the first wall towards the divertor region. At the divertor the heat is dissipated and the ions of the plasma are converted to neutrals and pumped from the vacuum vessel. Apart from a controlled power exhaust, the divertor allows the removal of helium ash and impurities, which otherwise accumulate and dilute or contaminate the fusion plasma [2]. As can be seen in figure 1.1 (b) the material of the first wall of ITER is beryllium (Be), while tungsten (W) is chosen for the divertor. The reasons for this choice are discussed in the following section. For a more in-depth description of nuclear fusion by magnetic confinement with respect to technological aspects and plasma physics the reader is referred to the references [2, 4–6].

1.3 Tungsten as Plasma-facing Material

The conditions to which plasma-facing components are exposed in present and future nuclear fusion devices are quite harsh and a wise material selection is a prerequisite for a successful operation of such devices. The fusion plasma influences and alters the material of the plasma-facing components which in turn affects the plasma, leading to a complex interdependent system. In the following the most important processes of plasma wall interaction, which led to the present accepted mix of plasma-facing materials in ITER, are reviewed. The energetic neutrons released in the nuclear fusion reaction impinge on the first wall and on the divertor alike, leading to the degradation of the plasma-facing components [10, 11]. Due to their low interaction with matter compared with charged particles, neutrons penetrate the material of the plasma-facing components to large depth. A direct collision of an energetic neutron with an atom of the host material results in a dense cascade in which many atoms are displaced from their original lattice positions. Thus, the irradiation with neutrons creates defects in the bulk of material exposed to the plasma. Furthermore, moderated neutrons can be captured by atoms of the host material leading to activation and transmutation of the material of the plasma-facing components and the supporting structure [12]. In addition, the neutrons can cause embrittlement and swelling of the material which changes the mechanical properties and the dimension of the potential plasma-facing material to some extent [13].

Beside the neutrons, also ions and neutral atoms of deuterium, tritium and helium impinge on the first wall and the divertor. Due to the magnetic confinement predominantly neutrals impinge on the first wall with estimated fluxes in the range of 10^{19} to $10^{21}\,\mathrm{m^{-2}s^{-1}}$ and particle energies of 8 to 300 eV. For the divertor ion and neutral fluxes larger than $10^{24}\,\mathrm{m^{-2}s^{-1}}$ with particle energies in the region of eV are expected [14]. In addition to the particles which are directly involved in the fusion reaction, also ions and neutrals of seeding gases, e.g. nitrogen, neon, argon and krypton, are present in the plasma. Those gases are injected in the divertor region to cool the plasma by energy dissipation through emission of line radiation in order to reduce the local heat load on the plasma-facing components of the divertor [15]. Compared with neutrons, the interaction of ions and neutrals with matter is high. Thus, the incident particles affect mainly the near-surface region of the plasma-facing components. One effect which is limited to the first few monolayers is erosion or sputtering. In this process atoms of the plasma-facing material are ejected due to the impact of energetic particles from the plasma [16–19]. Depending on the incident particles and the irradiated material, this physical sputtering can occur together with chemical effects which can enhance or reduce the material erosion [17]. Furthermore, the energetic particles can displace host atoms from their original lattice position, which leads to the generation of defects in the near-surface region [13]. Also a change in the surface morphology and composition of the plasma-facing materials can be caused by the impinging particles. Another issue is the excess of hydrogen isotopes induced into the plasma-wetted material and the resulting retention and permeation of radioactive tritium in and through the plasma-facing components.

In addition to the incident ions and neutrals, the plasma induces considerable heat loads on the divertor. During the normal operation mode of ITER approximately 10 to $20\,\mathrm{MW\,m^{-2}}$ are expected at the strike point where the plasma impinges and even higher ones for off normal events [20, 21]. In case of metals, those high heat loads can lead to embrittlement, once the recrystallization temperature is exceeded, or to local melting of the plasma-facing components [12]. Furthermore, the thermally induced stress can result in crack formation and ultimately in failure of the component. In order to prevent these events an effective heat removal is mandatory.

Not only are the plasma-facing components affected by the fusion plasma, but also the opposite is the case. The fusion plasma is strongly influenced by the atoms eroded from the plasma-facing components which can lead to a contamination of the plasma with fatal consequences. The accumulation of high-Z impurities in the core dilutes the fusion plasma and leads to an increased dissipation of energy by line radiation and bremsstrahlung which cools the plasma and finally terminates the fusion reaction [2].

Under consideration of all those effects, beryllium and tungsten are the best compromise and the most promising plasma-facing materials for applications in ITER [21, 22]. Beryllium is the designated material for plasma-facing components of the first wall, while tungsten is used for divertor components, as can be seen in figure 1.1 (b). The primary advantage of a low-Z material like beryllium is its reduced influence on the fusion plasma in contrast to high-Z material. When an eroded beryllium atom enters the plasma it becomes ionized. Once all electrons are stripped from the atom, no line radiation can occur. Furthermore, the low nuclear charge of beryllium atoms results in a tolerable emission of bremsstrahlung by the electrons of the plasma. Consequently, the energy dissipation and the resulting cooling of the fusion plasma is lower and a higher concentration of beryllium impurities can be tolerated compared to high-Z atoms. By choosing beryllium as plasma-facing material for the first wall, the priority is clearly on the reduced disturbance of the fusion plasma, since material properties regarding erosion, melting temperature and hydrogen retention are less convincing. However, it should be taken into account that the condition to which the first wall is exposed are less harsh as in the divertor region in normal operation mode.

Tungsten is used as plasma-facing material to address the extreme conditions prevailing in the divertor region of the fusion device [21]. The advantages of tungsten in such an environment are manifold and the most important ones are mentioned in the following. Regarding the material erosion, the high atomic mass of tungsten results in a strongly reduced sputter yield by light particles such as deuterium, tritium and helium compared to low-Z materials [16]. In terms of thermal properties, tungsten possesses an extremely high melting temperature of 3695 K in addition to a good heat conductivity which allows efficient removal of the induced heat [2, 12]. Another important advantage is the low solubility of hydrogen in tungsten [23] which results in a low retention of tritium compared with other materials, e.g. carbon [24]. This is favorable for two reasons. First, the artificially bred tritium is a precious resource in a nuclear fusion device and the retention of considerable amounts must be avoided to guarantee efficient fueling. Second, in order to meet radiation safety regulations for ITER, which currently foresee an in-vessel limit of tritium of 700 g [24], the tritium retention in plasma-facing components needs to be kept to a minimum.

However, this favorable low hydrogen retention of tungsten can be increased significantly during the operation of the fusion device. Defects generated by neutron irradiation can serve as traps for the hydrogen atoms and increase retention capability in the bulk of the material [24–26]. In addition, the incident ions and neutrals of the fusion fuel and ash [27–37] as well as from the seeding gas and other impurities [37–43] alter the potential hydrogen retention in the near-surface region. In case of a major maintenance event, which requires the opening of the vacuum vessel of the fusion device, it is reasonable to reduce the amount of tritium retained by the plasma-facing materials for radiation safety reasons. One method is heating the relevant components, which leads to the mobilization and the desorption of the retained tritium [24]. Another possibility to reduce the tritium inventory in the tungsten components before such an event would be to perform hydrogen isotope exchange in which the trapped tritium atoms are substituted by other non-radioactive hydrogen isotopes [44].

1.4 Hydrogen Isotope Exchange in Tungsten

In principle, the effect of hydrogen isotope exchange in tungsten describes the replacement of one trapped hydrogen isotope, e.g. deuterium (D), by another different isotope, e.g. protium (H). Unfortunately, the detailed processes which lead to the replacement are still unclear and subject of current research. In order to gain a better understanding of the effect, many experiments have been devoted to hydrogen isotope exchange in tungsten. The exchange of deuterium by protium or vice versa was studied by irradiating tungsten sequentially with ion beams [44, 45], plasmas [44, 46–48] or neutral beams [49–52]. Subject of these studies was the exchange at the surface [48–52], in the bulk [44–47, 51, 52] as well as in heavy-ion-beam-damaged [46, 47, 50] and undamaged [44, 45, 49] tungsten. Even the influence of helium in a protium plasma on the exchange of deuterium was investigated [53].

Several models have been proposed to simulate the observed experimental results, e.g. the local mixing model by Doyle et al. [54, 55], an analytical exchange model by Barton et al. [56] or a rate equation model by Markelj et al. [49, 52]. Those models differ in certain aspects, for instance, whether transport effects are included, if isotopic exchange is only considered at the surface or in the bulk and to the extent to which surface processes are taken into account. All models, except the one by Markelj et al. [49] which treats the exchange at the surface in detail, describe the hydrogen isotope exchange only empirically via the introduction of exchange cross sections or exchange probabilities. The underlying microscopic mechanism of the exchange in the bulk remained unknown so far.

A prerequisite to gain a microscopic understanding of the exchange effect, is to understand how hydrogen isotopes interact with traps in tungsten microscopically. One well established model to describe trapping and de-trapping of hydrogen in metals on a microscopic scale is provided by Krom et al. [57] and termed **classical model** in this thesis. This model is based on the assumption that one hydrogen atom occupies one trap site. Furthermore, each trap site is characterized by a well-defined de-trapping energy which needs to be overcome in order to release the hydrogen atom.

In contrast to this classical model, recent density functional theory (DFT) studies showed that single vacancies [58–61] as well as dislocations [62] in tungsten are capable of trapping several hydrogen atoms at a time. Furthermore, the de-trapping energy required to release a hydrogen atom from such a trap site depends on the number of atoms contained in the trap with the tendency to decrease as the number of trapped atoms increases. These theoretical considerations finally led to the development of the **fill-level model** [63, 64]. The attempt to explain the hydrogen isotope exchange observed by Roth et al. [44] on a microscopic scale within the framework of the classical model was not successful [63], i.e., the amount of deuterium released during the exchange with protium was underestimated. In contrast to that, the fill-level model, provides the possibility to explain the experimental data of Roth et al. [44, 63].

1.5 Purpose, Strategy and Outline of the Thesis

The greater purpose of this thesis is to contribute to a better understanding of the hydrogen-tungsten system which, despite its apparent simplicity, yields many unsolved questions. In particular, the here-conducted experiments and simulations intend to provide a deeper insight into the phenomenon of hydrogen isotope exchange in tungsten. The focus lies on the quest for further evidence which supports the fill-level model and discriminates the classical model as underlying mechanism of the exchange.

As will be outlined in detail in the following, the classical and fill-level model differ with respect to the possibility to exchange hydrogen isotopes in traps which do not show thermally activated de-trapping at the given temperature.

Hence, in this thesis different experimental scenarios are constructed at which the isotopic exchange of deuterium by protium should only be explainable in the framework of the fill-level model, but not in the classical model. The DFT calculations by Fernandez et al. [61] showed that up to twelve hydrogen atoms can be contained in one vacancy which corresponds to twelve possible fill levels with different de-trapping energies. However, at 300 K only up to six hydrogen atoms are retained in one vacancy since the de-trapping energies of higher fill levels are too small to prevent thermal release. In order to access also the fill levels with lower de-trapping energy the hydrogen isotope exchange experiments in this thesis are performed at low temperature in the range of 150 to 290 K. This also implies that the initially retained amount of deuterium which can be exchanged by protium is larger compared to higher temperatures, which is beneficial for two reasons. First, the effect of hydrogen isotope exchange is more prominent since the total exchangeable amount is larger. Second, from an experimental point of view it is easier to monitor a large quantity of deuterium than a small one. The hydrogen isotope exchange data obtained in those dedicated experiments is finally simulated based on the fill-level and the classical model. From the reproducibility of the experimental data by the simulations as well as from the comparison of the simulation results obtained with the different models new insights on the mechanism of hydrogen isotope exchange in tungsten are expected.

The setups and methods used in the experiments conducted in the scope of this thesis are presented in chapter 2. In particular, the dual beam experiment (DBE) in which the exchange of deuterium by protium in tungsten at low temperatures is studied in situ is described in detail. This includes nuclear reaction analysis (NRA), which is used to monitor the deuterium retention during the implantation and the exchange with protium, as well as mass spectrometry (QMS), which is applied to determine the effusion of deuterium from the sample during the experiments. Furthermore, the scanning electron microscope (SEM) for visual inspection of the tungsten samples is briefly presented and the electron backscattering diffraction (EBSD) method to obtain information on the grain orientation is explained. In addition, the preparation procedure of the tungsten samples used in the here-conducted experiments is reviewed.

In chapter 3 the transport of hydrogen isotopes in tungsten is briefly described and the principle of trapping and de-trapping within the classical and fill-level model is illustrated. In addition, the process of hydrogen isotope exchange is discussed for both models and the differences are highlighted. Furthermore, the fundamentals of the TESSIM-X code [63, 65] which is applied to simulate diffusion, trapping and exchange of different hydrogen isotopes in tungsten are introduced. In particular, the mathematical description of the classical and fill-level model within TESSIM-X is explained in detail. Finally, the SDTrimSP code [66, 67], which is used to determine essential input parameters for TESSIM-X, is briefly discussed.

The influence of the initial implantation of energetic deuterium ions at low temperature on the tungsten samples is investigated in terms of the deuterium retention and the surface morphology in chapter 4.

The experimental investigation of the hydrogen isotope exchange in tungsten at low temperature by means of nuclear reaction analysis and mass spectrometry is presented in chapter 5. The different scenarios in which hydrogen isotope exchange should only be observable when the fill-level model applies are illustrated and their experimental realizations are presented. The exchange of deuterium by protium is studied as a function of the deuterium amount prior to the exchange and as function of the temperature at which the exchange is conducted. A simple combinatorial model is used to interpret the experimental observations in the context of the fill-level model qualitatively. The role of different trap species is discussed and alternative exchange mechanisms, e.g. kinetic de-trapping of deuterium by energetic protium, are evaluated.

The simulation of the experimental data with TESSIM-X is covered in chapter 6. First, the input parameters and the assumptions which enter the TESSIM-X simulations are discussed. Subsequently, the de-trapping energies of the different fill levels and trap types are determined from the experimental data in the framework of the fill-level and the classical model. The simulations of the experimental hydrogen isotope exchange data is conducted on the basis of the fill-level and the classical model, each with and without the kinetic de-trapping mechanism discussed in chapter 5. The simulation results of the different models are compared in detail and suggestions for further experimental investigations are made.

Finally, the most important insights gained in this thesis are summarized in chapter 7.

Chapter 2

Experiments and Methods

In this chapter the experimental setups and methods which are used in this thesis are described. First, the technical details of the dual beam experiment (DBE), in which the hydrogen isotope exchange of deuterium by protium is investigated in situ with nuclear reaction analysis (NRA), are discussed. This includes the DBE flange and the corresponding UHV chamber, the ion source to implant the hydrogen isotopes, as well as the tandem accelerator which provides the energetic ^{3}He ions for NRA. Second, the principle of nuclear reaction analysis is reviewed and the data evaluation with SIMNRA 6.8 [68] and NRADC [69] is explained. Finally, the HELIOS NanoLab 600 scanning electron microscope, which is used to investigate the surface morphology and the crystallographic microtexture of the tungsten samples, is presented. In particular, the principle of the electron backscattering diffraction (EBSD) to determine the crystal orientation of individual grains is reviewed.

2.1 Dual Beam Experiment

The dual beam experiment, which was initially designed to investigate erosion of tungsten under simultaneous irradiation of different ion species [70], was modified in the course of this thesis to study deuterium retention in tungsten. The principle setup of the dual beam experiment is shown in figure 2.1. It consists of an ultra-high vacuum (UHV) chamber on which the DBE flange is mounted. Two ion sources, a duoplasmatron and a Cs-sputter ion source, with the associated beamlines are attached to the chamber. The whole experiment is connected to the 30 ° beamline of the 3 MV tandem accelerator which provides energetic ions for ion beam analysis and is described in appendix A.1. In contrast to the Cs-sputter ion source the duoplasmatron and the accelerator beamline share the same port into the UHV chamber.

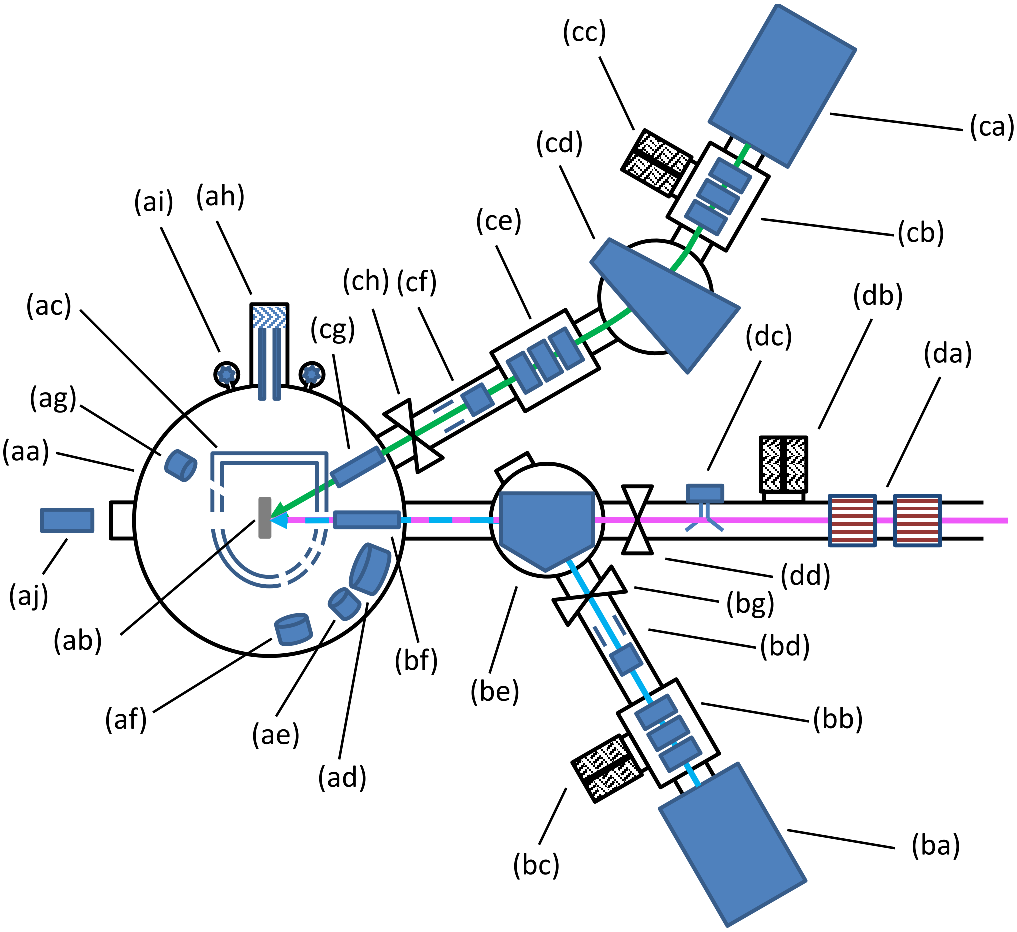

Figure 2.1: Schematic topview of the dual beam experiment: (aa) UHV chamber, (ab) sample, (ac) secondary electron suppressor, (ad) proton detector, (ae) RBS detector, (af) alpha detector, (ag) ERDA detector, (ah) quadrupole mass spectrometer, (ai) calibration leaks, (aj) CCD camera, (ba) duoplasmatron ion source, (bb) Einzel lens, (bc) turbo molecular pump, (bd) electrostatic x-y steerer, (be) bending magnet, (bf) shutter and aperture system, (bg) valve, (ca) Cs-sputter ion source, (cb) Einzel lens I, (cc) turbo molecular pump, (cd) bending magnet, (ce) Einzel lens II, (cf) electrostatic x-y steerer, (cg) shutter and aperture system, (ch) valve, (da) magnetic x-y steerer, (db) turbo molecular pump, (dc) beam profile monitor, (dd) valve.

2.1.1 UHV Chamber

The UHV vessel, on which the DBE flange is mounted with a rubber gasket, possesses a cylindrical shape with a diameter of 56.0 cm and a height of 63.3 cm. The vacuum is generated by the combination of a turbomolecular pump with a rotary vane pump as roughing pump. Furthermore, a cryopump is installed, which cools a copper plate at the bottom of the UHV chamber to 106 K. The pressure inside the UHV chamber is measured by a pressure gauge consisting of a Pirani and a cold cathode system covering a pressure range between 5×10^{-9} and 1×10^{3} mbar. The base pressure of the UHV chamber obtained without cryopump in operation is 5×10^{-8} mbar. Operating the cryopump results in a better pumping of the remaining water and a base pressure of $< 5 \times 10^{-9}$ mbar is achieved.

A Hiden HALO 201 quadrupole mass spectrometer is attached to the UHV chamber that can be operated in the multiple ion detection mode, which allows the detection of different masses as a function of time. By recording the sample temperature at the same time it is possible to perform in situ temperature desorption spectroscopy (TDS). In order to gain quantitative information from the mass spectra a calibration of the quadrupole mass spectrometer is mandatory. Thus, two D_2 calibration leak valves with leak rates of 7.5×10^{-8} and 1.0×10^{-7} atmscc/s and one H_2 calibration leak valve with a leak rate of 4.98×10^{-6} atmscc/s are installed at the chamber.

2.1.2 DBE Flange

All relevant devices regarding manipulation, heating and cooling of the samples as well as the detectors for ion beam analysis are mounted on the DBE flange shown in figure 2.2.

Manipulator

A 2-axis manipulator (a), depicted in figure 2.2, is installed on the DBE flange, allowing a vertical movement of the sample by 162 mm and a rotation of -32 to $+80\,^{\circ}$ with respect to the analysis beam. The UHV part of the manipulator is electrically isolated in order to measure the current on the manipulator created either by the ion beam analysis or the ion implantation. The sample stage, which accommodates up to two samples under study, the calibration sample holder, as well as the beam viewing system are mounted on the manipulator.

LN_2 Sample Cooling System

In order to investigate the behavior of hydrogen isotopes in tungsten below room temperature, the DBE setup has been upgraded with a sample cooling system, as can be seen from figure 2.2. It consists of a liquid nitrogen tank (b), a copper gauze (c) and a cooling finger (d), to which the sample holder (e)

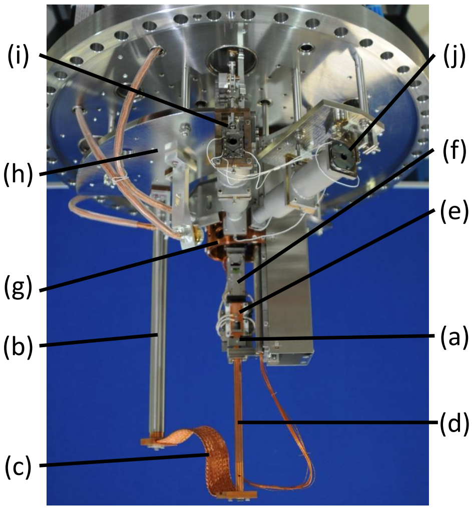

Figure 2.2: DBE flange (a) 2-axis manipulator, (b) liquid nitrogen tank, (c) Cu gauze, (d) Cu cooling finger, (e) sample stage, (f) calibration sample holder, (g) secondary electron suppressor, (h) detector stage, (i) shutter and aperture system of the ion beam analysis and duoplasmatron ion beams, (j) shutter and aperture system of ion beams provided by Cs-sputter ion source.

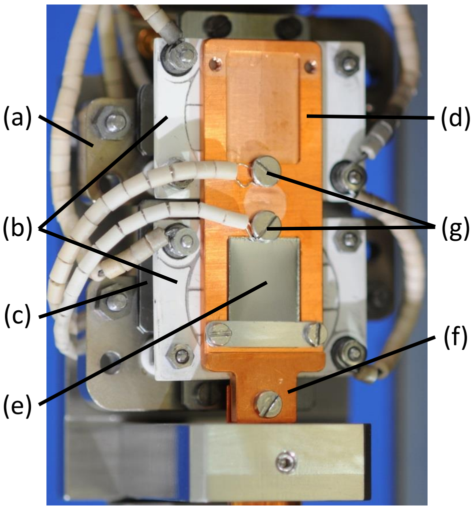

Figure 2.3: DBE sample stage (a) base plate, (b) boralectric® heater, (c) Ta heat shield, (d) Cu sample holder, (e) sample, (f) connection to cooling finger, (g) K-type thermocouple.

is attached. The liquid nitrogen tank is essentially a steel tube which reaches into the UHV chamber. The end of the tube inside the chamber is closed by a copper plug in order to ensure a good thermal connection to the copper gauze. The other end of the tube is attached to a reservoir of liquid nitrogen, which is automatically refilled. The length of the tube is designed to bring the liquid nitrogen close to the sample in order to minimize losses by thermal conduction. A positive side effect is that the tube itself acts as a cryo trap which improves the vacuum in the chamber. Since the mobility of the manipulator must not be constrained, a flexible copper gauze is used to connect the liquid nitrogen tank with the manipulator. The steel guiding rod of the manipulator has been replaced by a copper rod, which acts in addition as a cooling finger to which the sample holder is attached. An aluminum nitrate plate is inserted between the copper plug of the nitrogen tank and the copper gauze to provide electrical isolation of the manipulator while guaranteeing a good thermal contact.

Sample Stage

The sample stage, shown in figure 2.3, is mounted on the manipulator. It consists of a base plate (a) on which two boralectric® heaters (b) are attached. In order to prevent the base plate and the manipulator from heating up, a stack of three tantalum plates (c), which serves as a heat shield, is inserted between the heaters and the base plate. Up to two tungsten samples (e) can be clamped on the copper sample holder (d) which is screwed on the copper cooling finger (f). The sample holder is designed such that the rotation axis of the manipulator lies within the surface of the tungsten samples. The boralectric® heaters are pressed by screws to the backside of the sample holder in order to assure conductive heating and not only radiative heating as in the old design. The temperature measurement is realized by K-type thermocouples (g) clamped to the surface of the samples. In order to keep the manipulator electrically isolated, the measured thermovoltage is transferred to the Eurotherm 902 via an optocoupler, from where it is fed into the experiment computer. With this combination of cooling system and sample stage a sample temperature of 140 K is reached after 15 h. The Eurotherm 902 is also integrated in a temperature feedback loop, which allows to hold a desired sample temperature or to heat the sample with a defined heating rate of up to $2\,\mathrm{K\,min^{-1}}$. Furthermore, the manipulator contains a calibration sample holder, shown in figure 2.2 (f), which can be loaded with specific reference samples, e.g. amorphous deuterated carbon thin films (a-C:D) on silicon, to perform an energy calibration of the detectors.

Beam Viewing System

The shape and position of ion beams from the two ion sources as well as the analysis ion beam can be observed with the beam viewing system installed on the manipulator. The centerpiece of the system is a cesium iodine crystal which is stimulated to emit light by ion beam induced luminescence. The generated light is observed by a pixelfly qe CCD camera which is in line-of-sight to the accelerator beamline, as can be seen in figure 2.1 (aj). Charging of the crystal is avoided by a metal mesh at the front of the crystal. Furthermore, a silica glass disc is mounted at the backside of the crystal for mechanical support.

Pneumatic Shutter and Aperture System

The DBE flange is equipped with two pneumatic shutter and aperture systems which give control over the ion beam irradiation and define the size of the ion beams provided by the 3 MV tandem accelerator and the two ion sources. Since the ion beams from the accelerator and the duoplasmatron share the same port into the UHV chamber, as shown in figure 2.1 (bf), the corresponding shutter and aperture system, schematically depicted in figure 2.4, is more complex. It consists of two mobile plates, indicated as A 1 and A 2 with two circular apertures each, a shutter S and an aperture Sup 1 biased to −120 V with respect to ground. Ion beam analysis requires a small beam size, while for ion implantation a large beam size is preferred. For this reason A 1 and A 2 are designed with two apertures of different diameter one for ion beam analysis and one for ion implantation. Depending on the experiment, the required set of apertures is shifted into the beam by a pneumatic mechanism. The beam-defining apertures are located on A 2 and possess a diameter of 1.5 and 5.0 mm for ion beam analysis and ion implantation, respectively. The corresponding apertures on A 1 are slightly larger and have a diameter of 3.0 and 10.0 mm. In addition, A 1 is equipped with four isolated sector plates. By measuring the ion current on the sector plates, the horizontal and vertical position of the analysis ion beam with respect to the aperture can be determined which facilitates the alignment of the ion beam. In contrast to A 1 and A 2 the biased aperture Sup 1 is fixed and possess a diameter of 6.0 mm. The shutter S can be shifted into the ion beam to stop the implantation after the required fluence is obtained. The shutter and aperture system of the Cs-sputter ion source follows the same design, with the difference that the plates A 1 and A 2 are fixed and possess only one aperture each.

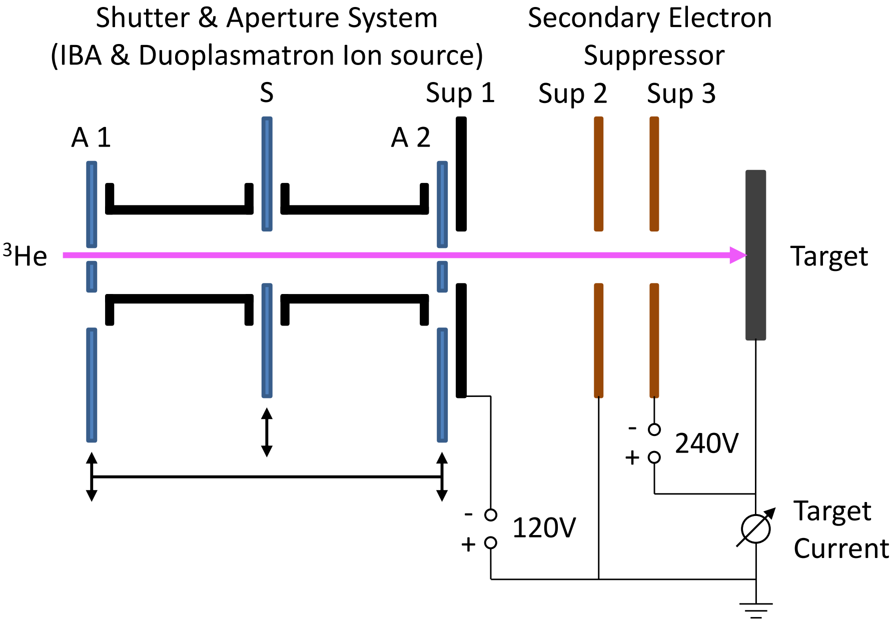

Figure 2.4: Pneumatic shutter and aperture system for ion beams provided by the 3 MV tandem accelerator and the duoplasmatron ion source with the applied bias voltages to suppress the effects of secondary electrons. The description is given in the text.

Secondary Electron Suppressor

The ion flux during implantation and ion beam analysis is determined by measuring the current created on the manipulator. In order to reliably determine the implanted fluence or the acquired charge during ion beam analysis a correct current measurement is inevitable. Ions impinging on the sample create secondary electrons which can leave the sample. Hence, the measured current on the manipulator, caused by positive ions entering and electrons leaving the sample, is larger than the actual incoming ion current. To address this problem the manipulator is surrounded by a secondary electron suppressor Sup 3, as illustrated in figure 2.4, which is on a negative potential of −240 V with respect to the manipulator. Hence, secondary electrons created by the ion impact are forced back to the manipulator by the electric field. In order to account for electrons which reach the suppressor the current on the manipulator as well as on the suppressor is measured. The grounded cage Sup 2 encloses the suppressor Sup 3 to shield the electric field. Since the guiding rod of the manipulator sticks out of the suppressor cage, the manipulator is kept on ground potential to avoid the attraction of electrons from other sources such as the pressure gauge. In addition, the aperture Sup 1 is biased to −120 V with respect to ground to repel secondary electrons generated at the beam-defining aperture A 2.

2.1.3 Detectors and Data Acquisition

Detectors

The detection of either backscattered projectiles, i.e., ^{3}He, or particles originating from the induced nuclear reaction, i.e., alpha particles and protons, which is discussed later in detail, is performed with two similar types of solid state detectors. A surface barrier detector (SBD) is used to monitor the protons, while passivated implanted planar silicon (PIPS) detectors are employed to measure the emitted alpha particles and the backscattered ^{3}He ions. The detectors are installed on the detector stage (a), shown in figure 2.5. The alpha (b) and the RBS detector (c) are mounted such that the incident ^{3}He ion beam, the surface normal of the sample and the beam of detected particles are within the same plane. The proton detector (d) is located out of this plane by 45 °. Furthermore, the angle of incidence of the ^{3}He ion beam on the sample is 90 ° with respect to the sample surface. In order to protect the detectors from reflected hydrogen isotopes during ion implantation a pneumatic shutter (g) which can cover all three detectors is installed.
The RBS detector, used to monitor the backscattered ^{3}He ions, possesses a thickness of 50 µm, an active area of 100 mm^2 and a stated energy resolution of 12 keV. It is placed under a scattering angle of 135 ° at a distance of 94.9 mm from the sample surface. A rectangular aperture of 11.3×2.1 mm^2 is installed in front of the detector, resulting in a measured detector solid angle of 1.18 ± 0.04 msr. The voltage applied on the detector is 41 V.
The alpha detector, which is applied to record the alpha particles released in the nuclear reaction, has a thickness of 700 µm and an active area of 300 mm^2. A voltage of 150 V is applied on the detector and the stated energy resolution is 15.2 keV. The detector is mounted with a rectangular aperture of 19.6×1.3 mm^2 under a scattering angle of 105 ° at a distance of 91.6 mm from the sample surface. The solid angle obtained from calibration measurements is 3.06 ± 0.17 msr. Since the spectrum of the backscattered ^{3}He ions would mask the spectrum created by the alpha particles, a 3.5 µm Mylar foil is placed in front of the detector to prevent the ^{3}He ions from entering.

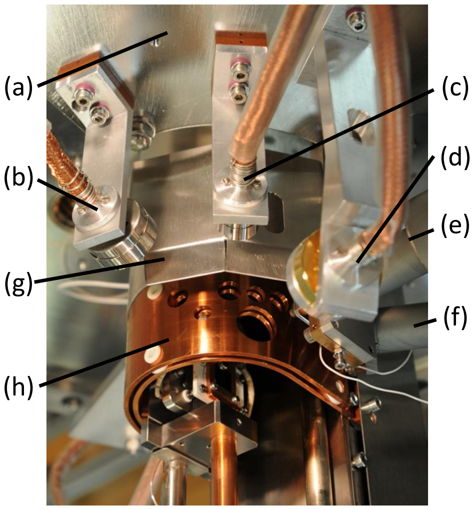

Figure 2.5: Detectors of the dual beam experiment (a) detector stage, (b) alpha detector, (c) RBS detector, (d) proton detector, (e) shutter and aperture system of ion beam analysis and duoplasmatron beamline, (f) shutter and aperture system of Cs-sputter ion source beamline, (g) detector shutter, (h) secondary electron suppressor

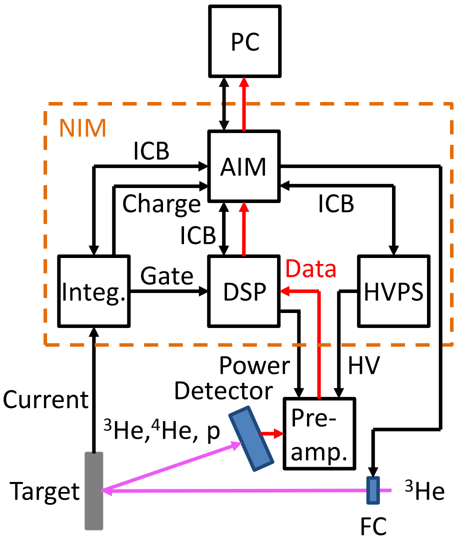

Figure 2.6: Schematic data acquisition of the dual beam experiment consisting of a pre-amplifier (Pre-amp.), detector and Faraday cup (FC) located at the experiment and a digital signal processor (DSP), high voltage power supply (HVPS), current integrator (Integ.) and acquisition interface module (AIM) contained in a nuclear instrumentation standard (NIM) crate.

The proton detector possesses a thickness of 1500 µm and an active area of 450 mm^2. A voltage of 200 V is applied on the detector and the specified energy resolution is 21 keV. It is mounted at a distance of 126 mm with respect to the sample surface at a scattering angle of 144.5 °. A circular aperture with a diameter of 24.0 mm^2 is installed on the detector, defining the measured solid angle to 21.30 ± 1.05 msr. In addition, it serves as clamp to keep the protective foil in front of the detector in place. A 12 µm Mylar foil with a 10 nm gold layer reduces the amount of backscattered ^{3}He ions entering the detector, which extends the lifetime and reduces the dead time during the measurement.

Data Acquisition

The data acquisition system of the DBE setup is schematically shown in figure 2.6. An energetic particle, e.g. ^{3}He ion, alpha particle or proton, which impinges on the detector creates a certain number of electron-hole pairs proportional to its energy. The high voltage, applied on the detector by the high voltage power supply (HVPS) through the pre-amplifier (Pre-amp.), separates the electrons from the holes and a current pulse on the detector is observed. This current pulse is essentially integrated by the pre-amplifier to obtain the charge created by the incident particle. The output signal of the pre-amplifier is an inverted tail pulse, with an amplitude proportional to the accumulated charge and therefore proportional to the particle energy. This analog signal is transferred to the digital signal processor (DSP), where it first undergoes a pile-up rejection and is subsequently transformed into a digital signal. Trapezoidal filtering is performed on the digitized signal to determine the pulse height. This information is transmitted to the acquisition interface module (AIM) which contains the multichannel analyzer (MCA). The MCA saves the event according to the pulse height, respectively particle energy, into a certain channel and thereby builds a histogram as the number of events increases. This histogram, reflecting the energy distribution of the measured particles, is transferred to the experiment computer. The AIM is the central unit in the data acquisition system, except for the data transfer, it communicates and controls the DSP, the HVPS and current integrator (Integ.) via the interconnection bus (ICB).

The comparison of different measurements, e.g. to assess the deuterium content in different samples, requires the reproducibility of the measurement process. This is ensured by defining the number of ions from the analysis beam impinging on the sample, which is equivalent to acquiring a certain ion charge. As soon as the measurement is started, a Faraday cup (FC), used as a shutter, is retracted from the beamline to let the ions pass to the sample. At the same time the current integrator, consisting of the integrator and an analog digital converter (ADC), starts to measure and integrate the ion current on the sample. After acquiring a certain incremental charge, the data is transferred to the AIM where it is summarized and saved. In order to prevent the DSP from acquiring data before the current measurement is started, the DSP is triggered by the Gate signal from the current integrator. Once the preset ion charge is reached, typically 1–20 µC, the AIM stops the data acquisition of the DSP and the current integrator and shifts the Faraday cup back into the beamline again.

2.1.4 Ion Sources

The DBE setup is equipped with two ion sources, a duoplasmatron (ba) and a Cs-sputter ion source (ca) as illustrated in figure 2.1, to generate ions from gaseous and solid materials, respectively. Due to superior stability, better spatial homogeneity and higher ion flux, the here-presented experiments are exclusively performed with the duoplasmatron. Hence, only the duoplasmatron and the associated beamline are described. For the operation principle of the Cs-sputter ion source and further information on different types of ion sources the reader is referred to [71].

The installed ion source is a Model PS 120 Duoplasmatron Ion Source manufactured by Peabody Scientific [72]. The key components are the filament, providing the electrons by thermionic emission and acting as cathode, an inter-

mediate electrode and an anode with the plasma expansion cup. Furthermore, a coil surrounding the ion source generates a strong axial magnetic field. During operation two gas discharge regions with different plasma densities are maintained. A plasma of low density between the filament, and the intermediate electrode, which acts as an anode, is established. The plasma is compressed by a double layer and guided through the channel of the intermediate electrode. The axial magnetic field between the intermediate electrode, now representing the cathode, and the anode compresses the plasma further. Through the small aperture in the anode the plasma leaks into the expansion cup from where the positive ions are extracted with a voltage of up to 10 kV [70, 71]. During operation with pure hydrogen gas, as is the case for the here-conducted experiments, the predominantly generated ion species are H_3^+ and D_3^+, respectively.
After extraction the ions are focused into the bending magnet (be) by an Einzel lens (bb) to which a voltage of up to 10 kV can be applied, as shown in figure 2.1. The bending magnet, acting as a mass separator, is used to select and transfer a specific hydrogen ion species with a well-defined energy to the UHV chamber. The ion implantation into the sample can be controlled by the shutter and aperture system, depicted in figure 2.4, and the ion current generated at the sample is measured with a Keithley 6487 Picoamperemeter. In order to adjust the ion beam vertically and horizontally, an electrostatic x-y steerer (bd), consisting of two pairs of deflection plates oriented in series perpendicular to each other, is installed in front of the bending magnet.
The here-conducted experiments require a homogeneous ion flux distribution across the implantation spot. This can be achieved by adjusting the Einzel lens (bd) such that the ion beam becomes defocused, which results in a slightly elliptical beam spot with small and large diameters of 7.0 and 7.2 mm, respectively.

2.2 Nuclear Reaction Analysis

Standard techniques for elemental analysis which rely on the properties of the element-specific electronic system, e.g. X-ray photoelectron spectroscopy, Auger electron spectroscopy or X-ray fluorescence spectroscopy, are not able to detect hydrogen, not to mention the isotopic sensitivity. However, alternative techniques which exploit other properties of the hydrogen atom, e.g. nuclear properties or mass, are able to identify hydrogen and its isotopes. Among those techniques are neutron scattering, nuclear magnetic resonance spectrometry (NMR), elastic recoil detection analysis (ERDA) and secondary ion mass spectroscopy (SIMS), each with its respective advantages and disadvantages [73].
Another method, which is applied in the here-conducted experiments, is nuclear reaction analysis (NRA) [74]. As the name already implies, the method takes advantage of specific nuclear reaction of the species under investigation with other provided particles. A well-known and frequently used nuclear re-

action to detect deuterium is the exothermic reaction of a ^{3}He nucleus with a deuterium nucleus to produce an alpha particle and a proton given by

$$^3_2\mathrm{He} + {}^2_1\mathrm{D} \longrightarrow {}^1_1\mathrm{p} + {}^4_2\mathrm{He} + 18.352\,\mathrm{MeV}, \tag{2.1}$$

or in standard nuclear physics notation as

$$\mathrm{D}\left({}^3\mathrm{He}, \mathrm{p}\right)^4\mathrm{He} \qquad \text{or} \qquad \mathrm{D}\left({}^3\mathrm{He},{}^4\mathrm{He}\right)\mathrm{p}, \tag{2.2}$$

depending whether the alpha particle or the proton is regarded as the remaining target-like product. By measuring the total yield and the energy spectrum of the particles emitted in this nuclear reaction, it is possible to quantify the amount of deuterium and gain information on the deuterium concentration as a function of depth, i.e., the deuterium depth profile, in the sample under study.

2.2.1 Depth Profiling of D in W

In figure 2.7 (a), the cross section of the D(^{3}He,p)^{4}He nuclear reaction is shown as a function of the ^{3}He ion energy in the laboratory system for the given measurement geometry of the protons, i.e., a scattering angle of 144.5 ° [75]. The cross section possesses a broad resonance at a ^{3}He ion energy of 0.63 MeV with a FWHM of 0.72 MeV and a maximum of approximately 60.4 mb sr^{-1}. At higher ^{3}He ion energies the cross section decreases, i.e., 6.1 mb sr^{-1} at 4.5 MeV, but does not become zero.

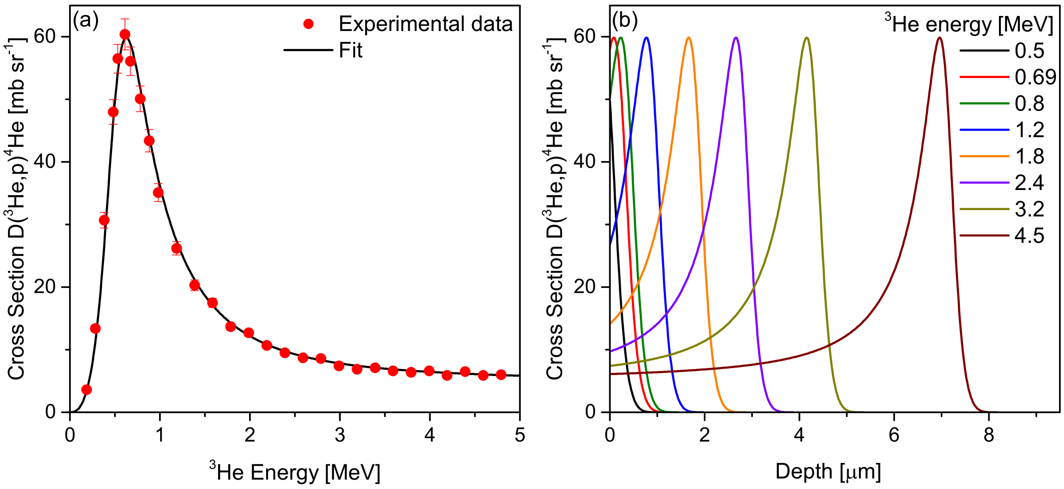

Figure 2.7: (a) Cross section of the D(^{3}He,p)^{4}He nuclear reaction in the laboratory system recorded in the proton measurement geometry as a function of the ^{3}He ion energy. (b) Cross section as a function of depth in tungsten for different ^{3}He ion energies used in the here-conducted experiments.

One possibility to probe the deuterium distribution in the sample is the so-called resonance method in which the total yield of protons released in the nuclear reaction for different ^{3}He ion energies is measured. During the propagation of the ^{3}He ions in the sample the ions lose energy due to interaction with the electronic system and by collision with tungsten nuclei, which is referred to as electronic and nuclear energy loss, respectively [13]. As the energy of the ^{3}He ions decreases the cross section for reaction with the deuterium in the sample changes according to figure 2.7 (a). The variation of the initial energy of the ^{3}He ions allows to shift the resonance of the nuclear reaction to specific depths and probe deuterium located at different depth with different sensitivity, as can be seen in figure 2.7 (b). Due to the finite cross section at higher ^{3}He ion energies, the measured total proton yield consists not only of protons from the resonance region, but also from the off-resonance region at lower depth. The depth resolution obtained with this method is limited to approximately 1 µm [76].

A more advanced approach to determine the deuterium distribution in the sample is the proton energy spectrum method [76]. In addition to the total proton yield obtained for different initial ^{3}He ion energies also the energy spectrum of the detected protons is measured. The recorded spectrum represents the product of the deuterium depth distribution with the cross section of the nuclear reaction, convoluted with the experiment response function. In principle the whole information of the deuterium distribution within the probing depth of the ^{3}He ions is contained in the spectrum. Hence, by using ^{3}He ions with an energy of 4.5 MeV the deuterium depth profile up to approximately 7.5 µm can be probed, as illustrated in figure 2.7 (b). However, the depth resolution depends on the ^{3}He ion energy and increases for decreasing energies and becomes best at the end of the ^{3}He ion range [76, 77]. In case of ^{3}He ions with an initial energy of 0.69 MeV, the depth resolution is 210 nm at the surface and decreases to 320 nm at a depth of 500 nm from where it improves to 190 nm at the end of ion range in a depth of 920 nm. Thus, in order to optimize the depth resolution to a specific depth several proton energy spectra with different initial ^{3}He ion energies are recorded.

Apart from the protons also the yield and energy spectrum of the alpha particles released in the D(^{3}He,^{4}He)p nuclear reaction can be measured to gain information on the deuterium distribution inside the specimen. Compared to the released protons, the energy of the alpha particles is lower, the electronic and nuclear energy loss in tungsten is larger and the detection angle is shallower. Thus, the detected alphas originate close to the surface in depths up to approximately 500 nm. The measured energy spectrum of the alphas contains therefore information of the deuterium distribution in the near-surface region of the specimen and provides, compared to the proton spectrum, a better depth resolution in the respective region. At the surface the depth resolution achieved with alphas released in the reaction of deuterium with ^{3}He ions of an energy of 0.69 MeV is 16 nm, while that achieved with protons is only 210 nm. Similar to the proton energy spectrum the measured alpha spectrum is a multiplication of the deuterium distribution in the sample with the energy-dependent cross section of the nuclear reaction, convoluted with the experiment response function.

2.2.2 Data Evaluation with SIMNRA and NRADC

The extraction of the deuterium depth profile from the measured data requires the decomposition of the energy spectra of the alphas and protons with NRADC [69] and SIMNRA 6.8 [68]. However, before the spectra can be processed, an energy calibration of the detectors and the measured spectra is required. This is achieved by measuring the alpha and proton spectra of a reference sample, consisting of an amorphous deuterated carbon thin film on silicon with a deuterium concentration of 34 at.% and a thickness of 270 nm.

For the energy calibration of the proton detector only one spectrum of protons released from the reference sample measured with ^{3}He ions of an energy of 2.4 MeV is required. As can be seen in figure 2.8 (a), the protons released in the nuclear reaction of ^{3}He with deuterium appear in the spectrum at a channel number of approximately 660. Due to the inverse kinematics of the nuclear reaction, the energy of the protons released in the reaction increases as the energy of the ^{3}He ion decreases [76]. Thus, the protons emerging from nuclear reactions at the surface of the a-C:D/Si sample appear at low channel number of the peak.

Beside the protons released in the nuclear reaction of ^{3}He with deuterium, also protons emitted in the reaction of ^{3}He with ^{12}C to ^{14}N are present in the spectrum, as can be seen from the three sharp peaks between channel 100 to 300. The three different energies of those protons, reflect the excited state of the remaining ^{14}N atom. In case of the protons with the highest energy, appearing at a channel number of approximately 300 and marked as p0, the ^{14}N atoms are in their ground state, while the ^{14}N atoms associated with the protons of lower energies, marked as p1 and p2, are in an excited state.

The energy of the measured protons originating from the different nuclear reactions can be calculated with SIMNRA for the given measurement geometry. After subtraction of the energy loss in the protective foil of the proton detector, the obtained proton energy can be assigned to the channels of the respective peaks illustrated in the spectrum by red stars. With this information a linear relationship between channel number and proton energy can be established and used to interpret the proton data of the actual samples.

In case of the alpha detector, shown in figure 2.8 (b), the energy calibration is based on the energy spectrum of the alphas emitted during the measurement of the reference sample with ^{3}He ions of four different energies, i.e., 0.5, 0.69, 0.8 and 1.2 MeV. The most energetic alpha particles which are recorded appear at high channel numbers and originate from the surface of the a-C:D layer. SIMNRA is used to calculated the energy of the alpha particles reaching the detector under consideration of the measurement geometry and the energy loss in the protective foil in front of the detector for the four ^{3}He ion energies.

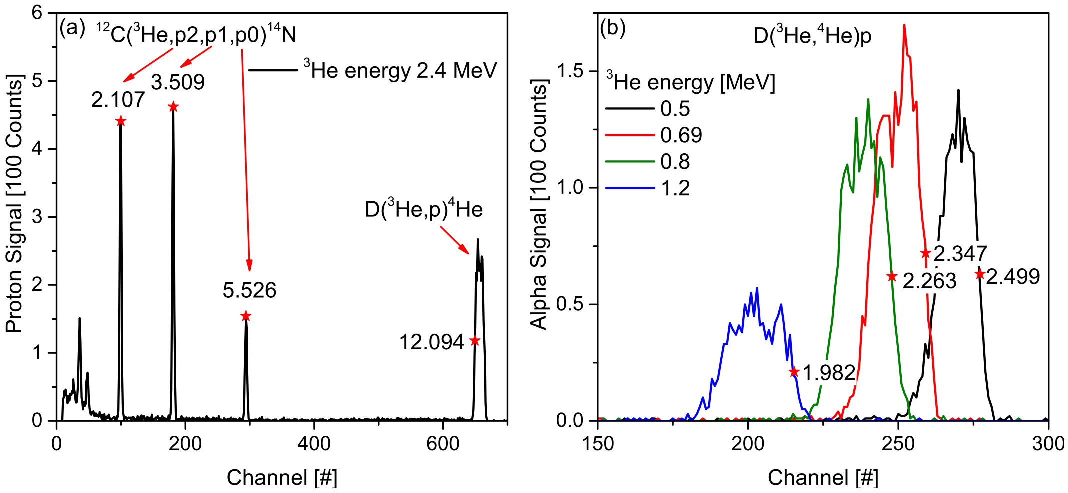

Figure 2.8: Energy calibration of the proton (a) and the alpha detector (b). In (a) the proton spectrum of the same a-C:D/Si reference sample, acquired with a ^{3}He ion energy of 2.4 MeV, is shown. The red stars mark the channels to which the energy calculated by SIMNRA is assigned in units of MeV. In (b) the raw spectra of the alphas emitted from a 270 nm thick a-C:D layer on silicon for measurements with ^{3}He ions of different energy is shown. The red stars mark the channels to which the alpha energy calculated by SIMNRA is assigned in units of MeV.

Those obtained alpha energies are assigned to the channels yielding half of the peak maximum at the high energy edge of the measured alpha spectra, as indicated by red stars in figure 2.8 (b) with the respective alpha energy in units of MeV. Based on that, a linear relation between the alpha energy and the channel number of the detector is obtained which is applied to the alpha spectra recorded for the samples of interest.

The energy-calibrated proton and alpha spectra are finally used as input for NRADC to gain the deuterium depth profile. NRADC is a Bayesian-based program which applies a Markov chain Monte Carlo (MCMC) technique to determine the most probably deuterium depth profile for the given experimental proton and alpha spectra by forward calculation [69]. A user-defined initial sample layout with a number of layers consisting of a background species, i.e., tungsten, and deuterium is generated. Under the restriction of only positive deuterium concentrations and layer thicknesses being larger than the depth resolution at the respective depth, number, width and deuterium concentration of the layers are varied randomly. For every sample layout the proton and alpha spectra for the given measurement geometry and ^{3}He ion energies are calculated and compared to the measured spectra. The sample layouts are assessed in the maximum likelihood approach, in which the discrepancy between simulated and experimental data is minimized and a large number of free parameters, e.g. number of layers, is penalized. The sample layout with the highest likelihood corresponds to the most probable deuterium depth profile. NRADC linearizes the forward calculation by assuming that the deuterium concentration does not affect the stopping of the involved particles in

the sample. In order to account for a high deuterium concentration which influences the stopping, the NRADC simulation is repeated with the deuterium depth profile of the preceding simulation entering the calculation as background. This procedure is conducted iteratively until subsequently obtained deuterium depth profiles do not change any more.
In figure 2.9 the typical NRADC output is illustrated. In (a) the experimental proton and alpha spectra obtained for different ^{3}He ion energies are compared to the respective spectra calculated from the corresponding most probable deuterium depth profile shown in (b).

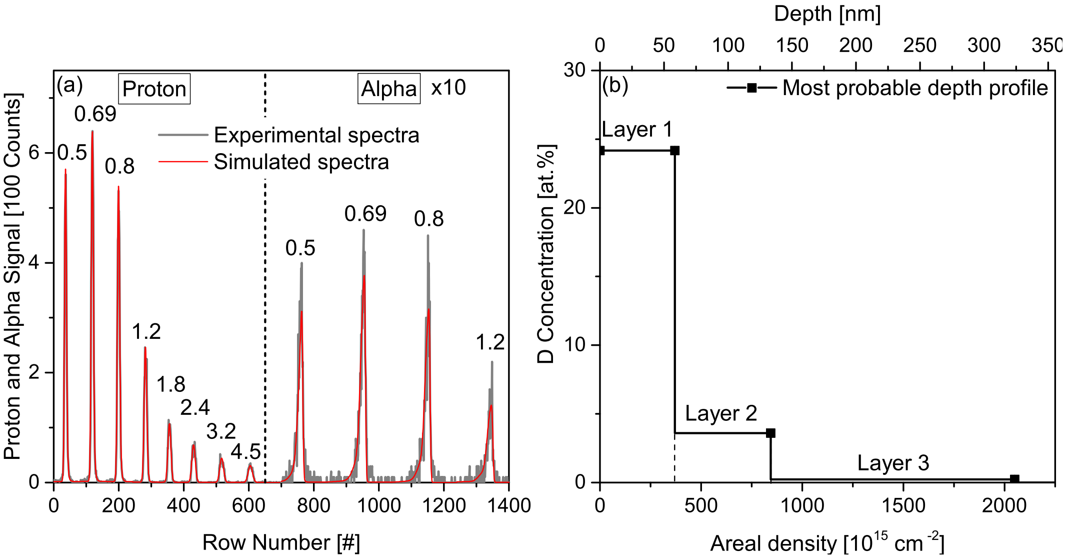

Figure 2.9: NRADC output: (a) Comparison of the experimental and simulated spectra calculated from the most probable deuterium depth profile shown in (b). The ^{3}He ion energies are given in units of MeV above the proton and alpha spectra. The alpha spectra are multiplied by a factor of ten for illustrative reasons.

The deuterium depth profile depicted in figure 2.9 (b) possess a step-like shape which contradicts the physical expectation of a continuous profile. However, under consideration of the limited experimental depth resolution and the forward calculation model, this is so far the best and most honest approximation. The deuterium concentrations displayed in the depth profile represent an average over the individual layers. The width of the different layers is initially given as areal density in units of cm^{-2} and converted into nm under the assumption that the atomic density corresponds to that of pure tungsten, i.e., $1 \times 10^{15}\,\mathrm{cm}^{-2} = 0.158\,\mathrm{nm}$ [68]. For a detailed description of NRADC, the reader is referred to Schmid et al. [69] and Manhard [78].

2.3 Electron Microscopy and Diffraction

In the following the scanning electron microscope HELIOS NanoLab 600, which is used to investigate the surface morphology and the crystallographic properties of the tungsten samples is presented. Since scanning electron microscopy (SEM) for surface imaging is a widely-used and well-established method, it will not be discussed within this thesis. For comprehensive reviews on scanning electron microscopy the reader is referred to the extensive literature available, e.g. [79, 80]. In order to investigate the crystallographic microtexture of the polycrystalline samples, i.e, the orientation of the individual grains with respect to the surface, electron backscattering diffraction (EBSD) is applied. Since this method might not be as familiar as imaging with a scanning electron beam, the principle of the EBSD technique will be briefly described.

2.3.1 HELIOS NanoLab 600

The HELIOS NanoLab 600 scanning electron microscope manufactured by FEI, schematically shown in figure 2.10 (a), is used to investigate the surface morphology of the tungsten samples and to obtain information regarding the surface orientations of individual grains. The heart piece of the HELIOS setup is the electron column in which the primary electron beam (solid red arrow) with energies between 0.35 to 30 keV is produced, condensed and focused onto the sample. In addition, it contains the x-y steering unit to scan the primary electron beam across the surface of the specimen. The sample under investigation is located on the sample stage, which allows to adjust its lateral position and height as well as to rotate and tilt the sample. The HELIOS setup is equipped with several detectors to gain information on the surface morphology as well as on the crystal structure of the sample.

The surface morphology is imaged by measuring the yield of electrons emitted from the sample as a function of the position of the primary electron beam. Secondary electrons (dashed blue arrows) are measured with the Everhart-Thornley detector (ETD) or the in-lens detector (TLD) located inside the electron column. Backscattered electrons from the primary electron beam (solid blue arrows) are detected by the concentric solid-state backscatter detector (CBS). The lateral resolution which can be achieved by imaging with secondary and backscattered electrons is approximately 1 nm [78].

In order to gain crystallographic information on the sample, electron backscattering diffraction (EBSD) can be performed in the HELIOS setup. The corresponding EBSD detector consists of a fluorescence screen and a camera which allows to record the diffraction patterns, i.e., the Kikuchi pattern, as a function of the primary electron beam position.

Furthermore, the HELIOS setup is equipped with a gallium ion source to perform focused ion beam (FIB) milling which allows to investigate the subsurface of the sample in cross sections or to prepare thin lamellas for scanning transmission electron microscopy (STEM). In addition, an energy-dispersive X-ray spectroscopy (EDX) system is installed to gain information on the elemental composition of the sample by the X-rays released in the interaction of the primary electrons with the sample atoms.

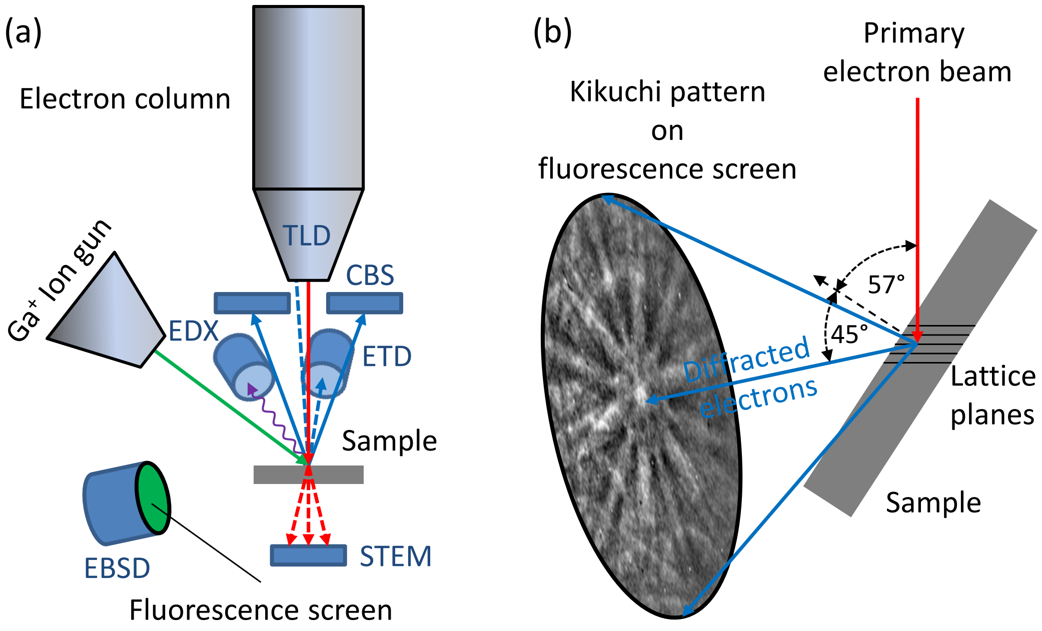

Figure 2.10: (a) Schematic of the HELIOS NanoLab 600 scanning electron microscope [78]. The setup is equipped with an Everhart-Thornley detector (ETD) and an in-lens detector (TLD) to detect secondary electrons (dashed blue arrows). Backscattered electrons (solid blue arrows) are measured with the concentric solid-state backscattering (CBS) detector. The transmission of primary electrons (dashed red lines) are monitored with the scanning transmission electron detector (STEM). The diffraction pattern of backscattered primary electrons is recorded with the electron backscattering diffraction (EBSD) detector. X-rays (violet arrow) are monitored with the EDX detector. (b) Principle of electron backscattering diffraction (EBSD).

2.3.2 Electron Backscattering Diffraction

Electron backscattering diffraction is conducted in the HELIOS setup by tilting the sample such that the primary electron beam impinges under an angle of 57 ° with respect to the surface normal. The EBSD detector is installed under an angle of 102 ° with respect to the primary electron beam, resulting in an angle of 45 ° under which the backscattered electrons are detected, as can be seen schematically in figure 2.10 (b).
The primary electrons which incident on the sample are scattered elastically and inelastically in all directions within the interaction volume. Hence, the scattered electrons can be regarded as a divergent source of electrons within the sample. Some of the elastically scattered electrons impinge on a family of crystal planes of the specimen such that the Bragg condition, given by

$$n\lambda = 2d_{hkl}\sin\theta_B, \tag{2.3}$$

with n being the diffraction order, λ the electron wavelength, d_{hkl} the interplanar spacing and θ_B the Bragg angle, is fulfilled. When the backscattered electrons are monitored on the fluorescence screen of the EBSD detector, an interference pattern, also known as Kikuchi pattern, can be observed on top of the background created by diffuse backscattered electrons [80, 81]. Based on these Kikuchi patterns, the crystallographic orientation of the grain at which the primary electron beam impinges can be inferred. The probability to match a specific crystal orientation successfully to the recorded Kikuchi pattern depends significantly on the quality of the pattern, which is determined by the degree of crystallinity of the investigated spot. Thus, the Kikuchi pattern can provide a qualitative measure to assess the condition of the near-surface crystal structure. Furthermore, by recording the Kikuchi patterns as a function of the position of the primary electron beam, the crystallographic properties of a certain area of the studied sample can be mapped, which is referred to as EBSD scan within this thesis.

For a more detailed description of the electron backscattering technique to investigate the crystallographic microtexture of a specimen, the book by Randle [81] is recommended.

2.4 Sample Preparation

The samples used for the here-conducted experiments are made of sintered and hot-rolled polycrystalline tungsten with a stated purity of 99.97 wt.%, manufactured by Plansee Holding AG [82]. The size of the samples is $12.0 \times 15.0\,\mathrm{mm}^2$ with a thickness of 0.8 mm. In order to ensure reproducibility of the experiments, only samples of the same manufacturing batch are used. According to Manhard et al. [83], the texture differs on the front and rear side of the samples. The front side, referred to as side A, shows mainly grains with $\{100\}$ and $\{111\}$ planes parallel to the surface and a $\langle 110 \rangle$ direction parallel to the rolling direction. The rear side, referred to as side B, exhibits predominately grains with a $\{110\}$ plane parallel to the surface and a $\langle 211 \rangle$, respectively $\langle 111 \rangle$, direction parallel to the rolling direction. The here-presented experiments are exclusively performed on side A of the samples.

The sample preparation procedure is as follows: After the samples were cleaned in an ultrasonic bath with isopropanol for 30 min, heat treatment is performed by electron beam heating in ultra-high vacuum at a base pressure lower than $1 \times 10^{-9}\,\mathrm{mbar}$. At first the samples are degassed at a temperature of approximately 1200 K for 20 min and subsequently heated to 2000 K for 5 min to provoke recrystallization of the grains. During this procedure the sample temperature is monitored with a disappearing filament pyrometer. The heat treatment results in the annealing of inherent defects and in the increase of the grain size up to 50 µm [83].

In the next step the samples are cast in cold-curing resin for mechanical and electrochemical polishing. Mechanical polishing is performed with abrasive paper of increasing grit size at 150 rpm for 2 min each. As the grit size is increased from 400 to 4000 the applied force is increased as well from 12 to 20 N. After mechanical grinding the samples are electrochemically polished with 1.5 wt.% NaOH by applying a bias of 19 V for 4 min. To a large extent the resin is removed by storing the samples in acetone for at least 12 h. The remaining parts of the resin are removed from the samples in an ultrasonic bath with ultra pure acetone for two times 30 min. Finally the surface is wiped with cotton bud soaked with ultra pure acetone and rinsed with de-ionized water. The cleanness of the sample surface is verified with an optical microscope.

In contrast to the sample preparation of preceding experiments, where recrystallization is performed after polishing, the sequence is reversed in order to avoid the appearance of grooves at the grain boundaries, as it is observed when recrystallization is the final step [83]. The defects induced in the recrystallized samples by mechanical grinding are within a depth of $< 1\,\mu m$ which is removed in the final electrochemical polishing step according to Manhard et al. [84].

Chapter 3

Hydrogen Isotopes in Tungsten: Principles and Modeling

In the first part of this chapter, the behavior of hydrogen isotopes in tungsten is discussed with respect to the potential energy surface as well as to diffusion and transport. Trapping and de-trapping of hydrogen within the classical [57] and the fill-level model [63, 64] is schematically illustrated. Subsequently, the principle of the hydrogen isotope exchange in tungsten based on the two different de-trapping models is explained. In the second part of this chapter, the TESSIM-X code [63, 65, 85], developed by K. Schmid to model the implantation, transport, retention, desorption as well as the exchange of different hydrogen isotopes in tungsten is introduced. The central diffusion-trapping equation of the code is reviewed and the mathematical realization of the classical and fill-level model is explained. In addition, possible boundary conditions to model different surface processes are presented. Finally, a very brief description of the technical implementation of TESSIM-X is given. Since important input for TESSIM-X is generated by SDTrimSP [66, 67], a short introduction to SDTrimSP is given at the end of the chapter.

3.1 Transport of Hydrogen Isotopes

Before the effect of hydrogen isotope exchange is discussed in greater detail, the review of some general properties of the hydrogen-tungsten system is obligatory. First, the potential energy surface of hydrogen in tungsten is discussed followed by a brief review of diffusion of hydrogen in tungsten.

In figure 3.1, the potential energy surface of hydrogen in tungsten is schematically illustrated [86]. It can be divided into a surface and a bulk region, as indicated by the dashed red line. The uptake of molecular hydrogen by tungsten is endothermic, as can be seen from the potential energy of hydrogen in the bulk being higher by E^{Sol} compared to the one of the individual components ($1/2\,\mathrm{H}_2$+W). This heat of solution is 1.1 eV per hydrogen atom [87].

At the surface hydrogen can be located in the physisorbed or chemisorbed

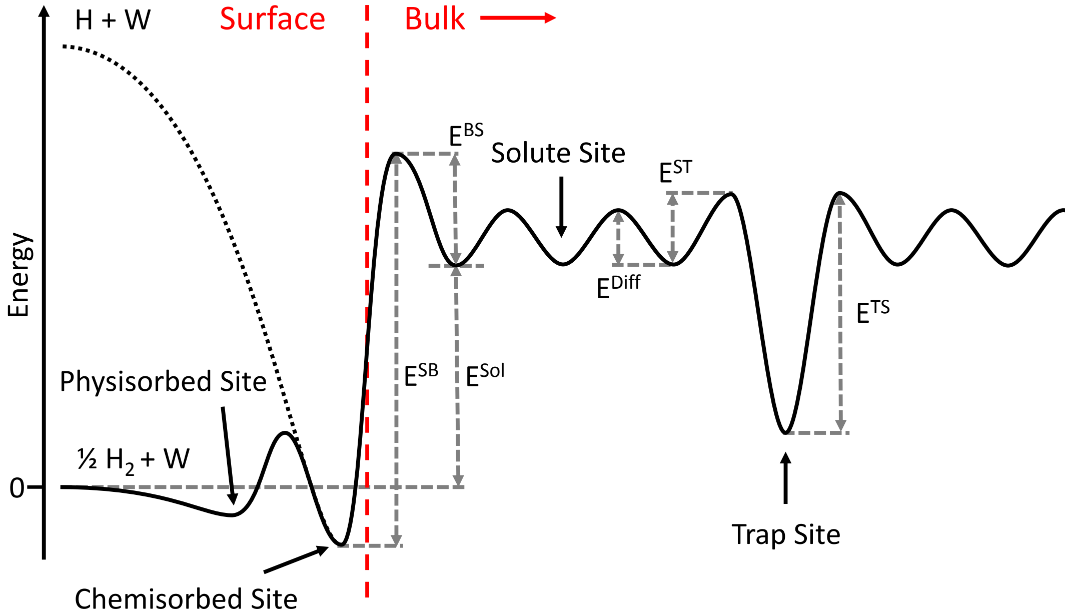

Figure 3.1: Schematic diagram of the potential energy surface of hydrogen isotopes in tungsten with the following energy barriers: E^{Sol}: Heat of solution, E^{SB}: Surface to bulk, E^{BS}: Bulk to surface, E^{Diff}: Solute site to solute site, E^{ST}: Solute site to trap site, E^{TS}: Trap site to solute site.

state, respectively. In the first one the binding results from the attractive van der Waals force, while in the latter one the electronic systems of the adsorbate and the tungsten substrate interact, e.g. by covalent bonds. In order to enter the bulk, dissociation of the hydrogen molecules is required, resulting in hydrogen atoms being chemisorbed at the surface. From this chemisorbed state, the atoms need to overcome the energy barrier between the surface and the bulk E^{SB}. For hydrogen atoms which leave the bulk the reversed process is required. First, the transition from the bulk to the chemisorbed state at the surface by surpassing the energy barrier E^{BS}, followed by the recombination of two hydrogen atoms into a molecule and finally the desorption of the latter one.

In the bulk the hydrogen atoms can occupy interstitial sites or trap sites. Interstitial sites are inherently present in a tungsten lattice and can be distinguished into tetrahedral and octahedral sites of the bcc lattice. It is energetically more favorable for the hydrogen atoms to occupy the tetrahedral sites instead of the octahedral sites, as has been confirmed by ion channeling experiments and ab initio calculations [88, 89]. Those tetrahedral sites are referred to as solute sites. The diffusion of hydrogen in tungsten is determined by overcoming the energy barrier E^{Diff} between two adjacent solute sites and is strongly depending on temperature.

According to Fukai [87], five different regimes can be distinguished. In the first regime, at very low temperature at which no phonons are present, the diffusion of the hydrogen atoms proceeds by coherent tunneling and is nearly independent of temperature. For slightly higher temperature, the appearance of the first phonons disturbs the coherent tunneling process which leads to the reduction of the hydrogen diffusivity. This is the regime of incoherent hopping. As the temperature is further increased, the regime of thermally activated tunneling is entered. In this regime many phonons are present which assist the diffusion of hydrogen atoms. Two different processes are distinguished, a non-adiabatic and an adiabatic process. In the first one, the lattice vibration leads to the reduction of the energy barrier between neighboring sites. Furthermore, there is a certain probability that the energy levels of the adjacent sites are adjusted by the lattice vibration, which allows the hydrogen atom to tunnel through the reduced energy barrier. In the adiabatic process the lattice vibrations reduce the energy barrier between two neighboring solute sites such that an excited quantum state of the hydrogen atom extends over both sites. In this way the excited hydrogen atom has a finite probability to transit to the other site. For even higher temperatures the regime of over-barrier jumps is entered in which the hydrogen atoms can be treated as classical particles. The diffusivity depends in an Arrhenius-like fashion on the temperature, reflecting the probability of the atoms to overcome the energy barrier E^{Diff} between adjacent sites by thermal excitation. In the last regime at highest temperature, the so-called fluid-like motion regime, the hydrogen atoms are no longer retained by the potential wells of the different sites, but propagate freely within the material.

Not only the temperature affects the diffusion, also the hydrogen-hydrogen interaction, which becomes relevant at high hydrogen concentrations, can influence the diffusivity of hydrogen atoms in metals, e.g. by site blocking [90]. Furthermore, the diffusivity of hydrogen can be altered by other external factors, e.g. a temperature gradient, a stress gradient or a gradient of the electrical potential, as summarized in reference [91].

Those considerations regarding the diffusion of hydrogen in tungsten hold for perfect crystals. However, in a real sample trap sites are present which can influence the transport of hydrogen in tungsten significantly. These trap sites are the consequence of lattice imperfections, e.g. vacancies, dislocations, grain boundaries, vacancy clusters or cavities, but can also be caused by impurities. Compared with the solute site, the trap site is characterized by a lower local minimum in the potential energy surface, as can be seen from figure 3.1. Hydrogen atoms can enter the trap site by surpassing the barrier E^{ST}. In order to leave the trap site an energy barrier of E^{TS} needs to be overcome. Since the required energy for de-trapping, E^{TS}, is significantly larger than the energy barrier between solute sites E^{Diff}, the probability to leave a trap site is considerably lower than for a solute site at the same temperature. Consequently, hydrogen atoms which enter a trap site become temporarily immobilized. It is reasonable to distinguish between solute hydrogen located in the solute sites, which is responsible for the diffusion of hydrogen, and the trapped hydrogen located in trap sites, which determines the hydrogen retention.

Depending on the given temperature and the required de-trapping energy, the trap sites can capture and retain hydrogen atoms and thereby reduce the transport of hydrogen atoms in tungsten. This effect can be addressed implicitly by defining an effective diffusion coefficient for hydrogen in tungsten which accounts for the trap site concentration in the material, as described by Schmid et al. [65]. Another possibility is to take the interaction of hydrogen atoms with trap sites explicitly into account as it is done in the **diffusion-trapping model**. In this case, the transport is considered as a continuing sequence of diffusion, trapping, de-trapping and diffusion. Compared with the implicit approach this requires a microscopical understanding of the trapping and de-trapping mechanism of hydrogen atoms at trap sites.

It should be mentioned that not every crystal imperfection reduces the transport of hydrogen. As discussed by Toussaint et al. [92], the diffusion of hydrogen parallel to grain boundaries can be faster compared with in-grain hydrogen diffusion. Thus, a network of grain boundaries could provide fast transport channels for hydrogen atoms.

More detailed information regarding the different properties of the hydrogen-metal system in general can be found in references [87, 91, 93, 94].

3.2 Trapping and De-trapping of Hydrogen Isotopes

In the following the two relevant microscopic models to describe the trapping and de-trapping of hydrogen isotopes on trap sites in tungsten are illustrated and their differences are highlighted.

3.2.1 Classical Model

The trapping and de-trapping of hydrogen isotopes at a given temperature within the classical model [57] is schematically illustrated in figure 3.2. The example shows the filling of initially empty traps during the deuterium implantation. For a better comprehension, the traps are depicted as rectangular potential wells with depths corresponding to the de-trapping energy required to release the retained deuterium atoms. Three traps, indicated as trap 1 to 3, with different de-trapping energies are shown in figure 3.2 (a). In addition, the dashed red line divides the present traps according to the required de-trapping energy into two groups. Those from which thermally activated de-trapping is possible at the given temperature, i.e., trap 2, and those from which no release can occur, i.e., trap 1 and 3. This strict separation is only for illustrative reasons. As de-trapping is assumed to proceed in an Arrhenius-like fashion, deuterium can in principle also be released from trap 3 but with a much lower probability than from trap 2. For a higher given temperature, the dashed red line would be shifted downwards indicating the possibility of additional release

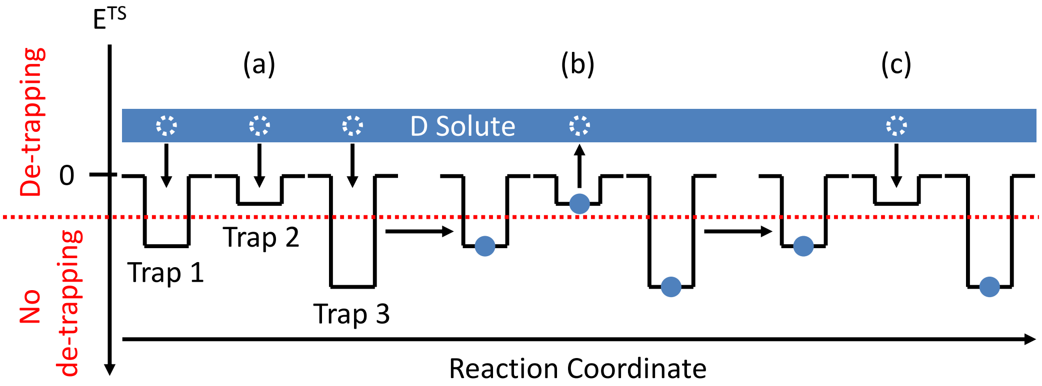

Figure 3.2: Schematic description of the classical model.

from traps with higher de-trapping energies. In contrast to that, for a lower given temperature the dashed red line would be shifted upwards.

During implantation, solute deuterium is present in the sample as indicated by the blue rectangle above the traps. The initially empty traps 1 to 3 can capture deuterium atoms from the solute, as displayed in figure 3.2 (a). From (b) it can be seen that for deuterium located in trap 1 and 3 the required de-trapping energy is too high and thermally activated de-trapping at the given temperature cannot occur, while the deuterium retained in trap 2 can be released. This empty trap site can be re-occupied by deuterium from the solute, as depicted in (c). Hence, during the deuterium implantation, which sustains the solute concentration, deuterium is continuously captured and released by trap 2. Once the implantation is stopped, the deuterium solute as well as the deuterium occupying trap 2 effuses from the sample and only the deuterium retained by trap 1 and 3 remains.

3.2.2 Fill-level Model

The principle of trapping and de-trapping in the framework of the fill-level model [63, 64] is schematically depicted in figure 3.3. Similar to the situation in figure 3.2, the filling of a fill-level trap with deuterium during implantation at a given temperature is illustrated. In accordance with the classical model, shown in figure 3.2, the trap is depicted as a rectangular potential well. The additional dashed black lines inside the rectangular trap indicate the possible fill levels with the associate de-trapping energy. The current fill level of the trap is represented by a solid black line on which the respective atoms are located. The dashed red line separates the fill levels with de-trapping energies which permit deuterium release from those which impede the release at the given temperature.

When deuterium implantation is started a solute concentration in the sample builds up and the initially empty traps capture deuterium atoms from the solute. However, in contrast to the classical model, a trap which is already

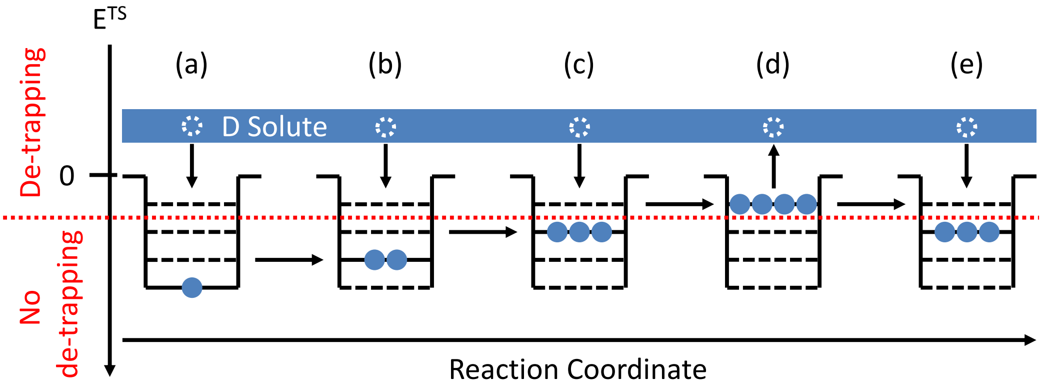

Figure 3.3: Schematic description of the fill-level model.

occupied with one deuterium atom can capture a second deuterium atom, as depicted in figure 3.3 (a). The uptake of the additional deuterium atom, which corresponds to the increase of the fill level of the trap, leads to a decrease of the de-trapping energy which is required to release one of the trapped deuterium atoms (b). The accumulation of deuterium atoms in the trap continuous which leads to a further increase of the fill level and consequently to a decrease of the required de-trapping energy. Up to the fill level reached in (c), the de-trapping energy is large enough to prevent the release of the trapped deuterium atoms, as indicated by the deuterium atoms being located below the dashed red line. The trapping of another deuterium atom from the solute induces a further increase of the fill level and a decrease of the de-trapping energy to a value low enough to permit the thermally activated release of the retained deuterium atoms. This situation is depicted in (d) with the trapped deuterium atoms being shifted above the dashed red line. The release of one deuterium atom from the trap, shown in (d), results in the reduction of the fill level and the increase of the required de-trapping energy to release one of the remaining deuterium atoms, as can be seen in (e). From the fill level shown in (e) no de-trapping of the retained deuterium is possible. However, a deuterium atom can be captured from the solute again which will rise the fill level and bring the trap back into the state shown in (d). Thus, as long as deuterium solute is present in the sample, the trap will be in a quasi equilibrium of trapping and de-trapping deuterium, similar to trap 2 in the classical model shown in figure 3.2. Once the implantation is stopped and the deuterium solute vanishes, the trap releases deuterium atoms until a fill level is reached at which the de-trapping energy is just sufficient to prohibit further thermally activated release, as illustrated in figure 3.3 (c) and (e). Hence, the underlying principle of the fill-level model is that the trapping or de-trapping of one hydrogen atom increases or decreases the required de-trapping energy of all hydrogen atoms which are contained in the trap.

3.3 Hydrogen Isotope Exchange

The principle of hydrogen isotope exchange based on the classical and the fill-level model is presented in the following and the fundamental difference of the models is highlighted.

3.3.1 Classical Model

The hydrogen isotope exchange of deuterium by protium at a given temperature in the classical model is schematically illustrated in figure 3.4. After the initial deuterium implantation, shown in figure 3.2, the protium implantation is started. Trap 1 and 3 are filled with deuterium atoms and it is assumed that the deuterium atom located in trap 2 is not yet released. This configuration is the initial state of the traps at the beginning of the protium implantation depicted in figure 3.4 (a). When the implantation is started, a protium solute is established in the sample. Since the de-trapping energy required to release the deuterium atom retained in trap 2 is low enough, the deuterium can be thermally de-trapped at the given temperature and released to the solute. This leads to a reduction of the total amount of deuterium retained by the three traps. However, this process does not require the presence of protium solute and would also take place without the protium implantation. The now unoccupied trap 2 can be re-occupied by a protium atom from the solute, as illustrated in (b). The net effect can be considered as the hydrogen isotope exchange of a deuterium atom by a protium atom. However, since thermally activated de-trapping is possible from trap 2, this captured protium atom can be released again as shown in (c). Similar to figure 3.2, as long as protium solute is present, trap 2 continuously captures and releases protium atoms. Furthermore, it can be seen from figure 3.4, that the deuterium retained in traps 1 and 3 is unaffected by the protium implantation and remains in the corresponding traps. Hydrogen isotope exchange within the classical model

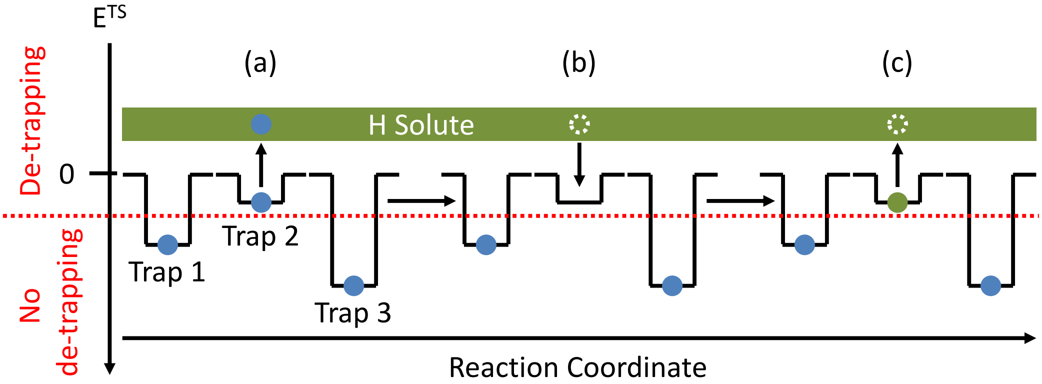

Figure 3.4: Schematic description of the hydrogen isotope exchange of deuterium by protium in the classical model.

can only take place when the de-trapping energy of the trap in which the deuterium atom is located is sufficiently low to permit thermally activated release at the given temperature.

3.3.2 Fill-level Model

Figure 3.5 explains the hydrogen isotope exchange of deuterium by protium at a given temperature in the framework of the fill-level model. After the initial filling of the trap with deuterium, depicted in figure 3.3, the trap is occupied with deuterium atoms up to a fill level at which the required de-trapping energy is just large enough to impede further release of deuterium. With the beginning of the protium implantation a certain amount of protium solute is created in the sample. As can be seen from figure 3.5 (a), the trap can capture a protium atom from the solute. This additional protium atom causes an increase of the fill level and a decrease of the required de-trapping energy. In (b) the required de-trapping energy is now sufficiently reduced to permit the thermally activated de-trapping of hydrogen isotopes at the given temperature. From the fill level shown in (b) either the recently captured protium atom or one of the deuterium atoms can be released to the solute. While the first process leaves the deuterium retention in the trap unchanged, the second process, which is illustrated in (b), reduces the deuterium content in the trap and describes the actual hydrogen isotope exchange process. The release of the deuterium atom from the trap leads to a reduction of its fill level and an increase of the de-trapping energy which prohibits further release of hydrogen isotopes, as shown in (c). Yet, the trap can capture another protium atom from the solute which rises its fill level and allows the release of either a protium or a deuterium atom. The latter case is shown in (d). Though, it is also possible that the trap captures the previously released deuterium atom, but less likely. With this iterative process of capturing a protium atom and releasing a deuterium atom instead, the initially trapped deuterium atoms can

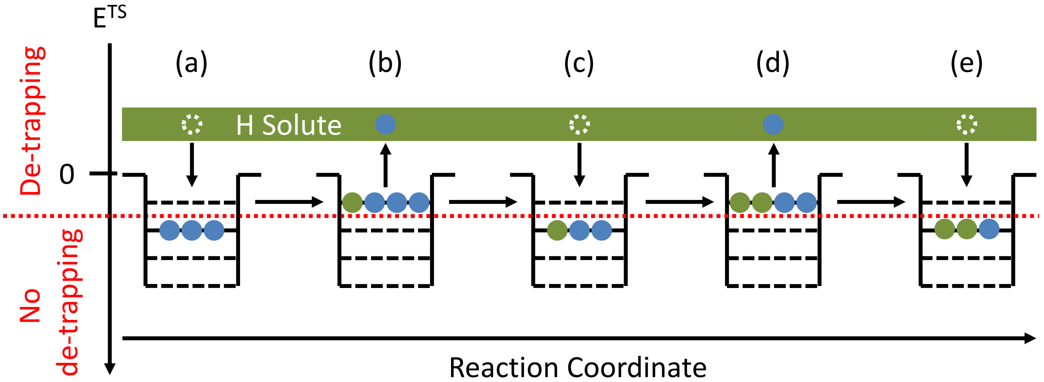

Figure 3.5: Schematic description of the hydrogen isotope exchange of deuterium by protium in the fill-level model.

be successively released from the trap, as shown in (e).
Regarding the hydrogen isotope exchange, the main difference between the two models can be summarized as as follows: In the classical model, the exchange of deuterium in traps which do not allow thermally activated release at the given temperature is not possible. In contrast to that, in the fill-level model deuterium atoms which are initially contained in traps that impede thermally activated de-trapping can be released by rising the fill level and thereby reducing the required de-trapping energy for all hydrogen isotopes in the trap. Hence, the difference of both models becomes most prominent, when the hydrogen isotope exchange is investigated on traps which do not allow thermal release at the given temperature.

3.4 TESSIM-X

The TESSIM-X code [63, 65, 85] used to simulate the transport and interaction of different hydrogen isotopes in tungsten is based on the physical model of diffusion-trapping. In principle, this model can be implemented via different techniques.
One is the Monte Carlo approach which describes the diffusion and trapping of individual particles as a stochastic process [95]. This allows to treat interactive processes of the diffusing species, e.g., self-trapping or site-blocking [90] on a microscopic scale. In addition, an extension towards higher dimensional systems can be achieved easier in the Monte Carlo framework. However, large systems, in which the distance of one jump between adjacent sites is small compared to the total dimension of the system, cannot be described efficiently with this technique due to extensive computational resources required.
Another possibility to implement the diffusion-trapping model is via the rate-equation approach [85, 96, 97]. Unlike the Monte Carlo approach, not the diffusion and trapping of individual particles is modeled, but the evolution of a diffusive and trapped particle concentration is simulated. This approximation neglects interactions on the microscopic scale with the advantage that large systems can be simulated with considerably higher efficiency. However, the extension to higher dimensions cannot be realized easily.
The intention of TESSIM-X is to model experimentally obtained data. In order to meet the experimental conditions such as the macroscopic sample size, the diffusion-trapping concept in TESSIM-X is realized in the form of a one-dimensional rate-equation model. Although TESSIM-X was initially developed to simulate the behavior of hydrogen isotopes in tungsten, it is not limited to this specific system, but can be used to model diffusion-trapping processes in other systems as well. In the following, the working principle of TESSIM-X will be explained and the most important equations will be reviewed in the context of hydrogen isotopes in tungsten. Furthermore, the implementation of the different trapping and de-trapping mechanisms, i.e., the classical model and the fill-level model will be explained. Since the code allows to model the

interaction of two different hydrogen isotopes, they are labeled isotope A and B accordingly. The following equations are described with respect to isotope A but hold without loss of generality for isotope B.

3.4.1 Diffusion-Trapping Equation

The rate-equation-based diffusion-trapping model strictly distinguishes between two different populations of hydrogen, the mobile solute hydrogen concentration $C_A^S(x,t)$ and the immobile trapped hydrogen concentration $C_A^T(x,t)$. The evolution of both hydrogen populations in time t and space x, as well as their interaction is described by the central partial differential equation of the TESSIM-X code given by:

$$\frac{\partial C_A^S(x,t)}{\partial t} = D_A(T(t))\frac{\partial^2 C_A^S(x,t)}{\partial x^2} + S_A(x,t) - \sum_{i=1}^{N_T}\frac{\partial C_{A,i}^T(x,t)}{\partial t}, \tag{3.1}$$

where $D_A(T(t))$ corresponds to the temperature-dependent diffusion coefficient of hydrogen isotope A in tungsten given by the Arrhenius term:

$$D_A(T(t)) = D_{0,A}\exp\left(-\frac{E_A^{\mathrm{Diff}}}{k_B T(t)}\right), \tag{3.2}$$

where $D_{0,A}$ is the pre-exponential factor, E_A^{Diff} the diffusion energy barrier, k_B the Boltzmann constant and $T(t)$ the temperature as a function of time. The diffusive transport of the solute hydrogen is described by the first term on the right-hand side in equation (3.1), which represents Fick's second law of diffusion [87]. The second term, $S_A(x,t)$, is the solute source term of hydrogen isotope A which is required to simulate the loading of the sample with hydrogen, e.g., by implantation and can be written as

$$S_A(x,t) = \frac{\Gamma_A^{\mathrm{imp}}(t)}{\rho_0}\zeta_A(x) \text{ with } \int_0^\infty \zeta_A(x)\,\mathrm{dx} = 1, \tag{3.3}$$

with $\Gamma_A^{\mathrm{imp}}(t) = (1 - R_{\mathrm{refl}})\,\Gamma_A^{\mathrm{irr}}(t)$ corresponding to the implanted flux of hydrogen isotope A, with $\Gamma_A^{\mathrm{irr}}(t)$ being the irradiated flux and R_{refl} the particle reflection coefficient. ρ_0 is the number density of tungsten and $\zeta_A(x)$ gives the distribution of the solute source as a function of depth and is related to the implantation profile of isotope A.

The last term in equation (3.1) couples the differential equations describing the evolution of the trapped concentration of hydrogen isotope A in traps of type i to the evolution of the solute hydrogen concentration. The sum over i accounts for the contribution of N_T different trap types that might be present in the sample. Depending on the experimental conditions the traps can either represent a sink or a source for the solute hydrogen. The filling of the traps reduces $C_A^S(x,t)$, while a release of hydrogen from the traps increases $C_A^S(x,t)$. The different models of trapping and de-trapping enter the diffusion-trapping equation via this last term and are discussed in the following.

3.4.2 Classical Model

The classical model [57] is characterized by the assumption that each trap can be occupied by only one hydrogen atom and each trap type has a fixed de-trapping energy. The concentration of hydrogen isotope A trapped in traps of type i, $C^{T}_{A,i}\left(x,t\right)$, can be altered either by hydrogen release or by trapping and is described by

$$\begin{aligned}\frac{\partial C^{T}_{A,i}\left(x,t\right)}{\partial t} &= \frac{D_{A}\left(T\left(t\right)\right)}{a_0^2\beta}\, C^{S}_{A}\left(x,t\right)\left(\eta_i\left(x,t\right)-\left(C^{T}_{A,i}\left(x,t\right)+C^{T}_{B,i}\left(x,t\right)\right)\right)\\ &\quad - C^{T}_{A,i}\left(x,t\right)\,\nu^{TS}_{A,i}\,\exp\left(-\frac{E^{TS}_{A,i}}{k_B T\left(t\right)}\right)\\ &\quad - C^{T}_{A,i}\left(x,t\right)\left(\epsilon_{AA,i}\left(x,t,E^{TS}_{A,i}\right)+\epsilon_{AB,i}\left(x,t,E^{TS}_{A,i}\right)\right). \end{aligned} \tag{3.4}$$

The first term on the right-hand side in equation (3.4) is the trapping rate and describes at which rate hydrogen isotope A is captured by traps of type i from the solute. The trapping rate is proportional to the available concentration of unoccupied traps, which is defined by the difference of the concentration of traps of type i, given by $\eta_i\left(x,t\right)$, and the already trapped concentration of isotopes A and B in traps of type i, $C^{T}_{A,i}\left(x,t\right)+C^{T}_{B,i}\left(x,t\right)$. Furthermore, the trapping rate of isotope A depends linearly on the available solute concentration $C^{S}_{A}\left(x,t\right)$ and on the rate to jump into the trap. The latter one is characterized by the diffusion coefficient $D_A\left(T\left(t\right)\right)$, given in equation (3.2), divided by the square of the tungsten lattice distance a_0 and the number of solute sites β per tungsten atom. This inherently assumes that the transition rate from a solute site to a trap site is equal to that for the transition between solute sites, since there is no additional energy barrier.
In order to implement the scenario of activated trapping, which assumes an additional energy barrier that needs to be overcome for the hydrogen atom to get trapped, an Arrhenius term with a higher energy than E^{Diff} and a different pre-exponential factor can be chosen. Furthermore, unsaturable traps, which yield an infinite capability to trap hydrogen, can be introduced in the code by neglecting the already trapped hydrogen concentration $C^{T}_{A,i}\left(x,t\right)+C^{T}_{B,i}\left(x,t\right)$ and using only $\eta_i\left(x,t\right)$ instead of the difference stated in the bracket. The evolution of the concentration of traps of type i can be simulated as well in order to address the formation and saturation of traps during the implantation by choosing an appropriate time dependence [98].
The two remaining terms on the right-hand side in equation (3.4) are the de-trapping rates of hydrogen isotope A from traps of type i via different mechanisms. The first one is the thermally activated release rate of isotope A which is characterized by the Arrhenius term with the de-trapping energy $E^{TS}_{A,i}$ and the attempt frequency $\nu^{TS}_{A,i}$. The last term allows to take the kinetic de-trapping of isotope A from traps of type i by direct collisions with energetic particles from an impinging hydrogen ion beam and generated recoils into

account. $\epsilon_{AA,i}\left(x,t,E^{TS}_{A,i}\right)$ and $\epsilon_{AB,i}\left(x,t,E^{TS}_{A,i}\right)$ correspond to the kinetic de-trapping of isotope A by an ion beam of isotope A and B, respectively. As can be seen from equation (3.5), exemplarily for $\epsilon_{AB,i}\left(x,t,E^{TS}_{A,i}\right)$, the kinetic de-trapping scales linearly with the implanted flux $\Gamma^{\mathrm{imp}}_{B}\left(t\right)$.

$$\epsilon_{AB,i}\left(x,t,E^{TS}_{A,i}\right) = \frac{\Gamma^{\mathrm{imp}}_{B}\left(t\right)}{\rho_0}\kappa_{AB}\left(x,E^{TS}_{A,i}\right) \tag{3.5}$$

$\kappa_{AB}\left(x,E^{TS}_{A,i}\right)$ accounts for the spatial distribution of the kinetic de-trapping term and can be approximated by the profile of the recoils of isotope A generated by implantation of isotope B. Furthermore, $\kappa\left(x,E^{TS}_{A,i}\right)$ depends on the de-trapping energy $E^{TS}_{A,i}$. Kinetic de-trapping of weakly trapped isotopes A is more efficient than that of strongly trapped ones. The thermally activated de-trapping as well as the kinetic de-trapping mechanisms require the presence of a trapped hydrogen concentration and are therefore proportional to $C^{T}_{A,i}\left(x,t\right)$.

3.4.3 Fill-level Model

The fill-level model [63–65], inspired by DFT calculations [58–61], assumes that each trap can be filled with several hydrogen atoms simultaneously. Depending on the fill level k, which corresponds to the total number of hydrogen atoms A and B in the trap, the de-trapping energy $E^{TS}_{A,i,k}$ of the trap varies, meaning that the de-trapping energy of all atoms in the trap increases or decreases when an atom is removed or added. Compared to the classical model it is not sufficient to consider only traps of different types, also the fill level k of the respective trap type i plays an important role. Thus, an additional sum over the fill level index k is required, as can be seen in equation (3.6), where $C^{T}_{A,i,k}\left(x,t\right)$ corresponds to the concentration of isotope A in traps of type i filled to the level k with isotope A and B.

$$\frac{\partial C^{T}_{A,i}\left(x,t\right)}{\partial t} = \sum_{k=1}^{k_{max}}\frac{\partial C^{T}_{A,i,k}\left(x,t\right)}{\partial t} \tag{3.6}$$

Trapping and De-trapping Rates

Before the equations which describe the evolution of the trapped hydrogen concentration in the fill-level model are discussed, it is useful to introduce the trapping rates $\chi_{A,i,k}\left(x,t\right)$ and de-trapping rates $\psi_{A,i,k}\left(x,t\right)$, given by equations (3.7) to (3.9). Depending on the fill level k in which the trapping or de-trapping occurs different cases have to be distinguished.

Trapping rate into $k = 1$

The trapping of hydrogen isotope A into the first fill level $k = 1$ of traps of type i is described by

$$\chi_{A,i,1}(x,t) = \frac{D_A(T(t))}{a_0^2\beta} C_A^S(x,t) \left(\eta_i(x,t) - \sum_{\tilde{k}=1}^{k_{\max}} \frac{C_{A,i,\tilde{k}}^T(x,t) + C_{B,i,\tilde{k}}^T(x,t)}{\tilde{k}} \right) \tag{3.7}$$

and corresponds to the initial filling of the traps. Hence the expression is very similar to trapping in the classical model given by the first term in equation (3.4). $\chi_{A,i,1}(x,t)$ is proportional to the solute concentration of isotope $C_A^S(x,t)$ and the probability to transit to the trap site, given by the first factor. Furthermore, $\chi_{A,i,1}(x,t)$ depends linearly on the concentration of unoccupied traps of type i given by the difference in the bracket. Compared to the classical model, the trapped hydrogen concentration $C_{A,i,k}^T(x,t) + C_{B,i,k}^T(x,t)$ needs to be divided by the respective fill level k and summed over k to obtain the occupied trap concentration.

Trapping rate into $1 < k \leq k_{\max}$

The trapping into a fill level k of traps of type i with $1 < k \leq k_{\max}$ is given by

$$\chi_{A,i,k}(x,t) = \frac{D_A(T(t))}{a_0^2\beta} C_A^S(x,t) \frac{C_{A,i,k-1}^T(x,t) + C_{B,i,k-1}^T(x,t)}{k-1}, \tag{3.8}$$

which is proportional to the concentration of traps of type i filled to the fill level $k - 1$. Trapping of hydrogen into traps filled to the maximum level $k_{\max}$ is not possible.

De-trapping rate from k

The de-trapping rate $\psi_{A,i,k}(x,t)$ describes the release of hydrogen isotope A from traps of type i at fill level k and can be written as:

$$\begin{aligned}\psi_{A,i,k}(x,t) = {} & C_{A,i,k}^T(x,t)\, \nu_{A,i,k}^{TS} \exp\left(-\frac{E_{A,i,k}^{TS}}{k_B T(t)} \right) \\ & + C_{A,i,k}^T(x,t) \left(\epsilon_{AA,i,k}\left(x,t,E_{A,i,k}^{TS}\right) + \epsilon_{AB,i,k}\left(x,t,E_{A,i,k}^{TS}\right) \right).\end{aligned} \tag{3.9}$$

This expression is essentially the same as in the classical model and consists of a thermally activated and a kinetic de-trapping contribution. The only difference is that the parameters, like $\nu_{A,i,k}^{TS}$, $E_{A,i,k}^{TS}$ and indirectly $\epsilon_{AB,i,k}\left(x,t,E_{A,i,k}^{TS}\right)$ and $\epsilon_{AA,i,k}\left(x,t,E_{A,i,k}^{TS}\right)$ are not only defined by the trap type i but also by the fill level k to which the traps are filled. Furthermore, the de-trapping rate $\psi_{A,i,k}(x,t)$ is not proportional to the hydrogen concentration trapped in trap type i but only to the hydrogen concentration existing in traps of type i occupied to fill level k.

Evolution of Trapped Hydrogen Concentration

In order to model hydrogen isotope exchange experiments two different hydrogen isotopes A and B need to be simulated at the same time. For a trap of type i filled to level k, k corresponds to the sum of the hydrogen isotopes A and B in the respective trap. Since the exact number of A and B in the trap is not known, the fractional occupancy, given by

$$\Lambda_{A,i,k}\left(x,t\right) \,=\, k\,\frac{C^T_{A,i,k}\left(x,t\right)}{C^T_{A,i,k}\left(x,t\right)+C^T_{B,i,k}\left(x,t\right)}, \tag{3.10}$$

is introduced to account for the isotopic ratio.

The evolution of the hydrogen concentration of isotope A in traps of type i filled to level k is given by equations (3.11) to (3.13). For a better comprehension of the equations the explicit time and space dependences are omitted. Depending on the observed fill level k, different cases have to be distinguished.

$\boldsymbol{k\,=\,1}$

The development of the concentration of isotope A in traps of type i in fill level $k=1$ is given by:

$$\begin{aligned}\frac{\partial C^T_{A,i,1}}{\partial t} =&\, \chi_{A,i,1}\ \text{(trapping into } k=1\text{)}\\ &-\left(\chi_{A,i,2}+\chi_{B,i,2}\right)\times\Lambda_{A,i,1}\ \text{(trapping into } k=2\text{)}\\ &-\left(\psi_{A,i,1}+\psi_{B,i,1}\right)\times\Lambda_{A,i,1}\ \text{(de-trapping from } k=1\text{)}\\ &+\left(\psi_{A,i,2}+\psi_{B,i,2}\right)\times\Lambda_{A,i,2}-\psi_{A,i,2}\ \text{(de-trapping from } k=2\text{)}\,.\end{aligned} \tag{3.11}$$

The term in the first line of equation (3.11) corresponds to the trapping of isotope A into the fill level $k=1$, which leads to an increase of $C^T_{A,i,1}$. The second line describes the trapping of either isotope A or B into the fill level $k=2$. This results in an increase of $C^T_{A,i,2}$ on expense of $C^T_{A,i,1}$, which decreases weighted by the fractional occupancy $\Lambda_{A,i,1}$ accordingly. The third line yields the direct de-trapping of either isotope A or B from level $k=1$ and leads to a decrease of $C^T_{A,i,1}$. The last line corresponds to the de-trapping of either isotope A or B from fill level $k=2$, which leads to an increase of $C^T_{A,i,1}$ weighted by the fractional occupancy $\Lambda_{A,i,2}$. When isotope A is released from level $k=2$ the increase of $C^T_{A,i,1}$ is smaller compared to the case when isotope B is released. This circumstance is taken into account by subtracting $\psi_{A,i,2}$.

$1 < k < k_{\max}$

For a fill level k with $1 < k < k_{\max}$, the evolution of the concentration of isotope A located in traps of type i is described by:

$$\begin{aligned}\frac{\partial C^T_{A,i,k}}{\partial t} &= \left(\chi_{A,i,k} + \chi_{B,i,k}\right) \times \Lambda_{A,i,k-1} + \chi_{A,i,k} \text{ (trapping into } k)\\ &\quad - \left(\chi_{A,i,k+1} + \chi_{B,i,k+1}\right) \times \Lambda_{A,i,k} \text{ (trapping into } k+1)\\ &\quad - \left(\psi_{A,i,k} + \psi_{B,i,k}\right) \times \Lambda_{A,i,k} \text{ (de-trapping from } k)\\ &\quad + \left(\psi_{A,i,k+1} + \psi_{B,i,k+1}\right) \times \Lambda_{A,i,k+1} - \psi_{A,i,k+1} \text{ (de-trapping from } k+1)\,.\end{aligned} \tag{3.12}$$

$C^T_{A,i,k}$ is not only increased by hydrogen isotopes A being trapped into fill level k as it is the case for $k = 1$. From the additional term in the first line of equation (3.12) compared to equation (3.11), it can be seen that the trapping of any hydrogen isotope A or B into the fill level k results in an increase of $C^T_{A,i,k}$. The reason for this is that the hydrogen isotopes formerly trapped in $k-1$ are shifted to k and $C^T_{A,i,k}$ is increased according to the fractional occupancy $\Lambda_{A,i,k-1}$. The other terms in equation (3.12) are equal to the case of $k = 1$.

$k = k_{\max}$

The concentration of isotope A retained in the highest fill level $k_{\max}$ of traps of type i is determined by:

$$\begin{aligned}\frac{\partial C^T_{A,i,k}}{\partial t} &= \left(\chi_{A,i,k} + \chi_{B,i,k}\right) \times \Lambda_{A,i,k-1} + \chi_{A,i,k} \text{ (trapping into } k_{\max})\\ &\quad - \left(\psi_{A,i,k} + \psi_{B,i,k}\right) \times \Lambda_{A,i,k} \text{ (de-trapping from } k_{\max})\,.\end{aligned} \tag{3.13}$$

Since neither trapping into nor de-trapping from fill levels $k > k_{\max}$ is possible, all terms relying on fill levels $k+1$ are omitted in the equation. $C^T_{A,i,k_{\max}}$ can only be increased by trapping hydrogen isotope A or B into fill level $k_{\max}$ as described before in equation (3.8). A decrease of $C^T_{A,i,k_{\max}}$ can only occur due to direct de-trapping from fill level $k_{\max}$.

3.4.4 Surface Processes

TESSIM-X allows to chose from different models describing processes at the surface. The most simple one is the diffusion limited boundary condition. This model assumes that the diffusion of hydrogen to the surface and not the desorption from the surface is the rate-limiting process. Thus every hydrogen atom which reaches the surface leaves the sample. In TESSIM-X this is implemented as Dirichlet boundary condition by pinning the solute hydrogen concentration at the surface to zero i.e. $C^S_A(0,t) = 0$.

Another possible type of boundary condition which can be applied in TESSIM-X is the Neumann boundary condition. In this case the condition is not assigned to the function, i.e. $C_A^S(x,t)$, but to the derivatives, e.g., $\frac{\partial C_A^S(x,t)}{\partial x}$. According to Fick's first law of diffusion [87], the diffusion flux is proportional to this derivative. Hence, this boundary condition allows to implement flux-limited boundary conditions, e.g., the recombination limited desorption model by Pick and Sonnenberg [99] used by TMAP 7 [96]. In contrast to the previous model, it assumes that the desorption of hydrogen from the surface is the process which determines the release. Consequently, the diffusive hydrogen flux from the bulk to the surface must balance the flux of hydrogen molecules desorbing from the surface. It should be mentioned that this model simplifies the processes taking place at the surface considerably by using only one parameter, i.e., the recombination rate coefficient.

A more sophisticated surface model, describing the physical and chemical processes at the surface in a rate-equation model, can be chosen in TESSIM-X. Here, the release of hydrogen atoms from the sample is considered as a two step process. In the first step, the hydrogen atoms transit from the bulk to a chemisorbed state at the surface. In a second step, the hydrogen atoms are removed from the surface by the Langmuir-Hinselwood process, an Eley-Rideal process [100] or due to sputtering by energetic ions. The first one describes the recombination of two hydrogen atoms at the surface to a hydrogen molecule, which subsequently desorbs. The second one accounts for a direct removal of a hydrogen atoms from the surface by colliding with molecules or atoms from the gas-phase. The last one treats the release of chemisorbed hydrogen atoms by direct collisions with energetic hydrogen ions impinging on the surface. This surface rate-equation model also allows to simulate the up-take of hydrogen by tungsten by gas or atomic hydrogen beam loading. In case of molecules this is described by the dissociative adsorption at the surface and the transition of the hydrogen atoms from the chemisorbed state into the bulk. For atomic hydrogen beam loading the dissociative step is omitted and the atoms are chemisorbed directly at the surface. In order to perform predictive simulations with such a complex surface rate-equation model the accurate determination of the parameters, i.e., the energy barriers, attempt frequencies and cross-section of reactions is mandatory [101–103].

3.4.5 Implementation

The partial differential equations (3.1), defining the diffusion of the hydrogen isotopes A and B, as well as the set of ordinary differential equations (3.4) or (3.6), describing the trapping and de-trapping of the different isotopes A and B, are solved by Mathematica Version 10.3 [104] or higher. The spatial dimension is defined to match the dimension of the sample and appropriately discretized either by a constant or a varying step-width. Based on this grid the finite difference method is applied and the obtained linear system of equations is solved using the "Backward Differentiation Formula" Solver IDA [105] from the Sundails (SUite of Nonlinear and Differential / ALgebraic equation Solvers) solver suite available in Mathematica.

3.5 SDTrimSP

Relevant inputs for the TESSIM-X simulations are generated by SDTrimSP 5.07 (Static-Dynamic TRansport of Ions in Matter Sequential and Parallel processing) [66, 67]. In this thesis, the code is used to determine the implantation profiles of protium and deuterium in tungsten and to calculate the depth distribution of hydrogen recoils generated during the implantation. Beside this application, SDTrimSP can be utilized to calculate sputtering yields and ion beam damage.

In general, SDTrimSP is a Monte-Carlo-based code to simulate the irradiation of an amorphous target with energetic projectiles as well as the resulting interaction of the target and incident atoms. For the target a mono-atomic material, a composition or a layered structure can be selected. The incident atoms are characterized by the element, the energy or energy distribution and the incident angle with respect to the surface of the target. In contrast to molecular dynamics (MD), where the equations of motion of all atoms in the target and the incident projectiles are solved simultaneously, SDTrimSP relies on the binary collision approximation (BCA) [19], in which only the interaction between the two involved scattering partners is considered.

The trajectory of one incident projectile atom is simulated as a sequence of independent scattering events, until the projectile is either stopped or emitted from the target. For each scattering event, the impact parameter, the azimuthal scattering angle and the distance to the next scattering partner are chosen randomly within appropriate boundaries. The scattering angle, which is the angle between the incoming and the asymptotic outgoing trajectory of the projectile, is determined by solving the scattering integral by applying the "Magic Formula" [106]. The Kr-C potential [107], which is a radial symmetric Coulomb potential with modifications to account for the screening of the core charge by the surrounding electrons, is chosen as interaction potential. From the scattering angle the energy loss, also referred to as nuclear energy loss, of the projectile is calculated. The energy loss of the projectile between subsequent scattering events due to electronic excitation of the target is taken into account via an equipartition of the Oen-Robinson [108] and the Lindhard-Schraff [109] model. Along its trajectory, the projectile atom collides with numerous target atoms. If the transferred energy from the projectile atom to the resting scattering partner is larger than the predefined displacement energy, a recoil atom is created. This recoil atom itself acts as projectile and may create other recoil atoms along its trajectory before it is stopped or ejected from the target. The result is a cascade of recoil atoms created by the initial incident projectile atom.

In order to extract collective information, such as the implantation profile, the recoil generation profile or the reflection coefficient the simulation is repeated for several thousand projectiles to gain data with sufficient statistics. In addition to the static mode, in which the change of the target composition during the implantation is neglected, SDTrimSP also offers a dynamic mode. Here, after the simulation of one projectile package, consisting of a predefined number of projectiles, the target composition and the corresponding parameters are updated and serve as input for the simulation of the next package of projectiles. In cases in which neither the target composition is changed significantly, nor severe sputtering of the target occurs, the static mode is a sufficient approximation to determine implantation and recoil profiles. However, if material erosion and sputtering is studied explicitly, a dynamic SDTrimSP simulation is inevitable.

For more information on the topic of interaction of ions with matter in general the reader is referred to Was [13] and with the focus on BCA-based simulations to Eckstein [19].

Chapter 4

Implantation of D into W at 150 K

In order to investigate the fill-level model as the underlying isotope exchange mechanism, the exchange of deuterium by protium in tungsten is performed under different conditions. However, the initial deuterium implantation is always performed in the same manner. At a sample temperature of 150 K deuterium with an energy of 3.0 keV/D and a flux of $8.4 \times 10^{17}\,\mathrm{D\,m^{-2}s^{-1}}$ is implanted under normal incidence into the tungsten samples until an irradiated deuterium fluence of $8.4 \times 10^{21}\,\mathrm{D\,m^{-2}}$ is reached. From previous experiments in which deuterium with energies ranging from 0.5 to 3.0 keV/D was implanted into single- and polycrystalline tungsten samples at temperatures between 350 and 700 K, the modification of the surface morphology is well-known [27, 98, 110]. In this context, the formation of deuterium gas-filled cavities, termed blisters, are one of the most prominent features. Due to the low temperature at which the deuterium is implanted in the present experiments, an even more severe change of the surface morphology of the tungsten samples is expected for twofold reason. First, the diffusion of deuterium in tungsten is considerably reduced at 150 K which leads to the build-up of a large amount of deuterium within the implantation zone. This accumulated deuterium can stress the tungsten lattice and cause a modification of the surface, e.g. the formation of blisters. Second, the fracture toughness of tungsten decreases with decreasing temperature [111, 112]. Hence crack propagation is facilitated at low temperature rendering the material more vulnerable to the formation of blisters. Thus, before the exchange of deuterium by protium in tungsten is studied in more detail, the implications of the energetic deuterium implantation at low temperature in terms of deuterium retention and concentration as well as in terms of modification of the surface morphology are investigated.

In the following chapter the experimental procedures to explore the development of the deuterium retention and the surface morphology during the low-temperature deuterium implantation into tungsten are briefly outlined and the outcomes are described. The results of the surface morphology studied during the deuterium implantation are evaluated and the gained insights are used to interpret the evolution of the retention and concentration of deuterium in tungsten. Finally, the obtained conclusions and results are set in relation to those found in contemporary literature.

4.1 Experimental Procedures

4.1.1 D Retention and Depth Profile

The evolution of the deuterium retention and concentration in tungsten at low temperature is studied in situ by NRA in the dual beam experiment. At a sample temperature of 150 K, deuterium with an energy of 3.0 keV/D and a flux of $8.4 \times 10^{17}\,\mathrm{D\,m^{-2}s^{-1}}$ is implanted stepwise into the tungsten specimens under normal incidence with respect to the surface. The deuterium implantation is started in steps of 0.8 to $1.5 \times 10^{20}\,\mathrm{D\,m^{-2}}$. Once an irradiated fluence of $1.6 \times 10^{21}\,\mathrm{D\,m^{-2}}$ is exceeded, the deuterium fluence per step is increased. First to 2.0 and then to $4.0 \times 10^{20}\,\mathrm{D\,m^{-2}}$ until the final irradiated deuterium fluence of $7.9 \times 10^{21}\,\mathrm{D\,m^{-2}}$ is reached. After each implantation step, the deuterium retention is probed by NRA using ^{3}He ions with an energy of 0.69 MeV. The NRA measurements are performed at the same spot and the acquired ion charge per measurement is 1 µC, resulting in a total accumulated ion charge of 37 µC at the end of the experiment. Once the final deuterium fluence of $7.9 \times 10^{21}\,\mathrm{D\,m^{-2}}$ has been irradiated on the sample, the homogeneity of the deuterium retention across the implantation spot is verified by NRA using again ^{3}He ions with an energy of 0.69 MeV. When the homogeneity is confirmed, NRA is performed with ^{3}He ions of eight different energies ranging from 0.5 to 4.5 MeV on a new spot. The acquired ion charge depends on the ^{3}He ion energy and is 4 µC for 0.5, 0.69 and 0.8 MeV and 6 µC for 1.2, 1.8, 2.4, 3.2 and 4.5 MeV, adding up to a total of 42 µC. The obtained data is post-processed by SIMNRA and NRADC to generate the deuterium depth profile. The integral of this depth profile yields the total amount of deuterium retained in the tungsten sample up to a depth of 7.5 µm. Assuming that this final deuterium retention corresponds to a certain number of proton counts per acquired charge measured with ^{3}He ions with an energy of 0.69 MeV, this number of proton counts can be set in relation to those obtained in the NRA measurements after the different deuterium implantation steps which finally allows to deduce the corresponding deuterium retention after each implantation step. This method of determining the deuterium retention is significantly faster than measuring a deuterium depth profile after each implantation step. However, it requires that the total amount of deuterium in the sample is probed by the ^{3}He ions with an energy of 0.69 MeV. Furthermore, the cross section for the D(^{3}He,p)^{4}He nuclear reaction must not change significantly in the depth region where the deuterium is located. It will be shown in the following section that both requirements are sufficiently fulfilled for the here-conducted experiments.

NRA measurements with ^{3}He ions of one energy are not sufficient to monitor the evolution of the deuterium depth profile during the implantation. In order to gain information on the deuterium concentration in the tungsten sample during deuterium implantation a slightly different approach than the previous one is applied. Deuterium is implanted into a virgin tungsten sample under the conditions stated above. After irradiation of specific deuterium fluences, i.e., 1.3, 2.5 and $8.4 \times 10^{21}\,\mathrm{D\,m^{-2}}$, the homogeneity of the deuterium retention in the implantation spot is verified and deuterium depth profiling by NRA with ^{3}He ions of eight different energies is performed as previously described. In order to minimize the influence of the ^{3}He analysis beam on the measured deuterium retention [113, 114], each depth profile of the subsequent fluences is measured at a different spot.

Once the highest fluence of $8.4 \times 10^{21}\,\mathrm{D\,m^{-2}}$ is irradiated and the NRA measurements at 150 K are finished, the sample is warmed-up to 290 K and kept at this temperature for approximately 114 h. After this period the sample is cooled down again to 150 K and another deuterium depth profile is measured. By comparing the depth profiles and deuterium retention before and after warm-up, a first impression on diffusive effects and the trapped deuterium inventory being released during warm-up is obtained.

4.1.2 Surface Morphology

In contrast to the investigation of the evolution of the deuterium retention and concentration, the development of a surface morphology during deuterium implantation at 150 K cannot be studied in situ, but is conducted as follows. The implantation of deuterium into the tungsten sample is carried out in the dual beam experiment with deuterium of an energy of 3.0 keV/D, a flux of $8.4 \times 10^{17}\,\mathrm{D\,m^{-2}s^{-1}}$ at a temperature of 150 K under normal incidence with respect to the sample surface. In order to save machine time of the dual beam experiment and the Helios setup, the deuterium implantation is not carried out stepwise at the same spot with SEM and EBSD performed in between. Instead seven implantation spots with different deuterium fluence ranging from 8.5×10^{19} to $1.7 \times 10^{22}\,\mathrm{D\,m^{-2}}$ are created on the same sample by restricting the deuterium ion beam with the ion beam analysis aperture with a diameter of 1.5 mm. Due to the divergence of the ion beam an implantation spot size with a diameter of 2.1 mm is achieved. Once the implantation of the seven spots is finished the sample is warmed up to 290 K and mounted in the Helios setup. On each implantation spot a series of backscattered electron images with increasing magnification is performed using an acceleration voltage for the electrons of 5.0 kV. After this visual characterization, EBSD with electrons accelerated by a voltage of 20.0 kV is performed on the very same region. In total an area of $100 \times 100\,\mathrm{\mu m^2}$ is scanned with a step width of 1 µm to obtain the crystallographic orientation of the individual grains with respect to the surface. Specific spots, e.g. the boundary of grains with significantly different surface orientation, are then studied in greater detail.

4.2 Results

4.2.1 Evolution of D Retention

The deuterium retention in tungsten as a function of irradiated deuterium fluence at a sample temperature of 150 K is shown in figure 4.1. For low irradiated fluences, approximately up to $1.6 \times 10^{21}\,\mathrm{D\,m^{-2}}$, a linear increase of the deuterium retention is observed. When the implantation is continued the increase of the deuterium retention is reduced. Finally, the retention levels off and saturates at a value of $2.07 \pm 0.25 \times 10^{21}\,\mathrm{D\,m^{-2}}$ for irradiated fluences larger than $6.0 \times 10^{21}\,\mathrm{D\,m^{-2}}$.

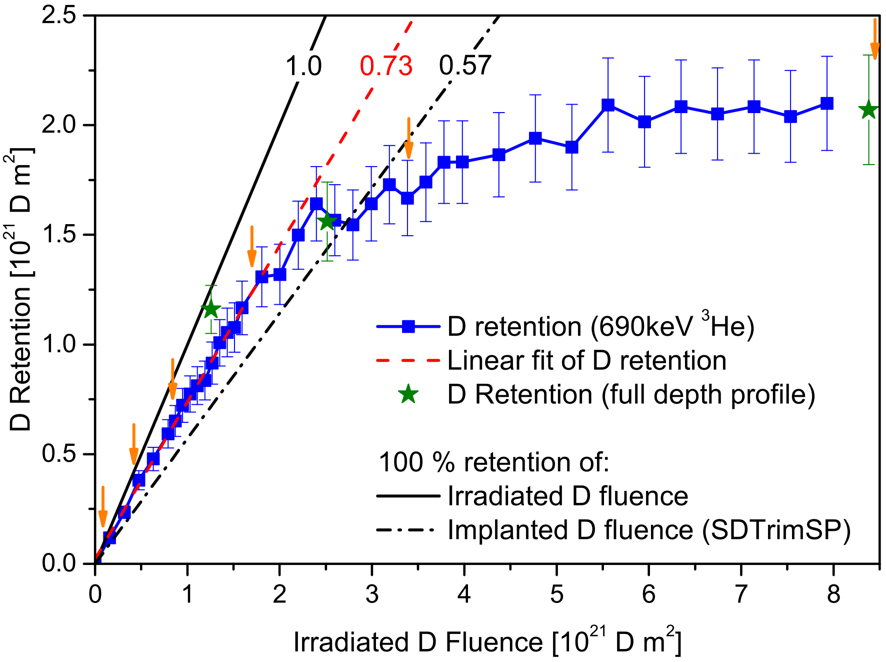

Figure 4.1: Deuterium retention in tungsten as a function of the irradiated deuterium fluence at 150 K. The deuterium implantation is conducted with an energy of 3.0 keV/D normal to the sample surface.

The case of 100 % deuterium retention of the irradiated fluence is illustrated in figure 4.1 by the solid black line and indicated with the slope of 1.0. The measured deuterium retention cannot exceed this line for physical reasons. However, only a certain portion of the irradiated deuterium fluence is actually implanted into the sample, while the other part is reflected. The particle reflection coefficient, which is the ratio of reflected to irradiated atoms, depends for a given projectile target combination strongly on the projectile energy and the angle of incidence. For the implantation conditions in the here-conducted experiment, a particle reflection coefficient of 0.43 for deuterium on tungsten is calculated by SDTrimSP with the parameters given in appendix A.2. Taking this reflection coefficient into account the dash-dotted black line shown in figure 4.1 is obtained which corresponds to the retention of 57 % of the irradiated

deuterium fluence. It can be seen that for fluences up to $2.6 \times 10^{21}\,\mathrm{D\,m^{-2}}$ the measured deuterium retention is systematically larger than predicted by SDTrimSP. A linear fit on the experimental data up to irradiated fluences of $1.6 \times 10^{21}\,\mathrm{D\,m^{-2}}$, indicated by the dashed red line, shows a retention of approximately 73 % of the irradiated deuterium fluence.
The green stars depicted in figure 4.1 correspond to the deuterium retentions obtained from the deuterium depth profiles shown in figure 4.2. The orange arrows indicate the irradiated deuterium fluences for which SEM and EBSD is conducted, shown in figures 4.3 and 4.4 (a) to (e).

4.2.2 Evolution of D Depth Profile

Beside the evolution of the deuterium retention also the development of the deuterium depth profile during the implantation is of interest. In figure 4.2 the depth profiles obtained for three different irradiated deuterium fluences are shown. After irradiation of a deuterium fluence of $1.3 \times 10^{21}\,\mathrm{D\,m^{-2}}$ at sample temperature of 150 K the deuterium depth profile shown as solid black line in figure 4.2 is obtained. Within the first 60 nm a deuterium concentration of 24 at.% is measured. For a depth between 60 to 130 nm a concentration of 5.8 at.% is observed, while for larger depth no deuterium is detected. As the implantation is continued to $2.5 \times 10^{21}\,\mathrm{D\,m^{-2}}$ irradiated fluence, the depth profile, indicated by the solid green line, shows an increase of the deuterium concentration close to the surface to 32 at.%. Furthermore, deuterium can be found in the sample up to a depth of 160 nm, though its concentration has not increased. After reaching the final deuterium fluence of $8.4 \times 10^{21}\,\mathrm{D\,m^{-2}}$, the depth profile depicted as solid blue line is measured. A further increase of the deuterium concentration to 42 at.% up to a depth of approximately 70 nm can be observed. In larger depth the deuterium concentration is similar to those found for lower irradiated deuterium fluences and the depth profile extends up to 170 nm into the bulk. By integrating the depth profiles in figure 4.2 over depth, the total amount of retained deuterium can be determined to 1.15 ± 0.12, 1.56 ± 0.18 and $2.08 \pm 0.25 \times 10^{21}\,\mathrm{D\,m^{-2}}$ for increasing irradiated deuterium fluence, respectively.
For comparison the deuterium implantation profile calculated by SDTrimSP with 10^6 projectiles for the given implantation conditions and an irradiated deuterium fluence of $1.3 \times 10^{21}\,\mathrm{D\,m^{-2}}$ is depicted in figure 4.2. The detailed parameters of the SDTrimSP simulation are stated in the appendix A.2. The deuterium implantation profile is simulated for this specific fluence since the deuterium retention is expected to increase linearly up to $1.6 \times 10^{21}\,\mathrm{D\,m^{-2}}$ according to figure 4.1. The calculated deuterium implantation profile possesses a maximum at a depth of 25 nm with a deuterium concentration of approximately 21 at.%. It can be seen that most of the measured deuterium is located within the calculated implantation zone up to 60 to 70 nm. Nevertheless, deuterium is also found up to 130 to 170 nm in the bulk, which is clearly behind

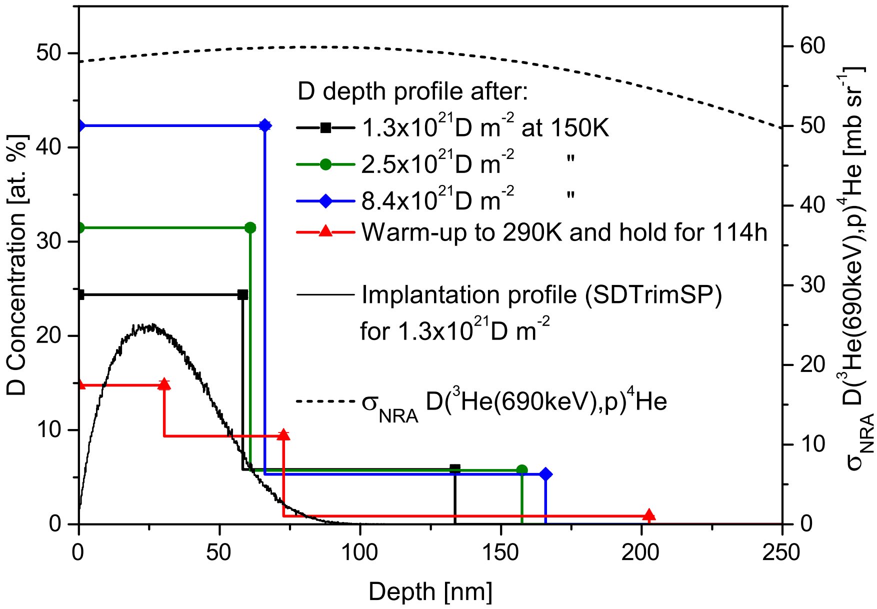

Figure 4.2: Deuterium depth profiles after irradiation of different deuterium fluences of 1.5, 3.0 and $8.4 \times 10^{21}\,\mathrm{D\,m^{-2}}$ at 150 K and after warm-up and hold at 290 K for 114 h following the highest irradiated deuterium fluence. NRA cross section σ_{NRA} of the $\mathrm{D(^3He,p)^4He}$ nuclear reaction as function of depth for ^{3}He ions with an energy of 0.69 MeV (dashed black line). Calculated implantation profile of deuterium in tungsten implanted with an energy of 3.0 keV/D under normal incidence with respect to the surface (thin solid black line).

the largest calculated implantation depth of approximately 100 nm.

After irradiation of the final deuterium fluence of $8.4 \times 10^{21}\,\mathrm{D\,m^{-2}}$ the sample is warmed up to 290 K and held at this temperature for approximately 114 h, before it is cooled down again to 150 K. The corresponding deuterium depth profile measured after this temperature treatment is shown as solid red line in figure 4.2. The deuterium concentration decreased considerably resulting in a profile with three steps. Close to the surface, within the first 30 nm, a concentration of 15 at.% is observed. Between 30 to 70 nm the concentration reduces to 9.3 at.% and further down to 0.9 at.% for even larger depth. Compared with the depth profile before the temperature treatment, deuterium can be detected up to 200 nm in the bulk which suggests an inward diffusion of deuterium. The total amount of retained deuterium is $0.61 \pm 0.04 \times 10^{21}\,\mathrm{D\,m^{-2}}$, which is approximately 30 % of the original deuterium retention at 150 K.

In addition to the depth profiles the NRA cross section σ_{NRA} of the $\mathrm{D(^3He,p)^4He}$ nuclear reaction for ^{3}He with an energy of 0.69 MeV is plotted as a function of depth in figure 4.2. It possesses a peak of $60.4\,\mathrm{mb\,sr^{-1}}$ at a depth of 80 nm and decreases towards the surface, where most of the deuterium is located, by 3 %. At 170 nm the cross section is lower by 5 % and at 200 nm by 8 %. The conclusion from the comparison of the deuterium depth profiles with the nuclear reaction cross section is twofold. First, in the here-conducted low-temperature experiments ^{3}He ions with an energy of 0.69 MeV probe the total amount of deuterium retained in the tungsten samples. Second, due to the minor variation across the depth of interest, the cross section can be regarded as constant in this region. As a consequence, the proton signal generated by the corresponding ^{3}He ions is proportional to the total amount of retained deuterium. Thus, it is sufficient to measure one depth profile using ^{3}He ions of eight different energies to obtain the total retained amount of deuterium and monitor the evolution of the retained deuterium by using ^{3}He ions with an energy of 0.69 MeV. For a comparison of deuterium retention derived by NRA with ^{3}He ions of one versus eight energies, the retention obtained from the depth profiles in figure 4.2 are plotted in figure 4.1. The good agreement between the differently derived deuterium retention values supports the assumption of a constant cross section in the relevant depth region.

4.2.3 Evolution of Blister Formation

In order to study the development of the surface morphology during implantation at 150 K, the sample is exposed to seven different deuterium fluences starting at 8.5×10^{19} up to $1.7 \times 10^{22}\,\mathrm{D\,m^{-2}}$. The SEM and EBSD images shown in figure 4.3 are recorded after irradiation of the lowest deuterium fluence of $8.5 \times 10^{19}\,\mathrm{D\,m^{-2}}$. The backscattered electron image (a) in figure 4.3 provides an excellent grain contrast which helps to identify individual grains. The grain size ranges between 10 to 40 µm which is the expected size after recrystallization at 2000 K for this tungsten material according to Manhard et al. [83].

In figure 4.3 (b), the EBSD scan of the region shown in image (a) is plotted in the IPF-Z color coding [81], without any further post-processing. By applying the IPF-Z color coding, shown in figure 4.3 (d), blue, green and red grains correspond to grains with an {111}, {110} and {100} plane parallel to the surface, respectively. Hence, the major crystal axis ⟨111⟩, ⟨110⟩ and ⟨100⟩ are oriented perpendicular to the sample surface. Grains which are less well oriented with respect to the surface are indicated by a mixture of the high symmetry colors shown in figure 4.3 (d). As can be seen from the EBSD scan, most of the grains are marked by a red, pink or orange color which indicates a preferred grain orientation close to the {100} plane with respect to the surface. Only a few grains, labeled by purple or bluish color, possess an orientation close to the {111} plane at the surface. No grains with a surface orientation close to the {110} plane are present in the EBSD scan. These findings are in good agreement with the experiments by Manhard et al. [83] which revealed a surface texture dominated by grains oriented close to the {100} plane with respect to the surface once the tungsten is recrystallized at 2000 K. Furthermore, in figure 4.3 (b) only a small portion of grains with an orientation close to the {111} plane and hardly any grains oriented close to the {110} plane with respect to the surface are observed. Apart from the colorful grains, also white squares are visible in the EBSD scan in figure 4.3 (b). They

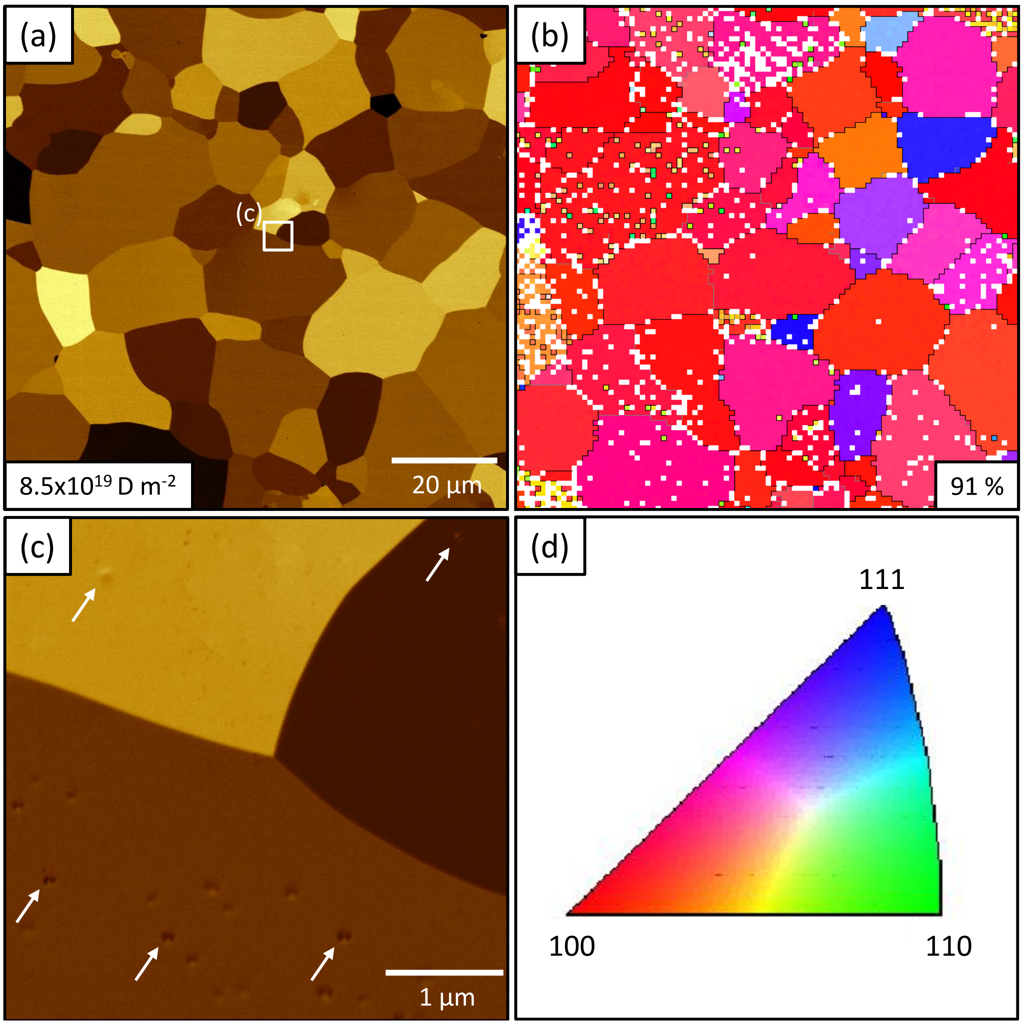

Figure 4.3: (a) Backscattered electron image of tungsten irradiated with deuterium of an energy of 3.0 keV/D at a sample temperature of 150 K with a fluence of $8.5 \times 10^{19}\,\mathrm{D\,m^{-2}}$. (b) EBSD image corresponding to the region shown in (a) with EBSD solving probability. (c) High magnification backscattered electron image of the region in (a) indicated by the solid white square. The white arrows mark some of the blisters on the grains. (d) Inverse pole figure with IPF-Z color coding used in (b).

correspond to EBSD spots, where the Kikuchi pattern could not be matched to a specific crystallographic orientation. Especially at grain boundaries, where the electron beam hits two or more grains simultaneously, the probability for a correct matching is lower compared with spots within a grain. As the raw data of the EBSD scan is shown in figure 4.3 (b), individual white pixels surrounded by eight pixels of the same color are very likely to belong to the same grain and would be interpolated in a post-process step. Without post-processing, the EBSD solving probability, which is in this thesis defined as the percentage of measured EBSD spots for which the Kikuchi pattern could be solved and a specific crystallographic orientation could be assigned, is 91 %. Furthermore, small and large angle grain boundaries are indicated by solid gray and black lines in figure 4.3 (b), respectively.

On image (a) in figure 4.3 no obvious change in the surface morphology compared with an unirradiated sample can be observed. However, the magnified image of the area indicated by the solid white square, shown in image (c), reveals the appearance of small features inside the grains. Some of them are marked by white arrows. The observed features have a circular shape with a diameter between 80 to 100 nm and are presumably the first blisters. This means that the initiation of blister formation takes place already below the lowest irradiated deuterium fluence of $8.5 \times 10^{19}\,\mathrm{D\,m^{-2}}$.

The further development of the surface morphology and the blisters during the deuterium implantation is shown in figure 4.4 (a) to (f) for increasing deuterium fluences from 4.2×10^{20} to $1.7 \times 10^{22}\,\mathrm{D\,m^{-2}}$, respectively. On the left-hand side the backscattered electron images are shown with the corresponding irradiated deuterium fluences indicated in the images. The level of magnification of the shown images is a compromise between the visualization of individual blister and the presentation of a large number of grains. On the right-hand side the section of the EBSD scan which corresponds to the area shown on the left-hand side is plotted. The percentage inserted in the EBSD scans yields the EBSD solving probability of the total $100 \times 100\,\mathrm{\mu m^2}$ scan.

By comparing the backscattered electron images of figure 4.4 (a) with those of figure 4.3, it can be seen that a five times higher irradiated deuterium fluence alters the sample surface significantly. The size of the blisters compared with those shown in image (c) of figure 4.3 has obviously increased. On some grains in image (a) of figure 4.4 a large quantity of densely packed, predominantly circular shaped blisters is detected. Furthermore, from the comparison of image (a) with the corresponding EBSD scan a clear dependence of the diameter and the number density of the blisters on the grain orientation with respect to the surface is observed. The grains on which massive blistering occurs are mainly of red color, corresponding to a surface orientation near the {100} plane. On the other hand, grains indicated in the EBSD scan by pink color, which is related to an orientation in between the {100} and {111} plane, show only sparse blistering. By comparing the EBSD scan of the region in figure 4.4 (a) with the one of figure 4.3 (a), it can be seen that the EBSD solving probability

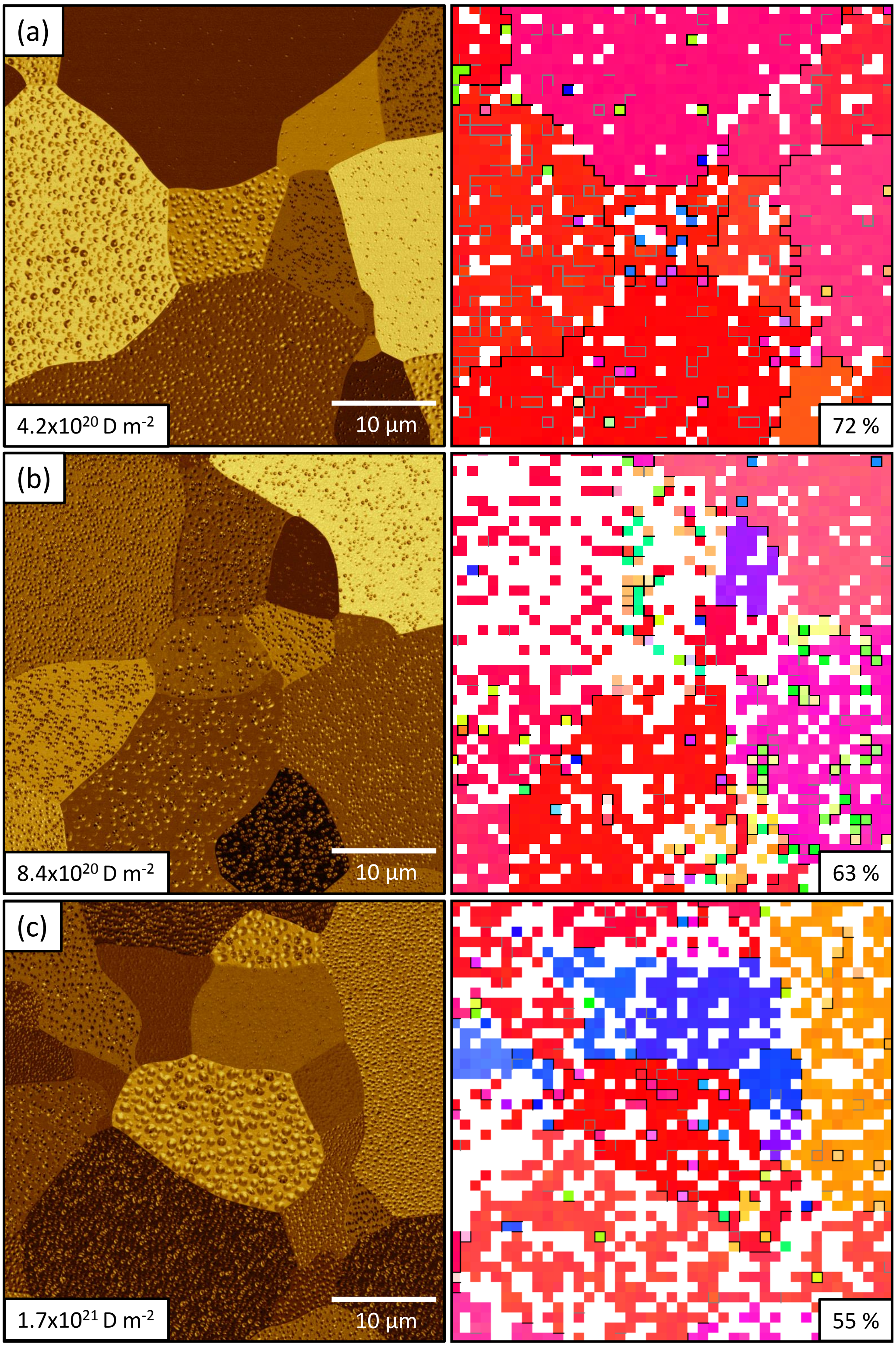
(a)
4.2x10^{20} D m^{-2}
10 µm
72 %
(b)
8.4x10^{20} D m^{-2}
10 µm
63 %
(c)
1.7x10^{21} D m^{-2}
10 µm
55 %

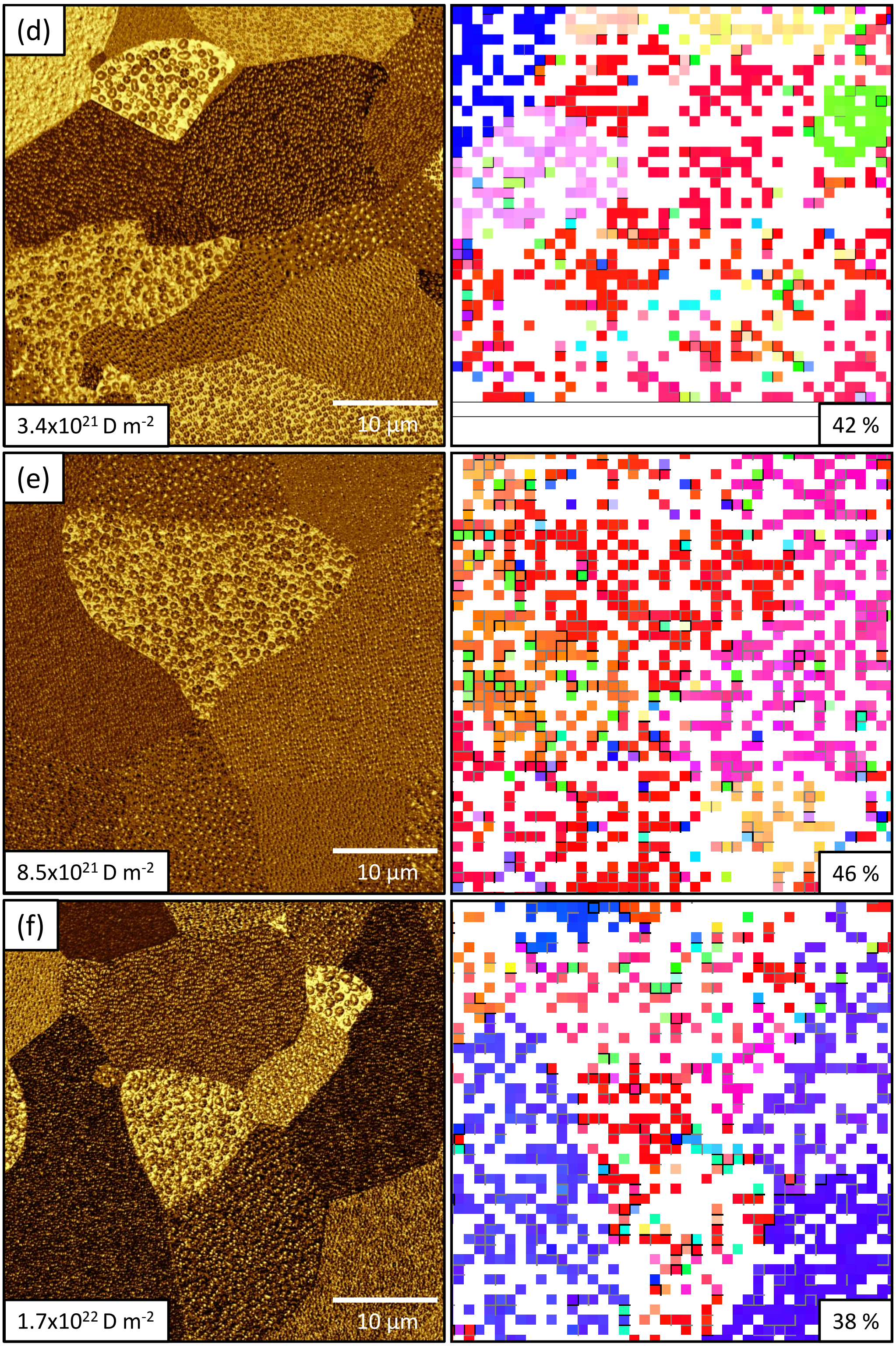

Figure 4.4: (a) to (f) Backscattered electron image (left) and corresponding EBSD scan (right) of tungsten irradiated with deuterium of an energy of 3.0 keV/D at a sample temperature of 150 K with fluences of 4.2×10^{19} to $1.7 \times 10^{22}\,\mathrm{D\,m^{-2}}$, respectively.

is reduced to 72 %.

For increasing irradiated deuterium fluences up to $1.7 \times 10^{21}\,\mathrm{D\,m^{-2}}$ the blisters appear to become larger, as can be seen from the backscattered electron images (b) and (c) in figure 4.4. For even higher fluences up to $1.7 \times 10^{22}\,\mathrm{D\,m^{-2}}$, shown in the images (d) to (f) of figure 4.4, the size of the blisters seems to remain constant. A comparison of the EBSD scans performed after irradiation of different deuterium fluences shows that the EBSD solving probability decreases with increasing fluence, from 91 % after irradiation of $8.5 \times 10^{19}\,\mathrm{D\,m^{-2}}$ to 38 % after $1.7 \times 10^{22}\,\mathrm{D\,m^{-2}}$.

The majority of the observed grains possess a plane at the surface with an orientation close to the $\{100\}$ plane. Therefore, the growth of the blisters is exemplarily studied on grains with a maximum derivation of $10\,^{\circ}$ from this specific orientation. Since the shape of the blisters is mainly circular, the blister diameter seems to be a suitable quantity to compare the size of the blisters at different implantation stages.

In figure 4.5 (a) the distribution function of the blister diameter with a binning width of 50 nm is shown as a function of the irradiated fluence up to $1.7 \times 10^{21}\,\mathrm{D\,m^{-2}}$. After irradiation with a deuterium fluence of $8.5 \times 10^{19}\,\mathrm{D\,m^{-2}}$ the distribution function shows one maximum.

Assuming a normal distribution of the blister diameter, a fit on the data yields an average diameter with the corresponding standard derivation of 160 ± 40 nm. Exposure of the sample to a deuterium fluence of $4.2 \times 10^{20}\,\mathrm{D\,m^{-2}}$ leads to a shift of the distribution function towards larger blister diameter of up to 800 nm. Furthermore, the distribution function of the blister diameter becomes bimodal. The two distinct peaks suggest the coexistence of a small and large blister population on the grains. By fitting the distribution function of the blister diameter with two normal distributions average blister diameters of 150 ± 40 and 450 ± 130 nm are obtained for the small and large blisters, respectively. After irradiation of $8.4 \times 10^{20}\,\mathrm{D\,m^{-2}}$ the blister diameter distribution function extends to even larger diameter, with the largest one at approximately at 900 nm. The previously observed peak at a blister diameter of 150 to 160 nm has vanished and the bimodal character of the distribution is not as clear as before. However, the distribution function possesses an asymmetric shape with a tail towards smaller blister diameters which might be an indication of the increase of the average diameter of the small blister population. The data is again fitted with two normal distributions yielding average blister diameters of 300 ± 120 and 540 ± 140 nm for the small and large blister population, respectively. As the deuterium implantation is continued to $1.7 \times 10^{21}\,\mathrm{D\,m^{-2}}$ irradiated fluence, the distribution function of the blister diameter shifts towards even larger diameter. The largest observed blister diameter is 1150 nm. Furthermore, the bimodal nature of the distribution function becomes visible again. A fit, consisting of two normal distributions, reveals an increase of the average diameter of the large blister population to 730 ± 140 nm. In contrast to that the average diameter of the small blister population has hardly changed

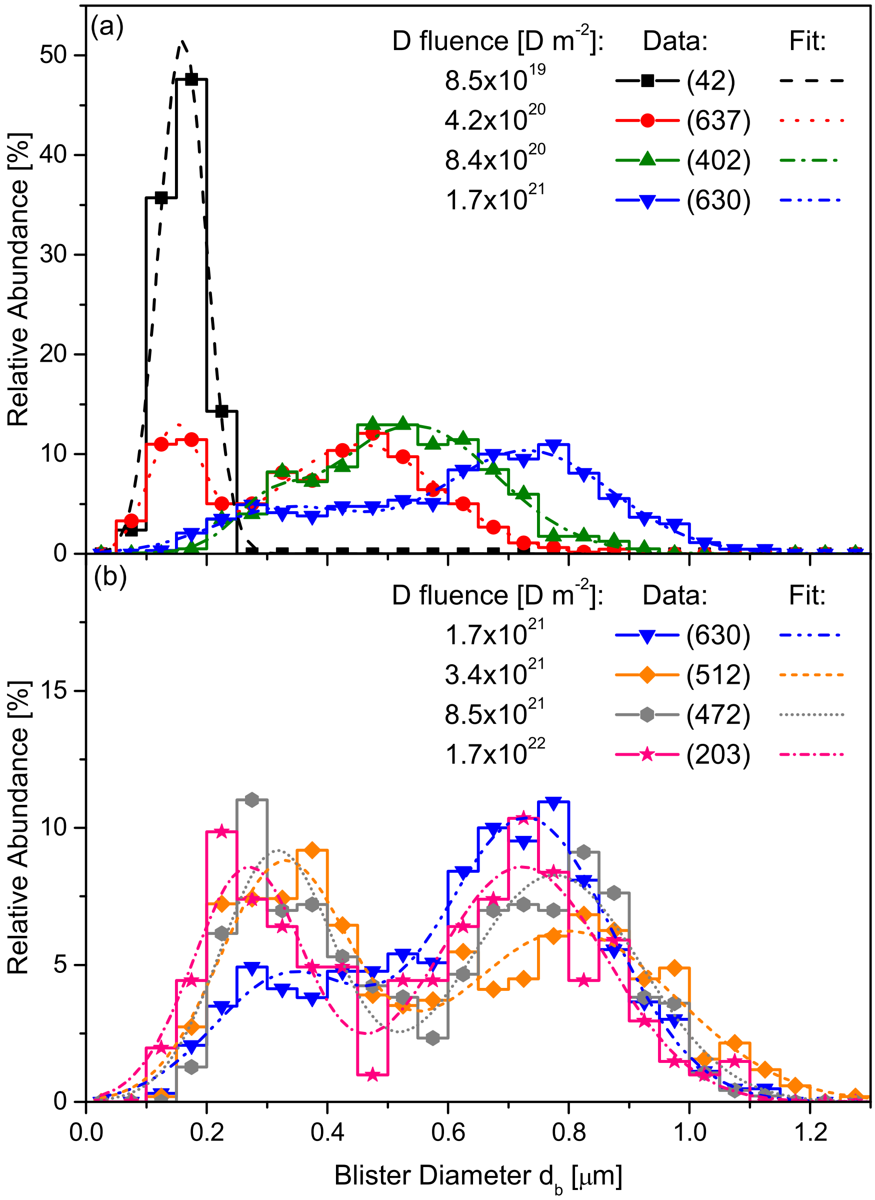

Figure 4.5: Distribution functions of the blister diameter of grains with an orientation with a maximum deviation of 10 ° from the {100} plane with respect to the surface for irradiated deuterium fluences of (a) 8.5×10^{19} to $1.7\times10^{21}\,\mathrm{D\,m^{-2}}$ and (b) 1.7×10^{21} to $1.7 \times 10^{22}\,\mathrm{D\,m^{-2}}$. The number of measured blisters is stated in the brackets.

and yields $330 \pm 120\,\mathrm{nm}$.

The distribution function of the blister diameter for irradiated deuterium fluences of 1.7×10^{21} to $1.7 \times 10^{22}\,\mathrm{D\,m^{-2}}$ is illustrated in figure 4.5 (b). It can be seen that once an irradiated fluence of $1.7 \times 10^{21}\,\mathrm{D\,m^{-2}}$ is exceeded a further increase of the fluence does not have a significant effect on the distribution function of the blister diameter. Especially no further shift towards larger blister diameter is observed in contrast to figure 4.5 (a). Moreover, the two peaks, corresponding to the small and large blister population, can be seen very clearly. The fit of each blister diameter distribution function with two normal distributions reveals a mean blister diameter of 330 ± 110, 320 ± 90 and $270 \pm 90\,\mathrm{nm}$ for the small blister population and 800 ± 180, 780 ± 140 and $720 \pm 140\,\mathrm{nm}$ for the large blister population for irradiated fluences of 3.4×10^{21}, 8.5×10^{21} and $1.7 \times 10^{22}\,\mathrm{D\,m^{-2}}$, respectively.

The following considerations regarding the statistics of the data shown in figure 4.5 should be kept in mind. As can be seen from the backscattered electron images in figure 4.4, the number of blisters per grain is sufficient to conduct a reliable statistical analysis of the blister diameter on the respective grain. Yet, the EBSD scan of an area of $100 \times 100\,\mathrm{\mu m^2}$, contains only a few grains which fulfill the requirement of a grain orientation deviating not more than 10 ° from the {100} plane with respect to the surface. Thus, the distribution functions of the blister diameter shown in figure 4.5 are composed from data of only a few grains each, which is not enough for a comprehensive statistical analysis. It is likely that variations of the blister diameter of grains with different grain orientations within the predefined maximum deviation of 10 ° lead to a biased distribution functions of the blister diameter to some extent. However, the main features, which are the observation of two different blister populations and the growth of the blisters to a limited size should be trustworthy.

4.2.4 Grain Orientation Dependence of Blistering

From the backscattered electron images and the EBSD scans shown in figure 4.4, the dependence of the blister properties on the grain orientation with respect to the surface are quite obvious. Hence, a more detailed analysis of this phenomenon is conducted. In order to have a sufficiently blistered tungsten sample as well as reliable crystallographic information, the implantation spot irradiated with a deuterium fluence of $4.2 \times 10^{20}\,\mathrm{D\,m^{-2}}$ is investigated. In figure 4.6 (a) to (d), the relevant blister parameters are illustrated as a function of the grain orientation with respect to the surface in the inverse pole figure [81]. Also the boundaries which mark a deviation of the grain orientation from the high symmetry planes with respect to the surface by 5 and 10 ° are indicated. In addition, a selection of backscattered electron images of different grains with varying surface orientation are shown and assigned in the inverse pole figures. In figure 4.6 (a) all analyzable grains of the $100 \times 100\,\mathrm{\mu m^2}$ EBSD scan from figure 4.4 (a), i.e., in total 59, are shown with their corresponding orientation.

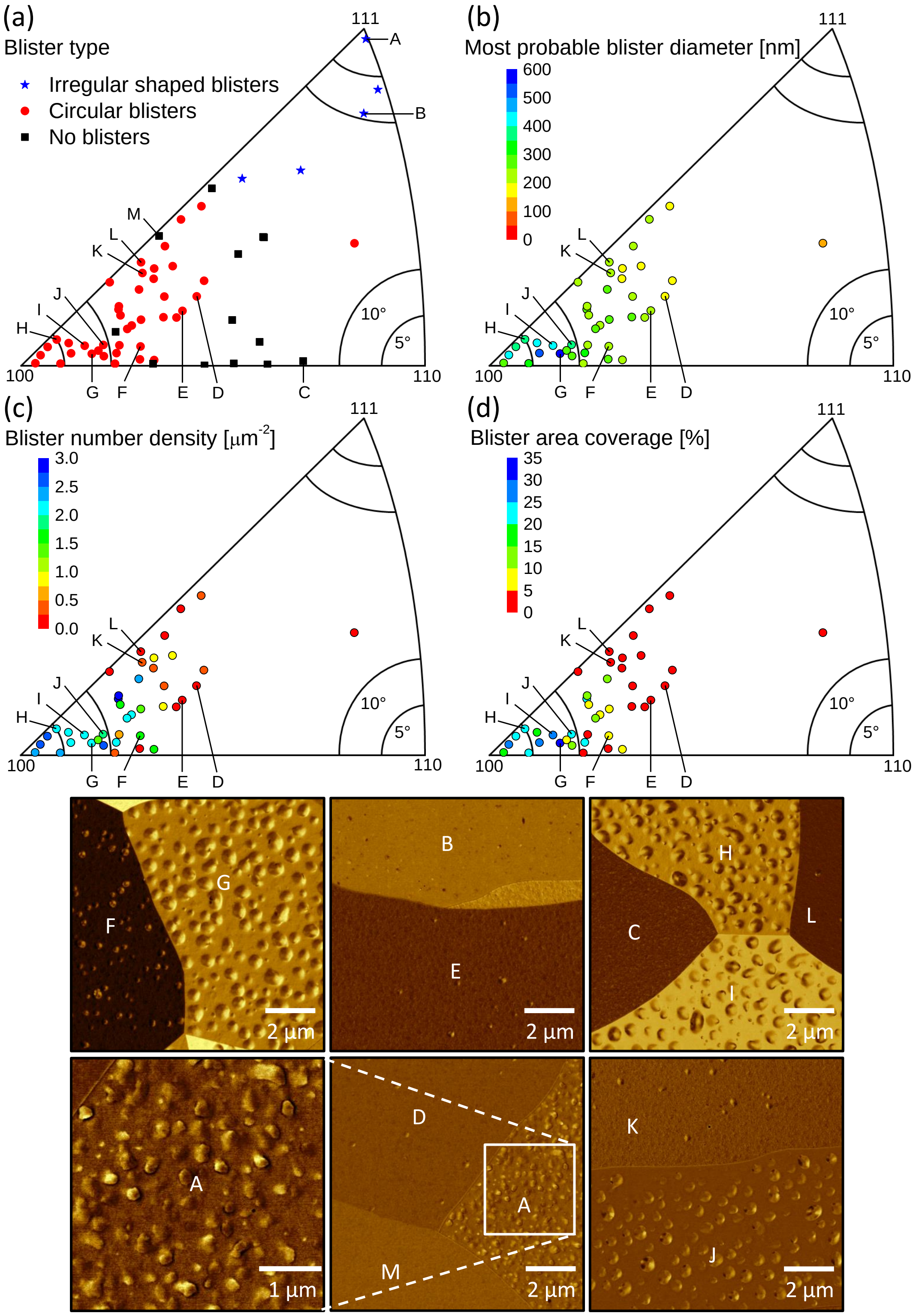

Figure 4.6: Grain-orientation-dependent blistering of tungsten exposed to deuterium with an energy of 3.0 keV/D at a sample temperature of 150 K up to a fluence of $4.2 \times 10^{20}\,\mathrm{D\,m^{-2}}$. The blister type, the most probable blister diameter, the blister number density and the area coverage are shown as function of the grain orientation with respect to the surface together with backscattered electron images of representative grains A to M.

The distribution of the grains in the inverse pole figure reflects the texture of the tungsten material. Most of the grains are located in the corner of the {100} plane, a few in the {111} corner and none in the {110} corner. The grains are distinguished according to the existence and the shape of the blisters, i.e., no blisters, circular blisters and irregular shaped blisters. Blister with circular shape are located predominately on grains with an orientation close to the {100} plane with respect to the surface, as can be observed from the backscattered electron images of grains D to L. When the grain orientation tends from the {100} towards the {111} plane, the circular shaped blisters become fewer, as can be seen by comparing grain H and L. Also grains without blisters are observed, e.g. grain M. As the grain orientation approaches the {111} plane, irregular shaped blisters appear on the grains, as depicted in the backscattered electron images of grain A. When the surface orientation of the grains changes from the {100} to the {110} plane, the circular blisters become smaller, as can be seen on grain G and F, and more grains with no blisters are observed, e.g. grain C. For grains with an orientation close to the {110} plane, no data is available due to the texture of the material.

The backscattered electron images of grains D to L show circular shaped blisters. However, the blister properties vary significantly between them. Therefore, a more detailed analysis of the grains containing circular shaped blisters is conducted. For each grain, the blister diameter distribution function, similar to those shown in figure 4.5, is determined together with the area of the respective grain.

In figure 4.6 (b) the most probable blister diameter of large blister population is plotted as a function of the grain orientation. It can be seen that the largest most probable diameters are observed for grains with an orientation that deviates by 5 to 10 ° from the {100} plane. The largest most probable blister diameter of nearly 600 nm is observed on grain G. Furthermore, the existence of a population of small blisters dispersed between the large blisters can be seen very clearly on the images of grain G, H and I. For grains whose surface orientation deviates by $\leq 5\,°$ from the {100} plane, a slightly smaller most probable blister diameter is observed. Grains which possess a surface orientation that deviates by more than 10 ° show lower most probable blister diameters. In addition, the most probable blister diameter seems to decrease, the further the grain orientation tends towards the {111} plane, as can be observed from grains D, E, K and L.

The number density of the blisters, illustrated in figure 4.6 (c), is calculated by dividing the number of detected small and large blisters per grain by the area of the respective grain. It can be seen that the number density of the blister tends to be higher for grains oriented within $\leq 10\,°$ to the {100} plane and seems to decrease the further the grain orientation deviates from this specific plane. This trend can be observed very illustratively by comparing the backscattered electron images of grain G and D. However, it seems that the grains which possess the largest most probable diameter do not yield the highest number density of blisters.

The percentage of area covered by blisters per grain, shown in 4.6 (d), is determined under the assumption of circular blisters. The total area covered by blisters per grain is calculated by summation of the squared and by $\pi/4$ multiplied blister diameter distribution function. The division by the area of the respective grain yields the percentage of area covered by blisters. By comparing the inverse pole figures of the most probable blister diameter (b) and the one of the area covered by blister (d), it can be seen that the grains showing the largest most probable diameter tend to have the largest area covered by blisters. In case of grain G this is approximately 31 %. The more the grain orientation with respect to the surface deviates from the $\{100\}$ plane, the lower is the area covered by blisters, as can be observed on the images of grain D, E, K and L.

4.3 Discussion

From the results in the previous section it can be seen that the deuterium retention and the concentration in tungsten during the deuterium implantation at low temperature evolve in parallel to the development of the surface morphology. A separate evaluation of the results would neglect interdependences among them. Therefore, the discussion of the results is structured as follows: At first the relevant results obtained from the investigation of the surface morphology evolving during the deuterium implantation are discussed. This includes the formation and development of the blisters, the evolution of the EBSD data as well as the grain orientation dependence of blistering. Finally, these insights are used to interpret the results obtained for the deuterium retention and the depth profiles during the deuterium implantation at low temperature. The results gained from the investigation of the surface morphology as well as from the deuterium retention and the depth profiles can be summarized as follows:

Surface Morphology:

1. The formation of blisters is already observed at the lowest irradiated deuterium fluence.

2. At low irradiated deuterium fluences an increase of the blister diameter is observed.

3. At high irradiated deuterium fluences no further increase of the blister diameter is observed.

4. An increase of the irradiated deuterium fluence results in a reduction of the EBSD solving probability.

5. The blister properties are strongly depending on the grain orientation with respect to the surface.
6. The largest blisters are observed on grains with a surface orientation deviating by 5 to 10 ° from the {100} plane.

Deuterium Retention and Concentration:

1. At low irradiated deuterium fluences a linear increase of the deuterium retention is observed.
2. The deuterium retention in the linear regime is larger than predicted by SDTrimSP.
3. At high irradiated deuterium fluences a saturation of the deuterium retention is observed.
4. An extremely high deuterium concentration, saturating at 42 at.%, is measured.

4.3.1 Initiation and Growth of Blisters

Nowadays, the interaction of deuterium with tungsten is predominately studied in linear plasma devices which intend to mimic the conditions prevailing in the divertor region of a nuclear fusion device. These setups produce deuterium plasmas from which a high flux of low-energy deuterium ions impinges on the tungsten sample. The blisters and surface morphologies found on those samples are manifold. With sizes and depths of blisters ranging from a few nm up to tens of µm [115, 116], from the blisters located at grain boundaries [116, 117] to intra grain blisters [116, 118–120], from circular [110] and irregular shaped blisters [118] to flat table-mountain-like shaped ones [121]. This large variety indicates that the appearance of blisters is influenced by many different parameters, e.g. sample temperature [110, 122], ion energy [123], ion flux [116, 124], ion fluence [123], grain orientation [125], material grade [117, 126] and finally surface finish [31, 127, 128].

However, the blisters created in the here-performed experiment do not fit to those observed in linear plasma devices with respect to their shape. Most of the intra grain blisters, generated by irradiation of tungsten with high flux and low energy deuterium ions, possess an irregular shape with sharp edges [29, 116, 118, 124, 125, 127, 129–132] or even facets or steps [120, 121, 133]. In contrast to that most of the here created blisters have a predominately circular shape. Furthermore, their appearance has more in common with blisters obtained by irradiation of metals with energetic helium ions [134–137].

In case of helium, the formation of blisters can be attributed to the low solubility of helium in metals and its self-trapping property [138], leading to an excess of helium which finally precipitates. For the implantation of protium into molybdenum at temperatures, ranging from 158 to 673 K, the formation of circular blisters at low temperature is observed, while no blisters are detected at high temperature [135]. It is argued that the formation of the blisters at low temperature is caused by an excess of protium, similar to the case of helium. It is very likely that this argument holds for the here-conducted experiment as well. The solubility of deuterium in tungsten is low and the reduced diffusion of deuterium out of the implantation zone at low temperature leads to substantial deuterium concentrations and local oversaturation. In addition to that, the fracture toughness of the material is reduced at low temperature [111, 112], promoting the initiation and propagation of cracks inside the grains.

The formation of blisters in metals driven by oversaturation of gaseous species of low solubility is assumed to proceed in several steps. A good overview of the basic theories associated with each step can be found in [137]. In the first step gas bubbles are formed in the material. It is generally assumed that the formation of gas bubbles, which finally evolve into the blister, require the presence of nucleation seeds. Vacancies [60], dislocations [62] as well as impurities and grain boundaries [139] have been proposed as possible nucleation sites. In the second step, once sufficient atoms of the gaseous species have accumulated to form the bubble, the growth of the bubble starts. For this initial growth at low temperatures different theories are suggested: The emission of dislocation loops from the overpressurized bubble [140] or the capture of vacancies produced by the ion beam in close proximity of the bubble [141]. The actual blister is formed in the third step. According to the interbubble fracture model [142, 143], lateral compressive stress exists in the bubble-containing layer parallel to the surface as well as tensile microstress between the bubbles perpendicular to the surface. The latter one leads to the fracture of the material parallel to the surface and generates the initial crack of the blister. Subsequent accumulation of gaseous species results in an increase of the pressure inside the blister, leading to the propagation of the crack and the growth of the blister. The further growth and the final appearance of the blister can be described by different models, e.g. the spherical shell model [144], the lateral compressive stress model [145], the crack growth model [146] or FEM simulations [147].

In the here-performed experiment the energy of the incident deuterium is 3.0 keV/D from which a maximum of 125 eV can be transferred to a tungsten atom [13]. The minimum energy to displace a tungsten atom from its original position in the lattice is 41 eV [148]. Hence, the deuterium implantation leads to the formation of vacancy-interstitial pairs which could serve as bubble nucleation site. The growth of precipitated deuterium bubbles cannot be observed in this experiment and probably requires other means of investigation, e.g. transmission electron microscopy. However, the growth of the resulting blisters is observed for increasing irradiated deuterium fluences, as can be seen from the backscattered electron images in figure 4.3 and figure 4.4 (a) to (c) as well as from the blister diameter distribution function illustrated in figure 4.5 (a). It can be assumed that the accumulation of deuterium in the blisters causes a pressure increase in the blister cavities which is relaxed by crack propagation, resulting in the growth of the blisters.

In between an irradiated deuterium fluence of 8.4×10^{20} to $1.7 \times 10^{21}\,\mathrm{D\,m^{-2}}$, the blister growth seems to stop, as can be observed from the backscattered electron images (c) to (f) in figure 4.4 and the hardly changing distribution function of the blister diameter in figure 4.5 (b).

One possibility which could explain this observation is that the available space for blister growth is limited. As soon as the blister diameter approaches the inter-blister distance, adjacent blisters hinder one another from growing to larger size.

Another mechanism which can explain the restriction of the blister size, is the rupture of blisters during the implantation at low temperature once a certain fluence is exceeded. Figures 4.7 (a) to (c) show high resolution secondary electron images of the tungsten sample irradiated with deuterium fluences of 4.2×10^{20}, 8.4×10^{20} and $1.7 \times 10^{21}\,\mathrm{D\,m^{-2}}$, respectively. For the highest fluence, shown in image (c), several of the blisters possess a very bright rim, as exemplarily highlighted by the white arrows. This is caused by enhanced emission of secondary electrons as it is often observed at edges or shine-throughs. The increased brightness indicates a detachment of the blister cap from the material underneath which corresponds to the rupture of the blister. This observation is also in agreement with the FEM simulations by Enomoto et al. [110] which showed that the largest stress occurs at the rim of a blister. Also for an irradiated deuterium fluence of $8.4 \times 10^{20}\,\mathrm{D\,m^{-2}}$ some ruptured blisters are observed, as shown and exemplarily indicated in image (b). Compared to image (c) the cracks at the blister rim are less obvious and harder to detect. In contrast to that no ruptured blisters are observed for the lowest fluence of $4.2 \times 10^{20}\,\mathrm{D\,m^{-2}}$, shown in image (a). However, it should be mentioned that the detection of ruptured blister is difficult. Only in some cases the signs of

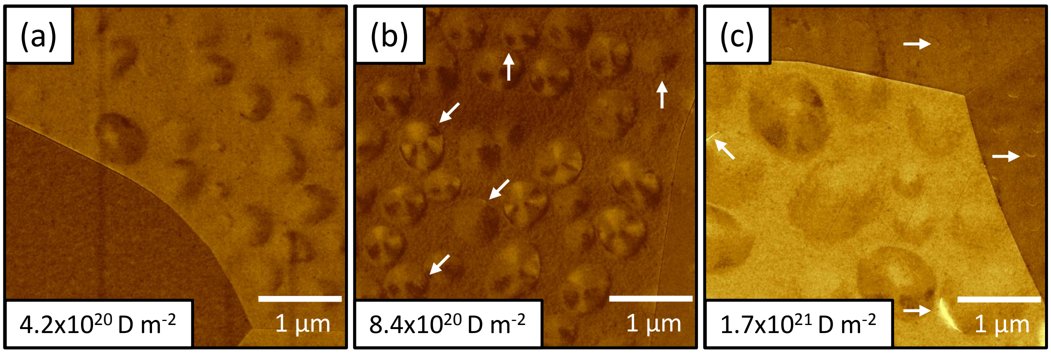

Figure 4.7: High resolution secondary electron images of tungsten irradiated at a sample temperature of 150 K with deuterium of an energy of 3.0 keV/D with fluences from 4.2×10^{20} to $1.7 \times 10^{21}\,\mathrm{D\,m^{-2}}$. Ruptured blisters are exemplarily marked with white arrows.

rupture are as prominent as shown in image (c). Consequently, no statistically significant result on ruptured blisters can be provided.

Also a combination of the two mechanisms might be possible. First, the blisters grow due to the accumulation of deuterium until the lack of available space constrains further growth. Second, continuing uptake of deuterium or coalescence of adjacent blisters, which might weaken the surrounding material, finally lead to the rupture of the blisters. However, it cannot be excluded that the rupture of the blisters takes place during the warm-up of the sample to room temperature.

Obviously, the mechanisms which are responsible for the initiation, growth and rupture of the blisters in the here-performed experiment are not entirely understood. Also the reason for the observed coexistence of a small and large blister population, shown in figure 4.5, remains unclear and requires more systematic experiments. In order to gain a more detailed understanding of the development of the blisters, in situ SEM investigations at variable sample temperature would be highly beneficial but are experimentally challenging.

4.3.2 Kikuchi Pattern

Apart from the crystallographic information of the individual grains, the EBSD scans, shown in figures 4.3 (b) and 4.4 (a) to (f), can also be used to qualitatively assess the condition of the near-surface crystal structure. The information depth of EBSD performed with electrons of an energy of 20.0 keV is approximately 20 to 50 nm. When the crystal structure within this depth is intact the diffraction of the elastically backscattered electrons is not disturbed. As a result the Kikuchi patterns are clearly visible, as shown in figure 4.8 (a) after irradiation of the lowest deuterium fluence of $8.5 \times 10^{19}\,\mathrm{D\,m^{-2}}$. The probability to find the correct crystallographic orientation of the underlying grain which is responsible for the observed Kikuchi pattern is high.

However, the diffraction of the electrons can be significantly disturbed by induced crystal defects and distortion. The reasons for the degradation of the near-surface crystallinity are manifold. First, the implanted deuterium possesses enough energy to displace tungsten atoms from their original positions in the lattice, leading to the formation of vacancy-interstitial pairs. Second, the emergence and growth of blisters with the associated stress and strain fields distort the surrounding tungsten lattice [110]. In addition, the formation of dislocations in the vicinity of the blisters is expected, as reported by Manhard [149]. Finally, the deuterium remaining in the sample could strain the tungsten lattice or influence the diffraction of backscattered electrons directly. Thus, the obtained Kikuchi patterns become blurred, as can be observed from figure 4.8 (b) recorded after irradiation with the highest deuterium fluence of $1.7 \times 10^{22}\,\mathrm{D\,m^{-2}}$. A successful identification of the surface orientation of the investigated grain is therefore less likely.

The EBSD solving probability obtained for the total scanned area can be used

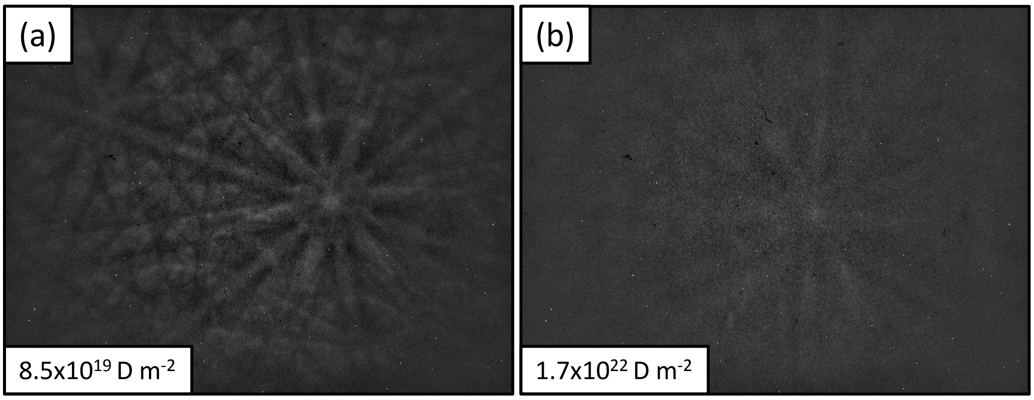

Figure 4.8: Kikuchi patterns of grains with a surface orientation deviating less than 5 ° from the {100} plane after an irradiated deuterium fluence of (a) 8.5×10^{19} and (b) $1.7 \times 10^{22}\,\mathrm{D\,m^{-2}}$.

as a qualitative indicator for the induced damage close to the surface. As can be seen from the EBSD scans shown in figure 4.3 and 4.4 (a) to (d), the EBSD solving probability decreases considerably for deuterium fluences up to $3.4 \times 10^{21}\,\mathrm{D\,m^{-2}}$. For higher deuterium fluences, illustrated in the EBSD scans of 4.4 (d) to (f), a less dramatic decrease is observed. This correlates with the stop of the blister growth and might correspond to a saturation of the defect concentration generated during the implantation of energetic deuterium ions.

4.3.3 Grain Orientation Dependence of Blistering

The reason for the observed dependence of blistering on the grain orientation with respect to the surface is not yet fully understood and requires a more detailed investigation. However, the appearance of the largest blisters on grains with a surface orientation close to the {100} plane suggests that ion channeling of deuterium in the tungsten lattice is involved. In a crystal lattice, sets of adjacent atomic planes along specific directions or atomic rows along high symmetry crystallographic axis provide channels. Deuterium ions which are injected into such a channel are reflected by the repulsive potential of the channel walls and thereby guided along the channel deeper into the bulk. A prerequisite for this ion channeling effect to occur is the nearly parallel alignment of the incident deuterium ion beam and the respective channel [13]. Thus, deuterium irradiated on grains for which the channeling conditions are met can penetrate the material to larger depth [150, 151]. This would lead to a larger deuterium concentration deeper in the bulk compared to grains for which no channeling occurs. Assuming that the depth of the blisters correlates with the ion implantation range, the initiation of the blister is expected at larger depth for grains which show ion channeling. As a consequence of the larger depth of blister initiation, the size to which the blisters can grow increases [17, 152]. As a result, the largest blister would occur on grains which possess an orientation with respect to the surface that allows channeling of the incident deuterium ion. A positive correlation between ion implantation range and blister size was also observed in case of molybdenum being irradiated with helium ions of different energies ranging from 7 to 350 keV/He [134, 153].

As proposed by the interbubble fracture model, the tensile microstress in between the gas bubbles perpendicular to the sample surface finally cracks the material and initiates the blisters. Hence, the capability of the material to withstand this stress, which is defined by the fracture toughness, is an essential parameter in the blister formation process. In cleavage experiments conducted on tungsten single crystals, a variation of the fracture toughness depending on the crystal plane of cleavage was observed [111, 112, 154]. At a temperature of 150 K the fracture toughness of a $\{100\}$ plane is 5.2 and 3.1 $\mathrm{MPa\,m^{1/2}}$ for a $\langle 001\rangle$ and $\langle 011\rangle$ crack front direction, respectively. In contrast to that the fracture toughness of a $\{110\}$ plane is 8.6 and 4.3 $\mathrm{MPa\,m^{1/2}}$, for the same crack front directions [111]. Due to the unavailable fracture toughness data for the $\{111\}$ plane and the absence of grains with a $\{110\}$ surface orientation in the here-conducted experiment, a further assessment of the influence of the fracture toughness on the blister formation is not possible.

Also on tungsten exposed in linear plasma devices to deuterium with ion energies of 38 to 55 eV, fluxes of 0.8×10^{22} to $1.5 \times 10^{24}\,\mathrm{D\,m^{-2}s^{-1}}$ at sample temperatures between 315 to 1293 K and fluences of 10^{26} to $10^{27}\,\mathrm{D\,m^{-2}}$, a grain orientation dependence of the blister formation was observed [33, 120, 121, 125, 129, 133, 155]. However, in contrast to the here-conducted experiments, the most severely blistered grains possess a surface orientation close to the $\{111\}$ plane. For grains oriented near the $\{100\}$ plane a reduced or no blister formation was reported. However, recent findings indicated that the occurrence of blisters on grains with a specific orientation under these conditions is also influenced by the sample polishing [127].

4.3.4 100 % D Retention

The insights gained in the discussion of the results obtained from the surface morphology study can be used to interpret the deuterium retention data. In figure 4.9, the deuterium retention from figure 4.1, the diameter of the large and small blister population shown in figure 4.5 as well as the EBSD solving probability in figures 4.3 and 4.4 are plotted as a function of the irradiated deuterium fluence. Furthermore, the linear fit on the deuterium retention for irradiated deuterium fluences lower than $1.6 \times 10^{21}\,\mathrm{D\,m^{-2}}$ and the SDTrimSP prediction of 100 % retention of the implanted deuterium are shown as dashed red and dash-dotted black line, respectively. Within the regime of linear increase of the deuterium retention up to an irradiated deuterium fluence of approximately $1.6 \times 10^{21}\,\mathrm{D\,m^{-2}}$, the blister diameter of the large and small blister population increases, which suggests that the implanted deuterium is captured by the blisters. A diffusing deuterium atom which encounters a closed blister

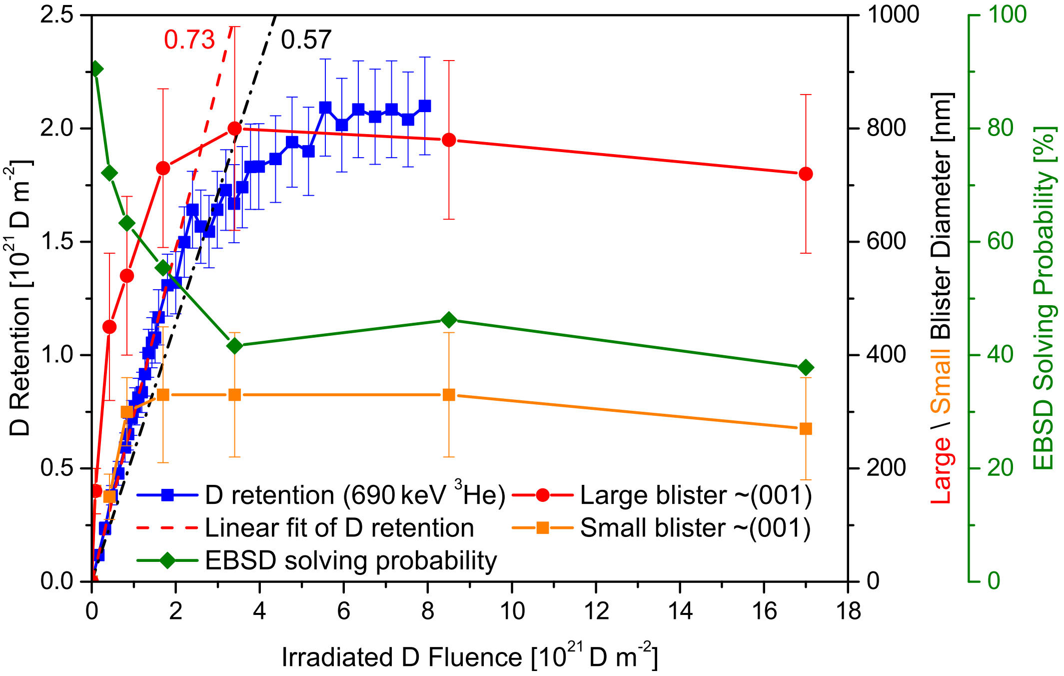

Figure 4.9: Deuterium retention, blister diameter of the large and small population on grains with a surface orientation close to the {100} plane and EBSD solving probability as a function of the irradiated deuterium fluence. Linear fit on the deuterium retention for irradiated fluences smaller $1.6 \times 10^{21}\,\mathrm{D\,m^{-2}}$ (dashed red line). 100 % retention of the implanted deuterium fluence calculated by SDTrimSP (dash-dotted black line).

transits from the bulk to the inner blister surface, where it can recombine with another deuterium atom and desorb as a molecule into the blister cavity. In order to leave the blister, the reverse process of dissociative adsorption and transition from the inner blister surface to the bulk is required. This process is very similar to the one taking place in experiments studying hydrogen gas loading of tungsten [23]. At low temperature the high energy barrier between the surface and the bulk suppresses the escape of deuterium trapped in the blister. Consequently, permanent trapping of deuterium in closed blisters at low temperature is very efficient. In addition, also the EBSD solving probability decreases significantly in this regime, indicating a successive damage and defect generation in the tungsten sample. It can be concluded that for irradiated deuterium fluences smaller than $1.6 \times 10^{21}\,\mathrm{D\,m^{-2}}$ trapping of deuterium is highly effective due to an excess of trap sites, e.g. vacancies, dislocations and blisters. In addition to the reduced diffusion of deuterium in tungsten at a sample temperature of 150 K, this excess of trap sites hampers the implanted deuterium from leaving the sample. Hence, it can be assumed that in the early stage of the deuterium implantation in the here-conducted experiments 100 % of the implanted deuterium is retained. This agrees well with results from previous experiments, dedicated to the implantation of deuterium with energies between 1.0 to 14.0 keV/D into stainless steel at a sample temperature of 150 K. In those experiments a 100 % retention of the implanted deuterium for low fluences, followed by saturation of the retention at higher fluences was observed [156].

Assuming a 100 % retention of the implanted deuterium for low fluences in the here performed experiment, a particle reflection coefficient of 0.27 is determined for deuterium on tungsten under the given irradiation conditions. Compared to the theoretical one of 0.43, the experimentally obtained particle reflection coefficient is lower by a factor of 0.62. This reduced particle reflection coefficient fits well to the experiments by Eckstein [157], in which the measured particle reflection coefficient of deuterium on tungsten for energies between 5.0 to 10.0 keV/D is systematically lower than the theoretical one.

A possible explanation of this observed discrepancy could be provided by the previously mentioned channeling of deuterium ions in the tungsten lattice. The reflection of irradiated deuterium ions is caused by backscattering on tungsten atoms close to the surface. Deuterium ions which impinge on grains with a surface orientation that facilitates channeling penetrate the sample to larger depth [150]. The probability for backscattering close to the surface is therefore reduced. Consequently, the particle reflection coefficient is lower. For grains which possess an orientation which impedes ion channeling, backscattering of deuterium ions close to the surface is more likely and the particle reflection coefficient is higher. The SDTrimSP code assumes an amorphous target and therefore neglects such effects attributed to the crystalline structure. The tungsten samples used in the here-conducted experiments are not amorphous but polycrystalline. As a consequence the average particle reflection coefficient is reduced compared to the one of an amorphous sample, resulting in a higher amount of implanted and consequently retained deuterium than predicted by SDTrimSP.

4.3.5 Saturation of D Retention

As can be seen from figure 4.9, for irradiated deuterium fluences exceeding approximately $1.6 \times 10^{21}\,\mathrm{D\,m^{-2}}$ the average blister diameter of the small and large blister population on grains with a surface orientation close to the $\{100\}$ plane does not increase further. This fluence coincides quite well with the irradiated deuterium fluence for which a deviation of the deuterium retention from the 100 % retention regime is observed. Under the assumption that the rupture of blisters occurs during the implantation, it can be expected that not all blister rupture at the same time. It is more likely that the blisters rupture gradually. Thus, as the deuterium irradiation is continued, more and more blisters rupture and release the captured deuterium. Consequently, the amount of deuterium retained by blisters decreases. From the fact that no decrease in the total deuterium retention is observed in figure 4.9, it can be deduced that the retained fraction of the implanted deuterium flux is larger than the flux of deuterium released by bursting blisters. Finally, when all blister cavities possess a connection to the surface, the blisters themselves can no longer act as quasi unsaturable traps for deuterium and do not contribute to the deuterium retention anymore. Though, the defects created in the vicinity of the blisters, e.g. dislocations [128], do contribute to the retention. In addition, the observed saturation of the deuterium retention, illustrated in figure 4.9, supports the assumption that the blisters rupture during the deuterium irradiation at low temperature and not during the warm-up to room temperature. If this would not be the case, the blister could accumulate more deuterium and a saturation would not be observed.

Another important effect caused by ruptured blisters is the enhanced re-emission of implanted deuterium as discussed in reference [152]. For blisters created under conditions similar to the here-performed experiment, it could be shown that deuterium atoms which encounter a ruptured blister are not retained but re-emitted from the sample. Thus, the transport of deuterium into the bulk behind the depth of the blisters, which was determined to approximately 200 nm, is reduced. As a result, the observed deuterium retention for a defined irradiated deuterium fluence is lower compared to an unblistered reference sample.

Furthermore, from figure 4.9 it can be seen that for irradiated deuterium fluences larger than $2.0 \times 10^{21}\,\mathrm{D\,m^{-2}}$ the EBSD solving probability decreases less strongly compared with lower fluences. As pointed out before this could be interpreted as a saturation of the defect concentration created by the energetic deuterium ions. In previous experiments the saturation of the defects generated by energetic ion implantation was studied extensively [158–161]. In those experiments, the tungsten specimens were irradiated with different fluences of energetic tungsten ions. The defects created by this self-implantation procedure were subsequently decorated with deuterium by plasma or ion beam loading and the resulting deuterium retention and the depth profile was measured with NRA. For low irradiated tungsten fluences the deuterium retention and concentration showed an increase. Once a certain fluence was reached no further increase was observed and the retention and concentration saturated at a level depending on the deuterium loading conditions [158–161]. It has been suggested that the observed effect is caused by a saturation of the vacancy concentration, assuming that sufficient tungsten interstitial atoms are present in the sample to annihilate with the generated vacancies immediately. This effect should be even more pronounced in the here-conducted experiment, since damaging and deuterium loading is not conducted sequentially, but happens simultaneously. This should facilitate the generation of vacancies due to the reduction of the formation energy [162] and stabilize the created vacancies presumably by occupation of the vacancies with deuterium atoms [163, 164]. Consequently, the vacancy concentration is expected to saturate at a higher level.

Taking all the experimental results into account it can be assumed that the observed saturation of the deuterium retention is caused by two effects: Ruptured blisters, which no longer act as quasi unsaturable traps, enhance the re-emission of implanted deuterium and reduce the deuterium transport into the bulk, and a saturation of the defect concentration in the respective depth. Consequently, during the deuterium implantation at low temperature a maximum trap site concentration is reached, which can be occupied with deuterium to a level depending on the temperature.

4.3.6 D Depth Profile

From the deuterium depth profiles shown in figure 4.2, it can be seen that a significant amount of deuterium is found in larger depth than calculated by SDTrimSP. This might be attributed to ion channeling of deuterium in the tungsten lattice as discussed before. In grains which allow channeling deuterium is implanted at larger depth compared with grains which impede ion channeling. The averaging over many grains with different surface orientation in the NRA measurement could finally lead to such a depth profile [150]. Another aspect is the slight shift of the edges of the two steps in the deuterium depth profile towards larger depth for increasing irradiated deuterium fluences. This might be an indication for deuterium diffusion into the bulk although the sample temperature is only 150 K and the mobility of deuterium should be very low.

Together with the deuterium retention, the deuterium concentration increases and finally saturates due to the already discussed reasons. The deuterium concentration of 42 at.%, measured when the tungsten sample is saturated with deuterium at 150 K, is one of the highest concentrations of deuterium in tungsten observed so far. Even after warm-up and hold at 290 K for 114 h, a deuterium concentration of 15 at.% is still observable. In the following, the here obtained concentrations are compared to some selected deuterium concentrations found in the contemporary literature to highlight the large range of deuterium concentrations in tungsten.

Depending on the tungsten grade and the conditions under which the samples are loaded with deuterium, the observed concentration can vary over orders of magnitude. The deuterium concentration in recrystallized undamaged tungsten, which yields a small defect concentration, can be rather low. Deuterium plasma loading with an energy of 200 eV/D at 320 K of such samples results in a deuterium concentration in the bulk below 10^{-2} at.% [44]. This small deuterium concentration can be altered significantly when the defect concentration in the material is increased. In deuterium retention experiments conducted on tungsten samples which were damaged by pre-irradiation with energetic ions and loaded with deuterium by plasmas or atomic beams, a deuterium concentration of up to 1.9 at.% is observed in the damaged zone depending on the sample temperature during loading [47, 103, 158, 165]. Even higher deuterium concentrations are observed in experiments conducted by Gao et al.

[164]. NRA with considerably enhanced depth resolution revealed the existence of a deuterium supersaturated surface layer (DSSL) with a thickness of 10 nm and a deuterium concentration up to 10 at.% in tungsten samples loaded in a plasma at 300 K. This value is in the range of the 15 at.% observed after warm-up to 290 K in the here-presented experiment. An even larger deuterium concentration can be achieved when the deuterium is incorporated into the lattice during the growth of tungsten layers. In dedicated magnetron sputtering co-deposition experiments deuterium concentration of up to 23 at.% were observed [166]. The only experiment in which a deuterium concentration comparable to the here measured 42 at.% is reported, was conducted by Zhao et al. [167]. After implantation of deuterium with an energy of 75 keV/D into tungsten foils at room temperature a deuterium concentration of 42 at.% was observed. However, the deuterium concentration is measured with NRA using the D(D,p)T nuclear reaction which is less well-known than the D(^{3}He,p)^{4}He reaction applied in the standard NRA method to detect deuterium. A comparison of the two different NRA methods is required to verify this extremely high deuterium concentration observed at room temperature.

4.4 Conclusion

The irradiation of tungsten at a sample temperature of 150 K with deuterium of an energy of 3.0 keV/D and a flux of $8.4 \times 10^{17}\,\mathrm{D\,m^{-2}s^{-1}}$, leads to a linear increase of the deuterium retention for fluences up to $1.6 \times 10^{21}\,\mathrm{D\,m^{-2}}$. Due to the reduced deuterium diffusivity at low temperature, the ongoing defect generation by the energetic deuterium ion beam and the continuation of blister growth, it can be assumed that within this linear regime 100 % of the implanted deuterium fluence is retained. A particle reflection coefficient of deuterium on tungsten of 0.27 is obtained for the given experimental conditions. Compared with the theoretical value of 0.43, the experimentally determined value is lower by a factor of 0.62, which is presumably the result of ion channeling in certain grains of the polycrystalline tungsten sample.

For irradiated fluences larger than $1.6 \times 10^{21}\,\mathrm{D\,m^{-2}}$ the deuterium retention starts to saturate and finally converges to $2.07 \pm 0.25 \times 10^{21}\,\mathrm{D\,m^{-2}}$. The onset of saturation appears to coincide with the irradiated deuterium fluence at which the growth of blisters on grains with a surface orientation close to the {100} plane stops. It is assumed that this stop of blister growth is associated with the rupture of the blister during the deuterium implantation at low temperature. Furthermore, the observed saturation of the EBSD solving probability might be associated with a saturation of the defect concentration. It can be concluded that the saturation of the deuterium retention is the result of ruptured blisters and a saturation of the created trap concentration. While the former ones can no longer act as quasi unsaturable traps for deuterium, the latter one is saturated with deuterium up to a level at which no significant thermally activated de-trapping occurs at the given temperature of 150 K. However, due to the low statistics in the study of the surface morphology the conclusions above can only be regard as preliminary.

Chapter 5

Exchange of D by H in W at Low Temperatures

This chapter is dedicated to the experimental investigation of the hydrogen isotope exchange in tungsten at low temperature within the ion implantation zone. Experiments are carried out applying nuclear reaction analysis (NRA) and mass spectroscopy (QMS) in situ. Three experimental scenarios to test the fill-level model as the underlying mechanism for hydrogen isotope exchange at low temperature are presented. The scenarios are designed such that an exchange should be observed within the fill-level model but not within the classical model. The obtained results are discussed in the context of the fill-level model. In addition, a simple urn model is devised to gain a qualitative understanding of the observed hydrogen isotope exchange from a combinatorial point of view. Furthermore, the influence of different trap types and the effect of blisters, investigated in chapter 4 and reference [152], on the hydrogen isotope exchange are assessed. Since the here-conducted exchange of deuterium by protium takes predominantly place in the ion implantation zone, other exchange mechanisms, e.g. sputtering and kinetic de-trapping, are evaluated. Eventually, the here derived results are compared with those reported in contemporary literature.

5.1 Initial D Implantation

The systematic investigations of the hydrogen isotope exchange in tungsten requires identical samples with respect to the trap concentration and surface morphology. As could be shown in the previous chapter, the irradiation of a sufficiently high fluence of energetic deuterium at low temperature leads to the saturation of the deuterium retention in the tungsten samples. This indicates the saturation of the trap concentration due to the saturation of the ion-beam-induced defects and the rupture of blisters. Thus, in order to prepare tungsten samples with the same trap concentration and surface morphology for the investigation of the hydrogen isotope exchange, all samples are initially implanted with deuterium under the same conditions until saturation of the deuterium retention is reached. In particular, deuterium with an energy of 3.0 keV/D and a flux of $8.4 \times 10^{17}\,\mathrm{D\,m^{-2}s^{-1}}$ is irradiated under normal incidence on the samples up to a fluence of $8.4 \times 10^{21}\,\mathrm{D\,m^{-2}}$. During the implantation the sample is cooled with liquid nitrogen and kept at 150 K by active heating.

Within the framework of the fill-level model, this initial deuterium implantation at temperature T_0 leads to the filling of the traps as schematically illustrated in figure 3.3. When the fill level is reached at which deuterium atoms can be released by thermally activated de-trapping at temperature T_0, the traps enter a quasi equilibrium of de-trapping and re-trapping deuterium atoms, as shown in figure 5.1 (a). Once the implantation is stopped, the traps release deuterium atoms until a fill level is reached at which the required de-trapping energy is large enough to prevent further thermally activated de-trapping at the given temperature T_0. This situation is schematically illustrated in figure 5.1 (b). Such deuterium saturated traps represent the basis for all three experimental scenarios described below.

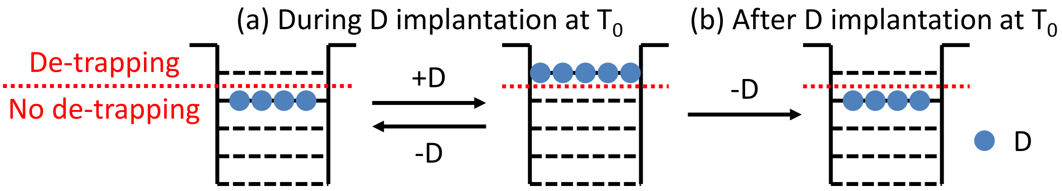

Figure 5.1: Schematic saturation of the deuterium retention in a trap (a) during and (b) after the initial filling by deuterium implantation.

5.2 Exchange after Ramp & Hold to Different Temperatures

5.2.1 Experimental Procedure

The first experimental scenario to test the fill-level model in the context of hydrogen isotope exchange is depicted in figure 5.2. The experiment starts with a sample in which the traps are saturated with deuterium at the temperature T_0, as shown in figure 5.1 (b). When the sample temperature is merely held at T_0, no loss of deuterium is expected, as can be seen in case (a) of figure 5.2. Hence, starting the protium implantation without prior heating the sample should result in the immediate exchange of deuterium by protium. As the traps are already saturated with deuterium, one additional protium atom in the trap would result in a fill level at which the required de-trapping energy is small enough to allow the release of either deuterium or protium from the trap at T_0. Assuming in a first order approach that deuterium and protium

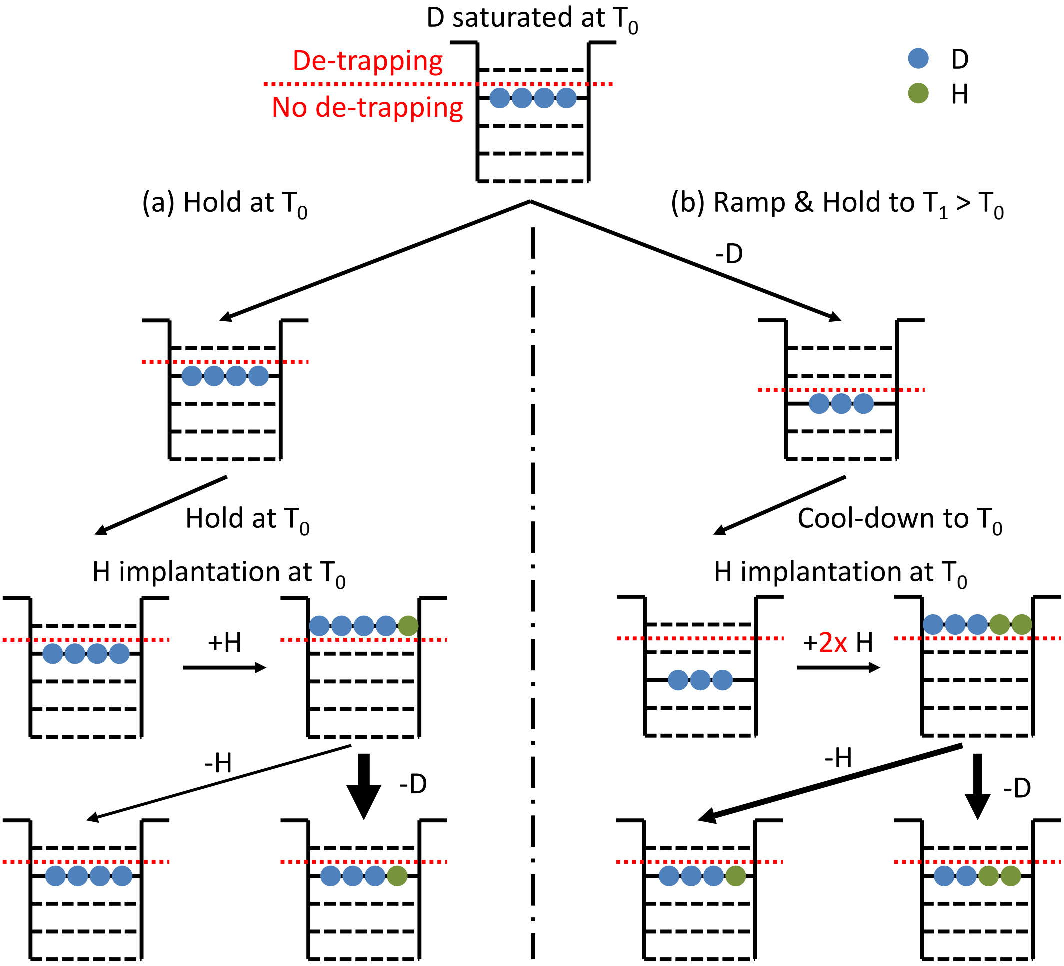

Figure 5.2: Schematic illustration of the exchange of deuterium by protium in a fill-level trap after Ramp & Hold to different temperatures.

have the same mass independent attempt frequency, the release probability of a specific hydrogen isotope depends only on the isotopic ratio in the respective trap. For the example shown in figure 5.2 (a), the release probability of a deuterium atom is four times higher than for a protium atom, as indicated by the black arrows of different thickness.

As illustrated in figure 5.2 (b), the situation is different when Ramp & Hold to T_1 is performed before the protium implantation is conducted at T_0. The temperature increase to T_1 causes a release of deuterium atoms from the traps. This results in a decrease of the fill level of the traps and an increase of the required de-trapping energy. The release of deuterium atoms proceeds until a fill level is reached at which the required de-trapping energy is large enough to prevent further thermally activated de-trapping of deuterium at the temperature T_1. In the subsequent protium implantation at temperature T_0, the traps can capture protium atoms from the solute which leads to an increase of the fill level. However, in order to observe an exchange of deuterium by protium at T_0, the traps need to be re-filled with protium up to a fill level with low enough de-trapping energy to allow significant thermal release of either protium or deuterium from the traps. Thus, in contrast to case (a), where the sample temperature is not increased prior to the protium implantation, the hydrogen isotope exchange cannot set in immediately, but requires the implantation of a certain amount of protium. Moreover, the isotopic ratio of deuterium to protium in the fill level from which the thermal de-trapping occurs is lower in figure 5.2 (b) than in (a). The probability to release a deuterium atom is only one and a half times larger than for a protium atom in the shown example.

From the gedankenexperiment shown in figure 5.2 the following three effects should be observable: First, if the sample temperature is not increased before the protium implantation, the exchange of deuterium by protium should set in immediately. Second, the higher the temperature T_1, the more protium is required to fill the traps and to trigger the exchange of deuterium by protium. Third, the higher the temperature T_1, the lower the isotopic ratio of deuterium to protium when the exchange sets in, which should result in a lower exchange rate of deuterium. Finally, it should be noted that in the experimental procedure discussed above the exchange of deuterium by protium is performed always at the same temperature T_0. In this way temperature-dependent parameters, such as the diffusion and recombination rate coefficient, are kept constant.

This proposed experiment is conducted on three consecutive days with four samples in total. On the first day, deuterium implantation is performed. On the second day, temperature Ramp & Hold is carried out and analyzed by NRA and mass spectrometry. The exchange of deuterium by protium is studied on the third day. In addition to the samples undergoing Ramp & Hold experiments to different final temperatures, hydrogen isotope exchange is also studied on a sample which is merely held at 150 K for 3 h on the second day. During the three days the sample is continuously cooled with liquid nitrogen.

First, deuterium is implanted into the sample according to the conditions described in section 5.1. 3 h after the implantation is finished the sample heating is stopped, resulting in a decrease of the sample temperature from 150 K to approximately 140 K.

Before the Ramp & Hold experiment is conducted, a deuterium depth profile is measured by NRA using ^{3}He ions of eight different energies ranging from 0.5 to 4.5 MeV to obtain the total amount of retained deuterium. In addition, the lateral homogeneity of the deuterium implantation spot is verified by performing NRA with 0.69 MeV ^{3}He ions across the spot. Furthermore, the quadrupole mass spectrometer, which is used to follow the D_2 and HD release during the Ramp & Hold experiment, is calibrated with a D_2 and a H_2 leak valve to allow a quantification of the deuterium mass spectra. The sample temperature is increased to 150 K, from which the actual Ramp & Hold experiment is started. During the ramp phase the sample temperature is increased with a heating rate of 0.5 K min^{-1} to the final temperature of 200, 250 and 290 K, respectively. In the hold phase the sample is kept at the particular temperature for 3 h. During the whole Ramp & Hold cycle NRA with 0.69 MeV ^{3}He ions is conducted in intervals of 10 min. According to chapter 4 this method allows to observe the development of the total deuterium retention during the Ramp & Hold. For each measurement an ion charge of 1 µC is acquired which corresponds to a measurement time of approximately 120 s. In addition, these NRA measurements are performed at a different spot than the previously measured deuterium depth profile in order to avoid the detection of helium induced artifacts [113, 114]. Once the Ramp & Hold cycle is completed, the sample heating is switched off which leads to a rapid decrease of the sample temperature by initially 5 to 11 K min^{-1} depending on the final hold temperature. The quadrupole mass spectrometer is calibrated again to check and correct for possible drifts of the mass spectra recorded during the Ramp & Hold cycle.

The hydrogen isotope exchange of deuterium by protium is conducted on the third day. First the sample temperature is increased again to 150 K. Subsequently a full deuterium depth profile with ^{3}He ions possessing the above stated eight energies is measured on a new spot to obtain the total amount of retained deuterium before the hydrogen isotope exchange is performed. The implantation of protium with an energy of 3.0 keV/H and a flux of 8.4×10^{17} H $\text{m}^{-2}\text{s}^{-1}$ is conducted stepwise up to an irradiated fluence of 8.4×10^{21} H m^{-2}. The incremental protium fluence is increased from 1.3 to 4.2×10^{20} H m^{-2} as the accumulated protium fluence increases. In between the protium implantation steps, nuclear reaction analysis with ^{3}He ions of an energy of 0.69 MeV is conducted on a new spot to probe the deuterium retention. In all performed hydrogen isotope exchange experiments an ion charge of 1 µC, corresponding to a measurement time of approximately 120 s, is acquired. The only exception is the hydrogen isotope exchange studied after Ramp & Hold to 290 K, in which an ion charge of 2 µC is acquired to gain sufficient counting statistics.

5.2.2 Results

The retained and released deuterium amounts measured simultaneously by NRA and mass spectroscopy in the three Ramp & Hold experiments to 200, 250 and 290 K are shown as a function of time in the figures 5.3, 5.4 and 5.5, respectively. Since the HD signal is negligible compared with the D_2 signal, only the latter one is considered in the data evaluation. The deuterium desorption rate, shown in the figures as solid gray line, is obtained by multiplying the D_2 signal by a factor of two to account for the molecular release.

In order to verify that the measured deuterium release origins from the deuterium implanted into the tungsten samples and not from deuterium adsorbed on cold parts of the experimental setup, a reference measurement is conducted. In this reference measurement the Ramp & Hold experiment to 290 K is essentially repeated with the exception that the shutter in front of the sample is closed during the deuterium implantation. As can be seen from the deuterium desorption rate of the reference measurement, shown as solid blue line in figure 5.5, no release of deuterium is observed. Hence, the measured deuterium release is caused by the deuterium implanted into the samples. The deuterium retention as a function of time determined by NRA during the Ramp & Hold experiments is illustrated as black squares in each figure. As can be seen in figures 5.3 to 5.5, the initial deuterium retention is very similar in each Ramp & Hold experiment and yields approximately $2.1 \times 10^{21}\,\mathrm{D\,m^{-2}}$. The NRA measurement itself also affects the deuterium release. During the NRA measurements the desorption rate of deuterium is increased. This is visible as spikes on top of the regular release signal without ongoing NRA measurement, as exemplarily indicated by the dashed black arrow in figure 5.3. In order to compare the QMS data of the released and the NRA data of the retained deuterium, the deuterium desorption rate is integrated and subtracted from the initial deuterium retention measured by NRA. The resulting curve is illustrated in each figure as solid red line. In addition, the measured sample temperature as a function of time is displayed as solid green line with the vertical dashed green line indicating the transition from the ramp phase to the hold phase.

From figure 5.3 it can be observed that the desorption of deuterium strongly increases as soon as the sample temperature is ramped up. After the first steep rise, the desorption rate increases less strongly, resulting in the appearance of a shoulder after approximately 24 min which corresponds to a temperature of

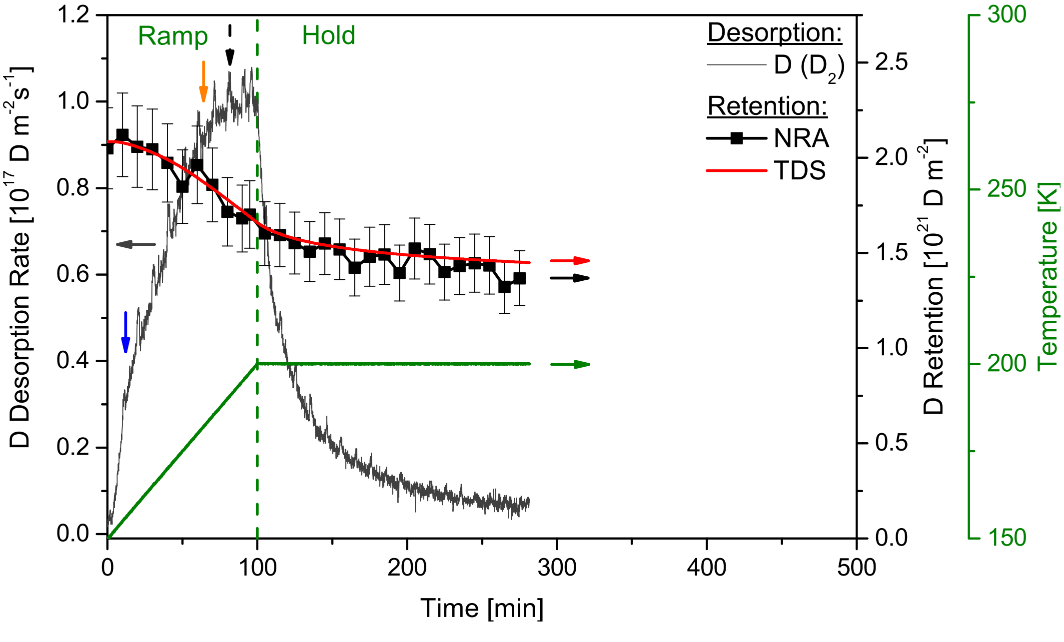

Figure 5.3: Deuterium desorption rate and retention during Ramp & Hold to 200 K.

162 K (blue arrow). After 68 min, i.e., a temperature of 183 K, the signal levels off, which leads to the formation of a kink in the deuterium desorption rate spectrum (orange arrow). Once the ramp phase is completed and the sample temperature is held at 200 K for 3 h, an exponential decrease of the deuterium desorption rate is observed.

Starting from $2.05 \pm 0.21 \times 10^{21}\,\mathrm{D\,m^{-2}}$, the deuterium retention determined by NRA appears to be constant for the first 30 min. Subsequently, an approximately linear decrease of the retained amount occurs until the end of the ramp phase at 100 min. The linearity of the decrease fits to the observed saturation of the deuterium desorption rate. During the hold phase the decrease of the deuterium retention becomes smaller which is inline with the exponential decline of the desorption rate. The final deuterium retention after the Ramp & Hold cycle is $1.41 \pm 0.14 \times 10^{21}\,\mathrm{D\,m^{-2}}$, indicating that 30 % of the initially retained deuterium is released. The evolution of the deuterium retention calculated from the deuterium desorption rate is in good agreement with the NRA measurement.

The deuterium desorption rate spectrum of the Ramp & Hold experiment to 250 K, shown in figure 5.4, exhibits the same low temperature features as the one to 200 K, illustrated in figure 5.3. As the sample temperature is ramped beyond 200 K, the deuterium desorption rate appears to remain nearly constant at $0.98 \times 10^{17}\,\mathrm{D\,m^{-2}s^{-1}}$. Once the final sample temperature of 250 K is reached, an exponential decrease of the deuterium desorption rate is observed during the hold phase of 3 h.

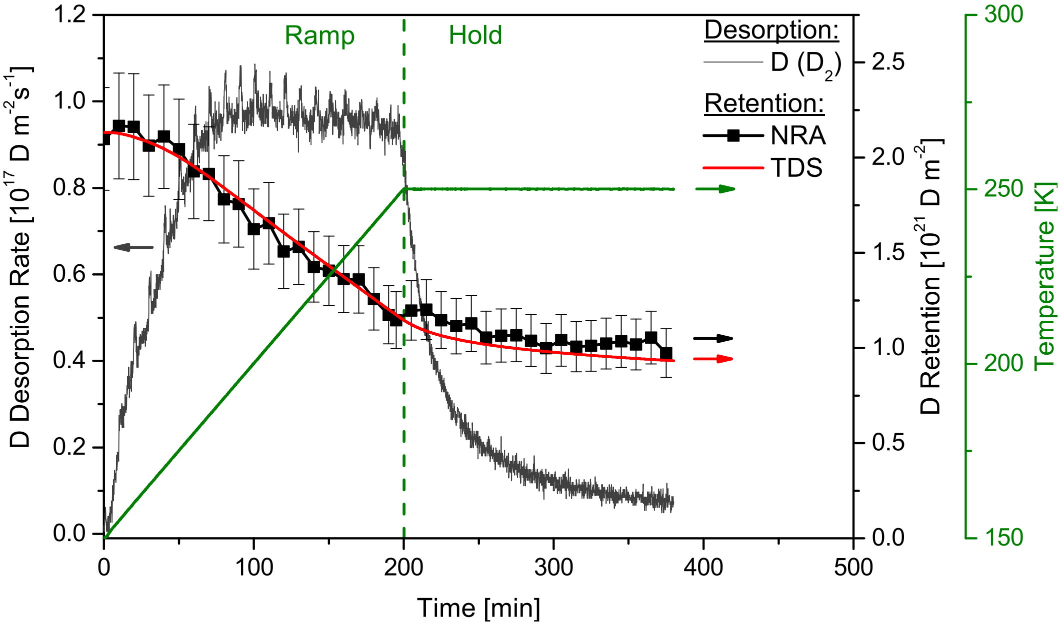

Figure 5.4: Deuterium desorption rate and retention during Ramp & Hold to 250 K.

The initial deuterium retention determined by NRA is $2.10 \pm 0.27 \times 10^{21}\,\mathrm{D\,m^{-2}}$.

When the sample temperature is increased the retention seems to be constant in the beginning and starts to decrease linearly after approximately 30 min until the ramp phase is finished. As already mentioned before, the linear decrease of the deuterium retention reflects the observed constant desorption rate. During the hold phase, at a temperature of 250 K, the deuterium retention declines slower and a final retention of $0.97 \pm 0.13 \times 10^{21}\,\mathrm{D\,m^{-2}}$ is reached after 3 h. Thus, approximately 54 % of the initially retained deuterium is released in the Ramp & Hold experiment to 250 K. The deuterium retention measured by NRA is consistent with the one calculated from the deuterium desorption rate spectrum.

The deuterium desorption rate recorded during the Ramp & Hold experiment to 290 K, shown in figure 5.5, is very similar to the previous ones in the respective temperature range. In addition, the desorption rate spectrum exhibits a dip at 200 min, respectively 250 K, which is probably due to a suddenly reduced thermal contact to the heater. After approximately 210 min, corresponding to a temperature of 255 K, a linear decrease of the deuterium desorption rate sets in until the end of the ramp phase with a final temperature of 290 K is reached. In the following hold phase an exponential decline of the desorption rate is measured, similar to the previous Ramp & Hold experiments.

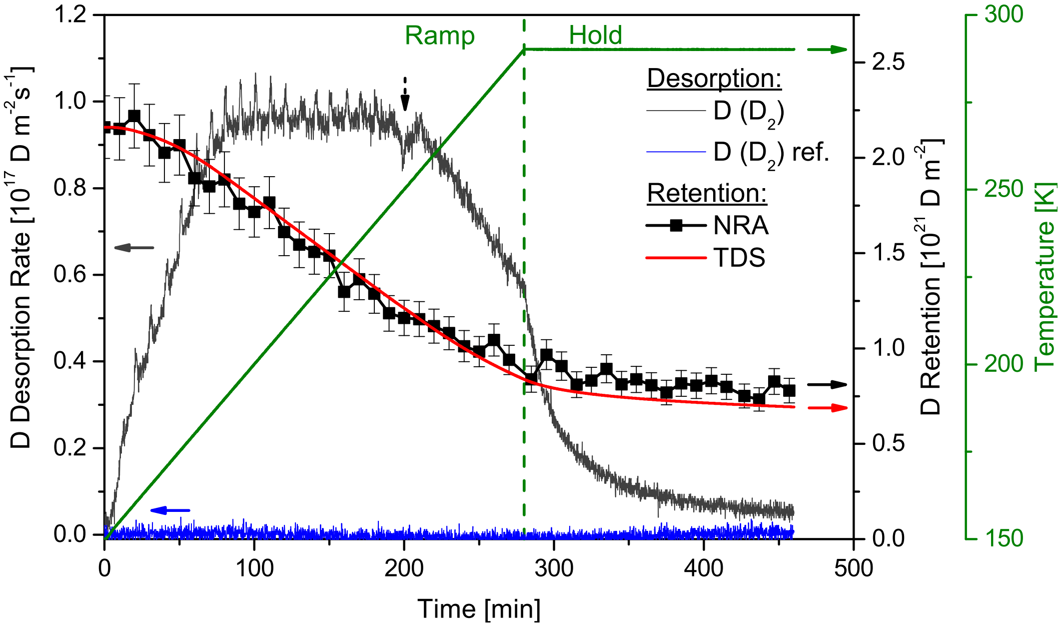

Figure 5.5: Deuterium desorption rate and retention during Ramp & Hold to 290 K.

An initial deuterium retention of $2.16 \pm 0.16 \times 10^{21}\,\mathrm{D\,m^{-2}}$ is determined by NRA before the sample temperature is ramped up. The decrease of the deuterium retention as a function of time, respectively temperature, shows up to 250 K the same behavior as in the experiment illustrated in figure 5.4. When the sample temperature exceeds 250 K the decrease of the deuterium retention is slightly reduced, which corresponds to the decrease of the deuterium desorption rate. However, a linear decrease in the desorption rate would correspond to a quadratic term in the evolution of the deuterium retention which is not observed in the NRA data and is probably beyond the capability of the NRA measurement. During the hold phase at a sample temperature of 290 K, the decline of the deuterium retention is further reduced and a final retention of $0.78 \pm 0.06 \times 10^{21}\,\mathrm{D\,m^{-2}}$ is obtained. Thus, 64 % of the initially retained deuterium is released during the experiment. The directly and indirectly acquired deuterium retention from the NRA and the mass spectrometry data respectively are in good agreement.

After the Ramp & Hold to different temperatures the hydrogen isotope exchange is investigated at a sample temperature of 150 K. Prior to the exchange of deuterium by protium a depth profile is measured to quantify the amount of deuterium retained in the tungsten sample. Figure 5.6 shows the deuterium depth profiles acquired after the sample temperature is only held at 150 K for 3 h as well as after Ramp & Hold to 200, 250 and 290 K, respectively. In the case where the sample temperature is held at 150 K for 3 h, a maximum deuterium concentration of 43 at.% within the first 68 nm is measured. Furthermore, the deuterium depth profile extends almost 200 nm deep into the bulk with a deuterium concentration of 2.5 at.%. After performing the Ramp & Hold experiments to 200, 250 and 290 K, the maximum deuterium concentration within 56 to 61 nm from the surface decreases to 31, 24 and 17 at.%, respectively. Compared to the depth profile recorded without prior Ramp &

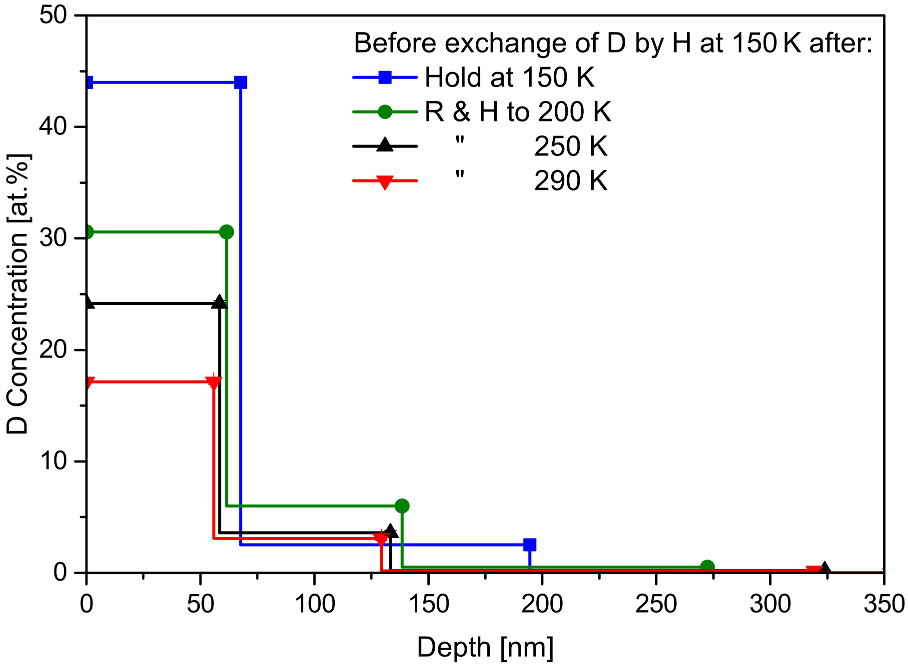

Figure 5.6: Deuterium depth profile before protium implantation at 150 K without and with prior Ramp & Hold to 200, 250 and 290 K for 3 h, respectively.

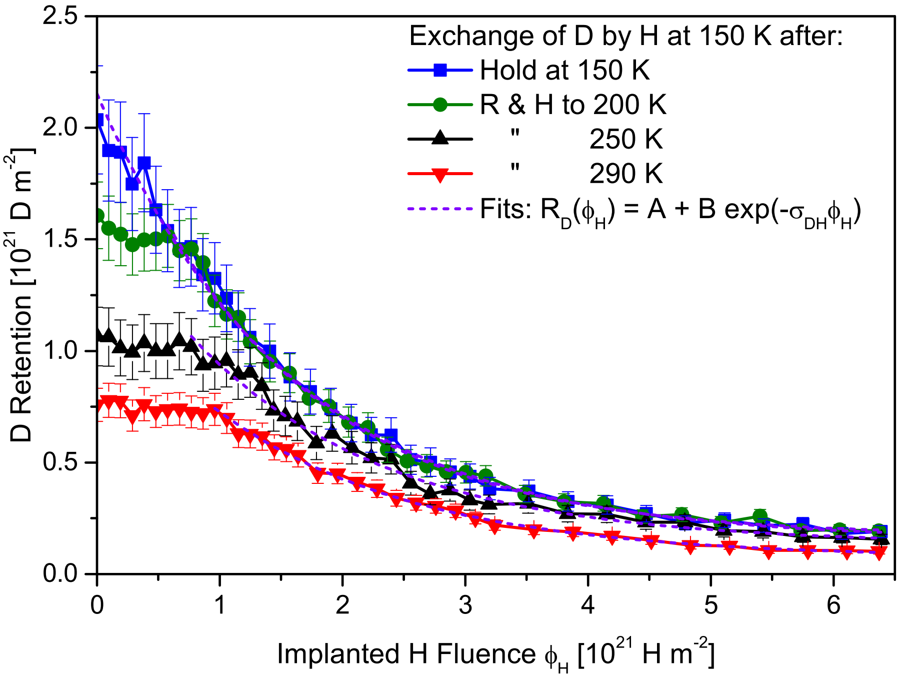

Figure 5.7: Deuterium retention during protium implantation at 150 K after the temperature is only held at 150 K for 3 h and with Ramp & Hold to 200, 250 and 290 K for 3 h, respectively.

Hold, the depth profiles measured after Ramp & Hold extend only 130 to 140 nm into the bulk, but possess a higher deuterium concentration at this specific depth. The reason for this could be an artifact from the evaluation process of the deuterium depth profile in the case of no prior Ramp & Hold. Nevertheless, the shape of the deuterium depth profiles are very similar and no significant diffusion of deuterium into the bulk is observed as the samples are heated to the different temperatures. This observation might be attributed to the presence of ruptured blisters, which enhance the re-emission of deuterium from the sample and prevent the transport into the bulk to some extent [152].

The deuterium retention during hydrogen isotope exchange at 150 K, after the samples were ramped to different temperatures or only held at 150 K, is shown as a function of the implanted protium fluence in figure 5.7. Unfortunately, the available techniques cannot be used to determine a particle reflection coefficient of protium on tungsten. Thus, a value of 0.24 is assumed to calculate the implanted protium fluence. This value is derived by correcting the simulated particle reflection coefficient of 0.39 by the factor of 0.62, which corresponds to the deviation of the experimental and simulated particle reflection coefficient found in chapter 4 for deuterium on tungsten under the given implantation conditions. The parameters of the SDTrimSP simulation to determine the particle reflection coefficient of protium on tungsten are listed in the appendix A.2.

As can be seen from figure 5.7, when the sample is just held at a temperature of 150 K, a reduction of the deuterium retention is observed directly after the first incremental protium fluence is implanted. If Ramp & Hold is performed before the hydrogen isotope exchange is conducted, the deuterium retention is constant at low implanted protium fluences. Once a critical amount of protium is implanted into the samples a decrease of the deuterium retention is measured. Obviously, the higher the temperature to which the sample was heated, and therefore, the lower the initially retained deuterium amount, the higher is the required protium fluence at which the deuterium retention starts to decrease. For Ramp & Hold temperatures of 200, 250 and 290 K, the critical implanted protium fluences are 0.6, 0.8 and $1.0 \times 10^{21}\,\mathrm{H\,m^{-2}}$, respectively.

In order to compare the results of the present hydrogen isotope exchange study with existing literature data, an exchange cross section σ_{DH} is determined by fitting the part of the deuterium retention curves in which the decrease is observed with

$$R_D\left(\phi_H\right) = A + B\,\exp\left(-\sigma_{DH}\phi_H\right). \tag{5.1}$$

A and B are fit parameters and ϕ_H corresponds to the implanted protium fluence. The parameter A can be regarded as the part of the retained deuterium which cannot be exchanged. The exchange cross sections and the other parameters obtained by fitting the deuterium retention are listed in table 5.1. The obtained exchange cross section σ_{DH}, is independent of the temperature to which the sample was heated in the preceding Ramp & Hold experiment and an average value of $0.64 \pm 0.03 \times 10^{-21}\,\mathrm{m}^2$ is determined. This result suggests that the exchange efficiency does not depend on the initial deuterium retention or concentration.

T [K]	A [$10^{20}\,\mathrm{D\,m^{-2}}$]	B [$10^{21}\,\mathrm{D\,m^{-2}}$]	σ_{DH} [$10^{-21}\,\mathrm{m^2}$]
150	1.53 ± 0.07	2.00 ± 0.03	0.64 ± 0.02
200	1.70 ± 0.08	2.06 ± 0.06	0.68 ± 0.02
250	1.34 ± 0.10	1.51 ± 0.07	0.63 ± 0.03
290	0.73 ± 0.04	1.21 ± 0.03	0.62 ± 0.02

Table 5.1: Fit parameters of isotope exchange of deuterium by protium at 150 K after Ramp & Hold to different temperatures.

5.3 Exchange at Different Temperatures

5.3.1 Experimental Procedure

Another experiment to investigate the fill-level model as the underlying exchange mechanism at low temperature is to exchange a defined amount of deuterium by protium at different temperatures, as schematically illustrated in figure 5.8. Just as in the previous experiment, a tungsten sample with traps

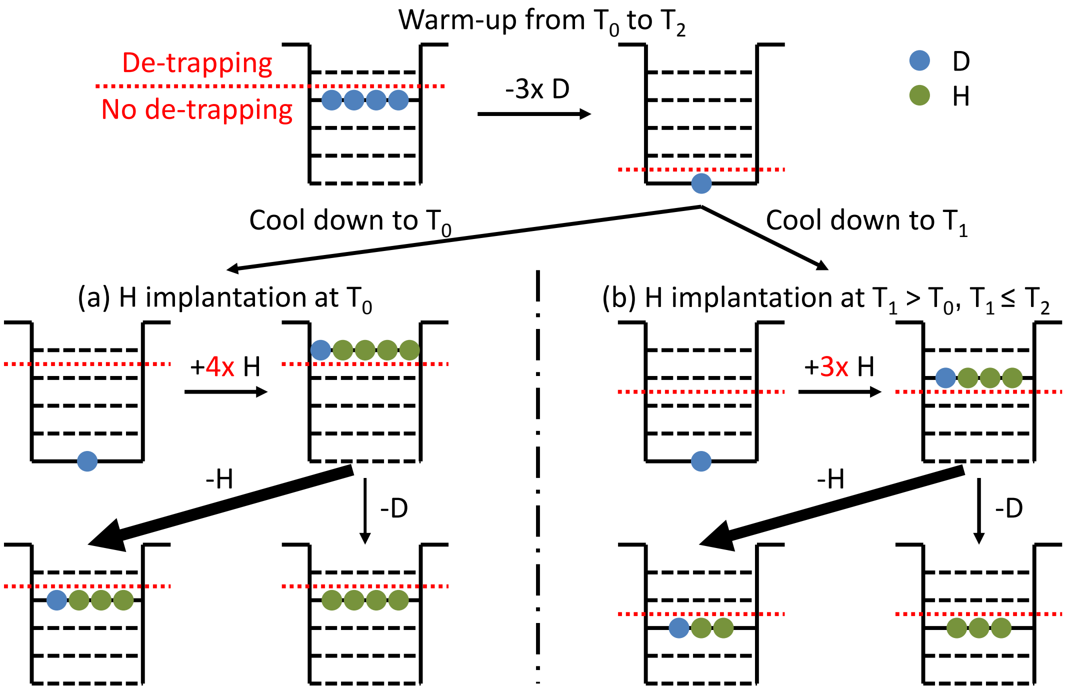

Figure 5.8: Schematic illustration of the exchange of deuterium by protium in a trap at different sample temperatures after warm-up.

saturated with deuterium at a temperature T_0 is used. In the first step, a defined deuterium retention is created by warming the sample from temperature T_0 to T_2. When the temperature is ramped up, an increasing number of deuterium atoms is released from the traps. As the number of deuterium atoms remaining in the traps is reduced, the required energy for de-trapping increases. Finally, the number of deuterium atoms in the traps has decreased to a fill level at which the required de-trapping energy is high enough to impede further thermal release of deuterium atoms at the temperature T_2. In a second step, illustrated in figure 5.8 (a), the sample is cooled down again to the temperature T_0 at which protium implantation is performed. The solute protium atoms are captured by the traps which still contain a certain number of deuterium atoms. As the number of hydrogen atoms in the traps increases, the fill level rises and the required de-trapping energy decreases. Once the traps are occupied up to a fill level at which the required de-trapping energy allows thermally activated release at the temperature T_0, either protium or deuterium atoms can leave the traps. As can be seen from the isotopic ratio in figure 5.8 (a), the probability to release a protium atom is four times higher than for a deuterium atom in this example.

The experiment is repeated with a new sample. However, as depicted in figure 5.8 (b), the sample is cooled down to T_1, which is higher than T_0 but lower than T_2. The protium implantation conducted at temperature T_1 results in the filling of the traps. Since the temperature is higher compared to T_0 in figure 5.8 (a), the release of hydrogen atoms from the traps occurs already at a lower fill level associated with a higher de-trapping energy. Consequently, the required amount of protium to fill the traps to the level from which the release occurs is lower compared to that in figure 5.8 (a). This implies, due to the same initial amount of retained deuterium in (a) and (b), that the isotopic ratio of deuterium to protium is higher in (b). Thus, in the depicted example the release probability of a protium atom is only three times higher than for a deuterium atom.

From the simple considerations in figure 5.8 two effects can be deduced. First, the amount of protium required to fill the traps to a level at which significant de-trapping and consequently hydrogen isotope exchange can occur decreases with increasing exchange temperature. Second, the exchange rate is higher at higher temperatures due to the increased isotopic ratio of deuterium to protium. Yet, in contrast to the previously described experiment, the exchange is performed at different temperatures which may alter the transport properties of the hydrogen isotopes in the material.

This gedankenexperiment is realized in two steps. In the first step, a defined inventory of deuterium, which can be exchanged at different temperatures in the second step, needs to be established in the sample. This is achieved by the initial deuterium implantation under the conditions stated in section 5.1. Once the final irradiated fluence of $8.4 \times 10^{21}\,\mathrm{D\,m^{-2}}$ is reached, the sample heating and the liquid nitrogen cooling is switched off. Consequently, the sample warms up to approximately 290 K within 18 h. After keeping the samples at 290 K for 114 h, the liquid nitrogen cooling is turned on again to cool the sample down to approximately 140 K.

In the second step, the hydrogen isotope exchange is performed. First, the lateral homogeneity of the implantation spot is checked and a deuterium depth profile is measured to determine the total deuterium retention, as in the previous experiment. Finally, the sample is heated to either 150, 200, 250 or 290 K, at which the protium is implanted. The energy of the implanted protium is 3.0 keV/H and the irradiated flux is $8.4 \times 10^{17}\,\mathrm{H\,m^{-2}s^{-1}}$. As in the other experiment, the implantation is performed in a stepwise fashion up to a final irradiated fluence of $8.4 \times 10^{21}\,\mathrm{H\,m^{-2}}$. The incremental protium fluence irradiated at each step is increased from $2.1 \times 10^{20}\,\mathrm{H\,m^{-2}}$ to $4.2 \times 10^{20}\,\mathrm{H\,m^{-2}}$, as the accumulated fluence exceeds $4.2 \times 10^{21}\,\mathrm{H\,m^{-2}}$. Like in the other experiment, the development of the deuterium retention is monitored on a new spot by NRA using ^{3}He ions with an energy of 0.69 MeV in between the individual protium implantation steps. For each measurement an ion charge of 2 µC is acquired, corresponding to a measurement time of approximately 240 s.

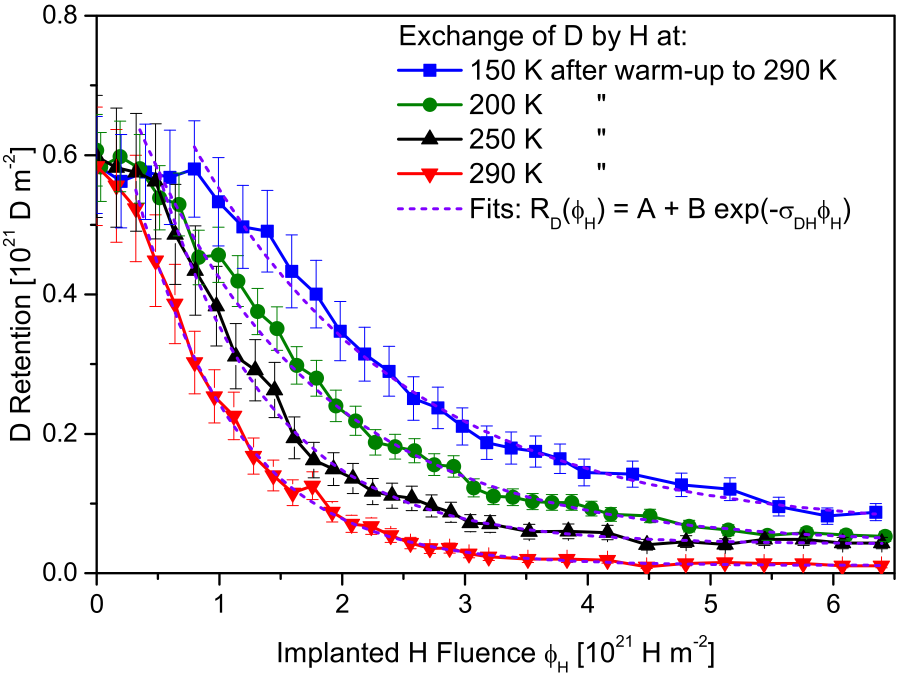

Figure 5.9: Deuterium retention during protium implantation at 150, 200, 250 and 290 K after prior warm-up and hold at 290 K for 114 h.

5.3.2 Results

Figure 5.9 shows the deuterium retention during the protium implantation at different temperatures after the sample was warmed-up and kept at 290 K for 114 h. The initially retained amount of deuterium is in all cases approximately $0.6 \times 10^{21}\,\mathrm{D\,m^{-2}}$. When the exchange of deuterium by protium is conducted at 150 K, a protium fluence of at least $0.8 \times 10^{21}\,\mathrm{H\,m^{-2}}$ is required to observe a decrease of the deuterium retention. For lower protium fluences the deuterium retention remains constant. As the sample temperature at which the protium implantation is carried out is increased, the critical protium fluence required to observe a reduction of the deuterium retention decreases. At 200 and 250 K, the deuterium retention starts to decline when an implanted protium fluence of approximately $0.4 \times 10^{21}\,\mathrm{H\,m^{-2}}$ is exceeded. In case of 290 K, a reduction of the retained deuterium amount sets in already after the first protium implantation step and becomes even stronger after $0.3 \times 10^{21}\,\mathrm{H\,m^{-2}}$. Furthermore, the decrease of the deuterium retention per implanted protium fluence increases, the higher the temperature at which the exchange is conducted.

In order to quantify this increase of the exchange efficiency, the regions in which the reduction of the deuterium retention is observed are fitted with equation (5.1). The determined isotopic exchange cross sections σ_{DH} together with the other fit parameters are given in table 5.2. The comparison of the exchange cross sections of deuterium by protium at 150 and 290 K reveals an increase by more than a factor of two. In addition, it can be seen from figure 5.9 and the fit parameter A in table 5.2 that the amount of deuterium remaining in the sample at the end of the isotope exchange experiment is inversely depending on the temperature. At 150 K approximately $0.6 \times 10^{20}\,\mathrm{D\,m^{-2}}$ remains in the sample, while at 290 K it is only $0.1 \times 10^{20}\,\mathrm{D\,m^{-2}}$.

T [K]	A $[10^{20}\,\mathrm{D\,m^{-2}}]$	B $[10^{20}\,\mathrm{D\,m^{-2}}]$	σ_{DH} $[10^{-21}\,\mathrm{m^2}]$
150	0.62 ± 0.06	0.87 ± 0.04	0.52 ± 0.03
200	0.41 ± 0.03	0.76 ± 0.02	0.68 ± 0.02
250	0.42 ± 0.02	0.92 ± 0.05	1.08 ± 0.03
290	0.11 ± 0.08	0.80 ± 0.04	1.24 ± 0.03

Table 5.2: Fit parameters of isotope exchange of deuterium by protium at different temperatures after warm-up and hold at 290 K for 114 h.

5.4 H Implantation between Two Ramp & Holds

5.4.1 Experimental Procedure

In the experiments discussed so far, the fill-level model is investigated in the context of the hydrogen isotope exchange by studying the decrease of the deuterium inventory during the protium implantation at a fixed temperature. Another possibility to examine the fill-level model as underlying exchange mechanism is to analyze the variation of the deuterium desorption rate spectrum as a consequence of a preceding protium implantation. The corresponding experimental scenario, in which the fill-level model is tested in two consecutive temperature Ramp & Hold cycles, is schematically depicted in figure 5.10.

As in the two previous scenarios, the experiment starts with a sample in which the traps are saturated with deuterium. In the first Ramp & Hold cycle the sample temperature is ramped from T_0 to T_1, with T_1 being lower than temperature T_2. As the number of deuterium atoms which occupy the traps decreases, the required energy for de-trapping increases. Holding the sample temperature at T_1, deuterium is released from the traps until a fill level is reached at which the required de-trapping energy is sufficient to suppresses further thermally activated release of deuterium. Subsequently, the sample is cooled down again to temperature T_0. The case in which no protium implantation is conducted before the second Ramp & Hold cycle is illustrated in figure 5.10 (a). In the second Ramp & Hold cycle the sample is heated up from T_0 to T_2 instead of T_1. While the sample temperature is below T_1 no release of deuterium atoms from the traps is expected. Simply because the traps are not filled to the level at which the de-trapping energy is sufficiently small to allow deuterium release below T_1. Once the sample temperature exceeds T_1, deuterium can be released from the traps.

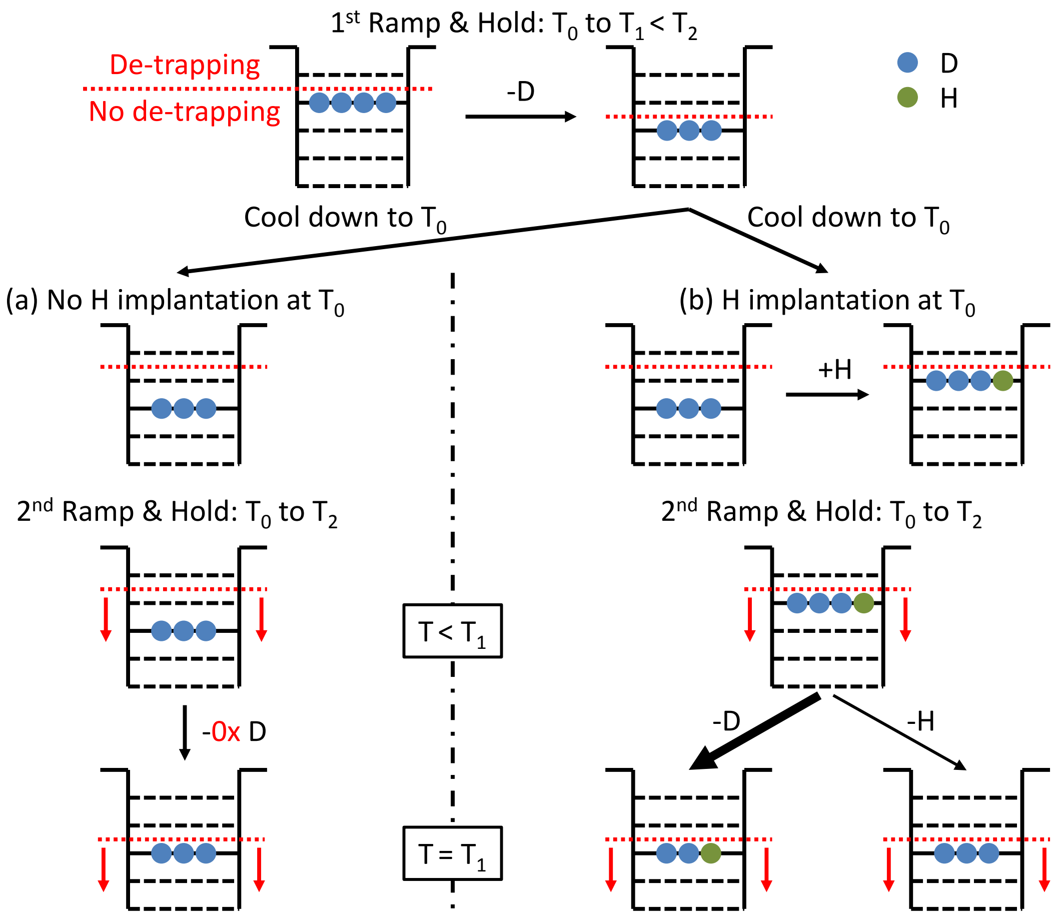

Figure 5.10: Schematic illustration of the protium implantation in between two consecutive Ramp & Hold cycles to increasing temperature.

The experiment is repeated with a new sample, but before the second Ramp & Hold cycle is performed, protium implantation at temperature T_0 is conducted, as illustrated in figure 5.10 (b). The traps which are still partly occupied with deuterium capture the implanted protium atoms from the solute. As the number of hydrogen atoms in the traps increases the necessary de-trapping energy decreases. The protium fluence needs to be chosen low enough in order to avoid loss of deuterium from the traps by hydrogen isotope exchange. On the other hand the protium fluence must be sufficient to fill the traps up to the highest level at which no de-trapping of hydrogen atoms occurs at temperature T_0. After the protium implantation is completed the sample temperature is ramped from T_0 to T_2. Since the traps are filled up to the maximum possible level at T_0, the release of deuterium and protium atoms from the traps is already expected for temperatures below T_1, with the corresponding release probability depending on the isotopic ratio. This is in contrast to the case in figure 5.10 (a), where the release of deuterium requires a sample temperature above T_1.

The experiment is realized on four subsequent days. Deuterium implantation is conducted on the first day, followed by the first Ramp & Hold cycle on the second day. Protium implantation is performed on day three and the second Ramp & Hold cycle is conducted on the fourth day. In order to study the effect of the intermediate protium implantation a second sample on which the protium implantation is omitted serves as a reference. The initial deuterium implantation is carried out as described in section 5.1. After the final irradiated deuterium fluence of $8.4 \times 10^{21}\,\mathrm{D\,m^{-2}}$ is reached, the sample is kept at 150 K for another 3 h. Following the calibration of the quadrupole mass spectrometer with the D_2 and H_2 leak valves, the first Ramp & Hold cycle is started. As in the experiment before, a heating rate of $0.5\,\mathrm{K\,min^{-1}}$, a final temperature of 200 K and a hold time of 3 h is chosen. Once the first Ramp & Hold cycle is completed, the sample heating is switched off and the calibration of the quadrupole mass spectrometer is repeated. On the third day, the protium implantation at 150 K is performed with an energy of 3.0 keV/H and a flux of $8.4 \times 10^{17}\,\mathrm{H\,m^{-2}s^{-1}}$. The irradiated protium fluence is $0.9 \times 10^{21}\,\mathrm{H\,m^{-2}}$ which is just below the fluence at which hydrogen isotope exchange occurs after Ramp & Hold to 200 K. Once the implantation is completed the sample is kept for another 3 h at 150 K, before the sample heating is switched off. On the fourth day, the second Ramp & Hold cycle is performed. The heating rate and the hold time are the same as in the first Ramp & Hold cycle, yet the final temperature is set to 290 K instead of 200 K. The quadrupole mass spectrometer is calibrated with the D_2 and H_2 leak valves before and after the Ramp & Hold cycle. As already mentioned, the whole experimental procedure is repeated with a reference sample which is not implanted with protium on the third day.

5.4.2 Results

The deuterium release spectra of two consecutive Ramp & Hold experiments to 200 and 290 K, without and with protium implantation conducted in between are shown in figure 5.11 (a) and (b), respectively. In both cases the release spectra observed in the first Ramp & Hold cycle to 200 K exhibit a similar shape which is in agreement with the previously discussed deuterium desorption spectrum in figure 5.3. The peak desorption rate at 200 K is $0.96 \times 10^{17}\,\mathrm{D\,m^{-2}s^{-1}}$ in (a) and $0.91 \times 10^{17}\,\mathrm{D\,m^{-2}s^{-1}}$ in (b). Integrating the desorption spectra yields a released deuterium amount of 0.59 and $0.55 \times 10^{21}\,\mathrm{D\,m^{-2}}$ for (a) and (b), respectively. The difference of 6.8 % might be the result of a slightly smaller initial amount of implanted deuterium in (b). Both values are smaller but within the uncertainty when comparing the difference of the initial and final deuterium retention derived by NRA in figure 5.3 which accounts to $0.64 \pm 0.09 \times 10^{21}\,\mathrm{D\,m^{-2}}$.

In the second Ramp & Hold cycle with no protium implantation conducted in

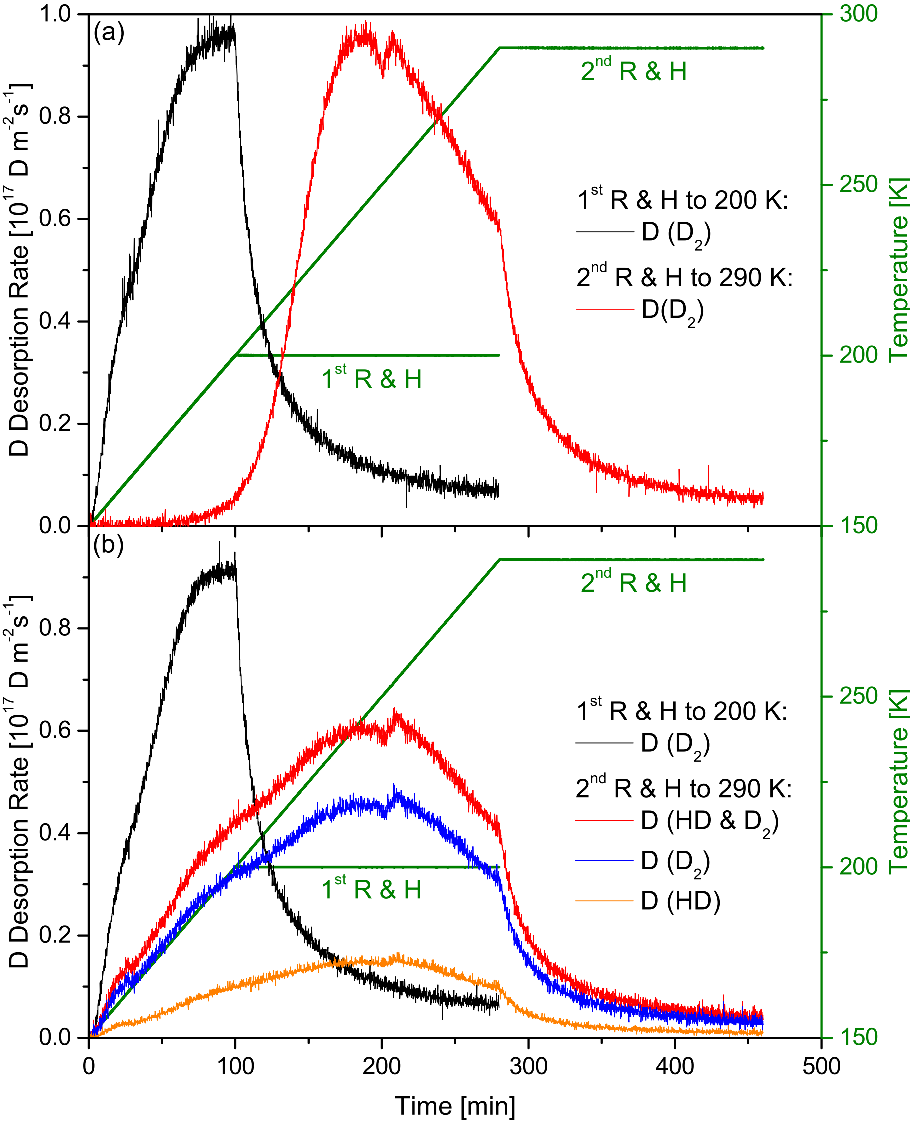

Figure 5.11: Deuterium desorption rate measured in two consecutive Ramp & Hold experiments (a) without and (b) with protium implantation at 150 K after the first Ramp & Hold cycle to 200 K, respectively.

between, shown in figure 5.11 (a), no release of deuterium is observed in the beginning. After a ramp time of 68 min, which corresponds to a temperature of 184 K, the deuterium desorption rate starts to increase slowly. Interestingly, this specific temperature coincides with temperature at which the kink in the desorption spectrum of the first Ramp & Hold cycle appears. Once the final temperature of 200 K of the first Ramp & Hold cycle is exceeded, the desorption rate grows significantly. It reaches a maximum of $0.95 \times 10^{17}\,\mathrm{D\,m^{-2}s^{-1}}$ after 187 min or 244 K. For higher temperatures the features already known from figure 5.5, such as the dip, the linear decrease, and once the ramp phase is finished, the exponential decrease are observed. The amount of deuterium released in the second Ramp & Hold cycle is $0.88 \times 10^{21}\,\mathrm{D\,m^{-2}}$. Together with the deuterium released in the first Ramp & Hold cycle, a total amount of $1.47 \times 10^{21}\,\mathrm{D\,m^{-2}}$ is released. This value is within the range of the deuterium release in the Ramp & Hold experiment shown in figure 5.5, which is determined by NRA to $1.39 \pm 0.15 \times 10^{21}\,\mathrm{D\,m^{-2}}$.

As can be seen from figure 5.11 (b), the situation is quite different when protium implantation is performed before the second Ramp & Hold cycle. Due to the presence of protium in the sample, deuterium is not only released as D_2, but also as HD. The shape of the D_2 and the HD spectra are very similar. Hence, after calibration of the individual spectra and under consideration of the different amount of deuterium per molecule the spectra are added. Compared with the deuterium release spectrum of the second Ramp & Hold experiment with no prior protium implantation, shown in figure 5.11 (a), two major differences are apparent. First, the desorption of deuterium is already observed directly after the temperature ramp is started, in contrast to the delayed rise illustrated in figure 5.11 (a). Two shoulders, after 24 and 74 min, corresponding to 162 and 187 K, respectively, are present in the spectrum. These features coincide well with the shoulder and the kink observed in the deuterium desorption rate spectra of the first Ramp & Hold cycles in figures 5.11 (a) and (b). The second difference is the maximum deuterium desorption rate of $0.64 \times 10^{17}\,\mathrm{D\,m^{-2}s^{-1}}$, which is only 67 % of the one measured in 5.11 (a). However, the amount of deuterium released in the second Ramp & Hold cycle in figure 5.11 (b) is $0.82 \times 10^{21}\,\mathrm{D\,m^{-2}}$ and thus 6.8 % lower than in the second Ramp & Hold cycle without prior protium implantation, shown in figure 5.11 (a). Since the deuterium release in the first Ramp & Hold cycle is already lower by 6.8 %, this implies that no deuterium is released during the protium implantation as it was intended. Accordingly, the total amount of deuterium released during both Ramp & Hold cycles with intermediate protium implantation is $1.37 \times 10^{21}\,\mathrm{D\,m^{-2}}$ and lower by 6.8 % compared to the one without protium implantation performed in between. From those results it can be concluded that the implantation of protium led to a redistribution of strongly to weakly trapped deuterium without decreasing the total deuterium amount.

5.5 Discussion

Evaluating the data from the previous sections, it can be seen that the deuterium retention as a function of the implanted protium fluence is characterized by two features. The first one is the critical implanted protium fluence at which the onset of the decrease in the deuterium retention appears. The second one is the efficiency at which the deuterium retained in the sample is exchanged by protium, represented by the hydrogen isotope exchange cross section. The dependence of both features on the exchange temperature and the initial deuterium retention can be described as follows:

Critical Protium Fluence:

1. The higher the deuterium retention prior to the isotope exchange, the lower the critical protium fluence at a given temperature.
2. The higher the exchange temperature, the lower the critical protium fluence for a given initial deuterium retention.
3. The protium implantation leads to an redistribution of strongly to weakly bound deuterium.

Exchange Cross Section of D by H:

1. The exchange cross section does not depend on the initial deuterium retention for a given temperature.
2. The higher the exchange temperature, the higher the exchange cross section at a given initial deuterium retention.

Figure 5.12 and 5.13 illustrate the results of the critical implanted protium fluence and the exchange cross sections obtained in the two different hydrogen isotope exchange experiments conducted with NRA. The linear fits in the figures are supposed to guide the eye and highlight trends in the data.
In the following the results regarding the critical protium fluence as well as the hydrogen isotope exchange cross section will be discussed qualitatively in the context of the fill-level model. Furthermore, the effects of different trap types on the observed exchange will be assessed and other alternative exchange mechanisms are evaluated. Finally, the data obtained in the here-conducted experiments are compared to the available literature.

5.5.1 Critical Protium Fluence

Interpreting the results in the context of the fill-level model, the observation of a critical amount of protium which is required to trigger a decrease in the

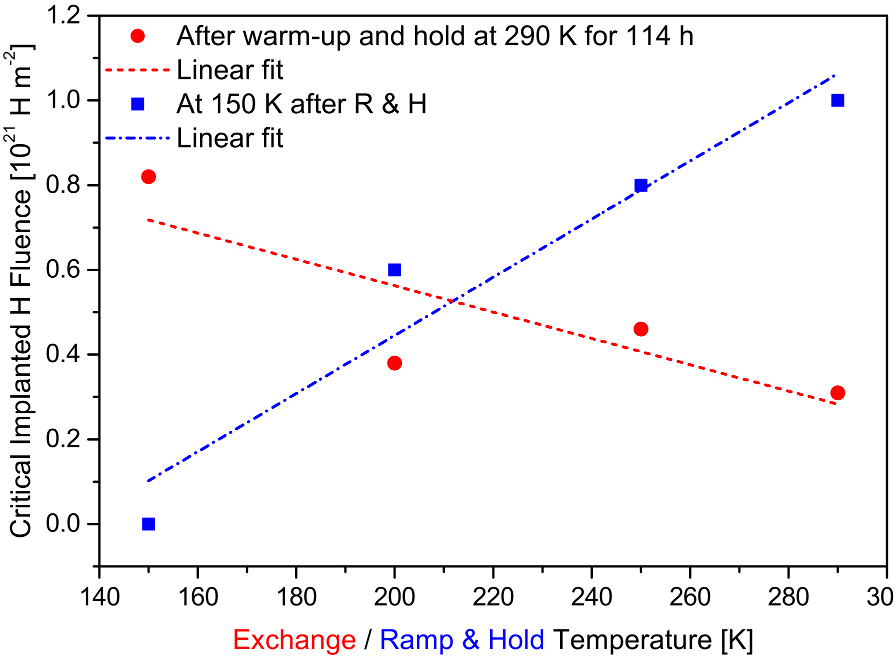

Figure 5.12: Comparison of the critical implanted protium fluence at which the decrease of the deuterium retention occurs in the different hydrogen isotope exchange experiments conducted with NRA.

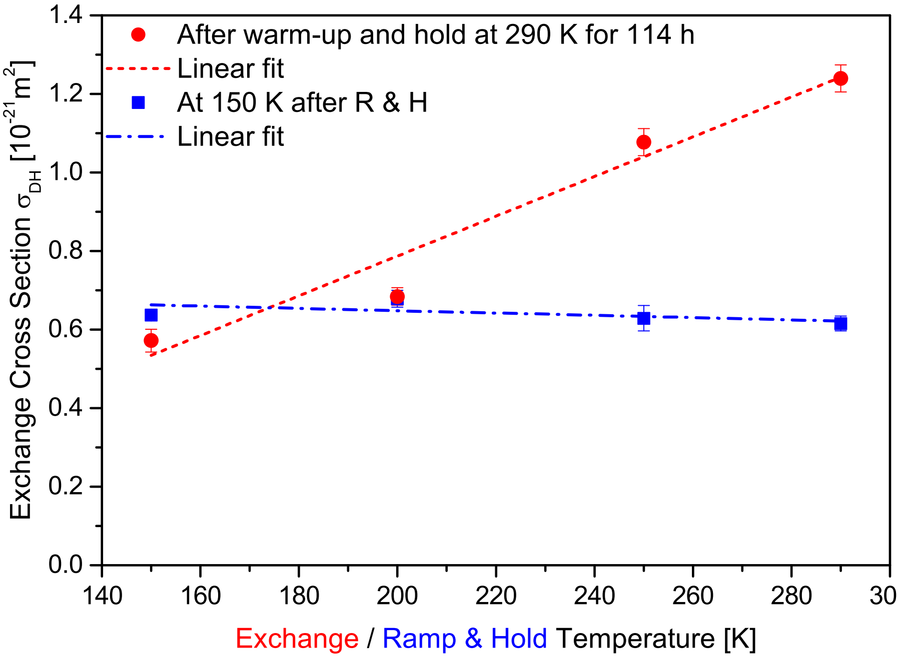

Figure 5.13: Comparison of the exchange cross section of deuterium by protium measured in the different hydrogen isotope exchange experiments conducted with NRA.

deuterium retention can be associated with the filling of traps. This implicitly assumes that the transport of deuterium, respectively protium, is not the dominating process. The influence of the transport can only be assessed with more sophisticated models such as TESSIM-X and will be discussed later in detail.

Under this assumption the dependence of the critical protium fluence on the initial deuterium retention can be explained qualitatively as follows: The lower the temperature in the preceding Ramp & Hold cycle, the higher the initial deuterium retention and consequently the higher the level to which the traps are filled. Hence, as shown in figure 5.12, less protium is required to fill the traps to a level with low enough de-trapping energy to allow thermal release of deuterium at a given temperature. Likewise, the relationship between the critical protium fluence and the temperature of the exchange can be explained. The higher the temperature at which the isotope exchange is conducted, the lower the required level to which the traps need to be filled for thermal de-trapping to occur. Since the initial deuterium retention is the same, less protium is required at higher exchange temperature, as illustrated in 5.12. Similarly, the observed shift of the onset of the deuterium desorption rate in the second Ramp & Hold cycle from high to low temperatures, observed in figure 5.11 (b), can also be assigned to trap refilling. The additional protium in the traps leads to the occupation of fill levels with reduced de-trapping energy. As a consequence, protium and deuterium can be released already at lower temperatures than that observed in the second Ramp & Hold cycle without prior protium implantation, shown in 5.11 (a). Furthermore, deuterium released from levels with low de-trapping energy cannot be released again from levels with high de-trapping energy, consequently the deuterium desorption rate at higher temperature is bound to be lower.

5.5.2 Exchange Cross Section

The dependences of the exchange cross section on the deuterium retention prior to the protium implantation and on the exchange temperature can be qualitatively understood by a simple combinatorial model described in the following. Within the fill-level model, the actual exchange process sets in once the trap is filled with a mixture of deuterium and protium up to a level with a low enough de-trapping energy to allow thermally activated release of either deuterium or protium. Qualitatively, such a fill-level trap could be considered as an urn to which a protium atom is added and either a deuterium or protium atom is drawn. Hence, in a qualitative first order approach an ensemble of such urns could be used to understand the principal relations of the hydrogen isotope exchange from a combinatorial point of view. This simple urn model neglects the transport of hydrogen and its subsequent desorption at the surface. Furthermore, it is assumed that the urns are only refilled with protium while refilling with released deuterium is not considered. In the fill-level picture, the temperature defines from which level the hydrogen is released, consequently it also defines the maximum possible number of deuterium and protium atoms in the trap. Hence, the temperature enters the urn model via the number of possible hydrogen atoms in the urns.

The initial state of the ensemble is characterized by the probability vector $\underline{p}\,(0)$ in equation (5.2), with $\left\|\underline{p}\,(0)\right\| = 1$. The entries $p_{D=0}$ to $p_{D=N}$ can possess values between 0 to 1 and correspond to the fraction of urns containing 0 to N deuterium atoms. The evolution of the initial state in one drawing event is described by the $(N+1) \times (N+1)$ transition matrix $\underline{\underline{M}}$, given in equation (5.2), where i is the index of the row, starting with 1, and N the possible number of hydrogen atoms in one urn.

$$\underline{p}\,(0) = \begin{pmatrix} p_{D=0}\,(0) \\ p_{D=1}\,(0) \\ p_{D=2}\,(0) \\ \vdots \\ p_{D=N}\,(0) \end{pmatrix}, \underline{\underline{M}} = \begin{pmatrix} 1 & \frac{1}{N+1} & 0 & \cdots & \cdots & 0 \\ 0 & \frac{N}{N+1} & \frac{2}{N+1} & \ddots & & \vdots \\ \vdots & 0 & \frac{N-1}{N+1} & \ddots & \ddots & \vdots \\ \vdots & & 0 & \ddots & \ddots & 0 \\ \vdots & & & \ddots & \ddots & \frac{i}{N+1} \\ 0 & \cdots & \cdots & \cdots & 0 & \frac{N+2-i}{N+1} \end{pmatrix}, \underline{b} = \begin{pmatrix} 0 \\ 1 \\ 2 \\ \vdots \\ N \end{pmatrix} \tag{5.2}$$

The diagonal and off-diagonal entries of the matrix correspond to the probability of drawing a protium or deuterium atom from the urn, respectively. By applying the transition matrix consecutively on the initial probability vector, as shown in equation (5.3), the state of the ensemble $\underline{p}\,(n)$, after n iteration is obtained.

$$\underline{p}\,(n) = \underline{\underline{M}}^{n}\underline{p}\,(0) \tag{5.3}$$

The accumulated average amount of deuterium retained in the urns after n iterations, $R_D\,(n)$, can be calculated by the following equation:

$$R_D\,(n) = \underline{p}\,(n) \cdot \underline{b}, \tag{5.4}$$

with $\underline{b}$, shown in equation (5.2), effectively weighting the respective portion of urns with the corresponding amount of retained deuterium atoms.

Lets assume $N = 5$ and an initial state $\underline{p}\,(0)$ with $p_{D=5}\,(0) = 1$, which represents the case where each urn is filled to the maximum with 5 deuterium atoms. The evolution of this ensemble as a function of iterations is shown in figure 5.14. In the beginning the fraction of urns containing 5 deuterium atoms is unity. After the first iteration the majority of urns lost a deuterium atom and the fraction containing four atoms reaches a maximum. As drawing deuterium from the urns is continued each fraction goes through a maximum. The position of the maximum increases as the number of deuterium atoms retained in the urns of the respective fraction decreases. Once 5 iterations are conducted a certain fraction of urns containing no deuterium appears and increases with every further iteration. After approximately 40 iterations most of urns lost their deuterium completely. The average deuterium retention of each fraction of urns as a function of the number of iterations is illustrated in figure 5.15. It can be seen that the accumulated average deuterium retention of the ensemble follows an exponential decrease.

To mimic the experimental situation, where hydrogen isotope exchange is studied as a function of the initial deuterium retention at a given temperature, the number of possible hydrogen atoms in one urn is set to $N = 5$ and the initial probability vector is altered to represent the cases of each urn containing 1 to 5 deuterium atoms. The acquired results are illustrated in figure 5.16 as black lines. It can be seen that the exponent of the exponential decrease of the accumulated average deuterium retention is always the same regardless of the initial retention. Even ensembles combined of arbitrary fractions of urns with a different initial number of deuterium atoms yield the same exponential decrease. This observation fits very well to the experimental result in which no dependence of the exchange cross section on the initial deuterium retention is found.

The hydrogen isotope exchange experiment to investigate the exchange of a given initial deuterium retention as a function of temperature, shown in figure 5.9, can also be addressed with the urn model. The initial probability vector is chosen such that each urn is occupied by two deuterium atoms and the number of possible hydrogen atoms in each urn is decreased from $N = 5$ to $N = 2$ to represent an increase of the exchange temperature. As can be observed from the red lines in figure 5.16, decreasing the maximum number of hydrogen atoms per urn results in a larger absolute exponent and a faster exponential decrease of the average deuterium retention. Hence from a pure combinatorial consideration a more effective hydrogen isotope exchange is obtained at higher temperature. This result is in good qualitative agreement with the experimental observation of an increased exchange cross section of deuterium by protium at higher temperatures. Nevertheless, it should be kept in mind that in this experiment the exchange is performed at different temperatures which affects the diffusion coefficient, the recombination rate as well as de-trapping and re-trapping of hydrogen. Thus, despite the same trap concentration, the transport properties of hydrogen in tungsten could be different.

5.5.3 Influence of Different Trap Types

The interpretation of the experimental data in the fill-level model rises the impression that only one trap type with levels of different de-trapping energies exists in the sample. This is of course not the case. At least three different trap types are present: Vacancies, dislocations and blisters.

The first type is created by the deuterium implantation itself. The energy of 3.0 keV/D is sufficient to displace tungsten atoms from their lattice positions and create interstitial-vacancy pairs. The vacancies, acting as trap sites for the

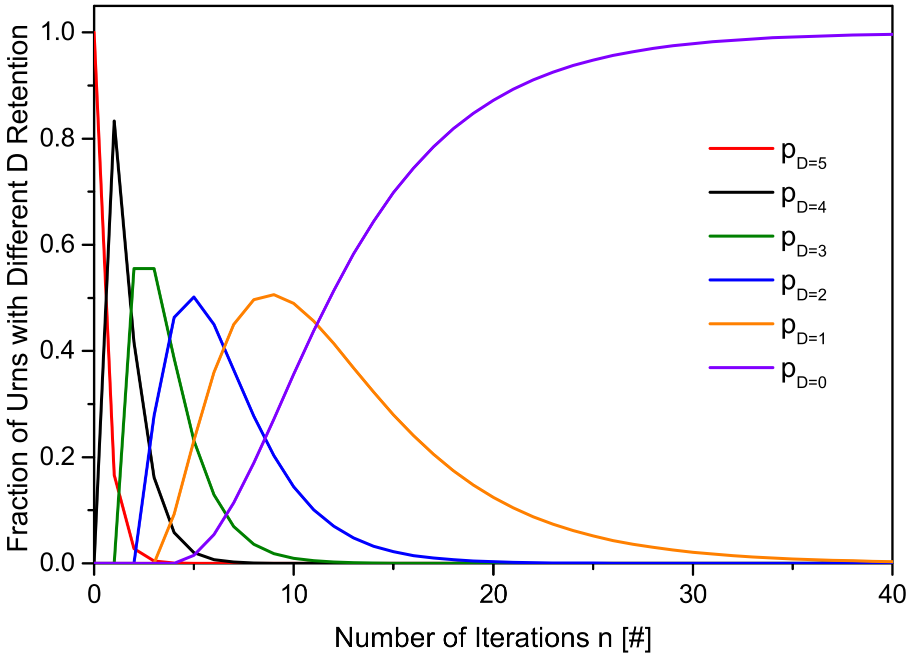

Figure 5.14: Evolution of the fraction of urns containing different amount of deuterium as function of iterations. In the initial state all urns are occupied with the maximum number of deuterium atoms $N = 5$.

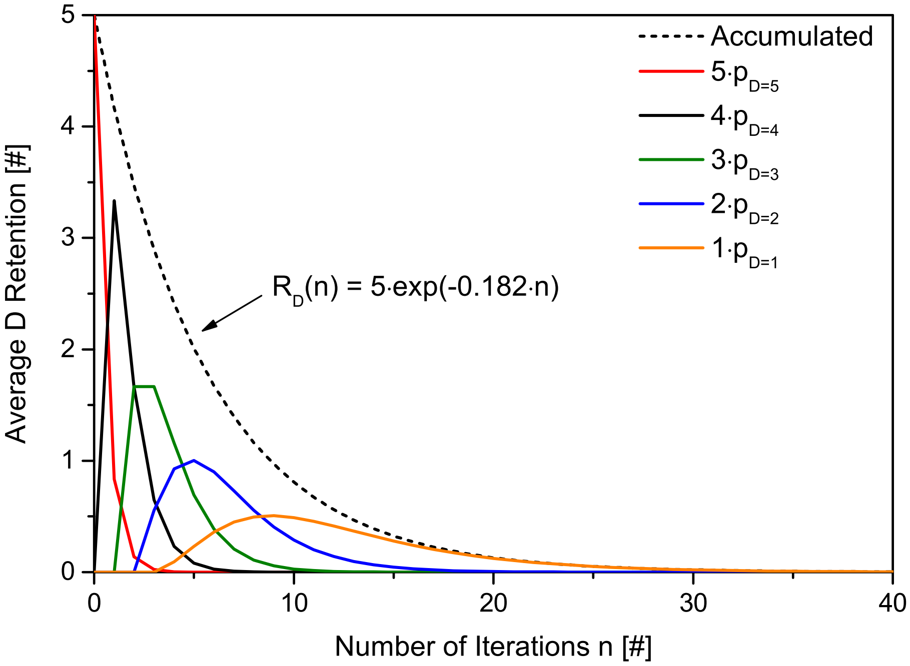

Figure 5.15: Evolution of the average deuterium retention per fraction of urns containing different amounts of deuterium and accumulated average deuterium retention of the urn ensemble as function of iterations. In the initial state all urns are occupied with the maximum number of deuterium atoms $N = 5$.

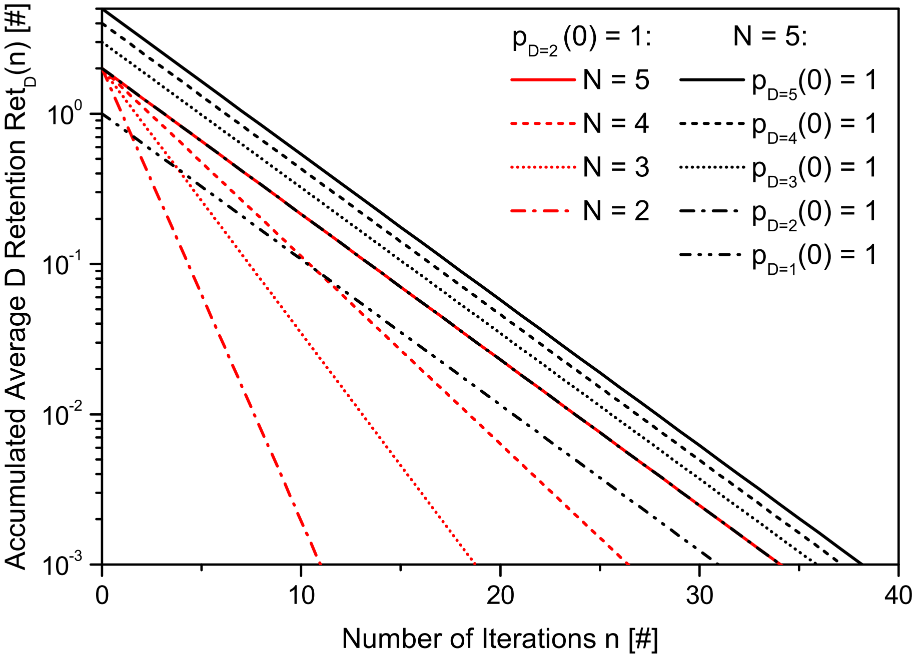

Figure 5.16: Accumulated average deuterium retention of the urn ensemble as function of iterations. Number of maximum hydrogen atoms per urn kept at $N = 5$ and number of deuterium atoms varied from 1 to 5 (black lines). Two deuterium atoms per urn and variation of the maximum number of hydrogen atoms per urn from $N = 5$ to $N = 2$ (red lines).

hydrogen isotopes, can be described with the fill-level model [58–61]. Regarding the dislocations, it was shown by Manhard et al. [149] that the emergence of blisters is accompanied with the appearance of dislocations in the proximity of the blisters. As shown in chapter 4, the conditions under which deuterium is implanted in the here-performed experiments lead to severe blister formation which also implies the presence of dislocations. According to DFT studies by Terentyev et al. [62] hydrogen being immobilized at a dislocation also shows a decrease of the required de-trapping energy as the number of hydrogen atoms trapped at the dislocation increases.

While vacancies and dislocations can be described in the framework of the fill-level model, blisters cannot. The role of blisters in the hydrogen isotope exchange process can be complex, depending whether the blister is closed or possesses a connection to the surface. When the blister is closed, the deuterium gas in the cavity needs to be removed. This requires the dissociative adsorption of deuterium molecules at the inner blister surface followed by the transition of deuterium atoms into the bulk. A mechanism in which the additional presence of protium in the blister as well as in the surrounding bulk material enhances the release of deuterium gas from the blister is not yet known. From an experimental point of view, the question whether hydrogen isotope exchange takes place in blisters could not be resolved so far. As discussed in chapter 4, the observed saturation of deuterium retention as well as the investigation of blisters by SEM imply that the blisters rupture already during the deuterium implantation. Since all hydrogen isotope exchange experiments are performed after the samples were saturated, the influence of closed blisters should be small. In contrast to that, an open blister could lead to a more efficient hydrogen isotope exchange. It could be shown that ruptured blisters close to the surface are responsible for an enhanced re-emission of implanted deuterium from the sample [152]. Compared to an unblistered sample, where the de-trapped deuterium atom needs to diffuse to the surface in order to leave the sample, the presence of open blisters provides an additional release channel. Consequently, the enhanced release of de-trapped deuterium atoms from the sample should result in a faster decrease of the deuterium retention and a more efficient isotopic exchange should be observed.

5.5.4 Alternative Exchange Mechanisms

So far the discussion of the experimental data was conducted under the assumption that the fill-level model describes the underlying mechanism of the hydrogen isotope exchange. However, the exchange of deuterium by hydrogen observed in the experiments could also be explained by other effects. The isotopic exchange takes predominantly place in the ion implantation range, therefore also ion-beam effects must be considered as a possible exchange mechanism. As an implanted protium atom propagates through the tungsten lattice it loses energy by electronic and nuclear stopping [13]. The first one describes the inelastic interaction of the implanted protium with the bound and delocalized electrons of the system. The second one considers the energy loss due to elastic collisions between the protium atom and other atoms in the target, which can be tungsten, deuterium or protium. When an incoming protium atom collides with a trapped deuterium atom and the transferred energy is sufficient, the deuterium atom can be kicked out of the trap. As the generated deuterium recoil atom propagates in the tungsten lattice it loses energy. Once it comes to rest at a different site, it starts to diffuse until it gets trapped again or leaves the sample. This kinetic de-trapping process is temperature independent and allows the removal of deuterium atoms from traps at temperatures which prohibit a thermally activated release.

In order to assess the relevance of this effect, SDTrimSP [66, 67] simulations of protium implantation into deuterium containing tungsten are conducted. Protium is implanted with an energy of 3.0 keV/H perpendicular to the surface. The deuterium concentration in the tungsten target is varied between 10 and 50 at.%. The displacement energy of deuterium atoms is altered within the range of the diffusion energy barrier of 0.25 eV [89] and the de-trapping energies up to 2.0 eV [86]. In the SDTrimSP simulations 10^5 protium projectiles are calculated with the parameters stated in appendix A.3. In figure 5.17 the simulated protium implantation profile and the deuterium recoil profile for specific deuterium concentrations and displacement energies are shown, all spectra are divided by the number of implanted protium atoms.

The shape of the protium implantation profile does not depend on the displacement energy of deuterium atoms but on the deuterium concentration in the tungsten target. As the deuterium concentration increases the stopping power of the target decreases, resulting in a larger penetration depth of the implanted protium. Consequently, the protium implantation profile broadens. The deuterium recoil generation profile, representing the origin of the recoils, depends strongly on the concentration and the displacement energy of deuterium in the tungsten target. The higher the deuterium concentration, the higher the probability of a collision between a protium and a deuterium atom. Hence, a larger number of deuterium recoil atoms are created at a higher deuterium concentration. In addition, as the penetration depth of protium atoms increases with increasing deuterium concentration, more deuterium recoils are created in larger depth, resulting in a broadening of the deuterium recoil profile. Furthermore, figure 5.17 shows that a lower displacement energy leads to the generation of a larger number of deuterium recoil atoms. The distance between the origin and the final position of the deuterium recoil atom is described by a log-normal distribution and depends slightly on the deuterium concentration and the displacement energy. The largest distances are observed for a concentration of 10 at.% and a displacement energy of 2.0 eV, with the corresponding mean value and standard derivation of 1.1 and 0.09 nm, respectively. Thus, it can be concluded that most of the created deuterium recoil atoms come to rest in close vicinity of their origin.

The integration of the deuterium recoil profiles, shown in figure 5.17, yields the ratio of the total number of deuterium recoil atoms created per implanted protium atom. Figure 5.18 summarizes this ratio as function of the deuterium concentrations for different displacement energies of deuterium atoms. As can be seen, the number of generated deuterium recoil atoms increases with increasing deuterium concentration and decreasing displacement energy. At low deuterium concentrations as well as at high displacement energies, most of the created deuterium recoils are generated by a direct collision with a protium atom. Hence, they can be regarded as first generation recoils or primary knock on atoms [13]. The dashed black polygon in figure 5.18 indicates the region where the majority of deuterium recoils belong to the first generation. For higher deuterium concentrations and lower displacement energies the effect of collision cascades becomes more important. Deuterium atoms are not only displaced by protium atoms but also by previously created deuterium recoil atoms. The dash-dotted black triangle in figure 5.18 marks the region in which the majority of deuterium recoil atoms belong to the second or later generation. In the most extreme case, i.e. a deuterium displacement energy of 0.25 eV and a concentration of 50 at.%, up to 150 deuterium recoils per implanted protium atom are created. It should be mentioned that the conducted SDTrimSP simulations consider only the de-trapping caused by direct collisions between the trapped deuterium atoms and other atoms. The extent to which an electronic

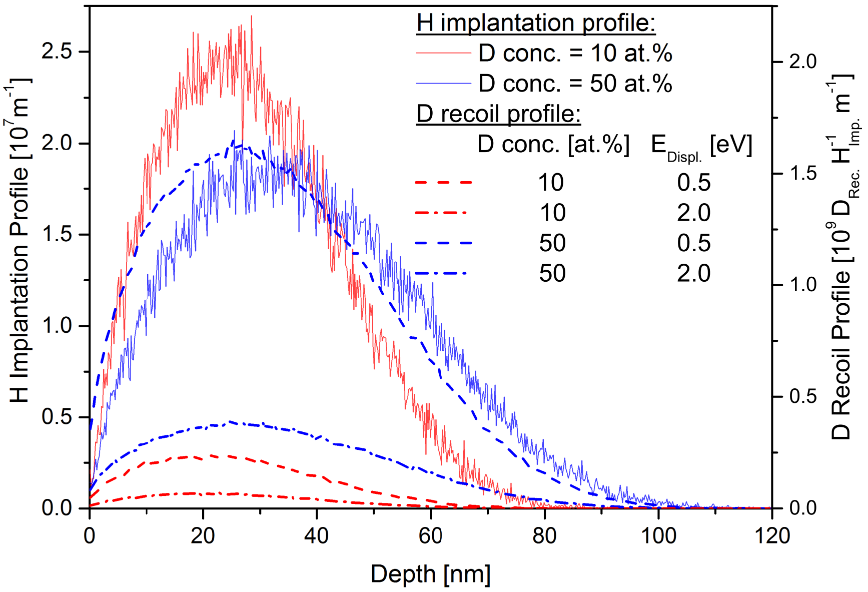

Figure 5.17: SDTrimSP simulations of 3.0 keV/H protium implantation into tungsten with different deuterium concentrations of 10 (red) and 50 at.% (blue). The protium implantation profiles are shown as solid lines. The deuterium recoil profiles are shown as dashed and dash-dotted lines for a displacement energy of 0.5 and 2.0 eV, respectively. All spectra are divided by the number of implanted protium atoms.

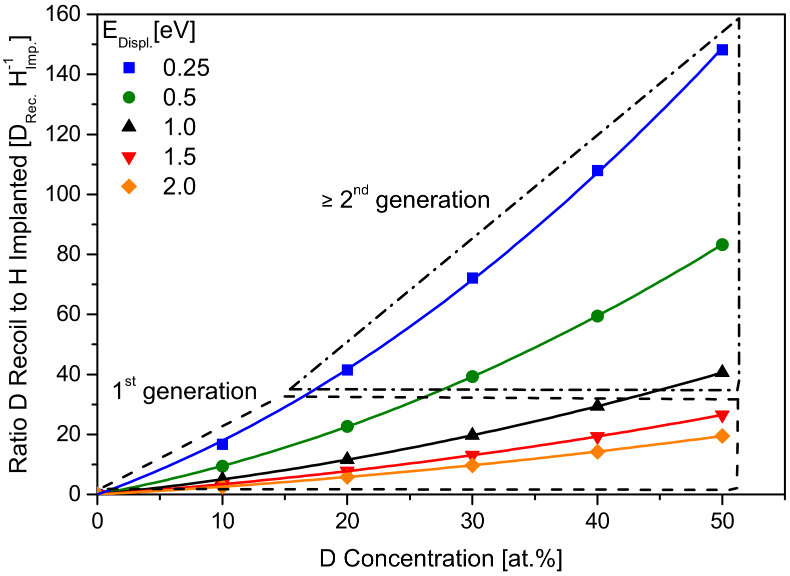

Figure 5.18: Deuterium recoil atoms per implanted protium atom as a function of deuterium concentration and displacement energy. (Dashed polygon) Deuterium recoils created mainly by incident protium atoms. (Dash-dotted polygon) Deuterium recoils created predominantly by other deuterium recoils.

excitation of the system, due to electronic loss of the implanted protium atom, contributes to the de-trapping of deuterium atoms is unknown.

Based on these simulations, the required time to displace all retained deuterium atoms in the sample once can be estimated. Addressing the most extreme scenario, i.e. the hydrogen isotope exchange experiment at 150 K without preceding Ramp & Hold, shown in figure 5.6 and 5.7. In this case the deuterium concentration and retention is 43 at.% and $2.04 \pm 0.24 \times 10^{21}\,\mathrm{D\,m^{-2}}$, respectively. Assuming a displacement energy of 0.25 eV, this corresponds to 120 created deuterium recoils per implanted protium atom. Dividing the deuterium retention by the implanted protium flux of $6.4 \times 10^{17}\,\mathrm{H\,m^{-2}s^{-1}}$ and 120, the required time to displace all retained deuterium atoms is approximately 30 s.

In the case where hydrogen isotope exchange is conducted at 150 K after Ramp & Hold to 290 K, an initial deuterium concentration of 17 at.% and a retention of $0.78 \pm 0.06 \times 10^{21}\,\mathrm{D\,m^{-2}}$ is measured. Accounting for the release of deuterium from traps with low de-trapping energy during the Ramp & Hold cycle, a displacement energy of 1.0 eV is assumed. At this specific displacement energy and deuterium concentration approximately 10 deuterium recoils per implanted protium atom are generated. The required time to displace all deuterium atoms is estimated to 120 s. Compared with the time to perform a hydrogen isotope exchange experiment, which is in the range of several hours, the kinetic de-trapping process is quite fast. Hence, as these rough estimates show, the kinetic de-trapping of deuterium by the protium beam is significant and must be considered as alternative exchange mechanism.

Beside the kinetic de-trapping some other exchange mechanisms are also possible but less likely. One possibility is the removal of the deuterium containing layer by sputtering with protium. Yet, sputtering occurs only within the first few monolayers from the surface. In order remove the deuterium located deeper in the bulk it is necessary to sputter the tungsten away. The sputter yield of pure tungsten by protium with an energy of 3.0 keV/H under normal incidence is 0.0015 W/H [168]. The irradiation of a protium fluence of $8.4 \times 10^{21}\,\mathrm{H\,m^{-2}}$ leads to the removal 1.3 nm of tungsten. For comparison, the deuterium depth profile extents in some cases up to 200 nm into the bulk. Unless the presence of deuterium in the tungsten lattice does not increase the sputter yield massively, the deuterium removal by sputtering seems less probable.

5.5.5 Comparison with Literature Results

Recently a lot of experiments have been conducted to investigate the hydrogen isotope exchange in tungsten under various conditions. Exchange was performed by exposing tungsten to ion beams [44, 45], plasmas [44, 46–48] and atomic beams [49–51, 163] of different hydrogen isotopes to study the exchange in the bulk, at the surface and in the near-surface region of heavy-ion-beam-damaged and undamaged tungsten. In addition, the exchange of deuterium in tungsten by a mixed protium-helium plasma was investigated [53].

Despite this large number of experiments only a few were evaluated in terms of exchange cross sections. One of those experiments was performed by Roth et al. [44] in which deuterium plasma-loaded tungsten samples were exposed to a protium ion beam with an energy of 200 eV/H at a sample temperatures of 320 and 450 K. The authors suggested two different mechanisms for the exchange close to the surface and in the bulk. The fit of the data with a sum of two exponential functions yields an exchange cross section of 10^{-22} to 10^{-21} and $10^{-25}\,\mathrm{m}^2$ for the near-surface and the bulk exchange, respectively.

Another experiment in which the exchange cross section for deuterium by protium in tungsten was determined, was conducted by Takagi et al. [48]. The samples were consecutively exposed at room temperature to a deuterium and a protium plasma with an approximate hydrogen isotope energy of 1 eV. The obtained exchange cross sections range from 3.2 to $5.4 \times 10^{-23}\,\mathrm{m}^2$.

A rather extensive study was conducted by Markelj et al. [50, 52]. The exchange of deuterium by protium in self-damaged tungsten samples was performed with a neutral atomic beam source with energies of the hydrogen isotopes of 0.28 eV. Similar to Roth et al. [44] the exchange close to the surface and in the bulk were investigated. For the near-surface exchange, cross sections of 0.9 ± 0.15 and $1.2 \pm 0.6 \times 10^{-22}\,\mathrm{m}^2$ were reported for sample temperatures of 380 and 480 K, respectively. For the bulk, exchange cross sections of deuterium by protium of 5.2 ± 0.5 and $6.5 \pm 0.3 \times 10^{-25}\,\mathrm{m}^2$ were derived for a sample temperature of 600 K.

Compared to the here-conducted experiments, in which the determined exchange cross sections of deuterium by protium range from 0.52 to $1.24 \times 10^{-21}\,\mathrm{m}^2$, most of the values found in the contemporary literature are lower. However, it should be noted that the experimental conditions differ significantly. The above stated literature exchange cross sections are obtained in experiments conducted at room temperature or higher and with low-energy hydrogen ions or atoms. In contrast to that, the current experiments are performed at temperatures at or below 290 K and with energetic hydrogen isotopes. In addition, the data obtained in the current study can be fitted with one exponential function compared to Roth et al. [44] and Markelj et al. [52] who fitted or modeled with two exponential functions. This difference could be explained by the low temperature at which the deuterium is initially implanted. Since most of the deuterium is located within the implantation zone, an exchange of deuterium by protium in the bulk becomes obsolete.

The only hydrogen isotope exchange experiment with comparable temperature and ion energy was conducted by Blewer et al. [156], though not on tungsten but on stainless steel. Deuterium and protium ions with energies ranging from 1 to 14 keV/(D,H) were sequentially irradiated at a sample temperature of 150 K. The obtained data were fitted with a sum of two exponential functions to account for an easy replaceable and a replacement resistant deuterium component. For the first one, an exchange cross sections of $0.79 \times 10^{-21}\,\mathrm{m}^2$ is determined which decreases to $0.11 \times 10^{-21}\,\mathrm{m}^2$ as the ion energy is increased from 1 to 14 keV/(D,H). For the latter one, a decrease of the exchange cross section from 1.2 to $0.11 \times 10^{-22}\,\mathrm{m}^2$ is derived accordingly. Especially the exchange cross section of the easy replaceable deuterium component obtained for low keV ion energies fits quite well to the here observed values despite the different material.

However, the data on exchange cross sections of hydrogen isotopes in tungsten is too sparse and the possible influencing parameters, e.g. temperature, ion energy, surface morphology or material grade, are too many to deduce global trends or dependences.

5.6 Conclusion

The experimental results regarding the critical implanted protium fluence are in good qualitative agreement with the simple considerations in the framework of the fill-level model conducted at the beginning of this chapter, although transport effects are not yet taken into account. In addition, the experimentally observed dependences of the exchange cross section of deuterium by protium on the temperature and the initial deuterium retention support the fill-level picture as well.

The exponential decrease of the deuterium retention during the exchange with protium, the independence of the exchange cross section from the initial deuterium retention and its qualitative temperature dependence could be reproduced with a simple urn model based on the fill-level framework.

Furthermore, SDTrimSP simulations and the thereon based estimations showed that the kinetic de-trapping of trapped deuterium atoms by energetic protium atoms must not be neglected. Due to the temperature independence of this de-trapping mechanism, deuterium can be released from a trap even if the corresponding de-trapping energy is large enough to suppress thermally activated de-trapping. Hence, the kinetic de-trapping mechanism combined with the classical model must be considered as alternative explanation of the experimental observations.

In order to assess the different possible exchange mechanisms a detailed modeling of the experimental data with TESSIM-X is carried out in the next chapter.

Chapter 6

Comparison of Exchange Mechanisms with TESSIM-X

In this chapter the results of the hydrogen isotope exchange experiments presented in the previous chapter are modeled by TESSIM-X [63, 65]. The fill-level model as well as the classical model, both with and without the kinetic de-trapping contribution of the ion beam, are applied. The relevant assumptions and input parameters entering the simulation are briefly reviewed. In a first step, the de-trapping energies of the traps and fill levels are determined by simulating the development of the deuterium desorption rate and the deuterium retention during the Ramp & Hold experiments. Based on these results the hydrogen isotope exchange under the different experimental conditions is simulated in the second step. The modeling results are discussed in detail for one specific experiment and the insights are transferred to interpret the results of the other simulation scenarios. Finally, the conclusions are drawn and an outlook for possible future experiments is provided.

6.1 Modeling Inputs and Procedure

In the following the inputs and assumptions which enter the TESSIM-X code, described in chapter 3, are presented. This includes the tungsten target as well as the diffusion, implantation, trapping and de-trapping of the hydrogen isotopes. In addition, the modeling procedure is illustrated on a specific example.

6.1.1 Target and Boundary Conditions

With respect to the tungsten target, in which the hydrogen isotope exchange is simulated, some assumptions are required. As shown in chapter 4, the implantation of energetic deuterium at low temperature leads to severe blistering of the tungsten samples. Moreover, it is anticipated that those blisters rupture during the initial deuterium implantation. It is shown in reference [152] that blisters generated under the same implantation conditions as in the here-performed experiments are located in a depth up to approximately 200 nm. In addition, the presence of those ruptured blisters leads to the re-emission of the implanted deuterium from the sample and reduces the transport of deuterium into the bulk considerably. Since TESSIM-X is a one-dimensional diffusion trapping code, the implementation of three-dimensional objects such as blisters is not possible.

However, in order to account for these effects in the simulation, the sample is approximated as a slab with a finite thickness of 200 nm and discretized with a grid of a step width of 1 nm. Since the blister depth depends on the grain orientation with respect to the surface, it would be more reasonable for a polycrystalline sample to model different thicknesses weighted according to the distribution function of the blister depth. However, since representative information of the blister depth distribution is not available and to keep an acceptable computation time, a single slab with a thickness of 200 nm is chosen. Furthermore, the simulation of a slab ignores the fact that despite the presence of blisters some hydrogen can migrate into the bulk, as can be observed from the deuterium depth profiles in reference [152]. Yet, based on the considerably higher defect concentration and the lower temperatures at which the hydrogen isotope exchange experiments are performed, it is questionable if significant transport of hydrogen isotopes beyond the depth of the blisters occurs. By comparing the deuterium depth profiles after the Ramp & Hold and before the hydrogen isotope exchange experiments in figure 5.6 with the depth of the blisters, this seems not to be the case. Thus, the simulation of a slab with a thickness of 200 nm seems reasonable.

On the front and rear side of the sample slab diffusion-limited boundary conditions are applied which pin the solute hydrogen concentration to zero, i.e. $C^S_{H,D}(0,t) = C^S_{H,D}(x_{max},t) = 0$. This approximation neglects surface reactions such as the recombinative desorption described in the Langmuir-Hinselwood process [100]. Yet, it needs to be evaluated if such surface reactions are relevant at temperatures down to 150 K and in the presence of an energetic deuterium or protium ion beam which effectively sputters hydrogen isotopes from the surface region.

6.1.2 Diffusion

The diffusion coefficient of solute protium in tungsten derived by Frauenfelder [23], with an energy barrier for diffusion of $E_H^{\mathrm{Diff}} = 0.39\,\mathrm{eV}$ and a pre-exponential factor of $D_{0,H} = 4.1 \times 10^{-7}\,\mathrm{m^2s^{-1}}$, is commonly used. However, it is assumed that the diffusion of hydrogen obtained for temperatures lower than 1500 K is influenced by trapping and does not represent the solute diffusivity. A recent evaluation of Frauenfelder's data by Heinola et al. [89], taking only the data at higher temperature into account, yields a diffusion energy barrier of $E_H^{\mathrm{Diff}} = 0.25\,\mathrm{eV}$ and a pre-exponential factor of $D_{0,H} = 1.58 \times 10^{-7}\,\mathrm{m^2s^{-1}}$.

These values are used to model the protium diffusion in tungsten for the present experiments. The diffusion parameters of deuterium in tungsten are derived by dividing the pre-exponential factor $D_{0,H}$ by the square-root of the isotopic mass ratio of deuterium and protium, resulting in $D_{0,D} = 1.12 \times 10^{-7}\,\mathrm{m^2s^{-1}}$. The energy barrier for diffusion is assumed to be equal for both isotopes, $E_H^{\mathrm{Diff}} = E_D^{\mathrm{Diff}} = 0.25\,\mathrm{eV}$. Furthermore, a concentration dependence of the diffusivity is not considered, neither is the effect of site-blocking taken into account [90]. Tunneling effects, which might be present at temperatures below 200 K [89], are beyond the scope of TESSIM-X and are not considered.

6.1.3 Implantation

In order to simulate the implantation of the hydrogen isotopes into the sample, a volume source term for solute deuterium, $S_D\,(x,t)$, and protium, $S_H\,(x,t)$, is implemented in TESSIM-X. SDTrimSP [66, 67] is used to generate the implantation profiles by simulating hydrogen isotopes of an energy of 3.0 keV/(H,D) impinging under normal incidence on a pure tungsten target. For these simulations 10^6 projectiles are calculated with the detailed parameters given in appendix A.2. The source distribution functions $\zeta_D\,(x)$ and $\zeta_H\,(x)$ are determined by fitting the area-normalized implantation profiles with a Gaussian function, as shown in figure 6.1. For protium and deuterium maxima at depths of 25 and 28 nm and standard deviations of 17 and 19 nm are obtained, respectively. Dynamic effects like the evolution of the implantation profiles towards larger depth, caused by a decrease of the stopping power as the hydrogen concentration increases, are not considered in the TESSIM-X simulations. The flux of the irradiated hydrogen isotopes is set to $8.4 \times 10^{17}\,\mathrm{(H,D)\,m^{-2}s^{-1}}$ with a reflection coefficient of 0.27 and 0.24 for deuterium and protium, respectively.

6.1.4 Trapping and Thermally Activated De-trapping

As already pointed out before, at least two microscopic trap types, i.e., vacancies and dislocations are present in the sample. However, in order to limit the number of parameters in the simulation to a reasonable value, some simplifying assumptions regarding the trap types as well as the trapping and de-trapping parameters are required. In case of the fill-level model only one trap type i with k_{max} different levels is considered. When the classical model is applied, N_T different trap types with equal trap concentration are used. Due to the multiple occupancy of the traps in the fill-level picture the total trap concentration is k_{max} times lower than in the classical model in order to obtain the same hydrogen retention capability. When both models are compared the number of fill levels equals the number of different trap types, i.e., $k_{max} = N_T$, which is considered as a free parameter to model the experimental data.

The depth profile of the hydrogen retention capability used as input for the simulations is based on the deuterium depth profile measured after deuterium

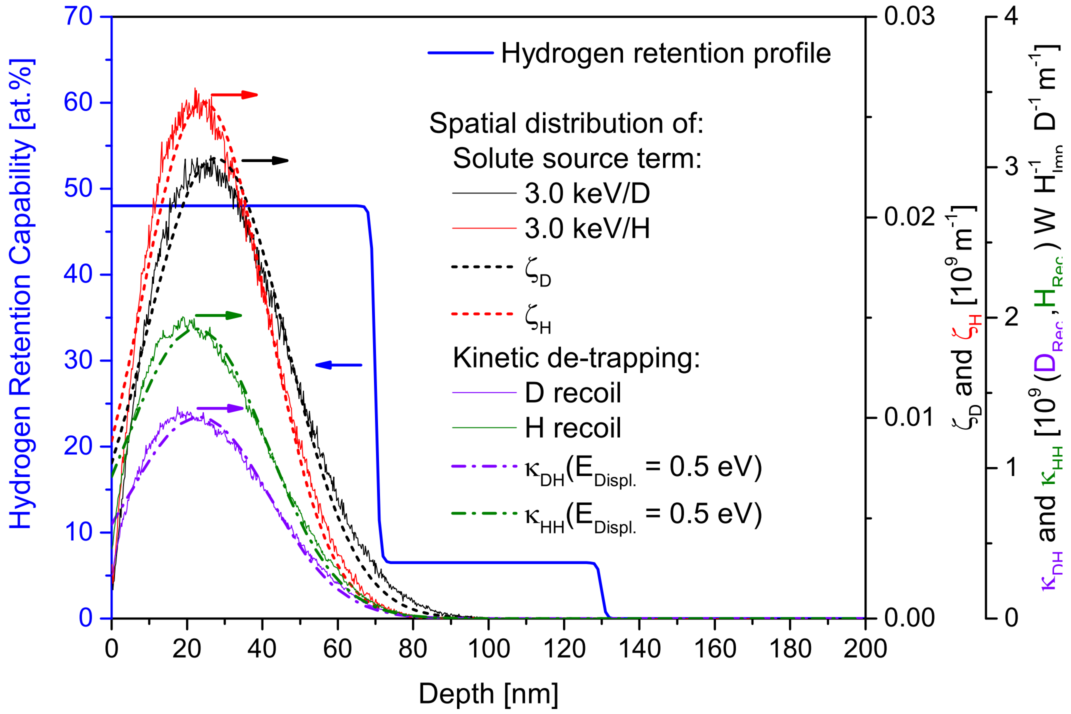

Figure 6.1: TESSIM-X inputs: Depth profile of the hydrogen retention capability (solid blue line). Area-normalized implantation profiles of protium and deuterium into tungsten with an energy of 3.0 keV/(H,D) under normal incidence calculated by SDTrimSP (solid black and red line). Gaussian fits of the implantation profiles to obtain the spatial distribution of the solute hydrogen source terms ζ_D and ζ_H (dashed black and red line). Deuterium and protium recoil profiles created by protium implantation into tungsten containing 20 at.% of the respective hydrogen isotope, calculated for a displacement energy of 0.5 eV by SDTrimSP (solid purple and green line). The profiles are divided by the hydrogen concentration and the number of implanted protium atoms. Gaussian fits of the processed recoil profiles to determine the spatial distribution of the kinetic de-trapping terms κ_{DH} and κ_{HH} (dash-dotted purple and green line).

implantation and hold at 150 K, depicted in figure 5.6, and consists of two steps as shown in figure 6.1. The first step is capable of retaining hydrogen up to a concentration of 48 at.% and a depth of 70 nm from the surface. The second step yields a maximum retainable hydrogen concentration of 6.5 at.% at a depth between 70 and 130 nm. Furthermore, an intrinsic hydrogen retention capability with a concentration of 1×10^{-4} at.% in the bulk is assumed. Compared with the measured deuterium depth profile a 12 % higher concentration is assumed to account for the loss of deuterium between the end of the implantation and the measurement of the depth profile.

It is necessary to mention that the depth profile of the hydrogen retention capability does not directly correspond to the trap distribution. In case of the fill-level model the profile in figure 6.1 needs to be divided by the number of fill levels to gain the depth profile of the trap. The same holds for the classical model, in which the profile is divided by the number of different trap types to obtain the depth profile of an individual trap type. A dynamic evolution of the trap depth profile is not considered [98]. The traps are assumed to be present in the sample from the beginning on and are merely filled during the initial deuterium implantation. This seems a reasonable assumption, since in all experiments presented in chapter 5 the samples are implanted with deuterium until saturation before the protium implantation is conducted.

Apart from the number of traps and their depth profiles, also assumptions with respect to the trapping and de-trapping itself are made, independent of the applied model. The concept of activated trapping, i.e., an additional energy barrier between solute and trap site, is not applied. The transition rate from a solute site to trap site equals that between solute sites. The release of hydrogen atoms from a certain trap type or fill level to the solute is an Arrhenius-like process as described by equations (3.4) and (3.9). The attempt frequency $\nu_{H,D}^{TS}$ is commonly approximated by the Debye frequency of tungsten which is in the order of $1 \times 10^{13}\,\mathrm{s}^{-1}$ and in good agreement with recent DFT calculation of the attempt frequency [61]. In the here-conducted simulations it is assumed that every fill level or trap type is characterized by the same attempt frequency, independent of the considered hydrogen species and the de-trapping energy, i.e., $\nu_H^{TS} = \nu_D^{TS} = 1 \times 10^{13}\,\mathrm{s}^{-1}$. The de-trapping energies of the fill levels k or trap types i are kept as free parameters with the restriction that $E_{H,i,k}^{TS} = E_{D,i,k}^{TS}$.

6.1.5 Kinetic De-trapping

As discussed in chapter 5, the kinetic release of trapped hydrogen isotopes by the impinging protium ion beam within the implantation zone must not be neglected. In TESSIM-X this kinetic de-trapping can be taken into account by the temperature-independent de-trapping terms $\epsilon_{AB,i}\left(x,t\right)$ and $\epsilon_{AA,i}\left(x,t\right)$ given by equation (3.5). The spatial distribution of this terms can be approximated by the recoil profiles calculated by SDTrimSP. Since the focus of the here-presented experiments is on the hydrogen isotope exchange of deuterium by protium, only the hydrogen recoils generated during the protium implantation are considered. The impinging protium atoms collide with trapped deuterium and protium atoms alike, thus the recoil profiles for both isotopes need to be simulated with SDTrimSP. Another aspect is that the shape of the hydrogen recoil profiles depends on the hydrogen concentration present in the tungsten sample, as can be seen in figure 5.17. This effect cannot be included in TESSIM-X. Instead the recoil profiles of protium and deuterium are approximated by SDTrimSP calculations assuming a concentration of 20 at.% of the respective isotope. The implantation of protium atoms with an energy of 3.0 keV/H under normal incidence on the surface of the target is simulated with SDTrimSP using 10^5 projectiles and the parameters given in appendix A.3. In order to take the dependence of the recoil generation on the de-trapping energy of the fill level or the trap type into account, the required displacement energy is varied from 0.3 to 2.0 eV in steps of 0.1 eV. The calculated sets of protium and deuterium recoil profiles are divided by the number of implanted protium atoms and the concentration of the respective isotope. Subsequently, these profiles are fitted by a Gaussian function in order to obtain a parametrization of the spatial distribution of the kinetic de-trapping as a function of the de-trapping energy of the different fill levels or trap types. In case of kinetic de-trapping of deuterium by protium the parametrized spatial distribution is given by

$$\kappa_{DH,i,k}\left(x, E^{TS}_{D,i,k}\right) = \\ 6.88 \times 10^{8}\,\mathrm{m}^{-1}\,\left(E^{TS}_{D,i,k}\,[\mathrm{eV}]\right)^{-0.959} \exp\left(-\left(\frac{(x\,[\mathrm{nm}] - 23.1)}{26.5}\right)^{2}\right) \tag{6.1}$$

and in case of protium by protium it yields

$$\kappa_{HH,i,k}\left(x, E^{TS}_{H,i,k}\right) = \\ 1.01 \times 10^{9}\,\mathrm{m}^{-1}\,\left(E^{TS}_{H,i,k}\,[\mathrm{eV}]\right)^{-0.929} \exp\left(-\left(\frac{(x\,[\mathrm{nm}] - 22.4)}{26.5}\right)^{2}\right). \tag{6.2}$$

These parametrized profiles are finally used as input for the TESSIM-X simulations. The deuterium and protium recoil profiles calculated with SDTrimSP and the corresponding Gaussian fits are illustrated in figure 6.1 for a displacement energy of 0.5 eV exemplarily. As can be seen, the generation rate of protium recoils is higher than that of deuterium recoils due to a more efficient energy transfer in protium-protium collisions than in protium-deuterium collisions.

6.1.6 Modeling Procedure

According to the conclusion drawn in chapter 5 the experimental hydrogen isotope exchange data is modeled in the framework of the classical and the fill-level model, both with and without taking the kinetic de-trapping mechanism into account. Thus, in total four different scenarios are simulated and evaluated for each conducted experiment. The modeling with TESSIM-X requires the simulation of the whole experimental cycle as illustrated exemplarily in figure 6.2 for the case of hydrogen isotope exchange conducted at 150 K after Ramp & Hold to 290 K. This includes (a) the initial deuterium implantation phase, (b) the Ramp & Hold phase and finally (c) the protium implantation and the hydrogen isotope exchange phase. The rest phases of 10000 and 1000 s after the deuterium implantation and the Ramp & Hold phases allow the system to reach an equilibrium state. In all phases the implanted flux, the retention and the desorption rate are simulated for both hydrogen isotopes.
Before the actual hydrogen isotope exchange experiments can be simulated the de-trapping energies of the different fill levels or trap types, which are

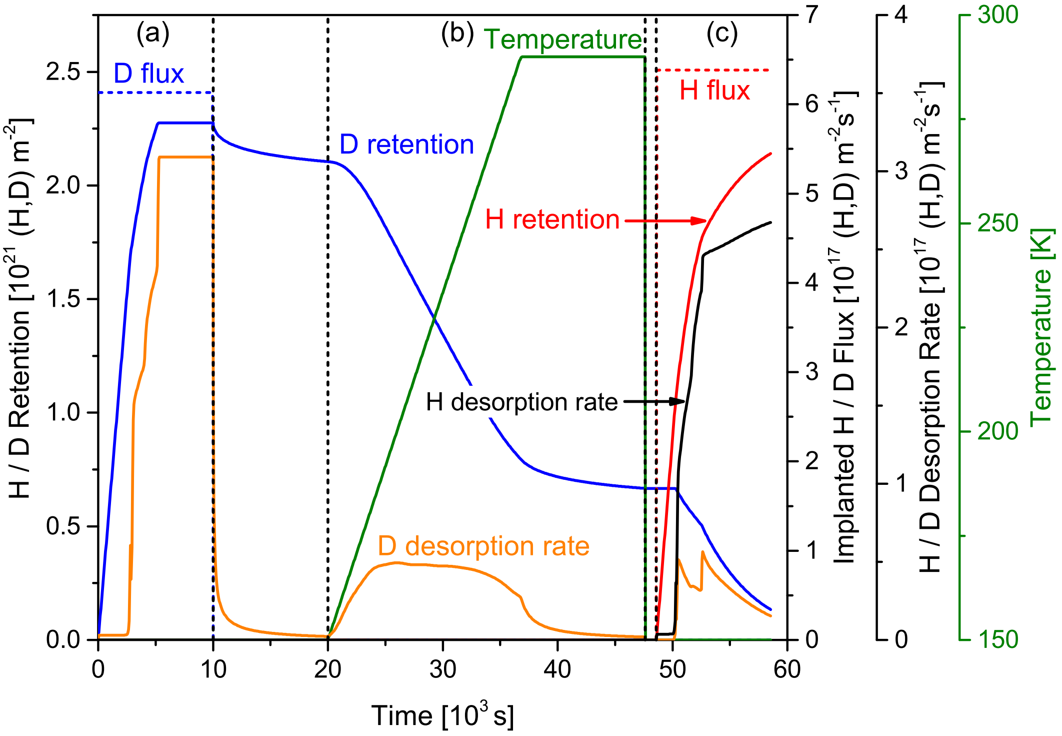

Figure 6.2: TESSIM-X simulation sequence shown exemplarily for hydrogen isotope exchange conducted at 150 K after Ramp & Hold to 290 K. (a) Deuterium implantation phase, (b) Ramp & Hold phase, (c) hydrogen isotope exchange phase. (a) and (b) are followed by a rest phase of 10000 and 1000 s, respectively.

free parameters, need to be determined. This is achieved by modeling the deuterium desorption rate spectra and the retention during the Ramp & Hold experiments to different temperatures. Since no ion implantation takes place in the Ramp & Hold phase, this modeling is conducted without applying the kinetic de-trapping mechanism. As no optimization algorithm is implemented in TESSIM-X yet, the number of trap types or fill levels with their de-trapping energies are adjusted manually. Starting with the trap type or fill level of the lowest de-trapping energy, further trap types or fill levels are consecutively added and their de-trapping energy is chosen such to reproduce the experimental data best. The so obtained de-trapping energies are then used to simulate the hydrogen isotope exchange after Ramp & Hold to different temperature, at different temperature and in between two Ramp & Hold cycles.

6.2 Modeling Results

6.2.1 De-trapping Energies of Trap Types and Fill Levels

The TESSIM-X modeling results of the experimental Ramp & Hold data from figures 5.3 to 5.5 for 200, 250 and 290 K in the classical and the fill-level framework are shown in figure 6.3. For the simulation 11 trap types or fill levels are required with the de-trapping energies listed in table 6.4. The maximum sample temperature reached in the Ramp & Hold experiments is 290 K. At this temperature approximately 36 % of the initially retained deuterium is still remaining in the sample. Since data for higher temperatures is not yet available, no de-trapping energies can be assigned to the trap types or fill levels in which the remaining deuterium is trapped. Consequently, some reasonable de-trapping energies, given by the first three entries in table 6.4, are assumed. The only constraint is that the energies are large enough to prevent deuterium release at 290 K. The application of 11 different fill levels is in agreement with recent DFT calculations [61] suggesting even 12 hydrogen atoms per vacancy. As can be seen from figure 6.3 (a), the classical and the fill-level model reproduce the deuterium desorption rate during the different Ramp & Hold experiments very well. Even the exponential decrease of the desorption rate during the hold phases fits nicely to the experimental data. However, one feature of the experimental spectra which is insufficiently reproduced is the steep rise of the desorption rate at the beginning of the temperature ramp and the first shoulder after approximately 24 min, corresponding to a temperature of 162 K. In figure 6.3 (b), the experimental deuterium retention and the corresponding TESSIM-X simulations during the different Ramp & Hold experiments are compared. The decrease of the deuterium retention in the ramp phase and the subsequent leveling in the hold phase are reproduced by the simulations for both models. However, the simulation of the Ramp & Hold experiment to 200 K overestimates the final deuterium retention, while in the case of 290 K it is slightly underestimated. Furthermore, it can be seen that the simulated deuterium retention in the case of the fill-level model is minimally but systematically smaller compared with the classical model. This effect is caused by a higher de-trapping rate in the fill-level model compared to the classical model. Thus, in order to reproduce the experimental data, the de-trapping energies of the fill levels are approximately 0.03 eV higher than those of the trap types in the classical model, as can be seen from table 6.4. The reason for the increased de-trapping can be found by comparing equations (3.4) and (3.9). In case of the classical model, the de-trapping rate is proportional to the concentration of hydrogen trapped in trap type i, given by $C^T_{A,i}$. In the most extreme case all traps of type i are filled, resulting in $C^T_{A,i} = \eta_i$. For the fill-level model the de-trapping rate is proportional to the concentration of hydrogen occupying the fill level k i.e. $C^T_{A,i,k}$. Filling all traps to level k corresponds to $C^T_{A,i,k} = k\,\eta_i$. Consequently, for this scenario $C^T_{A,i,k} = k\,C^T_{A,i}$ holds, which results in a k times higher de-trapping rate in the fill-level model

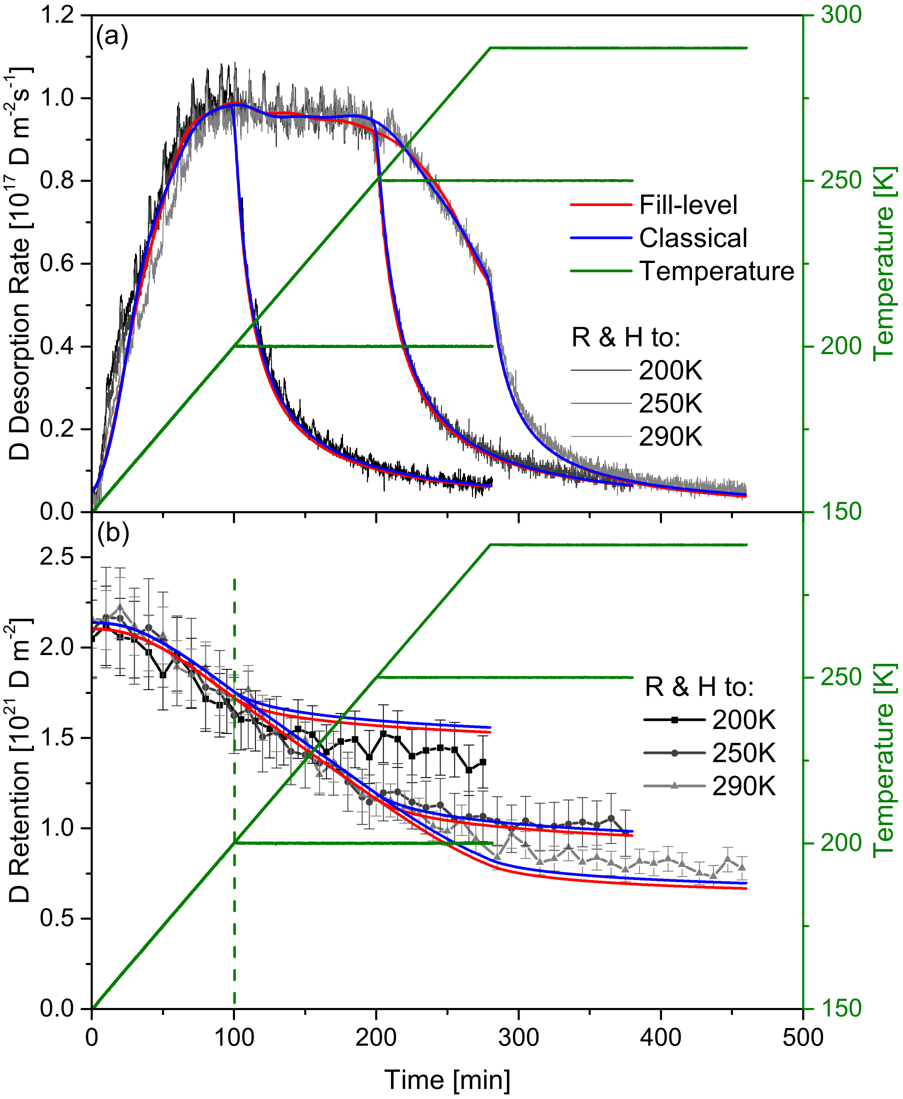

Figure 6.3: TESSIM-X modeling of (a) the experimental deuterium desorption rate and (b) the deuterium retention during the Ramp & Hold experiments to 200, 250 and 290 K, shown in figures 5.3 to 5.5, with the classical and the fill-level model.

i, k	1	2	3	4	5	6	7	8	9	10	11
Classical model:											
E_i^{TS} [eV]	1.60	1.59	1.58	0.83	0.735	0.675	0.63	0.58	0.53	0.485	0.43
Fill-level model:											
E_k^{TS} [eV]	1.60	1.59	1.58	0.85	0.763	0.71	0.66	0.61	0.56	0.512	0.45

Figure 6.4: De-trapping energies, E_i^{TS} and E_k^{TS}, of trap types and fill levels determined by the TESSIM-X simulations shown in figure 6.3.

compared to the classical model.

6.2.2 Exchange after Ramp & Hold to Different Temperatures

The derived de-trapping energies are finally used to model the exchange of deuterium by protium after Ramp & Hold to different temperatures. In figure 6.5 the experimental data from figure 5.7 is compared to the TESSIM-X simulations within the framework of (a) the fill-level and (b) the classical model, each with and without considering the kinetic de-trapping mechanism. In order to obtain the deuterium retention as a function of implanted protium fluence, the implanted protium flux is multiplied with the implantation time.

By applying the fill-level model without considering the kinetic de-trapping mechanism, shown as dashed lines in figure 6.5 (a), some of the experimental observations are qualitatively and partially quantitatively reproduced, while others are insufficiently described. The initial deuterium retention at the beginning of the protium implantation is well reproduced by the TESSIM-X simulations for all conducted experiments. Furthermore, the experimental observation of a critical protium fluence, which needs to be implanted in order to initiate the decrease of the deuterium retention when Ramp & Hold is performed before the exchange, is also observed in the simulated data. Even the increase of the critical protium fluence as a function of the final temperature reached in the preceding Ramp & Hold phase is correctly described. In addition, the final amounts of deuterium remaining in the sample after the protium implantation is finished fit to the experimentally obtained values.

However, some features of the experimental data are insufficiently reproduced by the simulations. In the case where no Ramp & Hold is conducted and the sample temperature is just held at 150 K, the experimentally observed decrease of the deuterium retention after implantation of the first incremental protium fluence is not reproduced. Yet, the largest discrepancy between the simulations and the experimental data can be found in the decrease of the deuterium retention itself. In all cases the TESSIM-X simulation underestimates the decrease of deuterium retention at the beginning of the protium implantation and overestimates it towards the end. Furthermore, in the decreasing part of the simulated deuterium retention curve a kink, which is due to the additional effusion of deuterium from the rear side of the sample, is observed. The position of the kink, indicated by dotted red circles, depends on the final temperature reached in the Ramp & Hold cycle, i.e., the lower the temperature, the lower the implanted protium fluence at which the kink occurs. A comparison of the decrease of the deuterium retention for protium fluences larger than the one which corresponds to the kink, shows a similar exponential decrease in all simulated cases. This observation is in good agreement with the results obtained with the urn model for fill-level traps in chapter 5. Repeating the simulations and taking the kinetic de-trapping of hydrogen isotopes by the

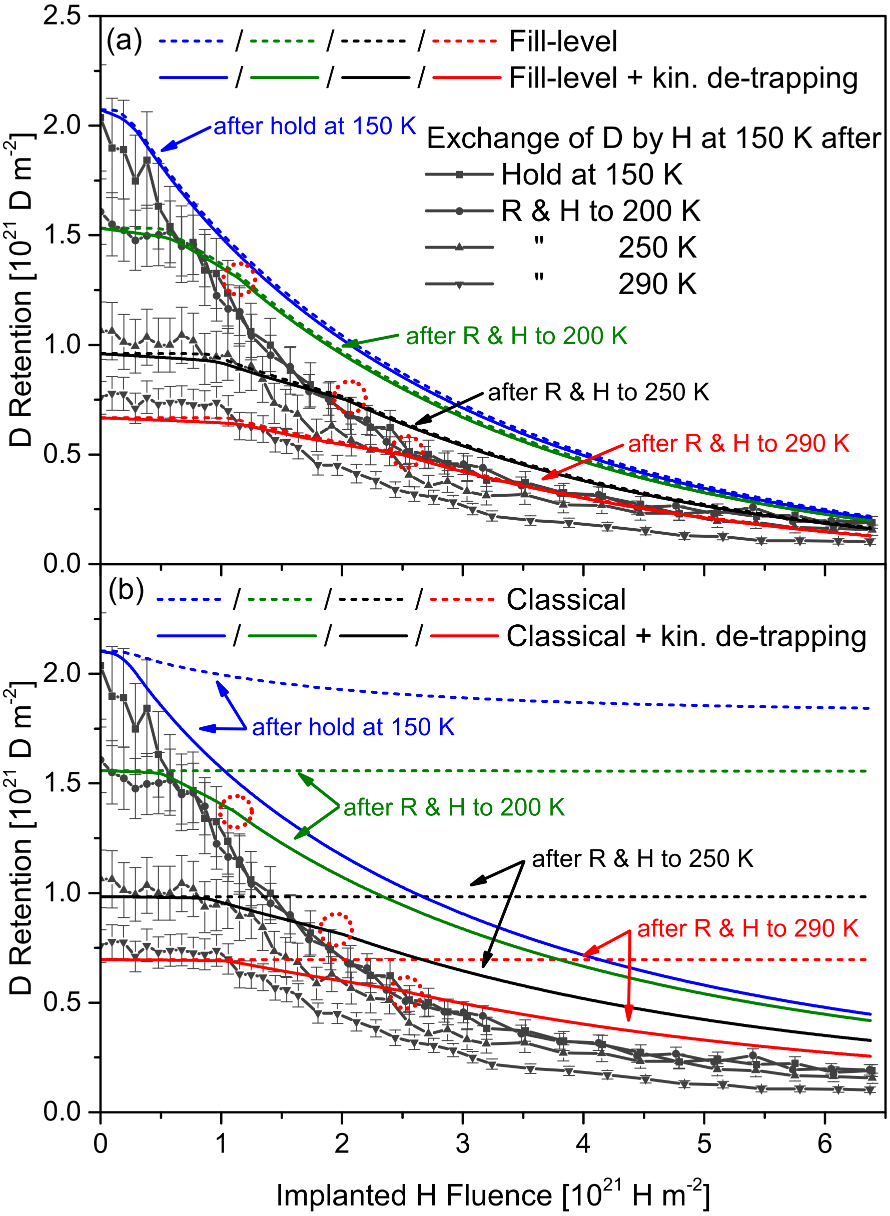

Figure 6.5: Comparison of TESSIM-X simulations and experimental data of deuterium exchanged by protium at 150 K after holding at 150 K and Ramp & Hold to 200, 250 and 290 K, shown in figure 5.7. Simulations are performed by applying (a) the fill-level and (b) the classical model, both with and without considering the kinetic de-trapping mechanism.

protium ion beam into account hardly changes the results. The only minor difference is that the deuterium retention decreases slightly before the critical protium fluence is implanted. Once the critical protium fluence is exceeded, the deuterium retention decreases equally in both cases.

In the case of the classical model without taking the kinetic de-trapping into account, shown as dashed lines in figure 6.5 (b), the experimental data cannot be reproduced at all. Only a slight decrease of the deuterium retention during the protium implantation is observed when the sample temperature is merely held at 150 K. At this temperature the traps with de-trapping energies of 0.43 and 0.485 eV release deuterium to the solute. When no protium is present in the sample, the de-trapped deuterium can be recaptured by the empty traps, resulting in slow effusion of deuterium from the sample. However, during the protium implantation a considerable amount of protium solute is present in the sample. Traps which released deuterium have therefore a higher probability to capture protium from the solute rather than the released deuterium. Hence, the presence of protium reduces the available amount of empty traps to recapture deuterium, which leads to a lower trapping rate of deuterium. The deuterium, which is effectively forced to stay in the solute, finally effuses from the sample, leading to a reduction of the deuterium retention. When all traps which are active at 150 K lost their deuterium and the deuterium solute is released from the sample the deuterium retention converges to a constant value. If Ramp & Hold to 200, 250 and 290 K is performed before protium is implanted at 150 K, no decrease in the deuterium retention is observed. This is expected since the traps which could de-trap deuterium at 150 K have already released their deuterium in the preceding Ramp & Hold cycle.

The situation is quite different when the kinetic de-trapping of hydrogen isotopes by the impinging protium ion beam is taken into account. As can be seen from the solid lines in figure 6.5 (b), the deuterium retention remains nearly constant in the beginning of the protium implantation. Once a certain critical implanted protium fluence is exceeded, a decrease in the deuterium retention is observed. Furthermore, the higher the sample temperature which is reached in the Ramp & Hold phase, the higher the protium fluence which needs to be implanted to trigger the decrease of deuterium retention. In the cases where Ramp & Hold is conducted before the exchange, the TESSIM-X simulation reproduces the measured critical protium fluence, at which the decrease sets in, very well. However, the experimentally observed immediate decrease of the deuterium retention when the sample is only held at 150 K is not described by the simulation. Here also a small critical protium fluence is required before the decrease of the deuterium retention begins. While the critical protium fluence is reproduced by the simulations, the rate at which the deuterium retention decreases is not. Compared to experimental data, the decrease of the deuterium retention per implanted protium fluence is less pronounced in the simulation. Furthermore, the amount of deuterium retained in the sample at the end of the protium implantation is overestimated by the simulations. Similar to the simulations based on the fill-level model, a kink in the decreasing part of the deuterium retention curve is observed, marked by dotted red circles in figure 6.5 (b). In addition, the exponential decrease of the deuterium retention for protium fluences larger than the one associated with the kink is comparable in all four TESSIM-X simulations.

6.2.3 Exchange at Different Temperatures

In figure 6.6 the measured deuterium retention during the isotope exchange of deuterium by protium at 150, 200, 250 and 290 K after warm-up and hold at 290 K for 114 h is compared to TESSIM-X simulations applying (a) the fill-level and (b) the classical model, both with and without considering the kinetic de-trapping mechanism.

The TESSIM-X simulations based on the fill-level model with and without the kinetic de-trapping, shown in figure 6.6 (a), reproduce the experimental data only qualitatively. The experimentally observed reduction of the critical protium fluence as well as the stronger decrease of the deuterium retention when the isotope exchange is conducted at higher temperatures is described by the simulations. Furthermore, the latter one is qualitatively in good agreement with the results obtained with the simple urn model for fill-level traps in chapter 5. In addition, it can be seen that the simulated deuterium retentions exhibit a kink in the decreasing part of the curve, which indicates, similar to the TESSIM-X simulations in figure 6.5, the additional effusion of deuterium from the rear side of the simulated tungsten slab. The higher the temperature at which the protium implantation is performed, the lower the implanted protium fluence at which the kink occurs.

Quantitatively, the TESSIM-X simulations overestimate the deuterium retention in all experiments shown in figure 6.6. The simulated initial deuterium retention at the beginning of the isotope exchange is slightly higher than the measured one. Furthermore, for the isotope exchange at 150 and 200 K the critical protium fluence, which needs to be implanted to cause a decrease of the deuterium retention, is overestimated in the simulation. The reproduction of the measured exponential decrease of the deuterium retention by the simulation is best for the isotope exchange conducted at 290 K and becomes worse for lower temperatures. The final deuterium retention fits best for the exchange performed at 200 and 290 K and is over- and underestimated for 150 and 250 K, respectively. Similar to the results in figure 6.5 (a), the consideration of the kinetic de-trapping mechanism in the framework of the fill-level model has only a minor effect on the simulation results. Merely the deuterium retention before the critical protium fluence is exceeded shows a slight decrease.

When the classical model without kinetic de-trapping is applied to simulate the experimental data, no significant decrease of the deuterium retention occurs, as can be observed from the dashed lines in figure 6.6 (b).

Including the kinetic de-trapping mechanism in the classical model, indicated

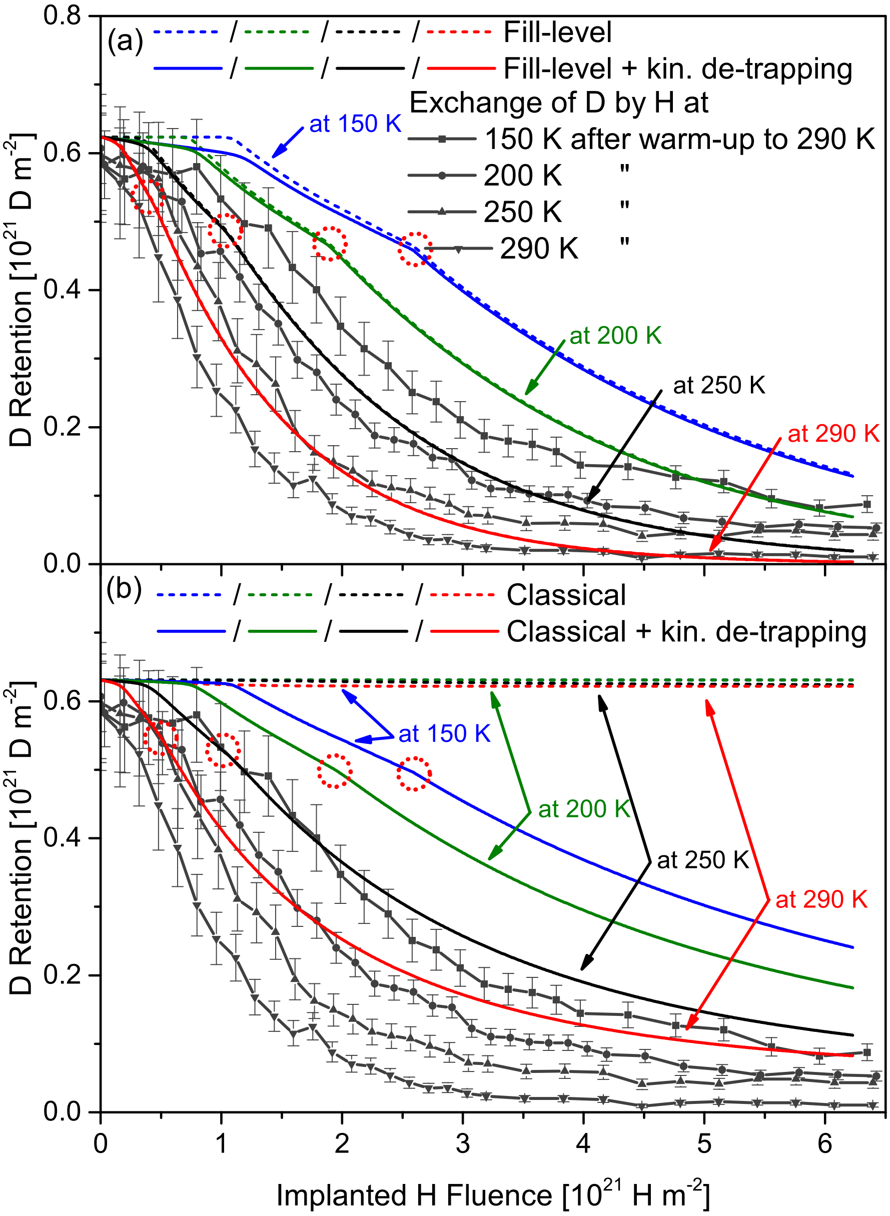

Figure 6.6: Comparison of the TESSIM-X simulations with the experimental data of the exchange of deuterium by protium at 150, 200, 250 and 290 K after warm-up and hold at 290 K for 114 h, illustrated in figure 5.9. Simulations are performed by applying (a) the fill-level and (b) the classical model, both with and without considering the kinetic de-trapping mechanism.

by the solid lines in figure 6.6 (b), the obtained simulation results are very similar to those determined with the fill-level model with and without kinetic de-trapping. The experimental data is again reproduced qualitatively. The dependence of the critical protium fluence on the temperature at which the isotope exchange is performed is correctly described. Moreover, the experimentally observed stronger decrease of the deuterium retention for increasing exchange temperatures is also reproduced by the TESSIM-X simulations. In accordance with the fill-level simulations, shown in figure 6.6 (a), the decreasing part of deuterium retention curve possesses a kink. From a quantitative perspective, the initial deuterium retention is overestimated analogue to the simulations conducted with the fill-level model. Also the final deuterium retention in the simulations are higher compared with the experimentally obtained values and the fill-level-based simulations. Furthermore, the rate at which the deuterium retention decreases is underestimated by the simulations for all exchange temperatures.

6.2.4 H Implantation between Two Ramp & Holds

Figure 6.7 compares the deuterium desorption rate measured during the second Ramp & Hold cycle to 290 K with and without prior protium implantation at 150 K, depicted in figure 5.11, with the simulation results of TESSIM-X. The results applying the fill-level and the classical model, with and without the kinetic de-trapping mechanism are shown in (a) and (b), respectively.

When no protium implantation is performed before the second Ramp & Hold cycle, all four models provide very similar results. This is expected, since no kinetic de-trapping can occur in the absence of an energetic protium ion beam. Consequently, the dashed and solid red lines in figure 6.7 (a) and (b) lie on top of each other. Furthermore, the de-trapping energies of the fill levels and trap types are specifically chosen to reproduce the deuterium desorption rate spectra, shown in figure 6.3 (a), best. In general, the TESSIM-X simulations for no intermediate protium implantation agree well with the experimental data of the second Ramp & Hold cycle. The experimentally observed delayed onset of the deuterium desorption at 68 min and the subsequent increase is sufficiently well reproduced. The only mismatch, independent of the applied model, is a small shift of the low temperature edge of the simulated deuterium desorption rate spectra towards lower temperatures with respect to the experimental one.

In the case where protium implantation is conducted in between the two Ramp & Hold cycles, the experimental data show substantial deuterium desorption already at the beginning of the second Ramp & Hold cycle and a lower maximum of the desorption rate. By applying the fill-level model without kinetic de-trapping, shown in figure 6.7 (a) as dashed blue line, the desorption of deuterium at the beginning of the temperature ramp as well as the lower maximum of the deuterium desorption rate can be reproduced. The release of deuterium occurring at low temperatures could be attributed to the filling of the traps

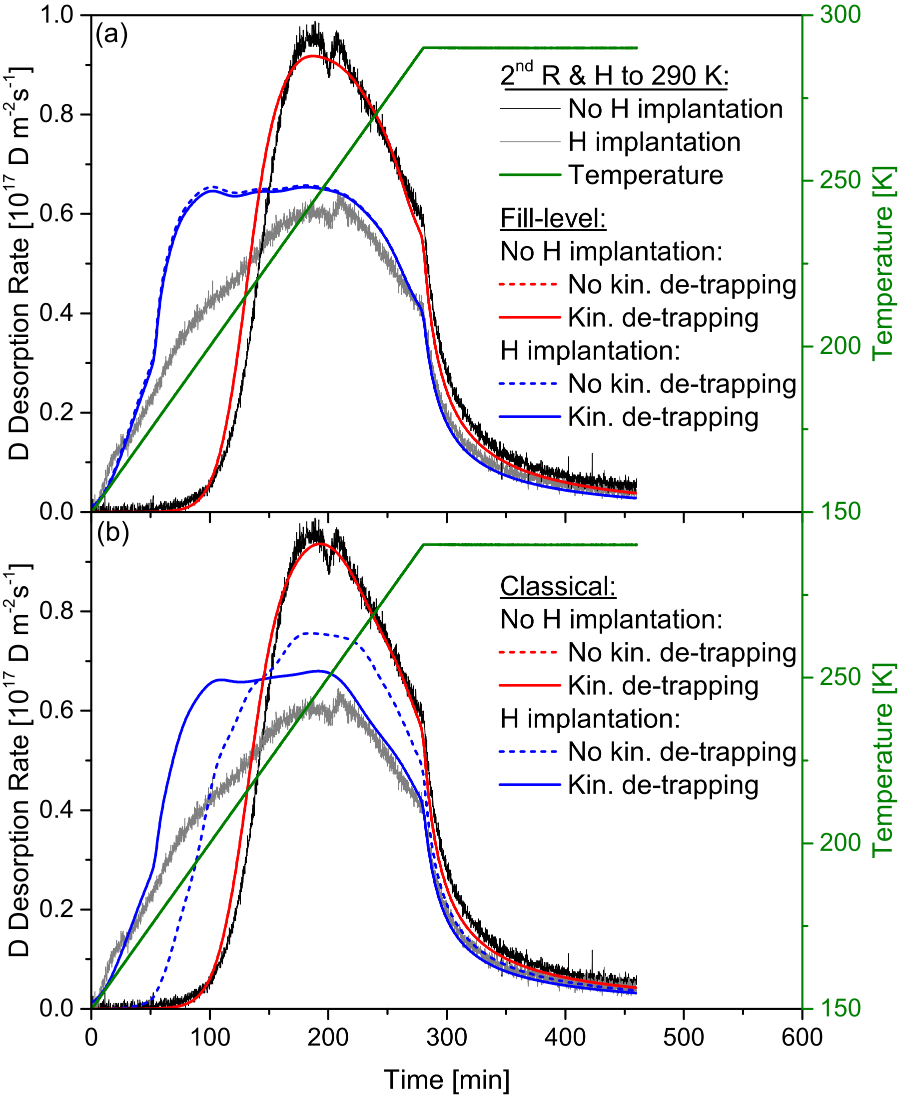

Figure 6.7: Comparison of the TESSIM-X simulations with the measured deuterium desorption rate of the second Ramp & Hold cycle to 290 K with and without prior protium implantation at 150 K, shown in figure 5.11. Simulations are performed by applying (a) the fill-level and (b) the classical model, both with and without considering the kinetic de-trapping mechanism.

with protium, leading to an increase of the fill level of the traps and reducing the required de-trapping energy. The lower maximum deuterium desorption rate is a consequence of this effect, since deuterium released at lower temperature is no longer available to be released at higher temperatures. A significant deviation of the simulated and the experimental spectrum is observed at approximately 50 min. The steep rise of the simulated deuterium desorption rate is the result of the additional deuterium effusion from the rear side of the 200 nm thick sample. Furthermore, the additional kinetic de-trapping has only little influence on the deuterium desorption rate spectrum simulated with the fill-level model.

When the classical model without kinetic de-trapping is applied to simulate the deuterium desorption rate during the second Ramp & Hold cycle with prior protium implantation, shown as dashed blue line in figure 6.7 (b), the deuterium desorption starts earlier compared with the case where no protium implantation is conducted. However, in contrast to the simulations based on the fill-level model, the deuterium release starts not immediately but after approximately 35 min. Furthermore, the maximum of the deuterium desorption rate is reduced compared to the case where no protium implantation is performed. Yet, it is still higher compared to the case where protium implantation is conducted in the fill-level model. These results can be explained as follows: After the first Ramp & Hold cycle to 200 K the traps with a de-trapping energy of 0.43, 0.485 and 0.53 eV are almost fully depopulated and half of the traps with a de-trapping energy of 0.58 eV have released their deuterium as well. A protium implantation conducted in the framework of the classical model without accounting for kinetic de-trapping at 150 K, results in the re-filling of those empty traps with protium atoms. In the beginning of the second Ramp & Hold cycle to 290 K, the traps with the lowest de-trapping energies, predominately filled with protium, release the protium to the solute. As the temperature is increased further, also the traps containing deuterium become active and release the deuterium. In the absence of protium the released deuterium can be recaptured by empty traps, resulting in a high re-trapping rate and slower transport. Consequently, the deuterium solute requires more time to reach the surface and deuterium desorption occurs later. However, in the presence of protium the empty traps can capture either protium or deuterium from the solute. If a protium is captured, the trap is occupied and unable to trap deuterium. Hence, the presence of protium effectively reduces the available amount of empty traps which leads to a lower trapping rate of deuterium and a faster transport of the solute deuterium to the surface. As a consequence the desorption of deuterium is observed earlier.

When the classical model is applied in combination with the kinetic de-trapping mechanism, the simulated deuterium desorption rate starts to increase already at the beginning of the second Ramp & Hold cycle, as can be seen in figure 6.7 (b). This behavior is in line with the experimental observation. At approximately 50 min, the simulated deuterium desorption rate increases considerably and deviates from the experimental spectrum. This feature is also observed when the fill-level model is applied, as illustrated in figure 6.7 (a), and corresponds to the release of deuterium from the rear side of the sample. Furthermore, a decrease of the maximum deuterium desorption rate is also observed in case of the classical model with kinetic de-trapping.

6.3 Discussion

Obviously, the TESSIM-X simulations applying the pure classical model do not describe the experimental observations, as can be seen from the figures 6.5 to 6.7. However, the classical model in which kinetic de-trapping is taken into account, as well as the fill-level model with and without the kinetic de-trapping mechanism provide qualitatively similar results. In order to explore the underlying reasons of this similarity, the different mechanism will be investigated separately. In the following only the classical model with the kinetic de-trapping and the fill-level model without the kinetic de-trapping are compared for the hydrogen isotope exchange experiment conducted at 150 K after Ramp & Hold to 290 K. First, the evolution of the deuterium retention during the protium implantation resolved for the different fill levels and trap types is considered, followed by the discussion of the corresponding solute and trapped deuterium depth profiles. The gained insights are transferred to interpret the results of the other isotope exchange experiments in the context of critical protium fluence and exchange cross section.

6.3.1 Evolution of D Retention

Fill-level-resolved D Retention

The temporal evolution of deuterium retained in the different fill levels as well as the total trapped amount of deuterium during the protium implantation is illustrated in figure 6.8 (a) for the fill-level model without kinetic de-trapping. At the beginning of the protium implantation approximately 70 % of the deuterium is located in traps which are filled to a level containing three deuterium atoms at a de-trapping energy of 1.58 eV. In traps of the next higher fill level, containing four deuterium atoms at a de-trapping energy of 0.85 eV, nearly 30 % are retained. Traps containing two or less deuterium atoms, as well as traps containing more than five deuterium atoms do not exist.

During the protium implantation, the traps are successively filled with protium atoms which results in an increase of the trap occupancy, i.e., the fill level, and causes a decrease of the required de-trapping energy. Consequently, as the traps transit from fill level three to four by capturing a protium atom, the deuterium amount retained in traps with fill level three decreases while it increases in traps with fill level four. This continues for higher fill levels as the protium implantation proceeds. It can be seen that the deuterium retention in the higher fill levels increases on the expense of the lower ones. For fill levels four to ten each deuterium retention curve possesses a maximum. The higher the fill level, the later is the respective maximum reached. As long as the highest fill level with a de-trapping energy of 0.45 eV is not yet reached, significant thermally activated de-trapping cannot occur. Thus, the total amount of retained deuterium is constant.

After a certain delay time with respect to the onset of the occupation of the highest fill level the decrease of the total deuterium retention occurs. It can be seen that the decrease proceeds in two stages. In the first stage, starting at approximately 1700 s, deuterium is released only through the front side of the sample, as indicated by the first vertical dash-dotted black line. In the second stage, beginning at nearly 4000 s and indicated by the second vertical dash-dotted black line, the solute deuterium has reached the rear side of the 200 nm thick simulated sample from which it effuses. As can be seen from the different slopes of the curve, the appearance of the additional loss channel leads to faster decrease in the total deuterium retention in the second stage compared with the first one. Another interesting feature in figure 6.8 (a) is the behavior of the deuterium retention in traps with the second highest fill level. Compared with the deuterium retention in traps with lower fill level it does not decrease to zero. The reason for this effect is that the thermally activated de-trapping from the highest fill level results in an increase of deuterium retention in traps with the second highest fill level.

Trap-type-resolved D Retention

Figure 6.8 (b) shows the deuterium retention in the different trap types as a function of time during the protium implantation at 150 K after Ramp & Hold to 290 K, simulated with the classical model including the kinetic de-trapping mechanism. At the beginning of the protium implantation, all traps with a de-trapping energy of 1.58 to 1.60 eV are filled with deuterium. Furthermore, approximately half of the available traps with a de-trapping energy of 0.83 eV are occupied as well. Traps of other types with lower de-trapping energy are empty.

During the protium implantation, the deuterium retained in all traps can be de-trapped kinetically by the protium ion beam and transferred to the solute. Any empty trap in the sample can capture either the freshly implanted protium or the previously released deuterium from the solute. Furthermore, the kinetic de-trapping acts on traps of any type and is independent of the sample temperature. Thus, the evolution of the deuterium retention in most of the different trap types is governed by the balance between kinetic de-trapping and re-trapping of deuterium. For the initially filled traps which require a de-trapping energy of 1.58 to 1.60 eV the deuterium retention decreases. Due to the large fraction of traps filled with deuterium compared with a small fraction of empty traps, the kinetic de-trapping outweighs the re-trapping of deuterium. The deuterium retained in traps with a de-trapping energy of 0.83 eV seems to

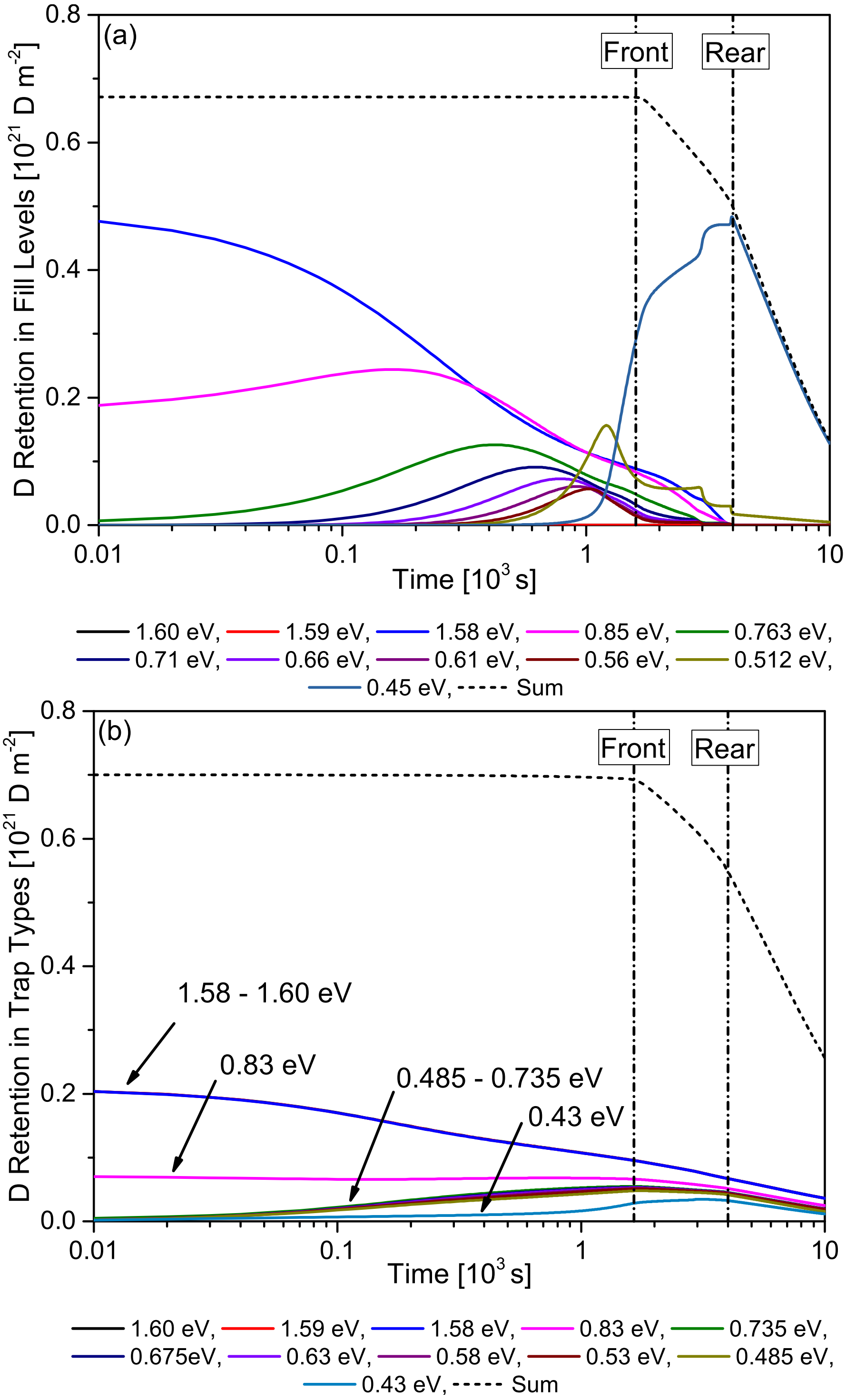

Figure 6.8: Simulation of the temporal evolution of the fill-level- and trap-type-resolved deuterium retention during the exchange of deuterium by protium at 150 K after Ramp & Hold to 290 K by applying (a) the fill-level model without kinetic de-trapping and (b) the classical model with kinetic de-trapping. The solid lines of different color represent the deuterium retained in fill levels or trap types of different de-trapping energy, the dashed black line corresponds to the total amount of trapped deuterium. The vertical dash-dotted black lines mark the effusion of the deuterium from the front and rear side of the sample, respectively.

be constant, at least as long as no deuterium is lost from the sample. Obviously, the kinetic de-trapping and the re-trapping of deuterium balance for this specific trap type. Since traps with a de-trapping energy of 0.43 to 0.735 eV are initially empty the effect of trapping deuterium is larger than the loss due to kinetic de-trapping. Consequently, the amount of deuterium retained by those traps increases until deuterium effuses from the sample. A special case are the initially empty traps possessing a de-trapping energy of 0.43 eV. In addition to the kinetic de-trapping also thermally activated de-trapping of hydrogen isotopes is significant at 150 K. Hence, the deuterium atoms captured by those traps are more likely to get de-trapped, resulting in a lower deuterium retention compared to traps with a de-trapping energy of 0.485 to 0.735 eV.

As can be observed from figure 6.8 (b), a major decrease of the total deuterium retention occurs at approximately 1700 s when the deuterium solute reaches the front side of the sample from where it effuses. At circa 4000 s a kink appears which corresponds to the effusion of deuterium from the rear side of the sample resulting in faster decrease of the total deuterium retention. The here observed two-staged decrease of the total deuterium retention is very similar to the simulation using the fill-level model shown in figure 6.8 (a). Nevertheless, some minor differences exist. For instance the higher final deuterium retention at the end of the protium implantation at 10000 s in figure 6.8 (b) compared with (a). This can be explained by the fact that the kinetic de-trapping is exclusively limited to the implantation zone in which the recoils are generated, while the release in the framework of the fill-level model applies also for the region behind.

Despite the different underlying physical models, the results regarding the total retained deuterium amount, shown in figure 6.8 (a) and (b) as dashed black lines, are very similar. In the fill-level model as well as in the classical model with kinetic de-trapping the net effect is a redistribution of tightly trapped deuterium to weakly trapped deuterium. This is achieved either by filling the traps with protium and thereby reducing the required de-trapping energy for deuterium or by kinetically de-trapping of deuterium from traps which require a high de-trapping energy and re-trapping by traps with a low de-trapping energy.

6.3.2 Evolution of D Depth Profile

The preceding investigation of the fill-level- and trap-type-resolved deuterium retention during the protium implantation provides already some insights in the differences and similarities of the respective models. However, the deuterium retention shown in figure 6.8 (a) and (b) is an integral value which does not contain the information on the spatial distribution of the deuterium in the sample. In order to gain insight into the transport behavior of deuterium during the protium implantation, the depth profiles of the trapped and solute deuterium need to be reviewed. In figure 6.9 and 6.10, the solute as well as the fill-level- and trap-type-resolved deuterium depth profiles during the protium implantation simulated with the fill-level model and the classical model with kinetic de-trapping are shown, respectively. In order to keep the number of profiles limited, the deuterium depth profiles are plotted in steps of 500 s for the first 2000 s, followed by steps of 1000 s until 4000 s and for larger times in steps of 3000 s. In addition, the position of the maximum of the protium implantation profile is indicated in the figures as vertical dashed black line.

Solute and Fill-level-resolved D Depth Profiles

For the fill-level model the solute and fill-level-resolved deuterium depth profiles are depicted in figure 6.9. **At the beginning** (black lines) of the protium implantation all deuterium is retained in traps with a fill level three or four. Neither exist traps filled to a higher or lower fill level, nor is deuterium solute present in the sample as can be seen from the top left figure.
After **500 s** (red lines) of protium implantation, the concentration of deuterium in traps with fill level three and four has decreased, with the strongest decrease coinciding with the maximum of the protium implantation profile, leading to a dip in the respective depth profiles. The occurrence of a dip at this specific depth is very plausible, since it is the position with the largest concentration of protium solute, leading to a high trapping rate of protium and an effective filling of the traps to higher fill levels. At some distance away from this position the protium solute concentration is lower, resulting in a lower trapping rate and consequently a smaller decrease of the deuterium concentration present in traps filled to level three and four. The concentration of deuterium in traps with fill level five has increased. Nevertheless, also here a small dip in the depth profile is visible. It can be seen that the concentration of deuterium in traps with fill level six to nine has increases substantially, showing a peaked depth profile. The deuterium concentration in traps with fill level ten and eleven is negligible, suggesting that the amount of introduced protium is not yet sufficient to rise the fill level of the traps to such high values. A prerequisite for the built-up of a deuterium solute concentration is the filling of the traps to a level at which thermally activated de-trapping of deuterium can occur. Since this is not yet the case, no significant amount of deuterium solute is present in the sample, as can be observed in the top left figure.
At **1000 s** (green lines) the deuterium concentration in traps with fill level three and four has decreased further. Also traps with fill level five show a reduction in the deuterium concentration. The previously peaked depth profiles of deuterium in traps with fill level six to nine show a dip, while traps with fill level ten and eleven appear with a peaked deuterium depth profile. This shows very illustratively the increase of the deuterium concentration in traps at a certain fill level on the expense of the deuterium concentration in traps filled to the level just below. Since thermally activated de-trapping from traps with fill level eleven, corresponding to a de-trapping energy of 0.45 eV, is significant at 150 K, the population of this specific fill level should lead to an

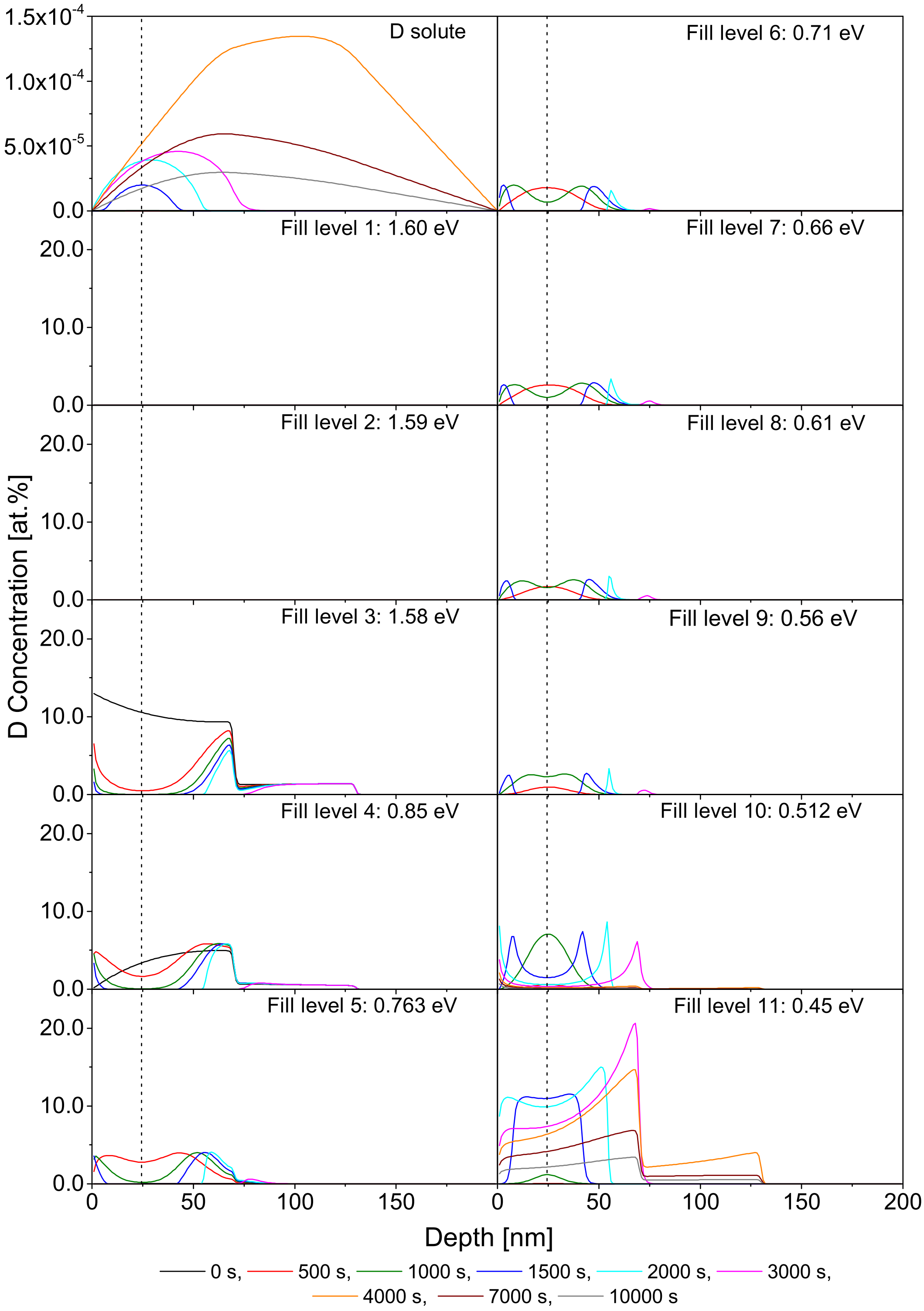

Figure 6.9: Evolution of the deuterium solute and fill-level-resolved deuterium depth profiles during the exchange of deuterium by protium at 150 K after Ramp & Hold to 290 K, simulated with the fill-level model. The maximum of the protium implantation profile is indicated by the vertical dashed black line. The scale of the deuterium concentration is the same for all figures showing different fill levels.

increase of the deuterium solute concentration. However, as can be seen from the top left figure the deuterium solute concentration is still at an insignificant low level. The reason for this is twofold. First, the deuterium concentration in traps with fill level eleven has increased but is still low, resulting in low de-trapping rate of deuterium. Second, traps with fill level ten are available in close proximity which can re-trap the deuterium released from traps with fill level eleven.

After implantation of protium for **1500 s** (blue lines), the deuterium concentration in traps with fill level three to nine has decreased to zero in the center of the protium implantation profile, resulting in deuterium depth profiles with two distinct peaks. A double-peaked profile is also observed for traps with fill level ten, though the concentration in between the peaks is not yet zero. The deuterium depth profile in traps with the highest fill level has increased considerably and possesses a plateau-like shape with steep edges. It also seems that these edges have moved to some extent into the bulk and to the surface. This observation shows very clearly the successive filling of the traps and the increase of the fill level, spreading from the position of the maximum of the protium implantation profile. For the deuterium concentration in traps of a certain fill level, this leads to profiles which are first peaked, then dipped and finally double-peaked, with the peaks being shifted towards the surface and the bulk as the protium implantation is continued.

Furthermore, the deuterium solute concentration has risen significantly and can now be observed in the top left figure. The strong increase is based on three effects. First, the deuterium concentration in traps with the highest fill level has increased considerably, resulting in a high thermally activated de-trapping rate of deuterium. Second, traps which are filled to the highest level cannot take up additional protium or deuterium. Hence the amount of available traps which can re-trap deuterium from the solute is reduced by the amount of these saturated traps. As a consequence, the deuterium is forced to stay in the solute, but the protium as well. Third, as trapping of hydrogen isotopes is reduced and protium implantation is continued, the protium solute increases faster than the deuterium solute, which is only increased by deuterium release from the traps. Consequently, traps which become available by thermal release of either protium or deuterium have a higher probability to be re-filled by protium than by deuterium.

2000 s (cyan blue lines) after the beginning of the protium implantation, the depth profile of deuterium retained in traps with the highest fill level has reached the surface and propagated deeper into the bulk. Also the previous plateau-like shape has vanished and a clear dip at the center of the protium implantation profile has appeared. For traps with the second highest fill level, it can be seen that the two peaks of the deuterium depth profile have moved apart. One is located directly at the surface and the other one is shifted to larger depth. In case of traps with fill levels lower than ten, the peak on the left-hand side of the maximum of the protium implantation profile has disappeared, while the one on the right-hand side is shifted into the bulk. Along with the deuterium located in traps with the highest fill level, the deuterium solute reaches the surface. The arrival of the deuterium solute front and the build-up of a significant concentration at the surface after implanting protium for 1500 to 2000 s, coincides very well with the onset of the decrease of the deuterium retention observed in figure 6.8 (a) at approximately 1700 s. Moreover, the deuterium solute front has proceeded to larger depth and an increase of the deuterium solute concentration in the bulk can be noted.

Implantation of protium for **3000 s** (pink lines), leads to a further expansion of the deuterium depth profile of traps with the highest fill level towards larger depth and a decrease of the concentration at the maximum of the protium implantation profile. This effect is also observed for the deuterium concentration in traps with a fill level five to ten, together with an overall decrease of the concentration. Furthermore, no deuterium is remaining in traps with fill level three and four in the first step of the trap depth profile. At 3000 s, the fill level of the traps located in the second step are increased by the filling with protium. In addition the deuterium solute has propagated deeper into the bulk (top left figure). While the bulk concentration of the deuterium solute has increased, the concentration close to the surface has decreased due to the loss of deuterium from the sample.

After **4000 s** (orange lines), the concentration profile of deuterium in traps with the highest fill level has extended to the rear side of the sample. Furthermore, no traps with fill level lower than ten exist in the sample anymore. Together with the traps filled to the highest level, also the deuterium solute has reached the rear side of the sample from where it can effuse. This event is marked by the kink in the total deuterium retention curve in figure 6.8 (a), indicating the onset of a stronger decrease in the deuterium retention by an additional deuterium loss channel.

For protium implantation times **exceeding 4000 s** (brown and gray lines), deuterium can escape the sample from the front and the rear side likewise, leading to a further decrease in the total deuterium retention as illustrated in 6.8 (a). The deuterium concentration in traps with fill level ten and eleven as well as the deuterium solute concentration decreases continuously.

Solute and Trap-type-resolved D Depth Profiles

Figure 6.10 shows the evolution of the solute and trap-type-resolved deuterium depth profiles during the protium implantation, modeled with the classical model including the kinetic de-trapping mechanism. **Initially** (black lines), all the retained deuterium is located in traps of type one to four. While all traps of type one to three are completely filled with deuterium, the traps of type four are only partially occupied. The deuterium depth profile of the latter one shows a monotonic decrease towards the surface as a result of the thermally activated de-trapping and effusion during the Ramp & Hold to 290 K. Furthermore, no deuterium solute is present in the sample at the beginning of the protium implantation.

After **500 s** (red lines) of protium implantation the kinetic de-trapping has caused a decrease in the concentration of deuterium located in the traps of type one to three. The deuterium depth profile of the respective trap types exhibits a dip at the position of the maximum of the recoil generation profile, which is very close to the position of the maximum of the protium implantation profile as shown in figure 6.1. For larger depth, where the kinetic de-trapping cannot occur, no reduction of the deuterium concentration is observed. The collision of incident protium atoms with trapped deuterium atoms results in the transition of the involved deuterium atoms to the solute. Hence, in contrast to the fill-level model, a very small amount of deuterium solute is present at the position of the maximum of the recoil generation profile. Deuterium located in the solute can be trapped by any empty trap, independent of the required de-trapping energy of the respective trap type. In case of traps of type four, which are initially partly filled with deuterium, the combination of kinetic de-trapping and re-trapping leads to a redistribution of deuterium from larger depth towards the surface, resulting in a flattening of the depth profile. Traps of type five to ten are initially empty and do not yield significant thermally activated de-trapping at 150 K in addition to the kinetic de-trapping. Hence, trapping of deuterium outbalances the de-trapping, leading to net trapping of deuterium. The increase of the deuterium concentration in those trap types is therefore very similar and show a slightly peaked depth profile with the maximum located approximately at the position of the maximum of the protium implantation profile. For traps belonging to the type with the lowest de-trapping energy the appearance of a peaked deuterium concentration profile can be observed as well. However, the increase is lower compared to those in trap types with higher de-trapping energy, due to the additional thermally activated de-trapping of deuterium. The thermally released deuterium is finally captured by traps with a higher de-trapping energy.

Continuing the protium implantation up to **1000 s** (green lines), the deuterium concentration in the traps with the three highest de-trapping energies has decreased further, indicating the prevalence of the kinetic de-trapping compared to the trapping of deuterium. For traps of type four, possessing a de-trapping energy of 0.83 eV, the deuterium depth profile has not changed significantly. This implies an equilibrium of trapping and de-trapping deuterium and explains the constant deuterium retention for traps of this type in figure 6.8 (b). Traps of type five to ten show a small increase of their broad-peaked deuterium depth profile. Compared with that the narrow-peaked deuterium depth profile of traps with the lowest de-trapping energy increases as well, but the relative increase is larger. Furthermore, the deuterium solute concentration at the position of the maximum of the protium implantation profile has increased slightly, as can be observed from the top left figure.

After **1500 s** (blue lines), a second dip at the position of the maximum of the protium implantation profile has appeared in the deuterium depth profiles of

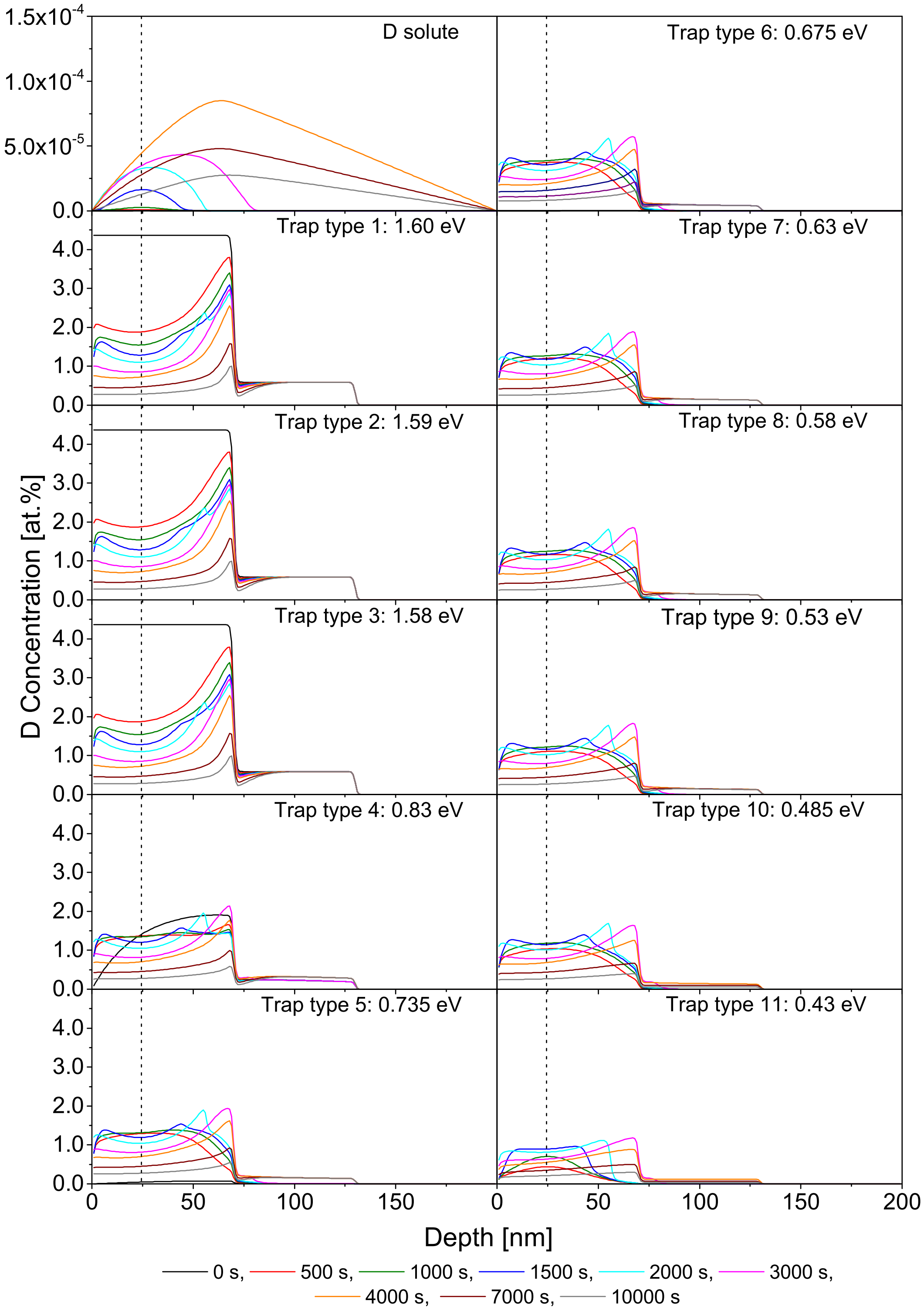

Figure 6.10: Evolution of the deuterium solute and trap-type-resolved deuterium depth profiles during the exchange of deuterium by protium at 150 K after Ramp & Hold to 290 K, simulated with the classical model including the kinetic de-trapping. The maximum of the protium implantation profile is indicated by the vertical dashed black line. The scale of the deuterium concentration is the same for all figures showing different trap types.

the traps one to three with a de-trapping energy of 1.58 to 1.60 eV. Also the previously flat and peaked deuterium depth profiles of traps of type four to ten show a dip at this specific depth, accompanied with two peaks at the rim of the dip. In case of traps with the lowest de-trapping energy the profile has evolved to a plateau-like profile. The reason for the appearance of the dip after 1500 s can be explained by the saturation of the empty traps with hydrogen isotopes. In the region of the dip, the amount of implanted protium together with the already present deuterium is large enough to fill all traps. Once all traps are occupied the re-trapping of either implanted or kinetically as well as thermally released hydrogen isotopes is hampered. Furthermore, the solute concentration of protium rises significantly due to implantation as well as kinetic and thermally activated release of trapped protium. Compared with that, the deuterium solute concentration is only increased by the de-trapping of deuterium. The result is a growing ratio of protium to deuterium solute. Consequently, the reduced amount of empty traps, created by kinetic or thermally activated de-trapping, are more likely to be filled with protium instead of deuterium. The appearance of the dip in the trapped deuterium depth profiles is therefore caused by two mechanisms. A generally reduced trapping rate and a relative increase of the protium trapping rate compared to the deuterium trapping rate. As a consequence of this effect, the deuterium solute concentration has increased considerably in the depth region where the traps are saturated. The peaks appearing at the rim of the dip in the deuterium depth profile of the traps of type four to ten, mark the boundaries of the regions with saturated and unsaturated traps. Deuterium which is released in the region of saturated traps diffuses to the boundaries of this region due to the low re-trapping. At the boundaries sufficient empty traps exist which capture the deuterium solute, leading to a local increase of the trapped deuterium concentration. From the existence of the peak in the trapped deuterium depth profiles between the surface and the protium implantation depth as well as from the top left figure, it can be concluded that the deuterium solute front has not yet reached the surface.

Another interesting feature, present in the deuterium depth profile up to a protium implantation of 1500 s, is the reduced concentration directly at the surface. This can be observed for traps of type one to ten, but is most prominent for the initially filled traps of type one to three. The reason for this occurrence is that deuterium which is kinetically de-trapped close to the surface has a certain chance to leave the sample instead of being re-trapped, which results in a local reduction of the deuterium concentration.

Protium implantation for **2000 s** (cyan blue lines) results in an expansion of the depth region in which the traps are saturated. As can be seen from the broadening of the dip in the deuterium depth profiles in traps of type one to ten and from the widening of the plateau-like profile of traps of type eleven, the saturation of traps has reached the surface. In addition, the deuterium concentration in the region of the protium implantation profile has decreased further, leading to an increase of the deuterium solute concentration. Together with the saturation of traps also the deuterium solute front has arrived at the surface from where deuterium can be released from the sample. This fits very well to the onset of the decrease of the deuterium retention observed at roughly 1700 s as shown in figure 6.8 (b).

Conducting protium implantation for **3000 s** (pink lines) leads to a the saturation of traps with hydrogen isotopes up to larger depth as can be inferred from the further expansion of the dip in the trapped deuterium depth profiles as well as the propagation of the deuterium solute front into the bulk. In the region which is affected by kinetic de-trapping, the deuterium concentration in all trap types decreases, which in turn results in an increase of the deuterium solute concentration in the bulk.

After **4000 s** (orange lines) the saturation of traps with hydrogen isotopes has advanced to the rear side of the sample, as can be observed from the increase of the deuterium concentration in traps of type four to eleven. During the preceding Ramp & Hold cycle to 290 K, deuterium retained in traps of these types is fully or partially released. Since kinetic de-trapping is not present in larger depth of the sample, a reallocation of deuterium from traps with high de-trapping energy to the empty ones with low de-trapping energy is not possible. As the hydrogen solute front propagates in this region, the empty traps are filled by either protium or deuterium, causing an increase of the trapped deuterium concentration. In the depth region where the kinetic de-trapping is occurring a further reduction of the deuterium concentration is observed. As can be seen from the top left figure, the deuterium solute has reached the rear side of the sample after 4000 s. The additional effusion from the rear side leads to faster decrease of the deuterium retention shown in figure 6.8 (b).

For protium implantation **exceeding 4000 s** (brown and gray lines), a further decrease of the deuterium concentration in all trap types can be observed in the depth region where kinetic de-trapping is present. Furthermore, no change in the deuterium concentration occurs behind that region for traps of type one to nine. Only for traps of type ten and eleven, a decrease of the deuterium concentration caused by thermally activated de-trapping is observed in this region. In addition, the deuterium solute concentration decreases successively as the protium implantation is continued. In total, a further decrease of the deuterium retention is the result.

From the comparison of the fill-level- and trap-type-resolved deuterium retention in figure 6.8 (a) and (b) as well as from the deuterium depth profiles in the figures 6.9 and 6.10 it can be concluded that an ensemble of classical traps with different de-trapping energies and the consideration of the kinetic de-trapping mechanism behave like a fill-level trap. In the fill-level model, the deuterium, initially located at a low fill level with a high de-trapping energy, is shifted to higher fill level with lower de-trapping energy by filling the trap with protium. In the classical model, deuterium is first located at traps with high de-trapping energy. The temperature-independent kinetic de-trapping mechanism reallocates the deuterium to the solute from where it can be trapped by traps of different de-trapping energy. If the de-trapping energy is high enough at the given temperature, the deuterium remains in the trap. If the de-trapping energy is low, the deuterium can be thermally released to the solute and might finally get captured by a trap with high enough de-trapping energy. This effect leads to a shift of deuterium retained in traps with high de-trapping energy to those with low de-trapping energy, similar to the fill-level model. Although the underlying mechanisms are different in both models, the net effect is very similar. As a consequence, the simulation of the quantities which are accessible by experiments, such as the deuterium retention and the desorption rate, yield very similar results.

6.3.3 Critical Protium Fluence

In both investigated models the occurrence of the critical protium fluence, which needs to be implanted to observe the decrease of the deuterium retention, is associated with the arrival of the deuterium solute front at the surface, as can be seen from figures 6.9 and 6.10 in comparison with figures 6.8 (a) and (b). In order to enable the solute front to propagate to the surface, the immobilization of the deuterium solute by traps on its way to the surface must be prevented. In case of the fill-level model this requires the filling of the respective traps to a fill level at which significant thermally activated de-trapping occurs. In case of the classical model with kinetic de-trapping the saturation of the respective traps of those types which do not show significant thermally activated de-trapping at the given temperature is necessary. Since the amount of hydrogen isotopes which can be retained by the respective traps at a given temperature is set to be very similar in both models, the required critical amount of protium is nearly identical for the same experimental conditions.

As can be seen in figure 6.5, the fill-level model as well as the classical model with kinetic de-trapping show an increasing critical protium fluence for a decreasing deuterium retention prior to the protium implantation. This can be explained as follows: In both models, the higher the deuterium retention prior to the exchange at a given temperature, the lower the required amount of protium, either to fill the respective traps to the fill level from which thermal de-trapping occurs or to saturate those types of the respective traps which do not show thermal de-trapping.

Similar to that the decrease of the critical protium fluence for increasing exchange temperatures observed in figure 6.6 for both models can be explained. In case of the fill-level model, the higher the temperature, the lower the fill level at which significant thermal de-trapping occurs. For the classical model with kinetic de-trapping applies, the higher the temperature, the lower the number of trap types which do not show thermal de-trapping. Hence, in both models a higher temperature results in a lower amount of protium which is needed to reach the required fill level or to saturated those trap types which do not show thermal de-trapping.

The similar results obtained by two models for the second Ramp & Hold to 290 K with protium implantation conducted before at 150 K, illustrated in figure 6.7, can be interpreted as follows: In case of the fill-level model the implanted protium shifts the deuterium from fill levels with high de-trapping energy to those with low de-trapping energy. Within the classical model the reallocation of deuterium by kinetic de-trapping and re-trapping has the same effect. In addition, the implanted protium fluence is sufficient to rise the fill level of the traps to a level at which de-trapping can occur or to saturate those trap types which do not show thermal de-trapping at 150 K. Hence, in both models, the deuterium which is released to the solute when the temperature is increased can propagate to the surface without being re-trapped. Consequently, the deuterium desorption is observed already at the beginning of the temperature ramp in the fill-level model as well as in the classical model with kinetic de-trapping.

6.3.4 Exchange Cross Section

While the appearance of a critical protium fluence in both models can be explained very illustratively with the deuterium solute front reaching the surface, the origin of the similar reduction of the deuterium retention is not that obvious from the TESSIM-X simulations. In case of the fill-level model the following two observations are made for the deuterium effusion from the front side as well as from the rear sides of the sample. First, despite different initial deuterium retentions a similar exponential decrease of the deuterium retention is observed in the fill-level model, when the exchange is performed at the same temperature, as illustrated in figure 6.5 (a). Second, the decrease of deuterium retention is enhanced when the temperature at which the exchange is conducted is increased, as can be seen in figure 6.6 (a). Both effects are in good qualitative agreement with the results of the simple combinatorial urn model applied to describe the exchange of deuterium by protium in fill-level traps, shown in figure 5.16. Nevertheless, from figures 6.5 (b) and 6.6 (b) it can be seen that also the TESSIM-X simulations using the classical model with kinetic de-trapping show exactly the same trends.

This observation can be understood in terms of an combinatorial urn model formulated for classical traps which also accounts for the kinetic de-trapping mechanism. The urn model for fill-level traps is very illustrative, since the trap by itself, saturated with a mixture of deuterium and protium atoms, can be directly identified as an urn. The possible number of hydrogen atoms N in such an urn is defined by the highest fill level from which thermally activated de-trapping is not yet possible at a given temperature. In case of an urn model for classical traps, one urn cannot be associated directly with one trap. Since the concentration of different trap types N_T is equal, it is reasonable to consider an urn composed of N_T classical traps. Yet, from those traps only the traps N from which no thermally activated de-trapping can occur at a given temperature are of interest. Thus in the urn model for fill-level traps as well as for classical traps, the maximum possible number of hydrogen atoms is the same at a given temperature. The kinetic de-trapping mechanism, which allows the release of protium or deuterium from traps of any de-trapping energy, is an essential component in the urn model for classical traps, since it provides the means to draw hydrogen atoms from the urn.

In accordance with the urn model for fill-level traps, transport effects and the re-trapping of released deuterium are neglected. It is further assumed that the probability for kinetic de-trapping of a hydrogen atom is independent of the de-trapping energy of the trap and that the kinetically emptied traps are re-occupied with protium. Taking these assumptions into account an urn model for an ensemble of urns consisting of classical traps can be formulated analog to the one for fill-level traps described by equations (5.2), (5.3) and (5.4). The only difference between the two urn models is that in case of urns composed of classical traps the deuterium is released first and the protium is added to the urns afterwards. Consequently, in the urn model for classical traps one hydrogen atom is drawn from N atoms, while in the urn model for fill-level traps one hydrogen is drawn from $N+1$ atoms. As a result, the probability of drawing a deuterium atom from an urn composed of classical traps is higher than for an urn consisting of a fill-level trap. The initial state of an ensemble of urns consisting of classical traps is given by probability vector $\underline{p}\,(0)$ in equation (6.3) with the vector norm $\left\|\underline{p}\,(0)\right\| = 1$. The entries of the vector $p_{D=0}\,(0)$ to $p_{D=N}\,(0)$ describe the initial fractions of urns occupied with 0 to N deuterium atoms and possess values from 0 to 1. The evolution of the ensemble in one drawing event is described by the $(N+1)\times(N+1)$ transition matrix $\underline{\underline{M}}$, with i being the row index beginning from 1.

$$\underline{p}\,(0) = \begin{pmatrix} p_{D=0}\,(0) \\ p_{D=1}\,(0) \\ p_{D=2}\,(0) \\ \vdots \\ p_{D=N}\,(0) \end{pmatrix},\ \underline{\underline{M}} = \begin{pmatrix} 1 & \frac{1}{N} & 0 & \cdots & \cdots & 0 \\ 0 & \frac{N-1}{N} & \frac{2}{N} & \ddots & & \vdots \\ & 0 & \frac{N-2}{N} & \ddots & \ddots & \vdots \\ \vdots & & 0 & \ddots & \ddots & 0 \\ \vdots & & & \ddots & \ddots & \frac{i}{N} \\ 0 & \cdots & \cdots & \cdots & 0 & \frac{N+1-i}{N} \end{pmatrix},\ \underline{b} = \begin{pmatrix} 0 \\ 1 \\ 2 \\ \vdots \\ N \end{pmatrix} \tag{6.3}$$

Compared with the transition matrix of the urn model for fill-level traps, the last row of $\underline{\underline{M}}$ in equation (6.3) consists only of 0. If the urn is filled with the maximum number of deuterium atoms, N, the reversed order of removing and replacing a hydrogen atom with a protium atom impedes the urn to keep all deuterium atoms. The state of the ensemble $\underline{p}\,(n)$ after n drawing events is determined by iterative multiplication of the transition matrix with the initial

probability vector according to equation (5.3). The development of the average deuterium retention in an urn $R_D(n)$ is derived by equation (5.4).
In figure 6.11 the accumulated average deuterium retention by an urn composed of classical traps is illustrated for two scenarios analog to the accumulated average deuterium retention per urn for fill-level traps in figure 5.16. In the first scenario, the maximum number of hydrogen atoms in the urn N is kept constant at $N = 5$ and the initial amount of deuterium per urn is varied from 1 to 5. This situation corresponds to the hydrogen isotope exchange conducted at 150 K after Ramp & Hold to different temperatures. Despite the different initial deuterium retentions the exponential decrease is the same, as can be seen from the identical slopes of the black lines in figure 6.11. In this case the urn model for classical traps shows qualitatively the same trend as the urn model for fill-level traps in figure 5.16. Yet, it can be observed that the decrease of the deuterium retention proceeds faster in case of urns consisting of classical traps than of fill-level traps. The reason for this is the reversed order of drawing and replacing a hydrogen atom with a protium atom.
In the second scenario, shown in figure 6.11, the initial amount of deuterium per urn is kept constant at 2 and the maximum number of hydrogen atoms per urn N is altered from 5 to 2. The variation of N imitates the hydrogen isotope exchange conducted at different temperatures after warm-up of the

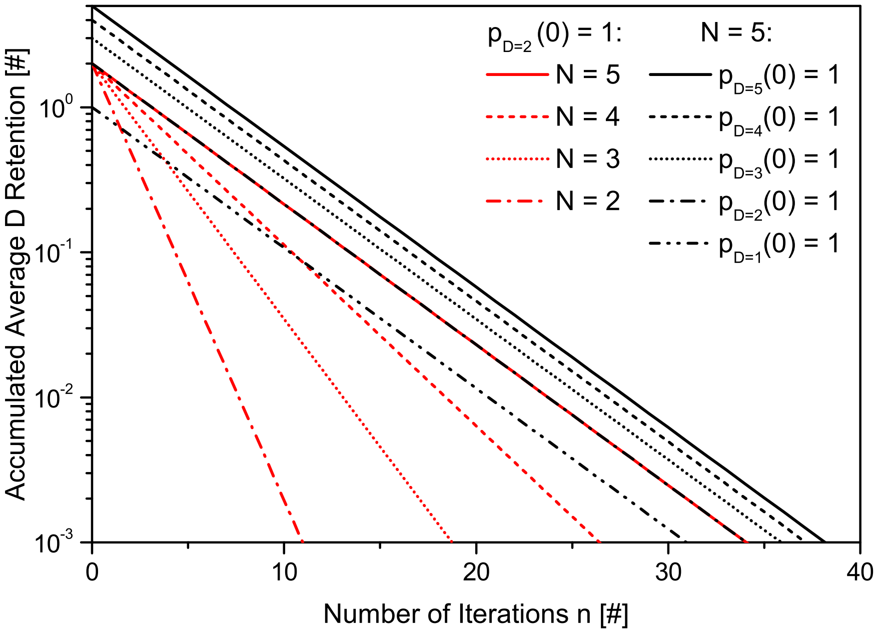

Figure 6.11: Accumulated average deuterium retention of the ensemble of urns consisting of classical traps as a function of iterations. Number of maximum hydrogen atoms per urn kept at $N = 5$ and number of initial deuterium atoms per urn varied from 1 to 5 (black lines) . Two deuterium atoms per urn and variation of the maximum number of hydrogen atoms per urn N from 5 to 2 (red lines).

sample to 290 K. A large N corresponds to a low temperature at which the exchange is performed. Similar to the results obtained with the urn model for fill-level traps, shown in figure 5.16, the deuterium retention per urn decreases exponentially, with the exponent depending on N. The lower N, the faster is the decrease of the deuterium retention, as can be seen from the steeper slopes of the red lines in figure 6.11. Also in this case, the deuterium retention decreases faster compared to the urn model for fill-level traps.
The comparison of figures 5.16 and 6.11 shows that the urn models for fill-level traps and classical traps provide qualitatively the same results. Furthermore, the trends in the reduction of the deuterium retention derived by the urn models are in good qualitative agreement with the one obtained with TESSIM-X. Although, transport effects and re-trapping of released deuterium is not considered and further simplifications regarding the kinetic de-trapping mechanism are required in the urn models. From this it can be inferred, that once the deuterium solute front has arrived at the surface and the reduction of the deuterium retention is proceeding, transport of deuterium is not the rate limiting process, but the exchange of deuterium by protium in the traps.

6.4 Conclusion

In the here-conducted simulations and in comparison with the experimental data, it could be shown that the pure fill-level model is able to explain the hydrogen isotope exchange observed at low temperature. In contrast to that, the pure classical model, in which only thermally activated de-trapping of hydrogen isotopes is considered, cannot explain the experimental data. However, as the exchange of deuterium by protium proceeds predominately in the implantation zone the kinetic de-trapping of deuterium must be considered. In case of the fill-level model, the additional kinetic de-trapping mechanism has only little influence on the simulation results. In contrast to that, the kinetic de-trapping process alters the results obtained with the classical model dramatically, leading qualitatively to similar results as the fill-level model.
The trapping and de-trapping mechanism of an individual trap in the classical framework differs from that of a trap in the fill-level model significantly. Yet, the collective behavior of traps in the classical model with kinetic de-trapping is very similar to the behavior of a trap in the fill-level model. In both models, the critical protium fluence required to observe a decrease in the deuterium retention is determined by the traps which need to be filled in order to allow the deuterium solute to reach the surface from where it can effuse from the sample. A comparison of the reduction of the deuterium retention in terms of a simple combinatorial urn model for classical and fill-level traps reveals similar trends. Furthermore, the results of the urn models agree well with those obtained with TESSIM-X. This implies that the exchange of deuterium by protium in the traps is the dominant process once the deuterium solute front has encountered the surface and not the transport of deuterium.

Finally, due to the similarity of the results obtained with the fill-level model with and without kinetic de-trapping as well as with the classical model with kinetic de-trapping, an unambiguous identification of the underlying mechanism which is responsible for the exchange of deuterium by protium in tungsten in the here-conducted experiments is not possible.

A possible solution of the problem of kinetic de-trapping is the separation of the implantation zone from the region where the hydrogen isotope exchange takes place. This could be achieved by performing hydrogen isotope exchange in the bulk of the tungsten sample far behind the implantation zone. Although the kinetic de-trapping is still occurring close to the surface, the exchange process in the bulk is not influenced. The experiment could be conducted similar to those in references [44, 51, 52], but with a temperature treatment in between the plasma or atomic beam loading of different hydrogen isotopes in order to exclude thermally activated release of the isotope already present in the sample. The exchange dynamics in the bulk could be investigated by NRA measurements. An alternative approach to separate the implantation zone and the exchange region is to study hydrogen isotope exchange in permeation experiments. At the front side of a tungsten foil with a thickness of several microns a defect-rich layer generated by tungsten self-damaging could be created similar to Tyburska et al. [169]. The different hydrogen isotopes are injected at the rear side of the foil by plasma loading or implantation. The filling of the defect-rich zone from the bulk with deuterium and the subsequent exchange by protium could be monitored by NRA. Another ansatz to circumvent the issue of kinetic de-trapping is to eliminate the implantation zone completely by conducting hydrogen isotope exchange experiments via sample loading from the gas-phase. Since the concentration of deuterium in tungsten achievable with gas loading is low compared to implantation or plasma loading, a large sample volume is required for the experiment. As NRA measurements would be tedious and incomplete, TDS or dedicated Ramp & Hold experiments would be a better choice to study the isotopic exchange in such samples. However, all of the proposed experiments need to be carried out at higher temperature since significant diffusive transport is required. Consequently, the occupation of traps or fill levels with low de-trapping energy is not possible.

Chapter 7

Summary

The intention of this thesis is the investigation of the hydrogen isotope exchange in tungsten at low temperature in order to gain a microscopic understanding of the underlying exchange mechanism. In particular, the fill-level and the classical model, which describe the trapping and de-trapping of hydrogen in tungsten microscopically, are compared and their capability to explain the hydrogen isotope exchange is assessed. The fill-level model, which assumes a multiple occupancy of traps with hydrogen atoms and an occupancy-dependent de-trapping energy, can in principle explain the isotopic exchange. In contrast to that, the classical model, which is characterized by single occupancy of traps with fixed de-trapping energy, can describe the isotopic exchange only in special cases. Thus, the here-conducted experiments aim to derive evidence which verifies the fill-level model as underlying exchange mechanism and discriminate it against the classical model.

Before the isotope exchange is investigated, the processes taking place during the implantation of energetic deuterium at low temperature are studied in terms of deuterium retention and surface morphology (4). The implantation of deuterium of an energy of 3.0 keV/D into tungsten at a temperature of 150 K leads to a linear increase of deuterium retention for irradiated fluences up to $1.6 \times 10^{21}\,\mathrm{D\,m^{-2}}$. Together with the deuterium retention the surface morphology of the tungsten samples evolves. The initiation of blisters is already observed at the lowest irradiated deuterium fluence of $8.5 \times 10^{19}\,\mathrm{D\,m^{-2}}$. Shape, size, number density and the area covered by the blisters are strongly depending on the grain orientation. The investigated recrystallized polycrystalline tungsten samples exhibit a texture of grains with a preferred surface orientation close to the $\{100\}$ plane. Within the linear retention regime the predominantly circular blisters on these grains increase in diameter. The growth of the blisters indicates the trapping of deuterium in the blister cavities and the reduction of the EBSD solving probability implies a proceeding creation of defects in the near-surface region which act as traps for deuterium. Within the linear retention regime trapping of deuterium is supposed to be highly effective due to a continuing production of traps sites. It can be assumed that the linear increase of the deuterium retention corresponds to 100 % retention of the implanted deuterium at this low temperature. The obtained particle reflection coefficient of deuterium on tungsten for the given implantation conditions is 0.27, which is lower than the theoretical value of 0.43 calculated by SDTrimSP. For irradiated deuterium fluences larger than $1.6 \times 10^{21}\,\mathrm{D\,m^{-2}}$, the deuterium retention deviates from this linear regime, starts to saturate and finally converges to a deuterium retention of $2.07 \pm 0.25 \times 10^{21}\,\mathrm{D\,m^{-2}}$. The SEM and EBSD data suggest that this behavior is presumably caused by the rupture of blisters and the saturation of defects created during the implantation of energetic deuterium ions. As the final concentration of trap sites is limited, the amount of deuterium which can be retained at a given temperature is limited as well. Once the tungsten sample is saturated with deuterium, a deuterium concentration of 42 at.% is measured at a sample temperature of 150 K which is one of the highest values observed so far.

The isotope exchange of deuterium by protium at low temperature is experimentally investigated in situ in different scenarios by NRA and mass spectroscopy (chapter 5). The scenarios are designed such that an exchange should be observed in case of the fill-level model, but not within the classical model. The dependence of the exchange on the amount of retained deuterium prior to the exchange as well as on the exchange temperature is studied. Furthermore, the influence of the protium implantation on the deuterium desorption rate during temperature Ramp & Hold experiments is investigated with mass spectroscopy in situ.

The experiments revealed that isotopic exchange of deuterium by protium in tungsten is possible at temperatures down to 150 K. Furthermore, in order to observe a reduction of the deuterium retention a certain critical protium fluence needs to be implanted. It is shown that the higher the deuterium retention before the exchange or the higher the temperature at which the exchange is performed, the lower is the required critical protium fluence. In addition, it is found that the exchange efficiency, empirically characterized by an exchange cross section, is independent of the deuterium retention before the exchange and becomes larger for increasing exchange temperatures. The observed dependences of the critical protium fluence are in good qualitative agreement with the fill-level model. Furthermore, an urn model, based on fill-level traps, is applied to understand the exchange process from a combinatorial perspective. The urn model reproduces the observed dependences of the exchange cross section qualitatively.

Since the observed hydrogen isotope exchange takes place mainly in the implantation zone, kinetic effects of the incident ion beam are discussed. Estimations based on SDTrimSP simulations show that sputtering is negligible, but the kinetic de-trapping of deuterium atoms by collisions with incident protium atoms or generated hydrogen recoils is significant and must be considered as an alternative exchange mechanism.

The hydrogen isotope exchange experiments are modeled with TESSIM-X in the framework of the fill-level and the classical model, each with and without taking the kinetic de-trapping mechanism into account (chapter 6). The TESSIM-X simulations, applying the fill-level model with and without kinetic de-trapping, are in good qualitative agreement with the observed exchange of deuterium by protium in all experimental scenarios. The dependence of the critical implanted protium fluence and the exchange cross section on the deuterium retention prior to the exchange and on the exchange temperature are correctly described by the simulations. Also the dependence of the deuterium desorption rate on a preceding protium implantation can be reproduced qualitatively.

In contrast to that, the TESSIM-X simulations based on the pure classical model cannot explain the experimental results at all. However, when the kinetic de-trapping mechanism is added, the experimental data can be reproduced qualitatively similar as with fill-level model. The solute and fill-level-resolved deuterium depth profiles in the fill-level model are compared in detail with the solute and trap-type-resolved deuterium depth profiles in the classical model with kinetic de-trapping. In this comparison it is demonstrated that during the protium implantation an ensemble of classical traps with kinetic de-trapping behaves similar to a single fill-level trap without kinetic de-trapping. As a result, the experimentally accessible quantities, i.e., the deuterium retention and the deuterium desorption rate, show the same dependences despite the different underlying trapping and de-trapping mechanisms. Thus, an unambiguous identification of the mechanism which is responsible for the hydrogen isotope exchange is not possible in the here-performed experiments.

However, the here-conducted experiments in combination with TESSIM-X simulations contribute significantly to a better understanding of the hydrogen-tungsten system. In particular, it is shown that the observed hydrogen isotope exchange can be reproduced with two models describing the trapping and de-trapping of hydrogen in tungsten on a microscopic scale. The introduction of an empirical cross section which describes the exchange process is in principle not necessary.

Appendix

A.1 3 MeV Tandem Accelerator

Energetic ions for ion beam analysis and ion beam damaging are produced by the electrostatic 3 MV tandem accelerator at IPP Garching, manufactured by High Voltage Engineering Europa B.V. [170]. The underlying ion acceleration concept, which also provides the name for this type of accelerator, is the twofold use of the applied high voltage to accelerate the ions by changing the polarity of the ions at the high voltage terminal. The ion acceleration and beam delivery process can be divided into the following steps. Negative ion generation, acceleration of negative ions, stripping off the electrons from the negative ions, acceleration of the positive ions and ion beam delivery to the specific experiment.

In the first step the negative ions are produced. Depending on the element from which the ions are generated, this is done either in a RF ion source or a Cs-sputter ion source [71]. ^{3}He and ^{4}He, which are the ions typically used for Rutherford backscattering spectroscopy (RBS) and nuclear reaction analysis (NRA) [74], are generated by the RF ion source. The ion source consists of a glass tube containing the gas, an RF oscillator coupled to tube to excite the gas into a plasma and four permanent magnets to confine the plasma by an axial magnetic field. Positive helium ions are extracted through an aperture and focused into the charge exchange channel containing lithium vapor. Some of the helium ions undergo a charge transfer processes acquiring two electrons from the lithium atoms, resulting in a metastable singly charged negative helium ion. Negative ions from elements other than helium, e.g. tungsten, are created in the Cs-sputter ion source, which is very similar to the source installed at the DBE setup [70]. The negative ions, generated by either of the two sources, are focused by a set of two Einzel lens into a magnet, which mass separates the ion beam and bends it by approximately 90 °into the accelerator tube. It should be noted that the possibility to form a negative ion is one major limitation of the tandem accelerator concept [171].

In the second step the negative ions enter the actual accelerator. It consists of the low energy accelerator tube, the high voltage terminal at which the electron stripping takes place and a high energy accelerator tube, all encapsulated in a steel tank containing SF_6 to prevent discharges. The accelerator tubes are made of alternating circular isolators and electrodes which grade the electric field from the high voltage terminal down to ground potential. Furthermore, a low magnetic field, generated by permanent magnets, prevents secondary electrons, created in the tubes, from being accelerated in the electric field. The high voltage of up to 3 MV is generated by a parallel driven, capacitively coupled Cockcroft-Walten type circuit. In the region of the high voltage terminal nitrogen gas is circulated by a turbo molecular pump. At the beginning of the low energy accelerator tube, the negative ions are focused into the stripper gas region by the so-called Q-snout electrode. After being accelerated to the high voltage terminal, the electrons are stripped from the ions by collisions with the nitrogen molecules. Since the negative ions undergo several charge transfer processes, acquiring and losing electrons, a distribution of ions with different positive charge states leaves the stripper gas region. As a consequence the energy of the ions gained in the high energy accelerator tube depends on the charge state of the positive ions. Hence, the total energy of the ions leaving the high energy accelerator tube is given by

$$E_{\text{Ion}}\left(n\right) = eV_{\text{Extrac.}} + \left(n+1\right)eV_{\text{HV}}, \tag{7.1}$$

with e being the elementary charge, $V_{\text{Extrac.}}$ the extraction voltage of the ion source, V_{HV} the high voltage at the terminal and n the charge state of the positive ions after electron stripping.

In the third step, after passing the high energy accelerator tube, the ions are focused by a electrostatic quadrupole triplet into a magnet which is used to select ions of a specific charge state and bend them into the beamline of the respective experiment. The position of the ion beam can be fine-adjusted with several electrostatic and magnetic steers located at different positions on the accelerator system and the beamline. The astigmatism of the ion beam can be controlled by adjusting the electrostatic quadrupole triplets. Furthermore, the accelerator system is equipped with several diagnostics to monitor the ion beam. The intensity of the beam is monitored by measuring the ion current on Faraday cups located before the individual experiments. The position, astigmatism and profile of the ion beam is observed on beam profile monitors, consisting of a pair of wires oscillating in the beam. The final ion beam diameter is defined by the aperture located in the individual experiments. For further information on the topic of electrostatic accelerators, the reader is referred to the comprehensive introduction by Hellborg et al. [172]

A.2 H and D Implantation into W

SDTrimSP 5.07 [66, 67] input parameters used to determine the implantation profiles of protium and deuterium in tungsten. The detailed description of the individual parameters can be found in reference [67].

```
H or D on W
&TRI_INP
idrel = 1
nh = 100000
nr_pproj = 10
idout = −1
flc = 1
ncp = 2
symbol = "H" ("D"), "W"
case_e0 = 0
e0 = 3000.00, 0.00
e_cutoff = 0.25, 2.205
e_displ = 2.0, 90.0
case_alpha = 0
alpha0 = 0.00, 0.00
qu = 0.00, 1.00
qubeam = 1, 0
charge = 0, 0
qumax = 1, 1
inel0 = 3, 3
isot = 0, 0
x0 = 0, 0
ltableread = .true.
sfin = 0
shth = −1.00
ipot = 1
irand = 31415
dns0 = 0.1, 0.06306
imcp = −1
isbv = 3
dsf = 5
iq0 = 0
ttarget = 2000
nqx = 1000
rhom = −2.0
lmatrices = .false.
lparticle_p = .false.
lparticle_r = .true.
ltraj_p = .false.
ltraj_r = .false.
ioutput_part = 0, 0, 0, 100000, 1000, 1000
lpart_r_ed = .true.
tableinp = "C:\SDTRIM.SP 5.07\tables"
nm = -1
```

A.3 H and D Recoil Creation by H Implantation into W

SDTrimSP 5.07 [66, 67] input parameters to calculate the recoil generation of protium and deuterium by protium implantation into a tungsten sample containing different concentrations of protium or deuterium. The detailed description of the individual parameters can be found in reference [67].

```
&TRI_INP
idrel = 1
nh = 10000
nr_pproj = 10
idout = −1
flc = 1
ncp = 3
symbol = "H", "H" ("D"), "W"
case_e0 = 0
e0 = 3000.00, 0.00, 0.00
e_cutoff = 0.25, 0.25, 2.205
e_displ = 2.0, 0.25 – 2.0, 90.0
case_alpha = 0
alpha0 = 0.00, 0.00, 0.00
qu = 0.0, 0.10 – 0.50, 0.90 – 0.50
qubeam = 1, 0, 0
charge = 0, 0, 0
qumax = 1, 1, 1
inel0 = 3, 3, 3
isot = 0, 0, 0
x0 = 0, 0, 0
ltableread = .true.
sfin = 0
shth = −1.00
ipot = 1
irand = 31415
dns0 = 0.1, 0.1, 0.06306
imcp = −1
isbv = 3
dsf = 5
iq0 = 0
ttarget = 2000
nqx = 1000
rhom = −2.0
lmatrices = .false.
lparticle_p = .false.
lparticle_r = .true.
ltraj_p = .false.
ltraj_r = .false.
ioutput_part = 0, 0, 0, 100000, 1000, 1000
lpart_r_ed = .true.
tableinp = "C:\SDTRIM.SP 5.07\tables"
nm = −1
```

Bibliography

[1] International Energy Agency, *World Energy Outlook 2016.* OECD Publishing Paris, 2016. (cit. on p. 1)

[2] T. J. Dolan, J. Brotankova, L. C. Cadwallader, A. E. Costley, D. P. Ivanov, W. Manheimer, M. Merola, R. W. Moir, M. J. Neumann, A. Parrish, and L. M. Waganer, *Magnetic Fusion Technology*, T. J. Dolan, Ed. Springer-Verlag London, 2013. (cit. on pp. 2, 3, 4, 5 and 6)

[3] A. Bradshaw, T. Hamacher, and U. Fischer, "Is nuclear fusion a sustainable energy form?" *Fusion Engineering and Design*, vol. 86, no. 9, pp. 2770 – 2773, 2011. [Online]. Available: http://www.sciencedirect.com/science/article/pii/S0920379610005119 (cit. on p. 2)

[4] M. Kikuchi, *Frontiers in Fusion Research II Introduction to Modern Tokamak Physics.* Springer International Publishing Switzerland, 2015. (cit. on pp. 3 and 4)

[5] ——, *Frontiers in Fusion Research Physics and Fusion.* Springer-Verlag London Limited, 2011. (cit. on p. 3)

[6] U. Stroth, *Plasmaphysik Phänomene, Grundlagen, Anwendungen.* Vieweg + Teubner Verlag | Springer Fachmedien Wiesbaden GmbH, 2011. (cit. on pp. 3 and 4)

[7] Max-Planck-Institut für Plasmaphysik. (10.08.2017). [Online]. Available: https://www.ipp.mpg.de/9778/tokamak (cit. on p. 3)

[8] J. Paméla, F. Romanelli, M. Watkins, A. Lioure, G. Matthews, V. Philipps, T. Jones, A. Murari, A. Géraud, F. Crisanti, and R. Kamendje, "The JET programme in support of ITER," *Fusion Engineering and Design*, vol. 82, no. 5, pp. 590 – 602, 2007. [Online]. Available: http://www.sciencedirect.com/science/article/pii/S0920379607000993 (cit. on p. 3)

[9] R. Aymar, P. Barabaschi, and Y. Shimomura, "The ITER design," *Plasma Physics and Controlled Fusion*, vol. 44, no. 5, p. 519, 2002. [Online]. Available: http://stacks.iop.org/0741-3335/44/i=5/a=304 (cit. on p. 3)

[10] V. Barabash, G. Federici, M. Rödig, L. Snead, and C. Wu, "Neutron irradiation effects on plasma facing materials," *Journal of Nuclear Materials*, vol. 283, pp. 138 – 146, 2000. [Online]. Available: http://www.sciencedirect.com/science/article/pii/S0022311500002038 (cit. on p. 4)

[11] V. Barabash, G. Federici, J. Linke, and C. Wu, "Material/plasma surface interaction issues following neutron damage," *Journal of Nuclear Materials*, vol. 313 - 316, pp. 42 – 51, 2003. [Online]. Available: http://www.sciencedirect.com/science/article/pii/S0022311502013302 (cit. on p. 4)

[12] Y. Ueda, K. Schmid, M. Balden, J. Coenen, T. Loewenhoff, A. Ito, A. Hasegawa, C. Hardie, M. Porton, and M. Gilbert, "Baseline high heat flux and plasma facing materials for fusion," *Nuclear Fusion*, vol. 57, no. 9, p. 092006, 2017. [Online]. Available: http://stacks.iop.org/0029-5515/57/i=9/a=092006 (cit. on pp. 4, 5 and 6)

[13] G. Was, *Fundamentals of Radiation Materials Science Metals and Alloys*. Springer-Verlag Berlin Heidelberg, 2007. (cit. on pp. 4, 5, 22, 48, 67, 70, 105 and 106)

[14] J. Roth, E. Tsitrone, A. Loarte, T. Loarer, G. Counsell, R. Neu, V. Philipps, S. Brezinsek, M. Lehnen, P. Coad, C. Grisolia, K. Schmid, K. Krieger, A. Kallenbach, B. Lipschultz, R. Doerner, R. Causey, V. Alimov, W. Shu, O. Ogorodnikova, A. Kirschner, G. Federici, and A. Kukushkin, "Recent analysis of key plasma wall interactions issues for ITER," *Journal of Nuclear Materials*, vol. 390 - 391, no. 0, pp. 1–9, 2009. [Online]. Available: http://www.sciencedirect.com/science/article/pii/S0022311509000506 (cit. on p. 4)

[15] A. Kallenbach, M. Bernert, R. Dux, L. Casali, T. Eich, L. Giannone, A. Herrmann, R. McDermott, A. Mlynek, H. W. Müller, F. Reimold, J. Schweinzer, M. Sertoli, G. Tardini, W. Treutterer, E. Viezzer, R. Wenninger, M. Wischmeier, and the ASDEX Upgrade Team, "Impurity seeding for tokamak power exhaust: from present devices via ITER to DEMO," *Plasma Physics and Controlled Fusion*, vol. 55, no. 12, p. 124041, 2013. [Online]. Available: http://stacks.iop.org/0741-3335/55/i=12/a=124041 (cit. on p. 4)

[16] H. H. Andersen, H. L. Bay, R. Behrisch, M. T. Robinson, H. E. Roosendaal, and P. Sigmund, *Sputtering by Particle Bombardment I Physical Sputtering of Single-Element Solids*, R. Behrisch, Ed. Springer-Verlag Berlin Heidelberg New York, 1981, vol. Topics in Applied Physics, no. 47. (cit. on pp. 4 and 6)

[17] R. Behrisch, G. Betz, G. Carter, B. Navinšek, J. Roth, B. M. U. Scherzer, P. D. Townsend, G. K. Wehner, and J. L. Whitton, *Sputtering by Particle Bombardment II Sputtering of Alloys and Compounds, Electron and Neutron Sputtering, Surface Topography*, R. Behrisch, Ed. Springer-Verlag Berlin Heidelberg New York Tokyo, 1983, vol. Topics in Applied Physics, no. 52. (cit. on pp. 5 and 70)

[18] R. Behrisch, W. Hauffe, W. O. Hofer, N. Laegreid, E. D. McClanahan, B. U. R. Sundqvist, K. Wittmaack, and M. L. Yu, *Sputtering by Particle Bombardment III Characteristic of Sputtered Particles, Technical Applications*, R. Behrisch and K. Wittmaack, Eds. Springer-Verlag Berlin Heidelberg New York London Paris Tokyo Hong Kong Barcelona Budapest, 1991, vol. Topics in Applied Physics, no. 64.

[19] W. Eckstein, *Computer Simulation of Ion-Solid Interactions*, U. Gonser, A. Mooradian, H. Lotsch, R. M. Osgood, M. B. Panish, and H. Sakaki, Eds. Springer-Verlag Berlin Heidelberg New York London Paris Tokyo Hong Kong Barcelona Budapest, 1991, vol. Springer Series in Materials Science, no. 10. (cit. on pp. 4, 47 and 48)

[20] H. Bolt, V. Barabash, G. Federici, J. Linke, A. Loarte, J. Roth, and K. Sato, "Plasma facing and high heat flux materials - needs for ITER and beyond," *Journal of Nuclear Materials*, vol. 307 - 311, Part 1, pp. 43 – 52, 2002. [Online]. Available: http://www.sciencedirect.com/science/article/pii/S0022311502011753 (cit. on p. 5)

[21] R. Pitts, S. Carpentier, F. Escourbiac, T. Hirai, V. Komarov, S. Lisgo, A. Kukushkin, A. Loarte, M. Merola, A. S. Naik, R. Mitteau, M. Sugihara, B. Bazylev, and P. Stangeby, "A full tungsten divertor for ITER: Physics issues and design status," *Journal of Nuclear Materials*, vol. 438, pp. S48 – S56, 2013. [Online]. Available: http://www.sciencedirect.com/science/article/pii/S0022311513000160 (cit. on p. 5)

[22] R. Aymar, "ITER status, design and material objectives," *Journal of Nuclear Materials*, vol. 307, pp. 1 – 9, 2002. [Online]. Available: http://www.sciencedirect.com/science/article/pii/S0022311502009376 (cit. on p. 5)

[23] R. Frauenfelder, "Solution and diffusion of hydrogen in tungsten," *Journal of Vacuum Science and Technology*, vol. 6, no. 3, pp. 388–397, 1969. (cit. on pp. 6, 72 and 112)

[24] J. Roth, E. Tsitrone, T. Loarer, V. Philipps, S. Brezinsek, A. Loarte, G. F. Counsell, R. P. Doerner, K. Schmid, O. V.

Ogorodnikova, and R. A. Causey, “Tritium inventory in ITER plasma-facing materials and tritium removal procedures,” *Plasma Physics and Controlled Fusion*, vol. 50, no. 10, pp. 103 001–, 2008. [Online]. Available: http://stacks.iop.org/0741-3335/50/i=10/a=103001 (cit. on p. 6)

[25] M. Shimada, Y. Hatano, P. Calderoni, T. Oda, Y. Oya, M. Sokolov, K. Zhang, G. Cao, R. Kolasinski, and J. Sharpe, “First result of deuterium retention in neutron-irradiated tungsten exposed to high flux plasma in TPE,” *Journal of Nuclear Materials*, vol. 415, no. 1, Supplement, pp. S667 – S671, 2011. [Online]. Available: http://www.sciencedirect.com/science/article/pii/S002231151000752X

[26] M. Shimada, G. Cao, T. Otsuka, M. Hara, M. Kobayashi, Y. Oya, and Y. Hatano, “Irradiation effect on deuterium behaviour in low-dose HFIR neutron-irradiated tungsten,” *Nuclear Fusion*, vol. 55, no. 1, p. 013008, 2015. [Online]. Available: http://stacks.iop.org/0029-5515/55/i=1/a=013008 (cit. on p. 6)

[27] A. Haasz, M. Poon, and J. Davis, “The effect of ion damage on deuterium trapping in tungsten,” *Journal of Nuclear Materials*, vol. 266 - 269, pp. 520 – 525, 1999. [Online]. Available: //www.sciencedirect.com/science/article/pii/S0022311598005868 (cit. on pp. 6 and 49)

[28] K. Tokunaga, M. Baldwin, R. Doerner, N. Noda, Y. Kubota, N. Yoshida, T. Sogabe, T. Kato, and B. Schedler, “Blister formation and deuterium retention on tungsten exposed to low energy and high flux deuterium plasma,” *Journal of Nuclear Materials*, vol. 337 - 339, pp. 887 – 891, 2005. [Online]. Available: //www.sciencedirect.com/science/article/pii/S0022311504009298

[29] G.-N. Luo, W. Shu, and M. Nishi, “Influence of blistering on deuterium retention in tungsten irradiated by high flux deuterium 10-100 eV plasmas,” *Fusion Engineering and Design*, vol. 81, pp. 957 – 962, 2006. [Online]. Available: //www.sciencedirect.com/science/article/pii/S0920379605006125 (cit. on p. 66)

[30] H. Iwakiri, K. Morishita, and N. Yoshida, “Effects of helium bombardment on the deuterium behavior in tungsten,” *Journal of Nuclear Materials*, vol. 307, pp. 135 – 138, 2002. [Online]. Available: http://www.sciencedirect.com/science/article/pii/S0022311502011789

[31] D. Nishijima, H. Iwakiri, K. Amano, M. Ye, N. Ohno, K. Tokunaga, N. Yoshida, and S. Takamura, “Suppression of blister formation and deuterium retention on tungsten surface due to mechanical polishing and helium pre-exposure,” *Nuclear Fusion*, vol. 45, no. 7, p. 669, 2005. [Online]. Available: http://stacks.iop.org/0029-5515/45/i=7/a=016 (cit. on p. 66)

[32] D. Nishijima, T. Sugimoto, H. Iwakiri, M. Ye, N. Ohno, N. Yoshida, and S. Takamura, "Characteristic changes of deuterium retention on tungsten surfaces due to low-energy helium plasma pre-exposure," *Journal of Nuclear Materials*, vol. 337, pp. 927 – 931, 2005. [Online]. Available: http://www.sciencedirect.com/science/article/pii/S002231150400741X

[33] M. Miyamoto, D. Nishijima, Y. Ueda, R. Doerner, H. Kurishita, M. Baldwin, S. Morito, K. Ono, and J. Hanna, "Observations of suppressed retention and blistering for tungsten exposed to deuterium-helium mixture plasmas," *Nuclear Fusion*, vol. 49, no. 6, p. 065035, 2009. [Online]. Available: http://stacks.iop.org/0029-5515/49/i=6/a=065035 (cit. on p. 71)

[34] V. K. Alimov, W. M. Shu, J. Roth, K. Sugiyama, S. Lindig, M. Balden, K. Isobe, and T. Yamanishi, "Surface morphology and deuterium retention in tungsten exposed to low-energy, high flux pure and helium-seeded deuterium plasmas," *Physica Scripta*, vol. 2009, no. T138, pp. 014 048–, 2009. [Online]. Available: http://stacks.iop.org/1402-4896/2009/i=T138/a=014048

[35] O. V. Ogorodnikova, T. Schwarz-Selinger, K. Sugiyama, and V. K. Alimov, "Deuterium retention in tungsten exposed to low-energy pure and helium-seeded deuterium plasmas," *Journal of Applied Physics*, vol. 109, no. 1, p. 013309, 2011. [Online]. Available: http://dx.doi.org/10.1063/1.3505754

[36] Y. Sakoi, M. Miyamoto, K. Ono, and M. Sakamoto, "Helium irradiation effects on deuterium retention in tungsten," *Journal of Nuclear Materials*, vol. 442, no. 1, pp. S715 – S718, 2013. [Online]. Available: http://www.sciencedirect.com/science/article/pii/S0022311512005193

[37] M. Baldwin, R. Doerner, W. Wampler, D. Nishijima, T. Lynch, and M. Miyamoto, "Effect of He on D retention in W exposed to low-energy, high-fluence (D, He, Ar) mixture plasmas," *Nuclear Fusion*, vol. 51, no. 10, p. 103021, 2011. [Online]. Available: http://stacks.iop.org/0029-5515/51/i=10/a=103021 (cit. on p. 6)

[38] M. Miyamoto, D. Nishijima, M. Baldwin, R. Doerner, Y. Ueda, K. Yasunaga, N. Yoshida, and K. Ono, "Microscopic damage of tungsten exposed to deuterium-helium mixture plasma in pisces and its impacts on retention property," *Journal of Nuclear Materials*, vol. 415, no. 1, pp. S657 – S660, 2011. [Online]. Available: http://www.sciencedirect.com/science/article/pii/S0022311511000201

[39] O. V. Ogorodnikova, K. Sugiyama, A. Markin, Y. Gasparyan, V. Efimov, A. Manhard, and M. Balden, "Effect of nitrogen seeding into deuterium plasma on deuterium retention in tungsten," *Physica*

Scripta, vol. 2011, no. T145, p. 014034, 2011. [Online]. Available: http://stacks.iop.org/1402-4896/2011/i=T145/a=014034

[40] L. Gao, W. Jacob, P. Wang, U. von Toussaint, and A. Manhard, “Influence of nitrogen pre-implantation on deuterium retention in tungsten,” *Physica Scripta*, vol. 2014, no. T159, p. 014023, 2014. [Online]. Available: http://stacks.iop.org/1402-4896/2014/i=T159/a=014023

[41] H. Lee, G. D. Temmerman, L. Gao, T. Schwarz-Selinger, G. Meisl, T. Höschen, and Y. Ueda, “Deuterium retention in tungsten exposed to mixed D+N plasma at divertor relevant fluxes in Magnum-PSI,” *Journal of Nuclear Materials*, vol. 463, pp. 974 – 978, 2015. [Online]. Available: http://www.sciencedirect.com/science/article/pii/S0022311514008344

[42] L. Cheng, G. D. Temmerman, P. Z. van Emmichoven, G. Ji, H. Zhou, B. Wang, Y. Yuan, Y. Zhang, and G. Lu, “Effect of neon plasma pre-irradiation on surface morphology and deuterium retention of tungsten,” *Journal of Nuclear Materials*, vol. 463, pp. 1025 – 1028, 2015. [Online]. Available: http://www.sciencedirect.com/science/article/pii/S0022311514009155

[43] T. Finlay, J. Davis, T. Schwarz-Selinger, Z. Siketić, and A. Haasz, “Deuterium retention in recrystallized tungsten irradiated with simultaneous deuterium-neon ion beams,” *Nuclear Materials and Energy*, 2017. [Online]. Available: http://www.sciencedirect.com/science/article/pii/S2352179116302046 (cit. on p. 6)

[44] J. Roth, T. Schwarz-Selinger, V. Alimov, and E. Markina, “Hydrogen isotope exchange in tungsten: Discussion as removal method for tritium,” *Journal of Nuclear Materials*, vol. 432, no. 1 - 3, pp. 341–347, 2013. [Online]. Available: http://www.sciencedirect.com/science/article/pii/S0022311512004138 (cit. on pp. 6, 7, 75, 108, 109 and 145)

[45] V. K. Alimov, B. Tyburska-Püschel, M. H. J. ’t Hoen, J. Roth, Y. Hatano, K. Isobe, M. Matsuyama, and T. Yamanishi, “Hydrogen isotope exchange in tungsten irradiated sequentially with low-energy deuterium and protium,” *Physica Scripta*, vol. 2011, no. T145, pp. 014 037–, 2011. [Online]. Available: http://stacks.iop.org/1402-4896/2011/i=T145/a=014037 (cit. on pp. 6 and 108)

[46] J. Barton, Y. Wang, T. Schwarz-Selinger, R. Doerner, and G. Tynan, “Isotope exchange experiments in tungsten with sequential deuterium and protium plasmas in PISCES,” *Journal of Nuclear Materials*, vol. 438, pp. S1183 – S1186, 2013. [Online]. Available: http://www.sciencedirect.com/science/article/pii/S0022311513002699 (cit. on pp. 6 and 108)

[47] J. Barton, Y. Wang, T. Dittmar, R. Doerner, and G. Tynan, “Deuterium retention in tungsten after heavy ion damage and hydrogen isotope exchange in PISCES,” *Nuclear Instruments and Methods in Physics Research Section B: Beam Interactions with Materials and Atoms*, vol. 332, pp. 275 – 279, 2014. [Online]. Available: http://www.sciencedirect.com/science/article/pii/S0168583X14003346 (cit. on pp. 6 and 75)

[48] I. Takagi, S. Nomura, T. Minamimoto, M. Akiyoshi, T. Kobayashi, and T. Sasaki, “Hydrogen-deuterium exchange on plasma-exposed W and SS surface,” *Journal of Nuclear Materials*, vol. 463, pp. 1125–1128, Aug. 2015. [Online]. Available: http://www.sciencedirect.com/science/article/pii/S0022311514008289 (cit. on pp. 6, 108 and 109)

[49] S. Markelj, O. V. Ogorodnikova, P. Pelicon, T. Schwarz-Selinger, and I. Čadež, “Temperature dependence of D atom adsorption on polycrystalline tungsten,” *Applied Surface Science*, vol. 282, pp. 478 – 486, 2013. [Online]. Available: http://www.sciencedirect.com/science/article/pii/S0169433213010970 (cit. on pp. 6, 7 and 108)

[50] S. Markelj, O. Ogorodnikova, P. Pelicon, T. Schwarz-Selinger, K. Sugiyama, and I. Čadež, “Study of thermal hydrogen atom interaction with undamaged and self-damaged tungsten,” *Journal of Nuclear Materials*, vol. 438, pp. S1027 – S1031, 2013. [Online]. Available: http://www.sciencedirect.com/science/article/pii/S0022311513002328 (cit. on pp. 6 and 109)

[51] A. Založnik, P. Pelicon, Z. Rupnik, I. Čadež, and S. Markelj, “In situ hydrogen isotope detection by ion beam methods ERDA and NRA,” *Nuclear Instruments and Methods in Physics Research Section B: Beam Interactions with Materials and Atoms*, vol. 371, pp. 167 – 173, 2016. [Online]. Available: http://www.sciencedirect.com/science/article/pii/S0168583X15011222 (cit. on pp. 6, 108 and 145)

[52] S. Markelj, A. Založnik, T. Schwarz-Selinger, O. Ogorodnikova, P. Vavpetič, P. Pelicon, and I. Čadež, “In situ NRA study of hydrogen isotope exchange in self-ion damaged tungsten exposed to neutral atoms,” *Journal of Nuclear Materials*, vol. 469, pp. 133 – 144, 2016. [Online]. Available: http://www.sciencedirect.com/science/article/pii/S0022311515303470 (cit. on pp. 6, 7, 109 and 145)

[53] N. Bobyr, V. Alimov, B. Khripunov, A. Spitsyn, M. Mayer, Y. Hatano, A. Golubeva, and V. Petrov, “Influence of helium on hydrogen isotope exchange in tungsten at sequential exposures to deuterium and helium-protium plasmas,” *Journal of Nuclear Materials*, vol. 463, pp. 1122 – 1124, 2015. [Online]. Available: http://www.sciencedirect.com/science/article/pii/S0022311514009647 (cit. on pp. 6 and 109)

[54] B. L. Doyle, D. K. Brice, and W. R. Wampler, "A local mixing model for deuterium replacement in solids," *Radiation Effects*, vol. 57, no. 3, pp. 81–88, 1981. [Online]. Available: http://dx.doi.org/10.1080/01422448008226505 (cit. on p. 7)

[55] W. Möller, F. Besenbacher, and J. Bottiger, "Saturation and isotope mixing during low-temperature implantations of hydrogen into metals," *Applied Physics A*, vol. 27, no. 1, pp. 19–29, 1982. [Online]. Available: http://dx.doi.org/10.1007/BF01197542 (cit. on p. 7)

[56] J. Barton, Y. Wang, R. Doerner, and G. Tynan, "Development of an analytical diffusion model for modeling hydrogen isotope exchange," *Journal of Nuclear Materials*, vol. 463, pp. 1129 – 1133, 2015. [Online]. Available: http://www.sciencedirect.com/science/article/pii/S0022311514010708 (cit. on p. 7)

[57] A. H. M. Krom and A. Bakker, "Hydrogen trapping models in steel," *Metallurgical and Materials Transactions B*, vol. 31, no. 6, pp. 1475–1482, 2000. [Online]. Available: http://dx.doi.org/10.1007/s11663-000-0032-0 (cit. on pp. 7, 31, 34 and 41)

[58] D. F. Johnson and E. A. Carter, "Hydrogen in tungsten: Absorption, diffusion, vacancy trapping, and decohesion," *Journal of Materials Research*, vol. 25, pp. 315–327, 2010. [Online]. Available: http://journals.cambridge.org/article_S0884291400006075 (cit. on pp. 7, 42 and 104)

[59] K. Heinola, T. Ahlgren, K. Nordlund, and J. Keinonen, "Hydrogen interaction with point defects in tungsten," *Phys. Rev. B*, vol. 82, p. 094102, 2010. [Online]. Available: http://link.aps.org/doi/10.1103/PhysRevB.82.094102

[60] L. Sun, S. Jin, X.-C. Li, Y. Zhang, and G.-H. Lu, "Hydrogen behaviors in molybdenum and tungsten and a generic vacancy trapping mechanism for H bubble formation," *Journal of Nuclear Materials*, vol. 434, no. 1 - 3, pp. 395 – 401, 2013. [Online]. Available: http://www.sciencedirect.com/science/article/pii/S0022311512006654 (cit. on p. 67)

[61] N. Fernandez, Y. Ferro, and D. Kato, "Hydrogen diffusion and vacancies formation in tungsten: Density functional theory calculations and statistical models," *Acta Materialia*, vol. 94, pp. 307 – 318, 2015. [Online]. Available: http://www.sciencedirect.com/science/article/pii/S1359645415003043 (cit. on pp. 7, 8, 42, 104, 115 and 118)

[62] D. Terentyev, V. Dubinko, A. Bakaev, Y. Zayachuk, W. V. Renterghem, and P. Grigorev, "Dislocations mediate hydrogen retention in tungsten," *Nuclear Fusion*, vol. 54, no. 4, p. 042004, 2014. [Online]. Available: http://stacks.iop.org/0029-5515/54/i=4/a=042004 (cit. on pp. 7, 67 and 104)

[63] K. Schmid, U. von Toussaint, and T. Schwarz-Selinger, “Transport of hydrogen in metals with occupancy dependent trap energies,” *Journal of Applied Physics*, vol. 116, no. 13, 2014. [Online]. Available: http://scitation.aip.org/content/aip/journal/jap/116/13/10.1063/1.4896580 (cit. on pp. 7, 8, 31, 35, 39, 42 and 111)

[64] U. von Toussaint, T. Schwarz-Selinger, and K. Schmid, “First-passage kinetic monte carlo on lattices: Hydrogen transport in lattices with traps,” *Journal of Nuclear Materials*, vol. 463, pp. 1075 – 1079, 2015. [Online]. Available: http://www.sciencedirect.com/science/article/pii/S0022311514008423 (cit. on pp. 7, 31 and 35)

[65] K. Schmid, J. Bauer, T. Schwarz-Selinger, S. Markelj, U. von Toussaint, A. Manhard, and W. Jacob, “Recent progress in the understanding of H transport and trapping in W,” *Physica Scripta*, vol. submitted, 2017. (cit. on pp. 8, 31, 34, 39, 42 and 111)

[66] W. Möller, W. Eckstein, and J. Biersack, “Tridyn-binary collision simulation of atomic collisions and dynamic composition changes in solids,” *Computer Physics Communications*, vol. 51, no. 3, pp. 355 – 368, 1988. [Online]. Available: http://www.sciencedirect.com/science/article/pii/0010465588901488 (cit. on pp. 8, 31, 47, 105, 113, 153 and 154)

[67] A. Mutzke, R. Schneider, W. Eckstein, and R. Dohmen, “SDTrimSP version 5.00 IPP 12/8,” Max-Planck-Institut für Plasmaphysik, Garching, Germany, 2011. [Online]. Available: http://pubman.mpdl.mpg.de/pubman/item/escidoc:2139848:1/component/escidoc:2139847/IPP%2012_8.pdf (cit. on pp. 8, 31, 47, 105, 113, 153 and 154)

[68] M. Mayer, “SIMNRA User’s Guide IPP 9/113,” Max-Planck-Institut für Plasmaphysik, Garching, Germany, 1997. (cit. on pp. 11, 23 and 25)

[69] K. Schmid and U. von Toussaint, “Statistically sound evaluation of trace element depth profiles by ion beam analysis,” *Nuclear Instruments and Methods in Physics Research Section B: Beam Interactions with Materials and Atoms*, vol. 281, no. 0, pp. 64 – 71, 2012. [Online]. Available: http://www.sciencedirect.com/science/article/pii/S0168583X12002042 (cit. on pp. 11, 23, 24 and 25)

[70] I. Bizyukov and K. Krieger, “Dual beam experiment for simultaneous irradiation of surfaces with ion species of gaseous and solid-state elements,” *Review of Scientific Instruments*, vol. 77, no. 4, pp. 043 501–043 501–10, 2006. (cit. on pp. 11, 20 and 151)

[71] D. Aitken, R. J. Anderson, A. E. Bell, I. G. Brown, C. Burkhart, E. Donets, B. F. Gavin, R. A. Gerber, A. J. T. Holmes, R. H. Hughes,

S. Humphries, Jr., J. Ishikawa, Y. Jongen, R. Keller, L. K. Len, K. N. Leung, C. M. Lyneis, N. Sakudo, P. Spädtke, and L. W. Swanson, *The Physics and Technology of Ion Sources*, I. G. Brown, Ed. John Wiley & Sons, Inc. New York Chichester Brisbane Toronto Singapore, 1989. (cit. on pp. 19, 20 and 151)

[72] Peabody Scientific, Peabody, MA 01960, USA. [Online]. Available: http://www.peabody-scientific.com/ (cit. on p. 19)

[73] J. Huot, D. Banks, H. Fritzsche, B. C. Hauback, H. Mauroy, R. Černý, M. H. Sørby, F. Klose, C. Rehm, Z. Tun, M. Wolff, B. Hjörvarsson, S. Sartori, K. D. Knudsen, A. Griesche, M. Große, B. Schillinger, M. A. Gharghouri, D. K. Ross, D. L. Roach, P. Berger, C. Raepsaet, H. Khodja, H. Becker, D. Rogalla, A. V. Skripov, and M. G. Shelyapina, *Neutron Scattering and Other Nuclear Techniques for Hydrogen in Materials*, H. Fritzsche, J. Huot, and D. Fruchart, Eds. Springer International Publishing Switzerland, 2016, vol. Neutron Scattering Applications and Techniques. (cit. on p. 20)

[74] M. Nastasi, J. W. Mayer, Y. Wang, C. Jeynes, R. L. Thompson, L. Shao, A. Misra, T. Calligaro, J. Dran, H. J. Whitlow, M. Ren, N. P. Barradas, M. Mayer, M. A. Reis, and F. Schiettekatte, *Ion Beam Analysis Fundamentals and Applications.* CRC Press Taylor & Francis Group Boca Raton London New York, 2015. (cit. on pp. 20 and 151)

[75] B. Wielunska, M. Mayer, T. Schwarz-Selinger, U. von Toussaint, and J. Bauer, "Cross section data for the D(^{3}He,p)^{4}He nuclear reaction from 0.25 to 6 MeV ," *Nuclear Instruments and Methods in Physics Research Section B: Beam Interactions with Materials and Atoms*, vol. 371, pp. 41 – 45, 2016. [Online]. Available: http://www.sciencedirect.com/science/article/pii/S0168583X15009222 (cit. on p. 21)

[76] M. Mayer, E. Gauthier, K. Sugiyama, and U. von Toussaint, "Quantitative depth profiling of deuterium up to very large depths," *Nuclear Instruments and Methods in Physics Research Section B: Beam Interactions with Materials and Atoms*, vol. 267, no. 3, pp. 506 – 512, 2009. [Online]. Available: http://www.sciencedirect.com/science/article/pii/S0168583X08013050 (cit. on pp. 22 and 23)

[77] B. Wielunska, M. Mayer, and T. Schwarz-Selinger, "Optimization of the depth resolution for deuterium depth profiling up to large depths," *Nuclear Instruments and Methods in Physics Research Section B: Beam Interactions with Materials and Atoms*, vol. 387, pp. 103 – 114, 2016. [Online]. Available: http://www.sciencedirect.com/science/article/pii/S0168583X16303780 (cit. on p. 22)

[78] A. Manhard, "Deuterium inventory in tungsten after plasma exposure: A microstructural study," Ph.D. dissertation, Augsburg University, 2012. (cit. on pp. 25, 26 and 27)

[79] L. Reimer, *Scanning Electron Microscopy Physics of Image Formation and Microanalysis*, 2nd ed., ser. Springer Series in Optical Sciences, P. W. Hawkes, Ed. Springer-Verlag Berlin Heidelberg, 1998, vol. 45. (cit. on p. 26)

[80] R. Reichelt, *Science of Microscopy.* Springer Science + Business Media, LLC, New York, 2007, vol. 1, ch. Scanning Electron Microscopy, pp. 133–272. (cit. on pp. 26 and 28)

[81] V. Randle, *Microtexture determination and its applications.* The Institute of Materials London, 1992. (cit. on pp. 28, 55 and 62)

[82] Plansee Holding AG, A-6600 Reutte, Austria. [Online]. Available: http://www.plansee-group.com (cit. on p. 28)

[83] A. Manhard, M. Balden, and S. Elgeti, "Quantitative microstructure and defect density analysis of polycrystalline tungsten reference samples after different heat treatments," *PM*, vol. 52, no. 8, pp. 437–466, 2015. [Online]. Available: http://dx.doi.org/10.3139/147.110354 (cit. on pp. 28, 29 and 55)

[84] A. Manhard, G. Matern, and M. Balden, "A step-by-step analysis of the polishing process for tungsten specimens," *PM*, vol. 50, no. 1, pp. 5–16, 2013. [Online]. Available: http://dx.doi.org/10.3139/147.110215 (cit. on p. 29)

[85] K. Schmid, V. Rieger, and A. Manhard, "Comparison of hydrogen retention in W and W/Ta alloys," *Journal of Nuclear Materials*, vol. 426, no. 1 - 3, pp. 247 – 253, 2012. [Online]. Available: http://www.sciencedirect.com/science/article/pii/S0022311512001730 (cit. on pp. 31 and 39)

[86] J. Roth and K. Schmid, "Hydrogen in tungsten as plasma-facing material," *Physica Scripta*, vol. 2011, no. T145, pp. 014 031–, 2011. [Online]. Available: http://stacks.iop.org/1402-4896/2011/i=T145/a=014031 (cit. on pp. 31 and 105)

[87] Y. Fukai, *The Metal-Hydrogen System Basic Bulk Properties*, R. Hull, R. M. Osgood Jr., J. Parisi, and H. Warlimont, Eds. Springer-Verlag Berlin Heidelberg, 2005, vol. Material Science, no. 21. (cit. on pp. 31, 32, 34, 40 and 46)

[88] S. T. Picraux and F. L. Vook, "Deuterium lattice location in Cr and W," *Physical Review Letters*, vol. 33, pp. 1216–1220, 1974. [Online]. Available: https://link.aps.org/doi/10.1103/PhysRevLett.33.1216 (cit. on p. 32)

[89] K. Heinola and T. Ahlgren, "Diffusion of hydrogen in bcc tungsten studied with first principle calculations," *Journal of Applied Physics*, vol. 107, no. 11, 2010. [Online]. Available: http://scitation.aip.org/content/aip/journal/jap/107/11/10.1063/1.3386515 (cit. on pp. 32, 105, 112 and 113)

[90] R. Kirchheim, "Hydrogen solubility and diffusivity in defective and amorphous metals," *Progress in Materials Science*, vol. 32, no. 4, pp. 261 – 325, 1988. [Online]. Available: http://www.sciencedirect.com/science/article/pii/0079642588900102 (cit. on pp. 33, 39 and 113)

[91] G. Alefeld, T. Schober, H. Wenzel, E. Wicke, H. Brodowsky, B. Baranowsky, R. Wiswall, B. Stritzker, H. Wühl, H. Wipf, and C. A. Wert, *Hydrogen in Metals II Application-Oriented Properties*, G. Alefeld and J. Völkl, Eds. Springer-Verlag Berlin Heidelberg New York, 1978. (cit. on pp. 33 and 34)

[92] U. von Toussaint and S. Gori, "Modeling hydrogen transport in large disordered systems," *Physica Scripta*, vol. 2014, no. T159, p. 014058, 2014. [Online]. Available: http://stacks.iop.org/1402-4896/2014/i=T159/a=014058 (cit. on p. 34)

[93] G. Alefeld, J. Völkl, H. Wagner, H. Peisl, T. Springer, A. C. Switendick, F. Wagner, G. Wortmann, W. E. Wallace, K. W. Kehr, R. M. Cotts, K. Sköld, H. Kronmüller, and A. Seeger, *Hydrogen in Metals I Basic Properties*, G. Alefeld and J. Völkl, Eds. Springer-Verlag Berlin Heidelberg, 1978. (cit. on p. 34)

[94] H. Wipf, H. Grabert, H. T. Schober, R. G. Barnes, D. K. Ross, H. Vehoff, and P. Dantzer, *Hydrogen in Metals III Properties and Applications*, H. Wipf, Ed. Springer-Verlag Berlin Heidelberg, 1997. (cit. on p. 34)

[95] A. Donev, V. V. Bulatov, T. Oppelstrup, G. H. Gilmer, B. Sadigh, and M. H. Kalos, "A first-passage kinetic monte carlo algorithm for complex diffusion-reaction systems," *Journal of Computational Physics*, vol. 229, no. 9, pp. 3214 – 3236, 2010. [Online]. Available: http://www.sciencedirect.com/science/article/pii/S0021999110000057 (cit. on p. 39)

[96] G. R. Longhurst and J. Ambrosek, "Verification and validation of the tritium transport code TMAP7," *Fusion Science and Technology*, vol. 48, p. 468, 2005. (cit. on pp. 39 and 46)

[97] E. Hodille, X. Bonnin, R. Bisson, T. Angot, C. Becquart, J. Layet, and C. Grisolia, "Macroscopic rate equation modeling of trapping/detrapping of hydrogen isotopes in tungsten materials," *Journal of Nuclear Materials*, vol. 467, pp. 424 – 431, 2015. [Online]. Available: http://www.sciencedirect.com/science/article/pii/S0022311515300660 (cit. on p. 39)

[98] O. V. Ogorodnikova, J. Roth, and M. Mayer, “Ion-driven deuterium retention in tungsten,” *Journal of Applied Physics*, vol. 103, no. 3, pp. 034 902–034 902–10, 2008. (cit. on pp. 41, 49 and 115)

[99] M. Pick and K. Sonnenberg, “A model for atomic hydrogen-metal interaction - application to recycling, recombination and permeation,” *Journal of Nuclear Materials*, vol. 131, no. 2, pp. 208 – 220, 1985. [Online]. Available: http://www.sciencedirect.com/science/article/pii/0022311585904593 (cit. on p. 46)

[100] P. W. Atkins, *Physical Chemistry*, 3rd ed. Oxford: Oxford University Press, 1986. (cit. on pp. 46 and 112)

[101] E. A. Hodille, Y. Ferro, N. Fernandez, C. S. Becquart, T. Angot, J. M. Layet, R. Bisson, and C. Grisolia, “Study of hydrogen isotopes behavior in tungsten by a multi trapping macroscopic rate equation model,” *Physica Scripta*, vol. 2016, no. T167, p. 014011, 2016. [Online]. Available: http://stacks.iop.org/1402-4896/2016/i=T167/a=014011 (cit. on p. 46)

[102] E. Hodille, A. Založnik, S. Markelj, T. Schwarz-Selinger, C. Becquart, R. Bisson, and C. Grisolia, “Simulations of atomic deuterium exposure in self-damaged tungsten,” *Nuclear Fusion*, vol. 57, no. 5, p. 056002, 2017. [Online]. Available: http://stacks.iop.org/0029-5515/57/i=5/a=056002

[103] A. Založnik, S. Markelj, T. Schwarz-Selinger, and K. Schmid, “Deuterium atom loading of self-damaged tungsten at different sample temperatures,” *Journal of Nuclear Materials*, vol. 496, no. Supplement C, pp. 1 – 8, 2017. [Online]. Available: http://www.sciencedirect.com/science/article/pii/S0022311517306827 (cit. on pp. 46 and 75)

[104] Wolfram Research, Inc., *Mathematica 10.3*, Wolfram Research, Inc., Champaign, Illinois, 2015. (cit. on p. 46)

[105] A. Hindmarsh and A. Taylor, “User documentation for IDA, a different-algebraic equation solver for sequential and parallel computers,” Lawrence Livermore National Laboratory report UCRL-MA-136910, 1999. [Online]. Available: https://computation.llnl.gov/casc/nsde/pubs/237206.pdf (cit. on p. 47)

[106] J. Biersack and L. Haggmark, “A monte carlo computer program for the transport of energetic ions in amorphous targets,” *Nuclear Instruments and Methods*, vol. 174, no. 1, pp. 257 – 269, 1980. [Online]. Available: http://www.sciencedirect.com/science/article/pii/0029554X80904401 (cit. on p. 47)

[107] W. D. Wilson, L. G. Haggmark, and J. P. Biersack, “Calculations of nuclear stopping, ranges, and straggling in the low-energy region,”

Phys. Rev. B, vol. 15, pp. 2458–2468, 1977. [Online]. Available: https://link.aps.org/doi/10.1103/PhysRevB.15.2458 (cit. on p. 47)

[108] O. S. Oen and M. T. Robinson, "Computer studies of the reflection of light ions from solids," *Nuclear Instruments and Methods*, vol. 132, pp. 647 – 653, 1976. [Online]. Available: http://www.sciencedirect.com/science/article/pii/0029554X76908065 (cit. on p. 47)

[109] J. Lindhard and M. Scharff, "Energy dissipation by ions in the keV region," *Phys. Rev.*, vol. 124, pp. 128–130, 1961. [Online]. Available: https://link.aps.org/doi/10.1103/PhysRev.124.128 (cit. on p. 47)

[110] N. Enomoto, S. Muto, T. Tanabe, J. Davis, and A. Haasz, "Grazing-incidence electron microscopy of surface blisters in single- and polycrystalline tungsten formed by H^+, D^+ and He^+ irradiation," *Journal of Nuclear Materials*, vol. 385, no. 3, pp. 606 – 614, 2009. [Online]. Available: http://www.sciencedirect.com/science/article/pii/S0022311509003213 (cit. on pp. 49, 66, 68 and 69)

[111] P. Gumbsch, J. Riedle, A. Hartmaier, and H. F. Fischmeister, "Controlling factors for the brittle-to-ductile transition in tungsten single crystals," *Science*, vol. 282, no. 5392, pp. 1293–1295, 1998. [Online]. Available: http://science.sciencemag.org/content/282/5392/1293 (cit. on pp. 49, 67 and 71)

[112] P. Gumbsch, "Brittle fracture and the brittle-to-ductile transition of tungsten," *Journal of Nuclear Materials*, vol. 323, no. 2 - 3, pp. 304 – 312, 2003. [Online]. Available: http://www.sciencedirect.com/science/article/pii/S0022311503003738 (cit. on pp. 49, 67 and 71)

[113] G. Wright, D. Whyte, and B. Lipschultz, "Measurement of hydrogenic retention and release in molybdenum with the DIONISOS experiment," *Journal of Nuclear Materials*, vol. 390 - 391, no. 0, pp. 544–549, 2009. [Online]. Available: http://www.sciencedirect.com/science/article/pii/S0022311509001767 (cit. on pp. 51 and 83)

[114] S. Markelj, T. Schwarz-Selinger, and A. Založnik, "Hydrogen isotope accumulation in the helium implantation zone in tungsten," *Nuclear Fusion*, vol. 57, no. 6, p. 064002, 2017. [Online]. Available: http://stacks.iop.org/0029-5515/57/i=6/a=064002 (cit. on pp. 51 and 83)

[115] M. Balden, S. Lindig, A. Manhard, and J.-H. You, "D_2 gas-filled blisters on deuterium-bombarded tungsten," *Journal of Nuclear Materials*, vol. 414, no. 1, pp. 69 – 72, 2011. [Online]. Available: http://www.sciencedirect.com/science/article/pii/S0022311511003904 (cit. on p. 66)

[116] M. ’t Hoen, M. Balden, A. Manhard, M. Mayer, S. Elgeti, A. Kleyn, and P. Z. van Emmichoven, “Surface morphology and deuterium retention of tungsten after low- and high-flux deuterium plasma exposure,” *Nuclear Fusion*, vol. 54, no. 8, p. 083014, 2014. [Online]. Available: http://stacks.iop.org/0029-5515/54/i=8/a=083014 (cit. on p. 66)

[117] M. Balden, A. Manhard, and S. Elgeti, “Deuterium retention and morphological modifications of the surface in five grades of tungsten after deuterium plasma exposure,” *Journal of Nuclear Materials*, vol. 452, no. 1â€“3, pp. 248 – 256, 2014. [Online]. Available: http://www.sciencedirect.com/science/article/pii/S0022311514002852 (cit. on p. 66)

[118] W. Shu, E. Wakai, and T. Yamanishi, “Blister bursting and deuterium bursting release from tungsten exposed to high fluences of high flux and low energy deuterium plasma,” *Nuclear Fusion*, vol. 47, no. 3, pp. 201–, 2007. [Online]. Available: http://stacks.iop.org/0029-5515/47/i=3/a=006 (cit. on p. 66)

[119] L. Gao, U. von Toussaint, W. Jacob, M. Balden, and A. Manhard, “Suppression of hydrogen-induced blistering of tungsten by pre-irradiation at low temperature,” *Nuclear Fusion*, vol. 54, no. 12, p. 122003, 2014. [Online]. Available: http://stacks.iop.org/0029-5515/54/i=12/a=122003

[120] Y. Jia, G. D. Temmerman, G.-N. Luo, H. Xu, C. Li, B. Fu, and W. Liu, “Surface morphology and deuterium retention in tungsten exposed to high flux D plasma at high temperatures,” *Journal of Nuclear Materials*, vol. 457, pp. 213 – 219, 2015. [Online]. Available: http://www.sciencedirect.com/science/article/pii/S0022311514008824 (cit. on pp. 66 and 71)

[121] S. Lindig, M. Balden, V. K. Alimov, T. Yamanishi, W. M. Shu, and J. Roth, “Subsurface morphology changes due to deuterium bombardment of tungsten,” *Physica Scripta*, vol. 2009, no. T138, pp. 014 040–, 2009. [Online]. Available: http://stacks.iop.org/1402-4896/2009/i=T138/a=014040 (cit. on pp. 66 and 71)

[122] V. Alimov, W. Shu, J. Roth, S. Lindig, M. Balden, K. Isobe, and T. Yamanishi, “Temperature dependence of surface topography and deuterium retention in tungsten exposed to low-energy, high-flux D plasma,” *Journal of Nuclear Materials*, vol. 417, no. 1 - 3, pp. 572 – 575, 2011. [Online]. Available: http://www.sciencedirect.com/science/article/pii/S0022311511001206 (cit. on p. 66)

[123] G.-N. Luo, W. Shu, and M. Nishi, “Incident energy dependence of blistering at tungsten irradiated by low energy high flux deuterium plasma beams,” *Journal of Nuclear Materials*, vol. 347, no. 1 - 2, pp. 111 – 117,

2005. [Online]. Available: http://www.sciencedirect.com/science/article/pii/S0022311505003752 (cit. on p. 66)

[124] L. Buzi, G. D. Temmerman, B. Unterberg, M. Reinhart, A. Litnovsky, V. Philipps, G. V. Oost, and S. Möller, “Influence of particle flux density and temperature on surface modifications of tungsten and deuterium retention,” *Journal of Nuclear Materials*, vol. 455, no. 1 - 3, pp. 316 – 319, 2014. [Online]. Available: http://www.sciencedirect.com/science/article/pii/S0022311514004164 (cit. on p. 66)

[125] H. Xu, Y. Zhang, Y. Yuan, B. Fu, A. Godfrey, G. D. Temmerman, W. Liu, and X. Huang, “Observations of orientation dependence of surface morphology in tungsten implanted by low energy and high flux D plasma,” *Journal of Nuclear Materials*, vol. 443, no. 1 - 3, pp. 452 – 457, 2013. [Online]. Available: http://www.sciencedirect.com/science/article/pii/S0022311513009501 (cit. on pp. 66 and 71)

[126] G.-N. Luo, K. Umstadter, W. Shu, W. Wampler, and G.-H. Lu, “Behavior of tungsten with exposure to deuterium plasmas,” *Nuclear Instruments and Methods in Physics Research Section B: Beam Interactions with Materials and Atoms*, vol. 267, no. 18, pp. 3041 – 3045, 2009. [Online]. Available: http://www.sciencedirect.com/science/article/pii/S0168583X09007150 (cit. on p. 66)

[127] Y. Zayachuk, I. Tanyeli, S. V. Boxel, K. Bystrov, T. Morgan, and S. Roberts, “Combined effects of crystallography, heat treatment and surface polishing on blistering in tungsten exposed to high-flux deuterium plasma,” *Nuclear Fusion*, vol. 56, no. 8, p. 086007, 2016. [Online]. Available: http://stacks.iop.org/0029-5515/56/i=8/a=086007 (cit. on pp. 66 and 71)

[128] A. Manhard, M. Balden, and U. von Toussaint, “Blister formation on rough and technical tungsten surfaces exposed to deuterium plasma,” *Nuclear Fusion*, vol. 57, no. 12, p. 126012, 2017. [Online]. Available: http://stacks.iop.org/0029-5515/57/i=12/a=126012 (cit. on pp. 66 and 74)

[129] K. Arshad, Y. Yuan, L. Cheng, J. Wang, Z.-J. Zhou, G. D. Temmerman, and G.-H. Lu, “Deuterium blistering in tungsten and tungsten vanadium alloys,” *Fusion Engineering and Design*, vol. 107, pp. 25 – 31, 2016. [Online]. Available: http://www.sciencedirect.com/science/article/pii/S0920379616302782 (cit. on pp. 66 and 71)

[130] H. Xu, G. Luo, H. Schut, Y. Yuan, B. Fu, A. Godfrey, W. Liu, and G. Temmerman, “Enhanced modification of tungsten surface by nanostructure formation during high flux deuterium plasma exposure,” *Journal of Nuclear Materials*, vol. 447, no. 1 - 3, pp. 22–27, 2014.

[Online]. Available: http://www.sciencedirect.com/science/article/pii/S0022311513012968

[131] H. Xu, W. Liu, G. Luo, Y. Yuan, Y. Jia, B. Fu, and G. D. Temmerman, “Blistering on tungsten surface exposed to high flux deuterium plasma,” *Journal of Nuclear Materials*, vol. 471, pp. 51 – 58, 2016. [Online]. Available: http://www.sciencedirect.com/science/article/pii/S0022311515303949

[132] W. M. Shu, A. Kawasuso, Y. Miwa, E. Wakai, G.-N. Luo, and T. Yamanishi, “Microstructure dependence of deuterium retention and blistering in the near-surface region of tungsten exposed to high flux deuterium plasmas of 38 eV at 315 K,” *Physica Scripta*, vol. 2007, no. T128, p. 96, 2007. [Online]. Available: http://stacks.iop.org/1402-4896/2007/i=T128/a=019 (cit. on p. 66)

[133] Y. Jia, W. Liu, B. Xu, G.-N. Luo, S. Qu, T. Morgan, and G. D. Temmerman, “Mechanism for orientation dependence of blisters on W surface exposed to D plasma at low temperature,” *Journal of Nuclear Materials*, vol. 477, pp. 165 – 171, 2016. [Online]. Available: http://www.sciencedirect.com/science/article/pii/S0022311516301921 (cit. on pp. 66 and 71)

[134] S. K. Erents and G. M. McCracken, “Blistering of molybdenum under helium ion bombardment,” *Radiation Effects*, vol. 18, no. 3-4, pp. 191–198, 1973. [Online]. Available: http://dx.doi.org/10.1080/00337577308232121 (cit. on pp. 66 and 71)

[135] G. Thomas and W. Bauer, “Surface deformation in He and H implanted metals,” *Journal of Nuclear Materials*, vol. 53, pp. 134 – 141, 1974. [Online]. Available: http://www.sciencedirect.com/science/article/pii/0022311574902347 (cit. on p. 67)

[136] J. Roth, R. Behrisch, and B. Scherzer, “Blistering of niobium due to 0.5 to 9 keV helium and hydrogen bombardment,” *Journal of Nuclear Materials*, vol. 53, pp. 147 – 153, 1974. [Online]. Available: http://www.sciencedirect.com/science/article/pii/0022311574902360

[137] S. Picraux, E. EerNisse, and F. Vook, Eds., *Applications of ion beams to metals.* Plenum Press New York, 1974. (cit. on pp. 66 and 67)

[138] W. D. Wilson, C. L. Bisson, and M. I. Baskes, “Self-trapping of helium in metals,” *Phys. Rev. B*, vol. 24, pp. 5616–5624, 1981. [Online]. Available: https://link.aps.org/doi/10.1103/PhysRevB.24.5616 (cit. on p. 66)

[139] J. Condon and T. Schober, “Hydrogen bubbles in metals,” *Journal of Nuclear Materials*, vol. 207, pp. 1 – 24, 1993. [Online]. Available:

http://www.sciencedirect.com/science/article/pii/002231159390244S (cit. on p. 67)

[140] G. Greenwood, A. Foreman, and D. Rimmer, "The role of vacancies and dislocations in the nucleation and growth of gas bubbles in irradiated fissile material," *Journal of Nuclear Materials*, vol. 1, no. 4, pp. 305 – 324, 1959. [Online]. Available: http://www.sciencedirect.com/science/article/pii/0022311559900303 (cit. on p. 67)

[141] R. Nelson, "Radiation blistering - An interpretation based on radiation-stimulated vacancy migration," *Journal of Nuclear Materials*, vol. 88, no. 2, pp. 322 – 324, 1980. [Online]. Available: http://www.sciencedirect.com/science/article/pii/0022311580902913 (cit. on p. 67)

[142] J. Evans, "An interbubble fracture mechanism of blister formation on helium-irradiated metals," *Journal of Nuclear Materials*, vol. 68, no. 2, pp. 129 – 140, 1977. [Online]. Available: http://www.sciencedirect.com/science/article/pii/002231157790232X (cit. on p. 67)

[143] W. Wolfer, "The role of gas pressure and lateral stress on blistering," *Journal of Nuclear Materials*, vol. 93, pp. 713 – 720, 1980. [Online]. Available: http://www.sciencedirect.com/science/article/pii/002231158090197X (cit. on p. 67)

[144] W. Primak and J. Luthra, "Radiation blistering: Interferometric and microscopic observations of oxides, silicon, and metals," *Journal of Applied Physics*, vol. 37, no. 6, pp. 2287–2294, 1966. [Online]. Available: http://dx.doi.org/10.1063/1.1708805 (cit. on p. 67)

[145] E. P. EerNisse and S. T. Picraux, "Role of integrated lateral stress in surface deformation of He-implanted surfaces," *Journal of Applied Physics*, vol. 48, no. 1, pp. 9–17, 1977. [Online]. Available: http://dx.doi.org/10.1063/1.323332 (cit. on p. 67)

[146] K. Kamada and Y. Higashida, "A fracture model of radiation blistering," *Journal of Applied Physics*, vol. 50, no. 6, pp. 4131–4138, 1979. [Online]. Available: http://dx.doi.org/10.1063/1.326493 (cit. on p. 67)

[147] J.-H. You, "Mechanics of tungsten blistering: A finite element study," *Journal of Nuclear Materials*, vol. 437, no. 1, pp. 24 – 28, 2013. [Online]. Available: http://www.sciencedirect.com/science/article/pii/S0022311513003930 (cit. on p. 67)

[148] F. Maury, M. Biget, P. Vajda, A. Lucasson, and P. Lucasson, "Frenkel pair creation and stage I recovery in W crystals irradiated near threshold,"

Radiation Effects, vol. 38, no. 1-2, pp. 53–65, 1978. [Online]. Available: http://dx.doi.org/10.1080/00337577808233209 (cit. on p. 67)

[149] A. Manhard, U. von Toussaint, M. Balden, S. Elgeti, T. Schwarz-Selinger, L. Gao, S. Kapser, T. Płociński, J. Grzonka, M. Gloc, and L. Ciupiński, "Microstructure and defect analysis in the vicinity of blisters in polycrystalline tungsten," *Nuclear Materials and Energy*, 2016. [Online]. Available: http://www.sciencedirect.com/science/article/pii/S2352179116300369 (cit. on pp. 69 and 104)

[150] M. Hou, C. Ortiz, C. Becquart, C. Domain, U. Sarkar, and A. Debacker, "Microstructure evolution of irradiated tungsten: Crystal effects in He and H implantation as modelled in the binary collision approximation," *Journal of Nuclear Materials*, vol. 403, no. 1 - 3, pp. 89–100, 2010. [Online]. Available: http://www.sciencedirect.com/science/article/pii/S002231151000245X (cit. on pp. 70, 73 and 75)

[151] E. V. Kornelsen, F. Brown, J. A. Davies, B. Domeij, and G. R. Piercy, "Penetration of heavy ions of keV energies into monocrystalline tungsten," *Phys. Rev.*, vol. 136, pp. A849–A858, 1964. [Online]. Available: https://link.aps.org/doi/10.1103/PhysRev.136.A849 (cit. on p. 70)

[152] J. Bauer, T. Schwarz-Selinger, K. Schmid, M. Balden, A. Manhard, and U. von Toussaint, "Influence of near-surface blisters on deuterium transport in tungsten," *Nuclear Fusion*, vol. 57, no. 8, p. 086015, 2017. [Online]. Available: http://stacks.iop.org/0029-5515/57/i=8/a=086015 (cit. on pp. 70, 74, 79, 88, 105, 111 and 112)

[153] C. R. Fahlstrom and M. K. Sinha, "Surface blistering of molybdenum irradiated with 75 - 350 keV helium ions," *Journal of Vacuum Science and Technology*, vol. 15, no. 2, pp. 675–678, 1978. [Online]. Available: http://dx.doi.org/10.1116/1.569670 (cit. on p. 71)

[154] J. Riedle, P. Gumbsch, and H. F. Fischmeister, "Cleavage anisotropy in tungsten single crystals," *Phys. Rev. Lett.*, vol. 76, pp. 3594–3597, 1996. [Online]. Available: https://link.aps.org/doi/10.1103/PhysRevLett.76.3594 (cit. on p. 71)

[155] W. Shu, G.-N. Luo, and T. Yamanishi, "Mechanisms of retention and blistering in near-surface region of tungsten exposed to high flux deuterium plasmas of tens of eV," *Journal of Nuclear Materials*, vol. 367 - 370, Part B, no. 0, pp. 1463–1467, 2007. [Online]. Available: http://www.sciencedirect.com/science/article/pii/S0022311507006241 (cit. on p. 71)

[156] R. Blewer, R. Behrisch, B. Scherzer, and R. Schulz, "Trapping and replacement of 1 - 14 keV hydrogen and deuterium in 316

stainless steel," *Journal of Nuclear Materials*, vol. 76, pp. 305 – 312, 1978. [Online]. Available: http://www.sciencedirect.com/science/article/pii/0022311578901629 (cit. on pp. 73 and 109)

[157] W. Eckstein, "Reflection (backscattering) IPP 17/12," Max-Planck-Institut für Plasmaphysik, Garching, Germany, August 2009. (cit. on p. 73)

[158] B. Tyburska, V. Alimov, O. Ogorodnikova, K. Schmid, and K. Ertl, "Deuterium retention in self-damaged tungsten," *Journal of Nuclear Materials*, vol. 395, no. 1 - 3, pp. 150 – 155, 2009. [Online]. Available: http://www.sciencedirect.com/science/article/pii/S002231150900854X (cit. on pp. 74 and 75)

[159] O. Ogorodnikova, B. Tyburska, V. Alimov, and K. Ertl, "The influence of radiation damage on the plasma-induced deuterium retention in self-implanted tungsten," *Journal of Nuclear Materials*, vol. 415, no. 1, pp. S661 – S666, 2011. [Online]. Available: http://www.sciencedirect.com/science/article/pii/S0022311510008305

[160] M. 't Hoen, B. Tyburska-Püschel, K. Ertl, M. Mayer, J. Rapp, A. Kleyn, and P. Z. van Emmichoven, "Saturation of deuterium retention in self-damaged tungsten exposed to high-flux plasmas," *Nuclear Fusion*, vol. 52, no. 2, p. 023008, 2012. [Online]. Available: http://stacks.iop.org/0029-5515/52/i=2/a=023008

[161] V. Alimov, Y. Hatano, B. Tyburska-Püschel, K. Sugiyama, I. Takagi, Y. Furuta, J. Dorner, M. Fußeder, K. Isobe, T. Yamanishi, and M. Matsuyama, "Deuterium retention in tungsten damaged with W ions to various damage levels," *Journal of Nuclear Materials*, vol. 441, no. 1, pp. 280 – 285, 2013. [Online]. Available: http://www.sciencedirect.com/science/article/pii/S002231151300826X (cit. on p. 74)

[162] S. Middleburgh, R. Voskoboinikov, M. Guenette, and D. Riley, "Hydrogen induced vacancy formation in tungsten," *Journal of Nuclear Materials*, vol. 448, no. 1, pp. 270 – 275, 2014. [Online]. Available: http://www.sciencedirect.com/science/article/pii/S0022311514000762 (cit. on p. 74)

[163] S. Markelj, T. Schwarz-Selinger, A. Založnik, M. Kelemen, P. Vavpetič, P. Pelicon, E. Hodille, and C. Grisolia, "Deuterium retention in tungsten simultaneously damaged by high energy w ions and loaded by d atoms," *Nuclear Materials and Energy*, 2016. [Online]. Available: http://www.sciencedirect.com/science/article/pii/S2352179116300692 (cit. on pp. 74 and 108)

[164] L. Gao, W. Jacob, U. von Toussaint, A. Manhard, M. Balden, K. Schmid, and T. Schwarz-Selinger, "Deuterium supersaturation in low-energy plasma-loaded tungsten surfaces," *Nuclear Fusion*, vol. 57, no. 1, p. 016026, 2017. [Online]. Available: http://stacks.iop.org/0029-5515/57/i=1/a=016026 (cit. on pp. 74 and 76)

[165] T. Schwarz-Selinger, "Deuterium retention in MeV self-implanted tungsten: Influence of damaging dose rate," *Nuclear Materials and Energy*, 2017. [Online]. Available: http://www.sciencedirect.com/science/article/pii/S2352179116301922 (cit. on p. 75)

[166] G. D. Temmerman and R. Doerner, "Deuterium retention and release in tungsten co-deposited layers," *Journal of Nuclear Materials*, vol. 389, no. 3, pp. 479 – 483, 2009. [Online]. Available: http://www.sciencedirect.com/science/article/pii/S0022311509004462 (cit. on p. 76)

[167] J. Zhao, Q. Wang, D. Liu, Z. Wang, K. Fang, T. Wang, and J. Kasagi, "Dynamical concentration and static retention of deuterium in tungsten foil studied by low energy D(d,p)T reaction and elastic recoil detection," *Nuclear Instruments and Methods in Physics Research Section B: Beam Interactions with Materials and Atoms*, vol. 360, pp. 139 – 144, 2015. [Online]. Available: http://www.sciencedirect.com/science/article/pii/S0168583X15008046 (cit. on p. 76)

[168] W. Eckstein, C. Garcia-Rosales, J. Roth, and W. Ottenberger, "Sputtering data IPP 9/82," Max-Planck-Institut für Plasmaphysik, Garching, Germany, February 1993. (cit. on p. 108)

[169] B. Tyburska, V. Alimov, O. Ogorodnikova, K. Ertl, K. Schmid, and J. Roth, "Trapping of permeating deuterium in defect induced at the rear side of tungsten samples," *Journal of Nuclear Materials*, vol. 415, no. 1, Supplement, pp. S680–S683, 2011. [Online]. Available: http://www.sciencedirect.com/science/article/pii/S0022311510007464 (cit. on p. 145)

[170] High Voltage Engineering Europa B.V. (HVE), 3812 RR Amersfoort, Netherlands. [Online]. Available: http://www.highvolteng.com/ (cit. on p. 151)

[171] R. Middleton, *A Negative-Ion Cookbook.* BNT TVDG, 1990. (cit. on p. 151)

[172] R. Hellborg, J. McKay, S. Mattsson, M. Eriksson, S. Sorensen, H. R. M. Hyder, K. A. Rezvykh, V. A. Romanov, D. Weisser, L. Rohrer, H. Schnitter, H. J. Whitlow, H. Timmers, V. Liechtenstein, L. Bartha, G. D. Alton, G. C. Harper, J. D. Larson, S. Bazhal, M. Friedrich, M. Roberts,

C. Samuelsson, G. A. Norton, S. Dobrescu, L. Marinescu, A. Gover, Y. Pinhasi, A. D. Roberts, T. E. Barnhart, R. J. Nickles, C. Fahlander, D. Rudolph, L. Corradi, T. Gozani, L. Fifield, J. Keinonen, Y. Zhang, K. Malmqvist, L. Curtis, I. Martinson, and M. Letournel, *Electrostatic Accelerators Fundamentals and Applications*, R. Hellborg, Ed. Springer-Verlag Berlin Heidelberg, 2005, vol. Particle Acceleration and Detection. (cit. on p. 152)

List of Publication

Articles

[1] K. Schmid, J. Bauer, T. Schwarz-Selinger, S. Markelj, U. von Toussaint, A. Manhard, and W. Jacob, “Recent progress in the understanding of H transport and trapping in W,” *Physica Scripta*, vol. submitted, 2017.

[2] J. Bauer, T. Schwarz-Selinger, K. Schmid, M. Balden, A. Manhard, and U. von Toussaint, “Influence of near-surface blisters on deuterium transport in tungsten,” *Nuclear Fusion*, vol. 57, no. 8, p. 086015, 2017. [Online]. Available: http://stacks.iop.org/0029-5515/57/i=8/a=086015

[3] R. Han, F. Blobner, J. Bauer, D. A. Duncan, J. V. Barth, P. Feulner, and F. Allegretti, “Toward interfacing organic semiconductors with ferromagnetic transition metal substrates: Enhanced stability via carboxylate anchoring,” *Chem. Commun.*, vol. 52, pp. 9805–9808, 2016. [Online]. Available: http://dx.doi.org/10.1039/C6CC05009C

[4] T. Sundermann, N. Müller, U. Heinzmann, W. Wurth, J. Bauer, R. Han, A. Kim, D. Menzel, and P. Feulner, “A universal approach to spin selective core-hole-clock measurement demonstrated for Ar/Co(0001),” *Surface Science*, vol. 643, pp. 190 – 196, 2016. [Online]. Available: http://www.sciencedirect.com/science/article/pii/S0039602815002605

[5] B. Wielunska, M. Mayer, T. Schwarz-Selinger, U. von Toussaint, and J. Bauer, “Cross section data for the $D(^3He,p)^4He$ nuclear reaction from 0.25 to 6 MeV,” *Nuclear Instruments and Methods in Physics Research Section B: Beam Interactions with Materials and Atoms*, vol. 371, pp. 41 – 45, 2016. [Online]. Available: http://www.sciencedirect.com/science/article/pii/S0168583X15009222

[6] F. Blobner, P. N. Abufager, R. Han, J. Bauer, D. A. Duncan, R. J. Maurer, K. Reuter, P. Feulner, and F. Allegretti, “Thiolate-bonded self-assembled monolayers on Ni(111): Bonding strength, structure, and stability,” *The Journal of Physical Chemistry C*, vol. 119, no. 27, pp. 15 455–15 468, 2015. [Online]. Available: http://dx.doi.org/10.1021/acs.jpcc.5b04351

[7] P. Feulner, F. Blobner, J. Bauer, R. Han, A. Kim, T. Sundermann, N. Müller, U. Heinzmann, and W. Wurth, “Ways to spin resolved core-hole-clock measurements,” *e-Journal of Surface Science and Nanotechnology*, vol. 13, pp. 317–323, 2015.

[8] F. Roth, J. Bauer, B. Mahns, B. Büchner, and M. Knupfer, “Electronic structure of undoped and potassium-doped coronene investigated by electron energy-loss spectroscopy,” *Phys. Rev. B*, vol. 85, p. 014513, 2012. [Online]. Available: https://link.aps.org/doi/10.1103/PhysRevB.85.014513

Talks

[1] J. Bauer, T. Schwarz-Selinger, K. Schmid, U. von Toussaint, W. Jacob, M. Balden, and U. Stroth, “Deuterium implantation into tungsten at low temperature,” 2016, DPG Frühjahrstagung, Hannover, Germany.

[2] J. Bauer, T. Schwarz-Selinger, K. Schmid, and M. Balden, “Dynamics of hydrogen in tungsten: Measuring the solute deuterium,” 2015, 10^{th} International A. A. Kurdiumov school of young scientists and "Interaction of Hydrogen Isotopes with Structural Material", Moscow, Russia.

Posters

[1] J. Bauer, T. Schwarz-Selinger, K. Schmid, M. Balden, A. Manhard, U. von Toussaint, and W. Jacob, “Influence of near-surface blisters on deuterium transport in tungsten: Experiment and modelling,” 2017, 16^{th} International Conference on Plasma-facing Materials and Components for Fusion Applications, Neuss/Düsseldorf, Germany.

[2] J. Bauer, T. Schwarz-Selinger, and K. Schmid, “Hydrogen isotope exchange in tungsten wiwith the implantation zone at low temperature,” 2016, 22^{nd} International Conference on Plasma Surface Interactions in Controlled Fusion Devices, Rome, Italy.

[3] J. Bauer, T. Schwarz-Selinger, K. Schmid, U. von Toussaint, and W. Jacob, “Investigation of dynamic effects of deuterium in tungsten by TDS and NRA,” 2015, 15^{th} International Conference on Plasma-facing Materials and Components for Fusion Applications, Aix-en-Provence, France.

Acknowledgment

First of all I would like to thank **Prof. Dr. Ulrich Stroth** who gave me the opportunity to pursue a PhD project under his supervision in the "Plasmarand und Wand" (E2M) division of the Max-Planck-Institut für Plasmaphysik. Furthermore, I am very grateful for **Dr. habil. Wolfgang Jacob**, the group leader of the "Plasma-Material-Wechselwirkung in Laborexperimenten" (PWI) group, who has risen my interest to the field of hydrogen isotopes in tungsten and managed to create a scientifically stimulative working environment which I enjoyed very much. I want to thank **Dr. Thomas Schwarz-Selinger** in several aspects. Once, for sharing his knowledge about ion beam analysis, mass spectrometry and UHV technology with me, which were essential for the experiments performed in this thesis. Second, for his commitment and supervision of this PhD project, as well as for his scientific contributions in form of discussions, ideas and technical support. Third, for his positive attitude and his ability to keep me motivated even in the case of scientific setbacks. Moreover, I want to acknowledge **Dr. Klaus Schmid**, who, apart from very fruitful scientific discussions regarding the hydrogen isotope exchange, had the patience to teach me NRADC, SDTrimSP and TESSIM-X, with the latter one requiring phone calls at a nearly daily base. With respect to the operation of the scanning electron microscope, the evaluation and interpretation of the data as well as the sample preparation, I would like to thank **Dr. Martin Balden**, **Dr. Armin Manhard** and **Gabriele Matern**, in addition to their valued scientific contribution. Furthermore, I am very grateful for the scientific discussion with **Dr. Udo von Toussaint**, who was significantly involved in the realization of the urn models used to investigate hydrogen isotope exchange from a combinatorial perspective. The expertise of **Dr. Matej Mayer** in the field of ion beam analysis in general, and the experimental realization of the technique as well as the evaluation of the data with SIMNRA in particular, is gratefully acknowledged on top of the beneficial scientific discussions. I also want to thank the operator team of the tandem accelerator in particular. Without the motivation and commitment of **Joachim Dorner**, **Michael Fußeder** and **Stefan Schindler**, a successful completion of the this PhD project would not be possible. With respect to the operation of the experimental setup used in this study, I am very glad to count on **Till Höschen**, who significantly improved the data acquisition and the manipulator control, and on **Arno Weghorn**, who provided valuable advices on CAD and exper-

iment design. In this context I also want to appreciate the work of **Rupert Brüderl** and the **team of the mechanical workshop** for the realization of those designs. Finally, I want to thank my former and present colleagues, **Dr. Gerd Meisl**, **Dr. Martin Oberkofler**, **Dr. Liang Gao**, **Dr. Karl Krieger**, **Stefan Kapser**, **Georg Holzner**, **Karsten Schlüter**, **Mikhail Zibrov**, **Rodrigo Arredondo Parra**, **Barbara Wielunska**, **Vassily Burwitz** and the **participants of the round table** for their scientific impulses, the lively discussions and the pleasant working atmosphere.
Finally, I am very happy and grateful for the understanding and encouragement by **my family** and my beloved girlfriend **Kristina**, who unconditionally supported me and kept me motivated throughout the ups and downs during my time as a PhD student.